University of Sussex

Mathematical modelling and analysis: adoption of Blockchain-based technologies, and coupled oscillators with distributed delays

Aleksandra Ross

Submitted for the degree of Doctor of Philosophy

University of Sussex

November 2020

Declaration

I hereby declare that this thesis has not been and will not be submitted in whole or in part to another University for the award of any other degree.

Signature:

Aleksandra Ross

Acknowledgements

First and foremost, I would like to thank my supervisor, Dr Yuliya Kyrychko, who offered continuous support, encouragement and invaluable advice. Without her tremendous approachable nature and kind help, this thesis would not have been possible.

I would like to thank EPSRC and American Express for the funding and giving me the opportunity to complete this study. I would also like to thank Dr Otti D'Huys, for her inspiration and guidance. I thank Dr Farzad Fatehi for his time and dedication. I also acknowledge my gratitude towards internal examiner Dr Ali Taheri, external examiner Prof. Jan Sieber, and Chair Prof. James Hirschfeld for taking the time to read this thesis, and making the viva a pleasant memorable experience. I am thankful for the inspiration, brilliance and wisdom of my friends and colleagues at the School of Mathematics and Physical Sciences.

Most importantly, I am grateful for my precious Amrita, family, Anton, Nessi and Bart, and forever thankful for their unconditional love and endless support.

Abstract

The aim of this thesis is to consider the degree to which biological systems and coupled oscillator networks, may be comparable in financial context, and to examine whether epidemiological models developed to explain the dynamics of infectious diseases may be practically applied to financial sectors. Evidently, epidemics and financial crises share certain general features, such as the global spread potential, due to rapid mobility of people, commodities, information and capital. Disease outbreaks may also induce market turbulence, necessitating catastrophic risk management, which is clear from the COVID-19 pandemic. The term financial is used broadly, for instance in Chapter 2 and Chapter 3 we consider Blockchain-based cryptocurrency markets.

Complex systems can be deconstructed into homogeneous interacting subsystems, represented as nodes of a network. The interactions between the subsystems are expressed as links between the nodes. In the case of Blockchain, one type of network would be depicting the blocks as nodes, and links between these blocks representing the chain. Another network would consist of nodes of the network being the users/miners, and the links describing the connections between them. The main idea of a decentralised Blockchain is the dynamical process of information transfer. Analysis of and insights into the Blockchain network is crucial for understanding the dynamics. Dynamics with time delays, as well as latency in the coupling are an important aspect in scientific and technological fields. Our focus for the second part of the thesis is to determine the influence of distributed delays on coupled phase oscillators.

Contents

List of Tables

List of Figures

Chapter 1

Introduction

1.1 Analysis of cryptocurrencies

1.1.1 Review

Over the last decade, researchers have been studying adaptations of epidemiological modelling approach to various kinds of social interactions, such as modelling of dynamics of online social networks, including the adoption and abandonment of such networks, infectiousness of Twitter hashtags, language competition, the dynamics of religious affiliations, the spread of ideas, memes and so forth [47, 128, 27, 104, 141, 38, 78, 140]. This section of the thesis analyses the dynamics of the Blockchain-based cryptocurrencies by adapting mathematical models previously used to successfully describe the spread of epidemics. The population dynamics that governs the adoption and diffusion of new technology has qualitatively similar traits to those observed in the dynamics of disease spreading. In epidemiological setting, the modelling allows one to estimate contact rates, duration of infectious periods, incubation time, and the final size of an epidemic. These quantities can be easily translated into the framework of modelling the adoption of Blockchain-based technology, such as cryptocurrencies, effectively allowing one to estimate the popularity and loss of interest in them.

In many cases, mathematical modelling cannot indicate specifically why the exposure to certain ideas leads to intellectual epidemics or epidemics of social interactions. However, it provides information on their intensity, duration, adoption and loss of interest rates. The simple and well known epidemiological models act as essential starting tools in fields where the concept of 'spreading' is applied, like the rapid diffusion of ideas and technology, this is further highlighted in Chapter 2.

1.1.2 Blockchain

Blockchain [5] is a distributed public ledger, which can be looked at as a list of transactions that is reproduced across a number of computers, instead of being stored on a central server. Blockchain is the technology underpinning many digital currencies, and the technology itself was designed to create Bitcoin. Invented by Satoshi Nakamoto in 2008 [108], Blockchain is seen as the main technological innovation of cryptocurrencies, since it stands as proof of all the transactions on the network. However, what is stored on the Blockchain does not have to be a currency unit - there is a myriad of other applications, such as smart contracts, digital signatures and identities, decentralised notary, and digital voting.

Blockchain applications are still being explored by companies and enthusiasts [8]. The trustworthy nature of Blockchain is of interest to many and can potentially have several applications. We predict that Blockchain is here to stay and it will transform how the digital society functions. Currently, various financial institutions are in the process of considering how Blockchain, the technology underpinning digital currencies, could in itself reshape the financial industry [6, 26].

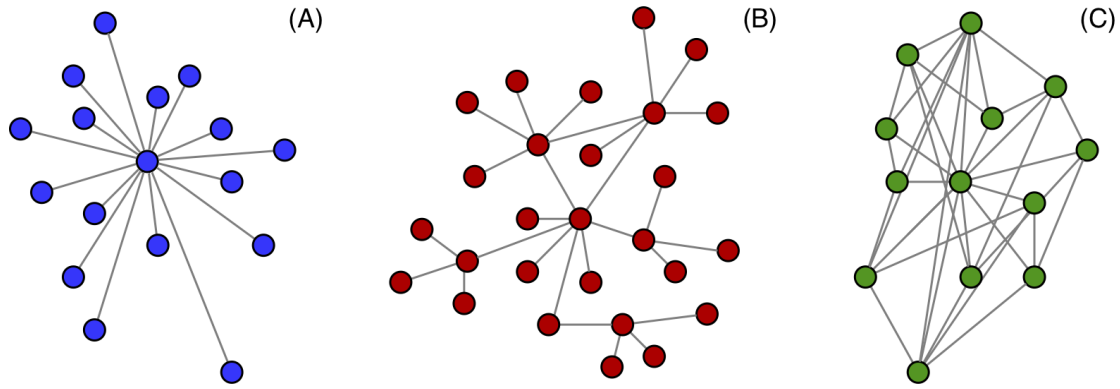

Figure 1.1: Types of ledgers: (A) centralised, (B) decentralised, (C) distributed.

A Blockchain consists of blocks containing specific transactions in a particular order, with computers linked to each other (as seen in Fig. 1.1 (C)) instead of a central server, making the Blockchain decentralised. Each and every node, or in other words participant, maintains, updates, and approves new entries. By having all the blocks in a chain, all nodes have the full history of transactions. This is in contrast to centralised systems (as demonstrated in Fig. 1.1 (A)), where the database is a snapshot of information at a specific point in time, and it is more prone to hacks and data leaks as there is one single point of failure. The members of a Blockchain network ensure that all blocks are in order, resulting in data validity and security. The nodes that perform this verification process are also

referred to as miners. After completing the verification process, known as Proof of Work, the nodes receive a reward; in some cases, such as Bitcoin and Ethereum (cryptocurrencies based on Blockchain), only the first miner receives this reward. New nodes joining a peer-to-peer (P2P) Blockchain network, receive a full copy of the chain. Fig. 1.2 encapsulates the process of adding a new transaction in a Blockchain network.

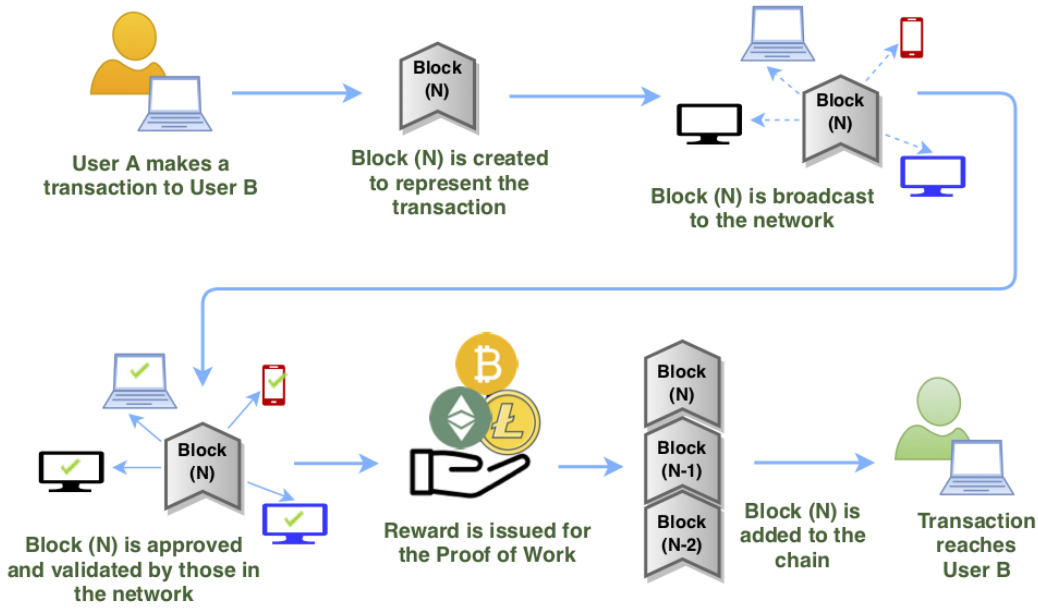

Figure 1.2: Schematic diagram of Blockchain transaction.

Blockchains are distributed; data is consensually shared and synchronised across the nodes in the network. By being a distributed ledger, Blockchain provides transparency, trust and data security. Blockchain can be either public or private; in many public Blockchains, the users are anonymous, whereas in private Blockchains, the users are not anonymous [32, 77, 103]. A common misconception is that users are identifiable in public Blockchains, however the word 'public' here means that the Blockchain network is fully decentralised; it can be joined by any individual, and the data can be viewed by all. Upon joining a public Blockchain, users receive a unique identity number, ensuring that the identity of that user remains unknown to others. Private Blockchains on the other side, are not open for everyone and a single organisation has authority over the network, meaning the entity of authority can control users' access to information.

Each block contains the hash of the block, the hash of the previous block, and some data that is relevant to that type of Blockchain. For example, in Bitcoin, this would be data about the receiver, sender and the amount of coins. Including the hash of the previous block is one of the main elements behind Blockchain's architecture, as it is what ensures a chain of blocks. Fig. 1.3 illustrates these elements in the first three blocks of a Blockchain.

The first block in the chain, sometimes referred to as the Genesis block, has no previous hash value [32].

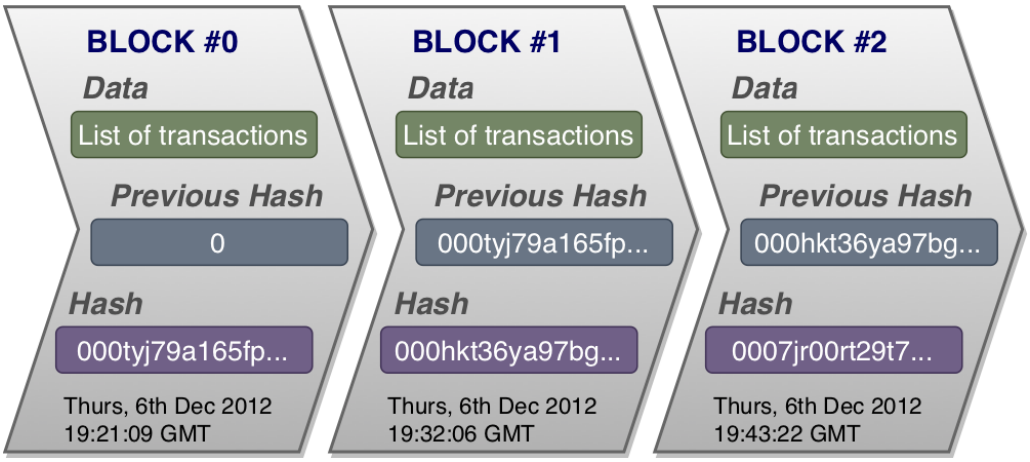

Figure 1.3: Blockchain structure example.

A hash is a sequence of some digits and letters. Each block hash is generated using a cryptographic hash, for example the one-way SHA-256 function. Each hash is almost unique, so it helps identify each block in the chain. Hashes are attached to blocks as soon as they are created or subsequently updated. This means that hashes allow easy detection of changes in blocks. The miners combine a random, whole number called nonce with the list of transactions in the block, to calculate a hash (using SHA-256 function or similar); this process is repeated for a number of nonce values until the miner finds a hash that is lower or equal to that set by the network difficulty. Searching for this low hash means miners will often test and discard millions of nonces, per second, before they find a hash that meets the network's requirements of n leading zeroes in the hash.

With most websites nowadays using ads to generate revenue, the concept and techniques considered in Chapter 2 could be used to monitor advertisement coverage, information spread to the intended user, and ad effectiveness [7, 111]. The application of Blockchain in digital advertising is quite significant, with many marketing companies looking into digital advertisement using the new technology. Blockchain advertising in marketing enables data to be trustworthy for all involved parties (ad buyer, publisher, consumer). Ad buyers can view the performance of their ads, and therefore determine if an ad is effective. The Blockchain structure means that records are tamper-proof, and can only be accessed by those who have the permission, making digital advertisement with Blockchain a solution that consumers can trust. Decentralised platforms running on Blockchain provide transparency and real-time tracking; it can also cut out the middlemen, meaning advertisers can buy ads directly from publishers. All this reduces the amount of fraud,

which is very common and comes at a high cost to advertisers.

At least 15 countries, including Russia, USA (West Virginia, Utah), Estonia, Sierra Leone, have conducted digital voting on various levels since 2018 [82]. The city of Zug in Switzerland did a successful experimental trial in 2018. The decentralised nature of Blockchain technology makes it suitable for many applications where trust is vital, whether that is in voting, finance, or advertisement.

1.1.3 Cryptocurrencies

Cryptocurrencies are digital money created from code, used in an autonomous P2P system, without bank/government dependencies. The initial release of Bitcoin was in 2009, and its success led to emergence of other alternative cryptocurrencies, referred to as Altcoins [146, 147, 148]. There are well over 3000 Altcoins on the market, most of which rely on the same or similar Blockchain technology as Bitcoin. Some of the cryptocurrencies considered in this research are Litecoin emerged in 2011, Mastercoin and Peercoin in 2012, and Ethereum in 2015.

We use data from 2013 onwards, and consider a five-year period in our initial analysis in Chapter 2. In Chapter 3, we revisit this topic to analyse segments of data up to 2020 and draw comparisons to our initial analysis. Although there exist cryptocurrencies which are not based on Blockchain technology (Ripple, IOTA and Byteball to name a few), in this thesis we will mainly be looking at Blockchain-based cryptocurrencies, and briefly consider Ripple in Chapter 3 to show that it follows similar trends.

Table 1.1: Cryptocurrency characteristics

Cryptocurrency	**Mechanism**	**Block creation**	**Max supply**
Bitcoin (BTC)	PoW	10 min	21 million
Litecoin (LTC)	PoW	2.5 min	84 million
Ethereum (ETH)	PoW $\rightarrow$ PoS	15-17 sec	Unlimited
Peercoin (PPC)	PoW & PoS	10 min	Unlimited
Mastercoin/OMNI (OMC)	PoW	3 min	620K
Ripple (XRP)	BC	3-5 sec	100 billion

Table 1.1 presents the characteristics of cryptocurrencies considered in our analysis, such as the duration of a block creation, the block generation mechanism, and the maximum coin supply. The block generation mechanisms, i.e., consensus mechanisms, in the table

are Proof-of-Work (PoW), Proof-of-Stake (PoS), Delegated Byzantine Consensus (BC). Ethereum is in the process of moving to PoS protocol (2020), Peercoin uses combination of PoW and PoS.

As reflected in Table 1.1, Bitcoin has a limited total coin supply, many other cryptocurrencies have followed the same path by capping the maximum limit. For those with a limited supply, i.e., Bitcoin, Litecoin, Ripple, the coin growth rate decreases over time, and upon reaching the maximum limit will converge to zero. The fixed supply differs for each cryptocurrency, as well as the block creation speed, hence some will reach the set maximum faster. Some Altcoins regulate the growth rate and the total amount of coins, i.e., Ethereum and Peercoin have an unlimited total supply. The scarcity of these is ensured by imposing an annual limit, so only a certain number of coins can be minted. By controlling the scarcity, the relative growth rate decreases over time, as there are fewer coins to mint [4].

Supply limit inevitably has an effect on cryptocurrency price. Unlike fiat currencies, this supply limit is not controlled by a centralised financial authority or government, but rather by the software algorithm. The algorithm is publicly known to all involved participants, made available from the cryptocurrency launch.

A limited supply encourages individuals to adopt faster; the incentive there, is to acquire as soon as possible in order to take advantage of potential future price increase. On the other side, the expectation for Altcoins that have an unlimited supply is that the cryptocurrencies will be inflationary in the first few years after they are launched, however eventually they will be deflationary if their demand increases sufficiently high.

Cryptocurrency adoption is on the rise, and the number of vendors/retailers that accept cryptocurrencies is constantly growing. Fiat currencies are dominated by the banks, and users must therefore trust banks. However, it is not uncommon for banks to lose accounts, payments, transfers, and such; centralised banks have a single point of failure. Blockchain technology is safe and secure, the wallet is in possession of the user, and the user is fully responsible for storing it safely (offline, encrypted, taking regular backups).

Fintech companies like Revolut are providing their customers with the ability to exchange between fiat and decentralised cryptocurrencies built on top of Blockchain. This reduces the barrier to entry as there is no requirement to mine for cryptocurrencies or consider cryptocurrency exchange platforms. What started of as a fiat currency exchange platform now also incorporates digital currencies, accessible to all types of individuals including those who are not particularly tech-savvy or looking to invest.

1.1.4 Mining

Mining involves attempting to find a numerical value, known as a nonce, that when combined with all open transactions can be hashed into a value that satisfies a certain complexity. Although calculating these numerical values is possible by almost any computer, having a set of GPUs (graphics processing units) that have a high hash rate (h/s, or hashes per second) improves the chances of being a successful miner (where the total value of the mined coin(s) outweighs the overheads of running the computer).

Blockchain mining is a process of yielding an encrypted string of data, known as hash. Bitcoin mining is the process of adding transaction records to the Blockchain. Bitcoin nodes use the Blockchain to distinguish legitimate Bitcoin transactions from attempts to double spend coins. Miners maintain a complete copy of the Blockchain and monitor the network for recently reported transactions, they then perform work in an attempt to fit all new and valid transactions into the current block. Since the number of Bitcoins is limited, the faster the calculation, the more coins can be collected by a miner.

The measure of complexity of finding a new block is recalculated every 2016 blocks, to a value such that the previous 2016 blocks would have been generated in exactly two weeks at this level of difficulty, which yields around one block every 10 minutes for Bitcoin and Peercoin, 10-20 seconds for Ethereum, and 2.5 minutes for Litecoin, as outlined in Table 1.1. With more new miners joining the network, the rate of block creation will go up, with the rate of mining going up accordingly, and the difficulty of block generation increasing as a consequence, pushing the rate of block creation back down. Blocks that do not meet the required complexity target will be rejected by everyone on the network, making them worthless.

1.1.5 Wavelet analysis

This section holds a summary of wavelet methodology, which we employ in Chapter 2 and Chapter 3. We make use of cross wavelet coherence analysis which can localise correlations between series and evolution in time and across scales. Short term dynamics of the time series can be analysed by observing the lower scales, and the long term dynamics with the high scales. A wavelet [112] is a complex-valued square integrable function which has the form

$$\psi_{u,s}(t) = \frac{1}{\sqrt{s}}\psi\left(\frac{t-u}{s}\right) \tag{1.1}$$

where s is scale (width of the wavelet), u is location, and t is time. Wavelets are functions

consisting of time and frequency domain components. In visual terms, this would appear as wave-like oscillations, standardly normalised around the zero mean,

$$\int_{-\infty}^{+\infty} \psi(t)dt = 0, \text{ and } \int_{-\infty}^{+\infty} |\psi|^2(t)dt = 1.$$

The projection of a wavelet $\psi(.)$ on the examined series $x(t)$ gives us a continuous wavelet transform $W_x(u,s)$, where $\psi^*(.)$ is a complex conjugate of $\psi(.)$,

$$W_x(u,s) = \int_{-\infty}^{+\infty} \frac{1}{\sqrt{s}} x(t)\psi^*\left(\frac{t-u}{s}\right)dt. \tag{1.2}$$

Original series can be reconstructed from the continuous wavelet transforms for given frequencies without any information loss. There exist a range of complex-valued wavelets that allow for a multivariate analysis. The Morlet wavelet [30, 71] provides a good balance between time and frequency localisation; therefore we conduct our analysis with the Morlet wavelet option using the Matlab package [71]. Morlet wavelet can be written as

$$\psi(t) = \pi^{-\frac{1}{4}} \exp(i\omega_0 t) \exp\left(\frac{-t^2}{2}\right), \tag{1.3}$$

where ω_0 is the central frequency of the wavelet. Setting $\omega = 6$ provides a good balance between time and frequency localisation [71, 124, 138, 31].

We employ the wavelet squared coherence to assess the cross-correlation behaviour over time and frequency. The continuous wavelet framework allows examining the relationship between two time series in time and across scales by generalising for a bivariate case. A continuous wavelet transform is generalised into a cross wavelet transform as

$$W_{xy}(u,s) = W_x(u,s)W_y^*(u,s), \tag{1.4}$$

with $W_x(u,s)$ and $W_y(u,s)$ as cross wavelet transforms of time series $x(t)$ and $y(t)$, and the asterisks denoting the complex conjugate [135].

The cross wavelet power $|W_{xy}(u,s)|$ is often used as a measure of co-movement between two time series since the cross wavelet transform is in general complex. The cross wavelet power exposes time-frequency space regions where the series have a common high power, and therefore it can be understood as a covariance localised in the time-frequency space. As for the standard covariance, however, the explanation power of $|W_{xy}(u,s)|$ is limited as it is not bounded. Taking this factor into account, the wavelet coherence is defined as

$$R^2_{x,y}(u,s) = \frac{|S\left(\frac{1}{s}W_{x,y}(u,s)\right)|^2}{S\left(\frac{1}{s}|W_x(u,s)|^2\right)S\left(\frac{1}{s}|W_y(u,s)|^2\right)}, \tag{1.5}$$

where S is a smoothing operator [136, 71]. The squared wavelet coherence can be interpreted as a square correlation localised in time and frequency, ranging between 0 and 1. However, the information about the direction of the relationship is lost. Consequently, a phase difference is introduced as

$$\phi_{x,y}(u,s) = \tan^{-1}\left(\frac{\mathcal{I}\left[S\left(\frac{1}{s}W_{xy}(u,s)\right)\right]}{\mathcal{R}\left[S\left(\frac{1}{s}W_{xy}(u,s)\right)\right]}\right), \tag{1.6}$$

where $\mathcal{I}$ is an imaginary part operator, and $\mathcal{R}$ is a real part operator, and $\phi_{x,y} \in [-\pi, \pi]$ [71, 87].

A phase difference of zero indicates that the time series move together at the specified frequency. A phase difference of π indicates an antiphase relation. Phase differences are indicated by the arrows in the wavelet coherence plots. Arrows pointing to the right indicate positive correlation (in-phase); arrows pointing to the left indicate negative correlation (antiphase). Arrows pointing down mean the first series leads and the second lags, and conversely, arrows pointing up mean that the second series leads the first. Often, the relationship is a combination of the two. Arrows point up and right when the series are positively correlated and the second series leads the first. The interpretation of phase relationships is partially dependent on specific expectations about the relationship; a leading relationship in in-phase can be a lagging relationship in the antiphase [71].

Wavelet Applications

The applications of wavelet and spectral methods for the study of nonlinear and dynamical processes in economics and finance are on the rise, with the recent developments including analysis of business cycles, asset prices, financial econometrics, and forecasting [64].

Aguiar-Conraria *et al.* [30] were one of the first to use cross-wavelet tools in an economic setup, to show that the relation between monetary policy variables and macroeconomic variables has changed and evolved with time. The authors illustrate how wavelet analysis can naturally be applied to the study of business cycles due to their periodic nature, or to any field of economics, or finance, especially when there is a distinction between short term and long term relations. Yang *et al.* [151] investigate the contagion and interdependence

of foreign exchange markets using the wavelet coherence analysis. Barunik *et al.* [37] use wavelet power spectra and wavelet coherence to uncover interesting dynamics of cross-correlations between Central European and Western European stock markets.

Krištoufek [87] applies wavelet coherence analysis techniques to study the potential drivers of Bitcoin prices, ranging from fundamental sources to speculative and technical ones, as well as the possible influence of the Chinese market. The author concludes that the Bitcoin forms a unique asset possessing properties of both a standard financial asset and a speculative one.

Phillips *et al.* [114] investigate whether relationships between online factors and price are dependent on market regime. Similarly to analysis conducted by Krištoufek [87], the authors use wavelet coherence to study co-movement between a cryptocurrency price and its related factors, they also test for financial asset bubbles to explore whether relationships change dependent on regime.

Mensi *et al.* [105] use wavelet transform approaches to show that a mixed portfolio, i.e., Bitcoin with other cryptocurrencies provides better diversification benefits for investors and portfolio managers. More recently, Goodell *et al.* [69] applied wavelet methods to daily data of COVID-19 world deaths and daily Bitcoin prices, their findings include that levels of COVID-19 caused a rise in Bitcoin prices.

1.1.6 Data

Interest data analysed in this thesis was retrieved from Google Trends [9] (GT). CoinMarketCap [14] was used for the daily closing price index (in USD) and market capitalisation data for each coin, therefore allowing us to calculate the number of coins in circulation (supply). As we are exploring a period of over 8 months, for higher accuracy, we downloaded daily interest data from GT in 8 month sections and rescaled, before chaining the sections. The raw data from Google Trends and CoinMarketCap, utilised in Chapters 2 and 3, can be found in an online repository [123].

Data transformation

Google Trends data, historical price and market capitalisation data are all non-stationary time series since they clearly exhibit trending patterns. The raw time series can be multimodal (multiple different maxima), which are not ideal for use in wavelet analysis [71]. For this reason, we transform this non-stationary data to stationary. There are a few possible ways to do so, we use the log return approach. Multiplicative relationships can

be transformed to additive relationships using logs, since $\log(xy) = \log(x) + \log(y)$. Likewise, logs convert exponential growth or decay, typically seen in financial/economic time series, to linear trends, enabling the use of linear models to understand the behaviour. Log returns are calculated by

$$Returns(i) = \log\left(\frac{x_i}{x_{i-1}}\right),$$

where x_i is the GT search interest, price index, or supply at timestep i. Log returns are stationary because they tend to oscillate around a mean. Properties of stationary time series do not depend on time at which the series is observed, and therefore the time series can be considered as growth rates rather than absolute values. Log returns are a common choice for modelling financial time series, due to their characteristics. They are additive, which makes them easier to compute.

1.1.7 Models

In this section, we review variations of SIR type models recently used to study spreads and forecasting predictions. In a network context, there are similarities between information diffusion and spreading of disease in a population. Epidemiological models are becoming increasingly popular in publications, not only in mathematics and biology, but also in generalist journals. It is interdisciplinary with applications in several fields where there is a concept of spreading. The SIR model is one of the base models for modelling an epidemic, it was introduced in 1927, by Kermack and McKendrick [83]. This is a compartmental model and it considers an individual to be in any one of three states based on their role in disease spread, S (susceptible), I (infected) and R (recovered). These compartments are functions of the time t, and change according to a system of differential equations. We will be applying a variation of the SIR model in Chapter 2 to cryptocurrency interest data.

New adaptations of the model have been experimented with, to study social interactions. Social networks such as Facebook, Twitter and Instagram provide users with a platform through which they can broadcast information. The use of epidemiological models to study the take-up/abandonment of social networks, information diffusion through these networks, and use of social networks for viral marketing to share product information has been vast in literature [47, 110, 52, 153, 119]. These networks can often be taken advantage of to spread rumours and misinformation.

Zhao *et al.* [153] extend the classical SIR model to study rumour spreading, they combine the impacts of temporal lag, spatial diffusion, media coverage. The study shows that the direct link from the 'ignorants' to the 'stiflers' advances the rumour terminal time

and reduces the maximum rumour influence. In addition, the forgetting and remembering mechanisms of 'hibernators' postpone the rumour terminal time and reduce the maximum rumour influence.

Nekovee *et al.* [110] introduce a new model of rumour spreading on complex networks by unifying the MK model of rumour spreading with the SIR model of epidemics. Their study shows that scale-free social networks are prone to the spreading of rumours, just as they are to the spreading of infections. They are relevant to the spreading dynamics of chain emails, viral advertising and large-scale information dissemination algorithms on the Internet.

Cannarella *et al.* [47] modify the traditional SIR model by incorporating infectious recovery dynamics, to describe the adoption and abandonment dynamics of user activity of online social networks. The proposed $irSIR$ model is validated using publicly available Google search query data for 'MySpace' as a case study of an online social network that has exhibited both adoption and abandonment phases, it is then applied to search query data for 'Facebook'.

Fibich [59] considers the diffusion of new products in social networks, where consumers who adopt the product can later 'recover' and stop influencing others to adopt the product. The author shows that the diffusion is described by the Bass-SIR model, which combines the Bass model for diffusion of new products with the SIR model for epidemics. It is concluded that diffusion in the proposed model only depends on the local structure of the social network, but not on the average distance between consumers.

Bettencourt *et al.* [38] proposed the $SEIZ$ (susceptible, exposed, infected, skeptic) model to quantify behavioural patterns, by capturing the adoption of Feynman diagrams using the publication counts after the second World War. They extract the general features for idea spreading and estimate the idea adoption process, concluding that the $SEIZ$ model can fit the long term idea adoption process with reasonable error.

More recently, Mutlu *et al.* [107] tackle the problem of predicting information cascades by presenting a novel variation of $SEIZ$ model that takes into account the cognitive processing depth of users. Information cascade is defined as the set of reactions from social media users to the original content which requires at least minimal physical and cognitive effort, their framework is tested on 1000 Twitter cascades.

Hill *et al.* [76] evaluate the spread of long-term emotional states across a social network. A novel form of the classical SIR disease model is introduced which includes the possibility for 'spontaneous' (or 'automatic') infection, in addition to disease transmission.

The authors show that long-term emotional states can spread between socially connected individuals, giving insight into the transmissive nature of positive and negative emotions.

Rodrigues *et al.* [120] apply SIR model to study the effects of a viral marketing strategy, conducting a set of simulation experiments to explore the influence of several controlled and external factors that could influence viral campaigns. The study exposes marketing implications identifying a number of strategies that can optimise marketing communication tool.

In psychology, there have been studies in how and why an individual's behaviour changes in response to behaviour of other members in the social group. A distinct attitude in a few individuals can rapidly spread to other individuals. Bayesian model selection approach has been applied by Mann *et al.* [101] to study the dynamics of how social cues can induce a spread of social behaviour in a group of people. It was found that depending on the set of infected people, clapping in an audience can vary, even when other parameters, such as presentation quality, are kept constant.

Funk *et al.* [63], explore the concept of epidemiology in the human behaviour when public campaigns and mass media reports are diffused, they describe the dynamics of disease spread, focusing on the relation between awareness and proximity of disease in the network. The authors conclude that changes in host behaviour can be triggered by public campaigns and mass media reporting, and also by person-to-person communication and influence from peers.

SIR type models have also been applied to investigate properties of file distribution in P2P networks. Lebnitz *et al.* [96] proposed an adapted SIR model (IDS) for file diffusion P2P file-sharing network based on biological epidemics. In P2P networks, the peer shares the downloaded parts of a file with other nodes in the network, therefore contributing to the distribution of the file within the network.

The SIR model considered in this thesis is quite successful in reproducing and explaining the real-world dynamics and behaviour of large populations for which the assumption of full mixing is a good approximation. However, despite the success and usefulness of applying fully mixed compartmental models to large populations, their utility tends to reduce significantly as population size decreases and network structure increases. To address the above, we will study smaller networks, in particular coupled oscillators in the second half of the thesis, as this would allow for modelling a number of interactions, unlike compartmental models, which treat individuals as well mixed.

1.2 Coupled oscillators and their synchronisation

This section of the introduction will cover synchronisation [115] phenomena in systems of coupled oscillators, and outline the earlier contributions to the field by Winfree [144, 145], Kuramoto [88, 89] and others. Introducing the Kuramoto order parameter as a measure of coherence, we discuss the effects of delayed coupling. In Chapters 4-6, we introduce systems of coupled phase oscillators and study the effect of distributed time delays [81, 56, 60].

We can define complex systems as a network [34, 132], where each node in the network is an oscillator, i.e., a dynamical process, and the network topology describes which oscillators interact with each other [40]. Using networks to depict complex systems enables us to study the relation between the dynamics and its topology. The autonomously oscillating parts interact and as a result, can lead to organised collective behaviour, like synchronisation.

Synchronisation occurrence in large populations of interacting elements is encountered in different disciplines such as physics, ecology, engineering, economics and social sciences [115, 133, 53, 67, 95, 57, 33, 72]. The concept of coordinated motion has been a subject of intense research efforts over the past years; a successful approach to the problem of synchronisation involves modelling each member of the population as a phase oscillator. The technological advancements over the years have facilitated modelling of oscillatory networks.

Systems of coupled oscillators [134] have been used to describe a variety of phenomena in scientific fields, ranging from brain activity behaviour to network modelling [152, 131, 143, 62, 122]. Research in this field allows for development in understanding of how a group of moving objects, such as murmuration of starlings, flocks of fireflies, crowds of people, or collections of autonomous robots can reach a consensus and move in formation without centralised coordination [115]. Synchronisation in complex systems occurs when the behaviour of the nodes in the network adjusts to that of other nodes [132]. Christiaan Huygens [115] was one of the first to record his observations on synchronisation, when he noticed two pendulum clocks hung on a wooden beam move in opposite swings concurrently. The oscillations of the pendulum interacted with the clocks, which in turn interacted with the wooden beam. These motions of the beam caused the pendulums to have exactly contrary swings - a phased-locked state of the system.

In 1967, Winfree proposed that large systems of interacting oscillators can be used to model many rhythmic processes in biology [144]. Winfree found that organised collective behaviour and formation of patterns are possible, even when there are differences between oscillators. Inspired by Winfree's work, in 1975, Kuramoto proposed a tractable model

for oscillator synchronisation, that has become one of the most representative models of coupled phase oscillators [88].

1.2.1 Oscillators in business and finance

We look at a few examples of work conducted in fields related to business and finance. Groth and Ghil [72] studied dynamical properties of business cycle fluctuations by applying the methodology of multivariate singular spectrum analysis to identify oscillator modes and to establish whether the modes are shared by clusters of phase- and frequency-locked oscillators. Yuichi *et al.* [152] analysed gross domestic product time series to find entrainment and partial phase locking to be direct evidence of synchronisation in business cycles. Synchronisation is explained by developing a coupled limit-cycle oscillator model, where the interaction due to international trade is interpreted as the origin of the synchronisation.

Financial markets can be thought of as complex systems with autonomous oscillating parts. Peron and Rodrigues [113] studied the time evolution of the phase coherence among stock prices, and verified that a synchronous state emerges in the system during financial crisis, influencing the market's direction. Financial asset price formation is dependent on human decision; every trade is a result of a human deciding to make the trade, or, by an algorithm developed by a human. Synchronisation in human decision making could therefore have a large impact on asset prices; research in this area is emerging.

Massad and Anderson [102] discuss three different pathways, in which financial markets can experience turbulent periods and contagion phenomena due to the synchronisation of human decision-making. The first pathway is caused by synchronisation of stock market indices, which are seen as a collection of coupled integrate-and-fire oscillators. Humans have a tendency to ignore small changes but act when a large change occurs, known as 'change blindness'. The integrate-and-fire dynamics is an effect of this 'change blindness'. The second pathway occurs as a result of feedback mechanisms between market performance and the use of certain decoupled trading strategies. The third pathway happens as a consequence of communication and its impact on human decision-making.

1.2.2 Network topology of cryptocurrencies and decentralised technologies

Blockchain technology has many similarities with networks. The structure of Blockchain itself is a type of network as the topology is a chain, with each node (block) linked to the next in a linear sequence, with the first and last nodes (blocks) having just one link

and the rest having two links. Additionally, the miners/users of Blockchain are connected to one another in a decentralised, P2P network; each miner/user can be represented as a node in the network. Depicting Blockchain/cryptocurrencies as networks and analysing their characteristics is an area that would benefit from further exploration.

The public availability of cryptocurrency transactions enables these financial interactions to be modelled as a complex network. This allows studying the Blockchain graph as well as the relationship between the Blockchain network features and cryptocurrency risk investment. Dey *et al.* [50] use this data to expand the ideas of network motifs and introduce a novel concept of chainlets, or Blockchain motifs, for cryptocurrency predictive analytics.

Past studies on correlations of financial markets have revealed collective market behaviour and strong correlations. Stošić *et al.* [129] use methods of random matrix theory and minimum spanning trees (MST) to analyse cross correlations between price changes of various cryptocurrencies. Analysis of these correlations allows to quantify the collective behaviour among constituents in the cryptocurrency market.

MST is also utilised by Francés *et al.* [61] to examine the cryptocurrency market and its dependencies, by modelling the graph nodes as cryptocurrencies and links constructed from the Pearson correlation matrix. By constructing a network in which nodes interact and affect each other, allows analysing the degree of co-operations between the cryptocurrencies and identifying the currencies that have greater influence on the price and market evolution.

The value of correlation networks as a tool for visually exploring interconnectedness of cryptocurrencies is highlighted by Burnie [46]. This study uses correlation networks to evaluate characteristics which may potentially impact the fluctuation of cryptocurrency prices. The paper provides evidence to suggest that token creation mechanism and token functionality are not particularly important determinants.

Jian and Dandan [79] summarise research outcomes of P2P networks from the perspective of complex network theory and state that there are many directions which can be further explored such as studying large scale P2P networks, to find the degree of influence of different nodes to the behaviour of network topologies and interaction between nodes. Ethereum is analysed by modelling the system as a complex network, by Ferretti and D'Angelo [58]. The accounts are defined as nodes, and the interactions between these accounts, recorded on the Blockchain, are modelled as links in the network.

1.2.3 Coupling topology and delay in the coupling

Coupling, delay, and topology are the three main factors characterising the interaction in a system of coupled oscillators [34, 99]. Displayed in Fig. 1.4, are the two examples of coupling topologies considered in Chapters 4-6, two mutually coupled oscillators with and without feedback.

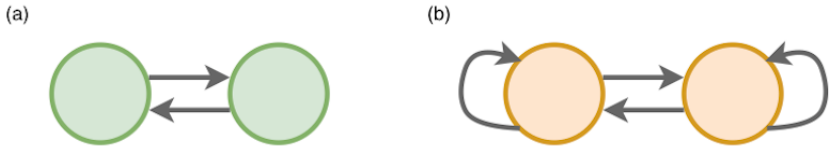

Figure 1.4: Schematic diagram. (a) Two mutually coupled oscillators. (b) Two mutually coupled oscillators with self feedback.

Information exchange between two different elements in a system involves the propagation of a signal with a finite speed, causing a communication delay [34]. Often, this delay cannot be ignored as it may lead to new phenomena not otherwise present in the description. Delays can occur naturally or be artificial in a range of applications [56].

Delay systems are often categorised as discrete, or distributed [55, 90]. With discrete delays, only the state at one past time is considered for the present time evolution, since the assumption here is that all delays are equal and constant. Discrete delays in the coupling of coupled phase oscillators also contribute to effect like the multistability of steady states [51]. In real world applications, the processing delay rarely has the same length at every time step, but instead follows a distribution with some mean value [55]. In this thesis our focus will be on distributed-delay systems.

Systems of almost identical oscillators that are weakly coupled are commonly expressed as Kuramoto oscillators, which assume that each oscillator has its own natural frequency associated with it, and information exchange between the oscillators is sinusoidally related by the phase difference between the oscillators. A phase-locked solution is when all oscillators are completely synchronised; the oscillators share the same frequency and each cycle of oscillations starts at the same time [115]. It is also possible to have synchronised states where oscillators share the same frequency however the cycles of oscillations do not start at the same time, but start in a defined relation that is constant in time. The Kuramoto order parameter must be adapted in order to determine these different states.

1.2.4 The Kuramoto order parameter

The Kuramoto order parameter is a measure of synchrony in systems of interacting oscillators,

$$r(t)e^{i\psi(t)} = \frac{1}{N}\sum_{j=1}^{N} e^{i\theta_j(t)}, \tag{1.7}$$

where we have $\theta_j(t)$ as the phase of individual oscillators at time t, with $j = 1, 2, \ldots, N$, and N being the number of oscillators in the system. $\psi(t)$ and $r(t)$ denote the mean-field in systems where all members are connected to each other, $r(t) \leq 1$ being the measure of phase coherence, and $\psi(t)$ the average phase. The order parameter is a complex number and defined as the normalised sum over the real and imaginary parts of all phases in complex plane.

The order parameter achieves its maximum $r = 1$ when all the phases are identical, it achieves its minimum $r = 0$ when the phases are balanced around the circle, such as evenly spread or in clusters that balance each other out. The parameter $r(t)$ is a synchrony measure of the population of oscillators often referred to as the phase coherence. Fig. 1.5 illustrates the dynamics of two coupled oscillators, cases (a) and (b) will be considered in Chapters 4-6.

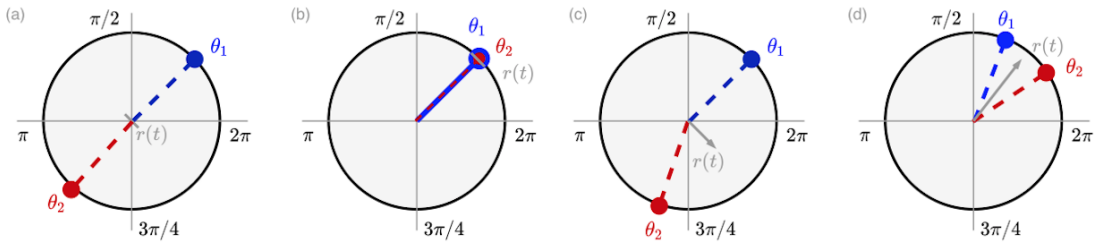

Figure 1.5: Schematic diagram for varying $r(t)$ for a system of two coupled oscillators. (a) Oscillators θ_1 and θ_2 are in antiphase, hence the order parameter is zero. (b) Oscillators θ_1 and θ_2 are in-phase, hence the order parameter is one, (c) Oscillators θ_1 and θ_2 are almost in antiphase, resulting in a small order parameter larger than zero. (d) Oscillators θ_1 and θ_2 are closer together resulting in a larger order parameter (closer to one).

1.2.5 Systems of N coupled phase oscillators with discrete and distributed time delays

This section introduces systems of coupled phase oscillators with discrete and distributed delays in the coupling function. We consider the case of discrete delays first,

$$\dot{\theta}_i(t) = \omega_0 + \frac{K}{K_i}\sum_{j=1}^{N} A_{ij} f\big(\theta_j(t-s) - \theta_i(t)\big), \tag{1.8}$$

where, $\theta_i(t)$, with $i = 1, 2, \ldots, N$, represents the phase variables of the individual oscillators at time t. The number of oscillators in the system is represented by N. K_i corresponds to the number of connections oscillator i has to other oscillators in the system. The coupling strength, described by K, couples an oscillator to its neighbours; f is a 2π-periodic coupling function; ω_0 is the natural frequency of the identical oscillators. The connectivity topology of the system is represented by the adjacency matrix $A_{ij\geq 0}$, which holds the information about all connections between the oscillators in the system, where A_{ij} are either one, if oscillator i is connected to oscillator j, or zero otherwise, $K_i = \sum A_{ij}$ is the total input received by the ith oscillator. Next, we consider the cases of distributed delays

$$\dot{\theta}_i(t) = \omega_0 + \frac{K}{K_i}\sum_{j=1}^{N} A_{ij} f\bigg[\int_0^{\infty} g(s)\theta_j(t-s)ds - \theta_i(t) - \beta\bigg], \tag{1.9}$$

where, $\theta_i(t)$, N, K_i, ω_0, K, A_{ij}, f are as above; $g(s)$ is the delay distribution, and β is the coupling phase parameter, which introduces a phase shift in the coupling function f. In the case of sinusoidal coupling function $f(\theta) = \sin(\theta)$, $\beta = \pi$ leads to repulsive coupling, the effects of which we consider later on in the thesis.

$$\dot{\theta}_i(t) = \omega_0 + \frac{K}{K_i}\sum_{j=1}^{N} A_{ij} \int_0^{\infty} g(s) f\big(\theta_j(t-s) - \theta_i(t)\big)ds, \tag{1.10}$$

taking the integral outside the coupling function f is the alternative implementation of distributed delays, which corresponds to independently assessed signaling events.

1.2.6 Distributed time delays

One can expect that exchanging information physically, or even digitally, takes some time - when a system is modelled with differential equations, a delay term is induced to represent this time delay. Therefore, time delays are ubiquitous [60, 81]. There are many biological and physical models where taking time delays into consideration is vital, a number of those assume that the delay is fixed, i.e., discrete delay models. Quite often it is more likely

that the delay will vary, hence some systems include distribution of delays, expressing the occurrence of delay in some range of values with a specified probability distribution $g(s)$.

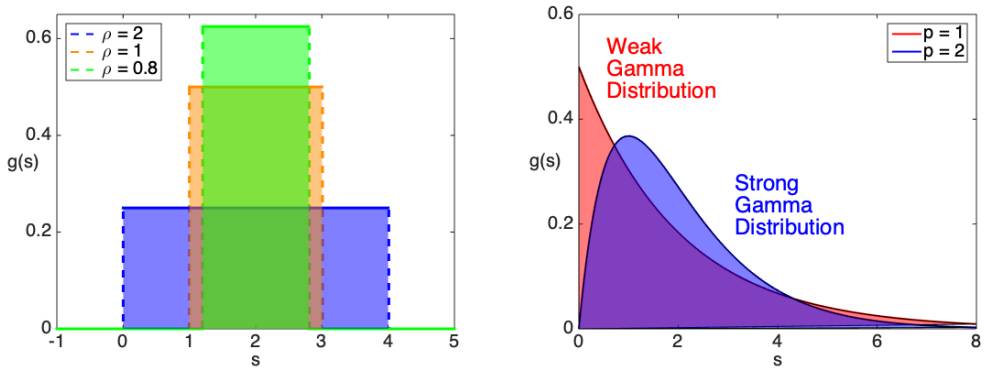

(a) Uniform (b) Gamma

Figure 1.6: (a) Uniform distribution of delay in the range $\rho = 0.8, 1, 2$ and mean delay $\tau = 2$. (b) Gamma distribution: two examples, weak and strong gamma distributions for $p = 1, 2$, and mean delay $\tau = \frac{p}{\gamma} = 2$.

In literature there are two commonly used delay distributions, those are presented in Fig. 1.6, and will be considered in Chapters 4-6, where the distributed delay is defined by an integral

$$\dot{\theta}_i(t) = \int_0^\infty g(s)\theta_i(t-s)ds, \tag{1.11}$$

where the function $g(s)$ is referred to as the kernel of the distribution, representing the probability of occurrence of a particular time delay with $g(s) \geq 0$, $g(s < 0) = 0$, normalised to unity, $\int_0^\infty g(s)ds = 1$. The value of the delayed phase $\dot{\theta}_i(t)$ characterises information about the past phases of oscillator i. The delay integral can be inside or outside the coupling function f, we consider the case of sinusoidal coupling, hence $\dot{\theta}_i(t) = \sin \int_0^\infty g(s)\theta_i(t-s)ds$, or $\dot{\theta}_i(t) = \int_0^\infty g(s)\sin\big(\theta_i(t-s)\big)ds$.

Laplace transform

The Laplace transform [142] of the function $g(s)$ is

$$\{\mathcal{L}g\}(\lambda) = \int_0^\infty e^{-\lambda s}g(s)ds. \tag{1.12}$$

Uniform distribution

The uniformly distributed delay kernel is given by

$$g(s) = \begin{cases} \dfrac{1}{2\rho} & \text{when} \quad \tau - \rho \leq s \leq \tau + \rho, \\ 0 & \text{otherwise}, \end{cases} \tag{1.13}$$

which has the mean time delay

$$\tau_m \equiv < \tau > = \int_0^\infty s g(s) ds = \tau, \tag{1.14}$$

and the variance

$$\sigma^2 = \int_0^\infty (s - \tau_m)^2 g(s) ds = \frac{\rho^2}{3}. \tag{1.15}$$

The parameter ρ determines the width and the height of the distribution. The Laplace transform [142] of the distribution $g(s)$ is computed as

$$\{\mathcal{L}g\}(\lambda) = \frac{1}{2\lambda\rho} e^{-\lambda\tau} \left(e^{\lambda\rho} - e^{-\lambda\rho}\right) = e^{-\lambda\tau} \frac{\sinh(\lambda\rho)}{\lambda\rho}. \tag{1.16}$$

Gamma distribution

The second example we consider, is the gamma distribution kernel, with an integer shape (or order parameter) p, and scale parameter γ,

$$g_\gamma^p(s) = \frac{s^{p-1} \gamma^p e^{-\gamma s}}{(p-1)!}, \tag{1.17}$$

where $\gamma, p \geq 0$.

The mean time delay is given by

$$\tau_m = \int_0^\infty s g(s) ds = \frac{p}{\gamma}, \tag{1.18}$$

and the variance

$$\sigma^2 = \int_0^\infty (s - \tau_m)^2 g(s) ds = \frac{p}{\gamma^2}. \tag{1.19}$$

The Laplace transform of the distribution $g(s)$ has the form

$$\{\mathcal{L}g\}(\lambda) = \frac{\gamma^p}{(\lambda + \gamma)^p}. \tag{1.20}$$

The uniform and gamma distributions have different types of support, the kernel of gamma distribution is continuous and positive on $(0, \infty)$; the uniform distribution has compact support $[\tau - \rho,\ \tau + \rho]$ and it is zero outside of the range. Hence, the two distributions have different characteristic equations; for gamma distributed delay the equation is a polynomial, whereas for uniformly distributed delay it is transcendental. The former

changes the system into ODE system with the use of linear chain method, the latter becomes discrete delay system. Both of these distributions have been successfully used in a number of different contexts, such as delayed driver response in traffic dynamics [127, 126], time delayed feedback control [66], genetic regulation [36], stem cell dynamics [28], population dynamics [42, 48, 106, 73], wireless communication object control [121], enhancement of noise-induced switching times [91], and dynamics of neutral systems [117].

Distributed time delays in the context of coupled oscillators have been considered by Kyrychko *et al.* [92], the authors studied the effect of coupling with distributed delay on the suppression of oscillations in a system of coupled Stuart-Landau oscillators. Their results indicate that larger widths of delay distribution increase the regions of amplitude death in the parameter space. In [93] Kyrychko *et al.*, for a system of coupled Stuart-Landau oscillators, obtain the conditions for amplitude death in terms of average frequency, frequency detuning, parameters of the coupling, coupling strength and phase, mean time delay, and the width of the delay distribution, identifying various branches of phase-locked solutions.

Rahman *et al.* [118] have studied a globally coupled network of oscillators, they found that increasing the width of uniform distribution for the same mean delay allows aging transition to happen for a smaller coupling strength and a smaller proportion of inactive elements. Kyrychko *et al.* [94] in their paper on synchronisation of network oscillators with distributed delay coupling, develop a generalised master stability function approach. The authors use a generic example of Stuart-Landau oscillators, and show how the stability of synchronized solutions in networks with distributed delay coupling can be determined through a semi-analytic computation of Floquet exponents.

Schuster and Wagner [125] have shown that in a system of coupled phase oscillators, two coupled limit oscillators can synchronise such that they share the same frequency and phase, without the presence of a time delay. Amplitude death is possible in systems of coupled oscillators with amplitude of oscillation, e.g. coupled Stuart-Landau oscillators. Sufficiently strong coupling, and a sufficiently wide-spread distribution of intrinsic frequencies can cause coupling-induced state of zero amplitude, in other words, an amplitude death.

1.2.7 Discrete delays model literature example

D'Huys *et al.* [51] examined the effect of coupling delays on the synchronisation properties of various network motifs. The authors studied the Kuramoto model with delayed coupling,

considering the case of discrete delays and two coupled oscillators.

$$\begin{aligned}\dot{\theta_1}(t) &= 1 + \kappa \sin(\theta_2(t-\tau) - \theta_1(t)),\\ \dot{\theta_2}(t) &= 1 + \kappa \sin(\theta_1(t-\tau) - \theta_2(t)).\end{aligned} \tag{1.21}$$

The coupling is attractive if the coupling strength $\kappa > 0$, with oscillators evolving to a symmetric state $\theta_1(t) = \theta_2(t) = t$. The coupling is repulsive if $\kappa < 0$, with oscillators tending towards an antiphase oscillation $\theta_1(t) = \theta_2(t) + \pi = t$. The solutions with $\theta_1(t) - \theta_2(t) = \text{const.}$, are different from multiples of π that occur at special delays τ. The authors state that if there is a coupling delay, the system still exhibits frequency-locked symmetric and antisymmetric states, and multiple solutions with different locking frequencies become possible. The frequencies can be found by solving $\omega = 1 - \kappa \sin(\omega\tau)$, for the in-phase state, and $\omega = 1 + \kappa \sin(\omega\tau)$ for the antiphase. Using the method from [54] by Earl and Strogatz to determine the stability of the anti-phase solutions, the authors state that an anti-phase solution is stable if and only if $\kappa \cos \omega\tau < 0$. In Chapters 4-6 we further extend System (1.21) by inclusion of distributed time delay.

1.3 Thesis Outline

This chapter outlined the analysis of the dynamics of the Blockchain-based cryptocurrencies by adapting mathematical models successfully used to describe the spread of epidemics. The population dynamics that governs the adoption and diffusion of new technology has qualitatively similar traits to those observed in the dynamics of the disease spreading. These quantities are translated into the framework of modelling the adoption of Blockchain-based technology, such as cryptocurrencies, effectively allowing one to estimate the popularity and loss of interest in them, we look further into this in Chapters 2-3.

This chapter also briefly introduced models based on a system of coupled phase oscillators with discrete and distributed delays in the coupling. We considered whether the formulation with discrete delays in the coupling of the oscillators is sufficient to capture all effects introduced by delayed communication in systems. In order to answer this question, we introduce a model of phase oscillators with distributed delays in the coupling. In Chapters 4-6 of this thesis we present our results.

Results from Chapters 4 and 6 have been summarised in a research paper:

- A. Ross, S.N. Kyrychko, K.B. Blyuss, Y.N. Kyrychko. Dynamics of coupled Kuramoto oscillators with distributed delays. (Submitted, April 2021).

Chapter 2

Analysis of Cryptocurrencies Using Google Trends Data

Various cryptocurrencies have emerged as possible competitors to fiat currencies, with the underlying Blockchain technology spreading and gaining recognition. This chapter analyses and estimates the proliferation of such cryptocurrencies. SIR type model is adapted to describe the take-up and abandonment of the Blockchain-based technology by the general population. Publicly available Google Trends data is used for model validation and prediction testing, reflecting the interest generated by the cryptocurrencies discussed. The data reflects the search queries, including "Blockchain", "Bitcoin", "Litecoin" and several other cryptocurrencies. Using the least-squares method we find the best fit for parameters, such as the take-up rates reflecting the interest in Blockchain mining amongst the population, and the abandonment rate, i.e., the loss of interest.

2.1 Methods

2.1.1 Google Trends data

One of the new measures used to estimate the attention to various factors is Google Trends (GT), which gives the popularity of search queries over time. These query indices are often correlated with various economic indicators and are generally helpful for prediction [9]. GT delivers data on the frequencies of search terms categorised by geographical location and time, relativising the data to the total search volume, therefore making it normalised. In the current information age, this publicly available data can be used by anyone with Internet access, and given the online nature of the Blockchain technology in general and cryptocurrencies in particular, the most attention is attracted through the Internet. Re-

search using GT data has experienced a dramatic rise in recent years, a report released by the research company comScore shows that in January 2015 about 64.4% of all online searches in the US were conducted through Google [97]. Moreover, given that 93% of all online traffic starts from search engines [39], it becomes obvious why GT data is a very good proxy for online attention in particular, as well as attention in general. In 2018, Jun *et al.* [80] conducted a network analysis of 657 research papers that used GT, concluding that GT use has dramatically increased in the last decade for describing and diagnosing trends, and the focus of research has gradually shifted to forecasting changes. Since Google begun the GT service to share aggregated information on the volume of queries for different search terms, having access to this big data in a free, easily available and comparable way, has been instrumental for modelling financial markets [116, 35, 41, 84, 43, 86]. For example, Preis *et al.* [116] analysed changes in Google search queries for finance related search terms, and found patterns that can be interpreted as early warning signs of stock market moves.

There are several studies related to the use of GT data for analysing the behaviour of various cryptocurrencies. Krištoufek [85] used GT data and Wikipedia visits, and found a strong correlation between the price of the cryptocurrency and internet searches; it was also shown that not only internet searches influence prices but prices also influence internet searches. Similar conclusions are drawn by *idatavox* [2]. Garcia *et al.* [65] have studied the formation of price bubbles on the example of Bitcoin by using the data on volume of information sharing online, price on online exchanges, user base growth and volume of information search. Their analysis shows that there are two feedback loops, namely, a reinforcement cycle between search volume, word-of-mouth and price, and a user adoption cycle between search volume, number of new users and price. The study also suggests that waves of growth of the Bitcoin were driven by the corresponding waves of new users from public opening to the currency. Nasir *et al.* [109] conducted a brief study analysing the predictability of Bitcoin volume and returns using GT. Their findings suggest that the frequency of Google searches leads to positive returns and a surge in Bitcoin trading volume.

2.1.2 Model

The classical susceptible-infectious-recovered (SIR) model was first considered by Kermack & McKendrick, and is used for prediction, and analysis of epidemic dynamics in a population [83]. Such model has been used in recent studies to describe the dynamics of

social interactions [47, 128].

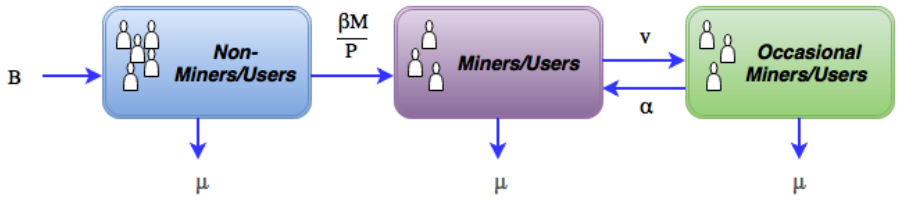

Figure 2.1: Schematic representation of the transition of users across the three classes.

Since our interest lies in exploring the longer term persistence and dynamics of cryptocurrencies we adapt the classical SIR model with the incorporated demography to describe the temporal evolution of interest in the Blockchain-based cryptocurrencies by drawing the equitable analogues to the SIR model parameters. We interpret the susceptible population, N, as the population of all individuals interested in but not currently using the Blockchain-based technology. The infected population, M, corresponds to current Blockchain miners/users. The recovered population, O, is equivalent to the population of individuals who are using the Blockchain-based technology from time to time. Members of the population transition between classes based on the following system of ordinary differential equations

$$\left.\begin{aligned} \frac{dN}{dt} &= B - \frac{\beta NM}{P} - \mu N, \\ \frac{dM}{dt} &= \frac{\beta NM}{P} - vM + \alpha O - \mu M, \\ \frac{dO}{dt} &= vM - \alpha O - \mu O, \end{aligned}\right\} \tag{2.1}$$

where $N(t) + M(t) + O(t) = P$.

Table 2.1: Definitions of parameters of System (2.1)

Parameters	**Description**
β	transmission rate of non-miners/users to miners/users
v	transmission rate of miners/users to occasional miners/users
α	the rate of reactivation of active mining/using for occasional miners/users
B	the rate of take-up of cryptocurrencies and/or Blockchain-based technology
μ	the rate of permanent loss of interest in cryptocurrencies and/or Blockchain-based technology

Analysis of changes in query volumes for search terms related to Blockchain and different cryptocurrencies provides an estimate on behavioural patterns, which can be analysed by comparing our model to data. In order to validate the model, we use GT data as a proxy for the dynamics of take-up/loss of interest in various cryptocurrencies.

Least squares statistic

$$LS = \sum_{i=1}^{n} (\text{data}_i - \text{model}_i)^2, \quad (i = 1, \ldots, n).$$

The model parameters are chosen so that they minimise the sum of squared differences between the model prediction and the data. The scripts to find a best fit for the GT data are implemented using the SIR function script from [137].

Wavelet coherence analysis

$$R^2_{x,y}(u,s) = \frac{|S\left(\frac{1}{s}W_{x,y}(u,s)\right)|^2}{S\left(\frac{1}{s}|W_x(u,s)|^2\right)S\left(\frac{1}{s}|W_y(u,s)|^2\right)}$$

To determine the relationship between the reviewed cryptocurrencies, we use the wavelet transform coherence (WTC) method [71], conducting a one-to-one comparison of the time series of the searched keywords. WTC helps analyse the coherence and phase lag between two time series as a function of both time and frequency, a similar approach has been used in [87], determining the main drivers of the Bitcoin price.

2.2 Results

Google Trends data fitting

In order to quantify the interest in Blockchain-based cryptocurrencies, we collected and analysed the GT weekly datasets in December 2016 on queries for the words “bitcoin”, “litecoin”, “mastercoin”, “peercoin”, “ethereum”, and “blockchain” [9]. To avoid ambiguity the cryptocurrencies were selected so that the names differ and are not associated with anything else, in addition all considered cryptocurrencies are of varying price range, market capitalisation, and popularity. The aim is to determine the differences in behaviour, and compare the dynamics. Although it is impossible to distinguish the reason for internet users to search for information related to Blockchain technology, the GT data serves as a very good proxy to estimate the user interest and involvement.

Ethereum was launched in 2015, but it had been announced in 2013. Unsurprisingly, as one of the first cryptocurrencies with features such as smart contracts, it captured a lot of interest before the official launch and start of trading, with potential adopters eagerly waiting for the launch. Hence, we take the dates from 2013 onwards into account when analysing Ethereum.

The GT query data for the cryptocurrencies is assumed to be representative of the magnitude of the mining population compartment of the model, used to analyse the search query data by curve fitting the mining population curve generated by the model to the search query data. The data analysis was performed in R, with a special emphasis on finding the optimal parameters in the model to obtain the best possible fit. We apply the least squares approximation to System (2.1), where parameters are chosen from a given interval allowing for minimisation of the sum of the squared distances between the model prediction and the data.

Each plot displays the GT data for a specified search term and the best fit dynamical curve based on the model. The weekly data is broken down into two to three sections, followed by evaluating a range of parameter values and calculating the best fit for each part, which are then appended together.

The process for finding the best β, v, α and μ variables involves some trial and improvement. We split the dataset for each search term into sections, such that each section has at most one large peak in it. We then initialise arrays for β, v, α and μ, with ranges of possible values for the first section of the dataset. For each of β, v, α and μ, we apply the NMO function script to find the model fit. Using the dataset and the model fit values, we can find the total sum of squares for miners/users quantity and consequently can select the combination of parameters that give the least squares statistic. Experimenting with arrays of different ranges leads to finding the best β, v, α and μ values for the model. We then create another set of arrays with values around these optimal variables and repeat the process for the remaining peaks.

For the first section, the miner/user population (number of infected individuals) is 1, the occasional miner/user population (number of recovered individuals) is 0. For the subsequent sections, the number of miners/users and occasional miners/users carries on from the previous section. The total population value remains constant. Tables A.1 - A.6 with the optimal parameter sweep values for each search term can be found in Appendix A.

Although there are qualitative similarities and differences between the reviewed cryptocurrencies, the search interest follows the same general pattern: an initial peak resulting

in a high level of searches, followed by the decline, and eventually, the number of searches stays at a low steady level. Analysis of historical performances of these cryptocurrencies could help develop an improved investment strategy, as well as provide future projection in other possible networks.

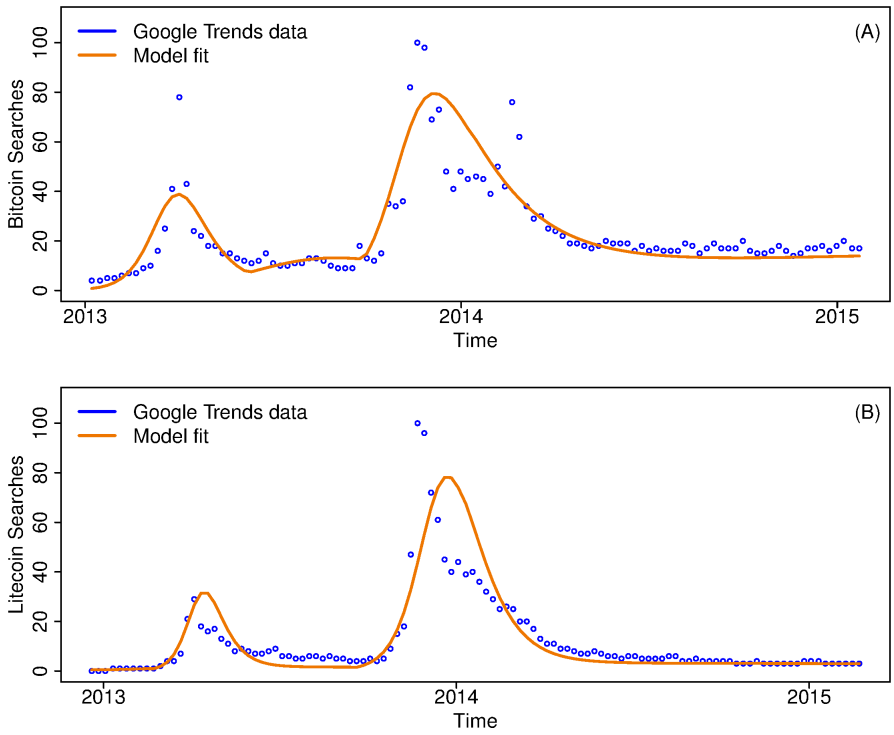

Figure 2.2: Worldwide Google search interest: (A) Bitcoin GT data fitting, (B) Litecoin GT data fitting.

Fig. 2.2 shows that the time trends in Google search interest for Bitcoin and Litecoin are roughly paralleled, the initial peak followed by a drop can be explained by the following two events, US Senate holding hearing on risks of virtual currency, resulting in high interest and Bitcoin trading at 1242 USD, followed by China's central bank banning Bitcoin transactions, which explains the drop in price, as well as interest [1]. It is also believed that the spike was caused by low exchange rates between the two cryptocurrencies, so the price drop of Bitcoin triggered the loss of interest in Litecoin, making it evident that Bitcoin is the driver for Litecoin [3].

With Bitcoin, Litecoin, Mastercoin, and Peercoin, the so-called life cycle is short-lived, peak followed by decline and somewhat stability. In all four cases, it takes up to two years to reach a stable point, as can be seen from Figs. 2.2 and 2.3. In the case of Litecoin, Mastercoin, and Peercoin, the interest drops down to almost the starting level, for Bitcoin the point of stability is considerably higher. As can be seen from Fig. 2.4 (A), Ethereum

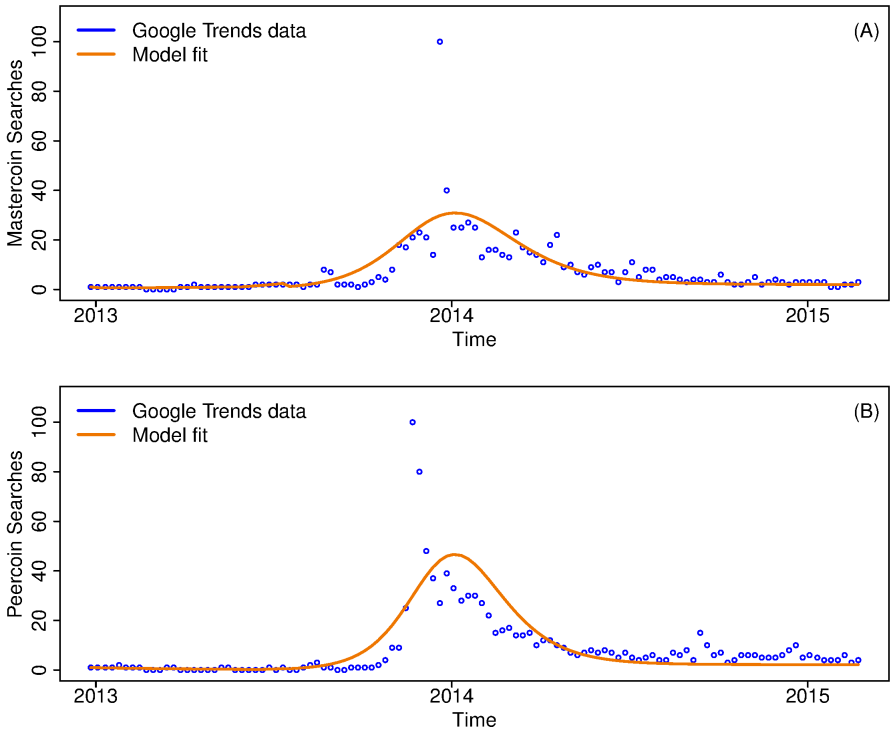

Figure 2.3: Worldwide Google search interest: (A) Mastercoin GT data fitting, (B) Peercoin GT data fitting.

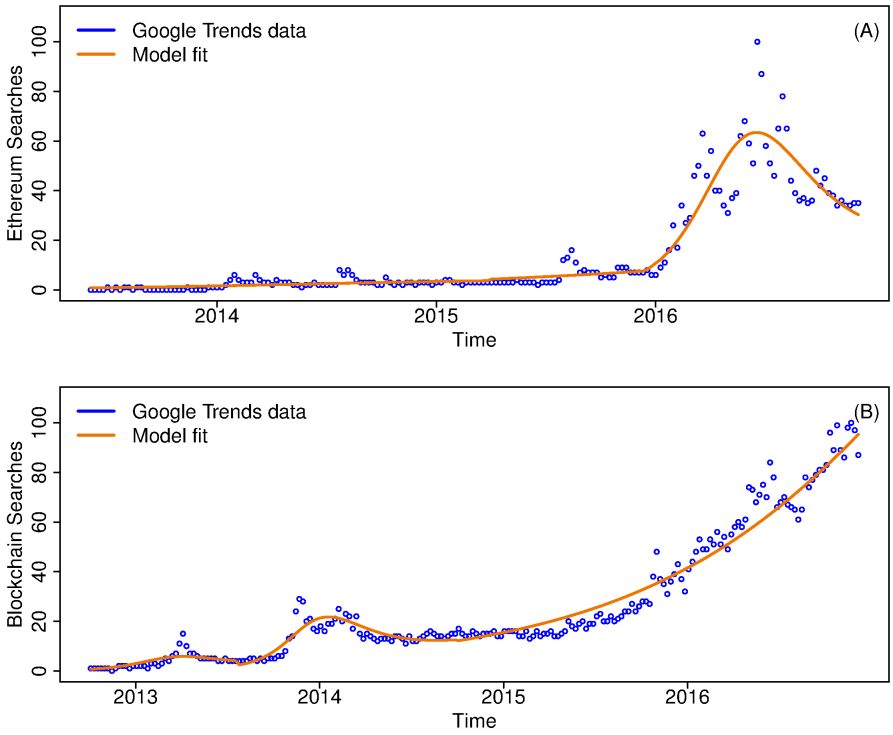

Figure 2.4: Worldwide Google search interest: (A) Ethereum GT data fitting, (B) Blockchain GT data fitting.

has grown at a significant rate over the course of 2016, and its value is largely powered by its ability to leverage the application of smart contracts within its code. However, Ethereum's future is uncertain, the network could be at a stage now where it follows the same route of decline and stability, unless further diversification and advertisement takes place. So the open question remains of whether it has reached the top yet. Fig. 2.4 (B) shows a growing trend in Blockchain since 2014, an increasing interest can only be attributed to a diverse and expanding range of applications unlike cryptocurrencies.

The initial high growth and volatility of the reviewed cryptocurrencies are the result of news, hype, speculation, and adoption in the early stages of the life cycle. This is also evident from the significantly high correlation between price movement and GT searches for the cryptocurrencies [14, 87].

2.2.1 Wavelet coherence analysis

In this section, we are using daily data to analyse relationships in time frequency space between two time series. Google Trends provides daily data (up to eight months), weekly (up to five years), or monthly (over five years). To obtain daily series for Google searches, we download the data in eight months blocks, these blocks are then rescaled and concatenated. Plots of the daily data, and corresponding log returns can be found in Appendix A, Figs. A.1 - A.3.

This section describes the co-movement of the GT interest in the reviewed cryptocurrencies by resorting to cross wavelet analysis using daily data, covering a four year period from 2013 to 2017, for Bitcoin, Blockchain, Litecoin, Mastercoin, Peercoin, and a three year period from 2014 to 2017 for Ethereum comparisons.

The phase differences between the two data series are indicated by arrows. Arrows pointing to the right show in-phase behaviour (positive correlation), i.e., they move in the same direction, having cyclical effects on each other. Arrows pointing to the right and up, indicate that the two datasets are positively correlated and the second is leading, if they point to the right and down then the same relationship holds but the second one lags. If the arrows point down, then the first dataset is leading and the second is lagging. Arrows pointing up indicate that the second dataset is leading and the first is lagging. Arrows pointing to the left illustrate that the variables are out-of-phase (negatively correlated), i.e., they have anti-cyclical effects on each other. If the arrows point to the left and up, the first dataset is leading, and if they point to the left and down, the first dataset is lagging.

The horizontal axis shows the time, and the vertical axis shows the period. The

relationships that occur at the start of the data interval are positioned on the left side of the diagram, those on the right are relationships that occurred at the end of the data interval. Higher period bands, or lower frequencies, are positioned near the bottom of the diagram and are of interest to those with long term prospects; lower bands, or higher frequencies, are near the top and are of interest to those with shorter term prospects.

Wavelet coherence plots highlight areas in the time-frequency space where the two series co-move. In all plots, the statistically significant correlations are indicated by the thick black contour (the 5% significance level against red noise). Higher coherence (correlation) is highlighted by warmer colours at that location in the time-frequency space. The colour bar corresponds to the significance level of the Monte-Carlo test, 1 (red) indicates high correlation (coherence) between two time series, 0 (blue) no correlation (coherence). Due to the nature of finite time series and wavelets, the beginning and end of the wavelet coherence are affected by the discontinuities at the edges. The region below the thin black line indicates the cone of influence, and is shown as a blurred light blue shade separating less reliable regions. Grinsted *et al.* [71] and Torrence *et al.* [135] have written detailed studies on significance testing and derivation of background spectra.

Fig. 2.5 presents the cross wavelet coherence for the Bitcoin interest compared to Blockchain, Litecoin, Mastercoin, and Peercoin. The compared variables are mostly positively correlated across all scales. In Fig. 2.5 (A) the datasets are in-phase with each other at almost all scales and during the entire examined period. In the 2013 to 2015 section, Blockchain leads Bitcoin at low scales (4 to 16 days), however at high timescales (128 to approximately 450 days) the two variables are highly correlated and Bitcoin is the driver. From 2015 onwards there is less correlation across all scales, and no apparent leader, with Blockchain driving Bitcoin in 2015 at 128 days scale, and Bitcoin briefly leading at medium scales between 16 and 64 weeks in 2016. Fig. 2.5 (B) shows in-phase movement across lower scales (4 to 16 days), no apparent leader. At medium timescales Bitcoin leads Litecoin (16 to 64 days) from mid 2014 to beginning of 2016. There is high strong positive correlation long term between 128 and approximately 500 days, Bitcoin leads Litecoin 2013 to mid 2014, the two variables move in-phase until 2015.

In Fig. 2.5 (C) Bitcoin and Mastercoin are positively correlated across all scales from 2013 to 2015, with Bitcoin leading Mastercoin during that period. Post 2015, the relationship between the two variables is unstable with a phase change at medium scales in 2016. In Fig. 2.5 (D) we observe one island of high coherency at high timescales between 128 and 400 days, Bitcoin is an evident leader from 2015 onwards. At low timescales there are

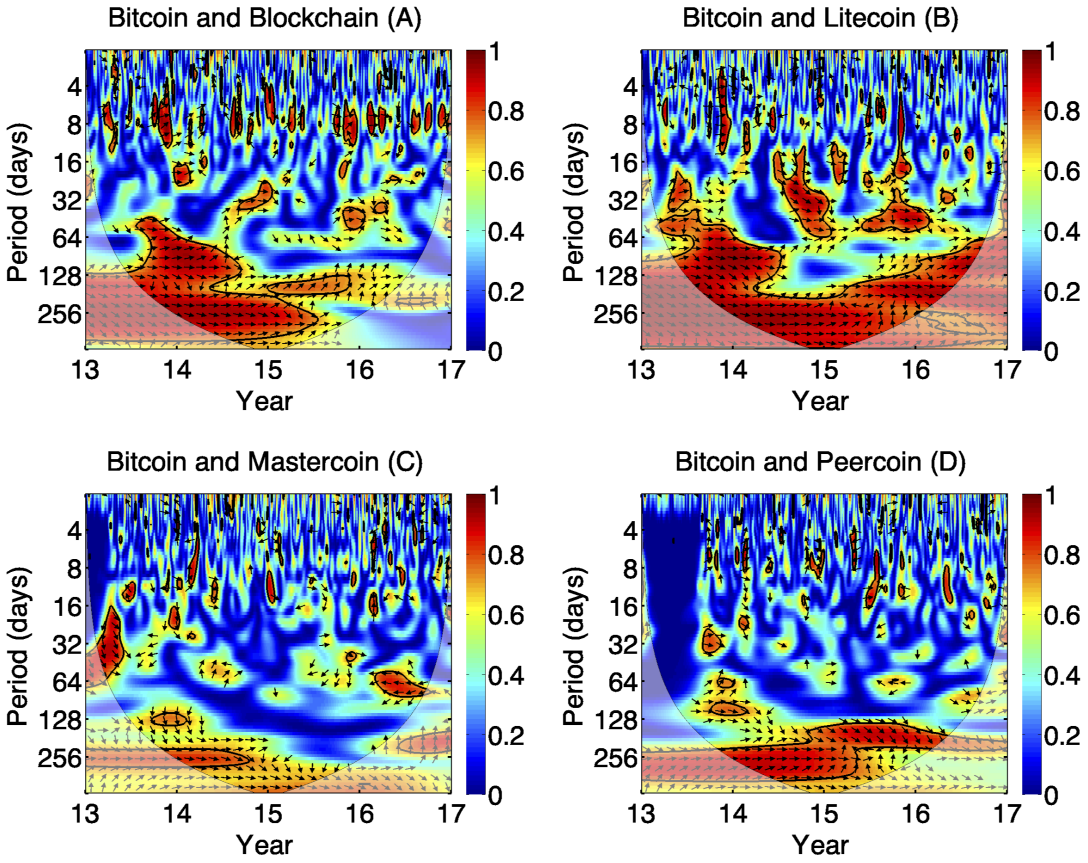

Figure 2.5: Wavelet coherence of the daily GT interest: (A) Bitcoin and Blockchain, (B) Bitcoin and Litecoin, (C) Bitcoin and Mastercoin, (D) Bitcoin and Peercoin.

limited areas of co-movement, with positive (in-phase) and negative (antiphase) correlation. Bitcoin seems to drive Peercoin at medium scales between 2013 and 2014, which is explained by the peak of interest in Figs. 2.2 (A), 2.3 (B).

Fig. 2.6 (A) highlights that overall Blockchain is an evident leader from 2014 to 2016 across lower and medium scales. In 2013, Litecoin leads Blockchain at medium scales between 16 and 64 days. The popularity of Litecoin seems to briefly drive interest in Blockchain technology at higher scales between 2015 and 2016. The two variables mostly move in-phase up until 2016 and are highly positively correlated long term, at medium scales between 16 and 32 days. In first half of 2016, we observe a change of behaviour from in-phase to antiphase with increase of interest in Blockchain technology taking lead. In Fig. 2.6 (B) there is a lack of longer-term relationship between the two datasets. Blockchain almost always leads Mastercoin short term between 1 and 8 days up until 2016. There are two small islands of higher coherency between 8-32 and 64-128 timescales in 2014, similarly to other comparisons, where Mastercoin lags. Mastercoin seems to briefly lead Blockchain at the end of 2014 between 32 to 64 days, followed by a phase change suggesting that

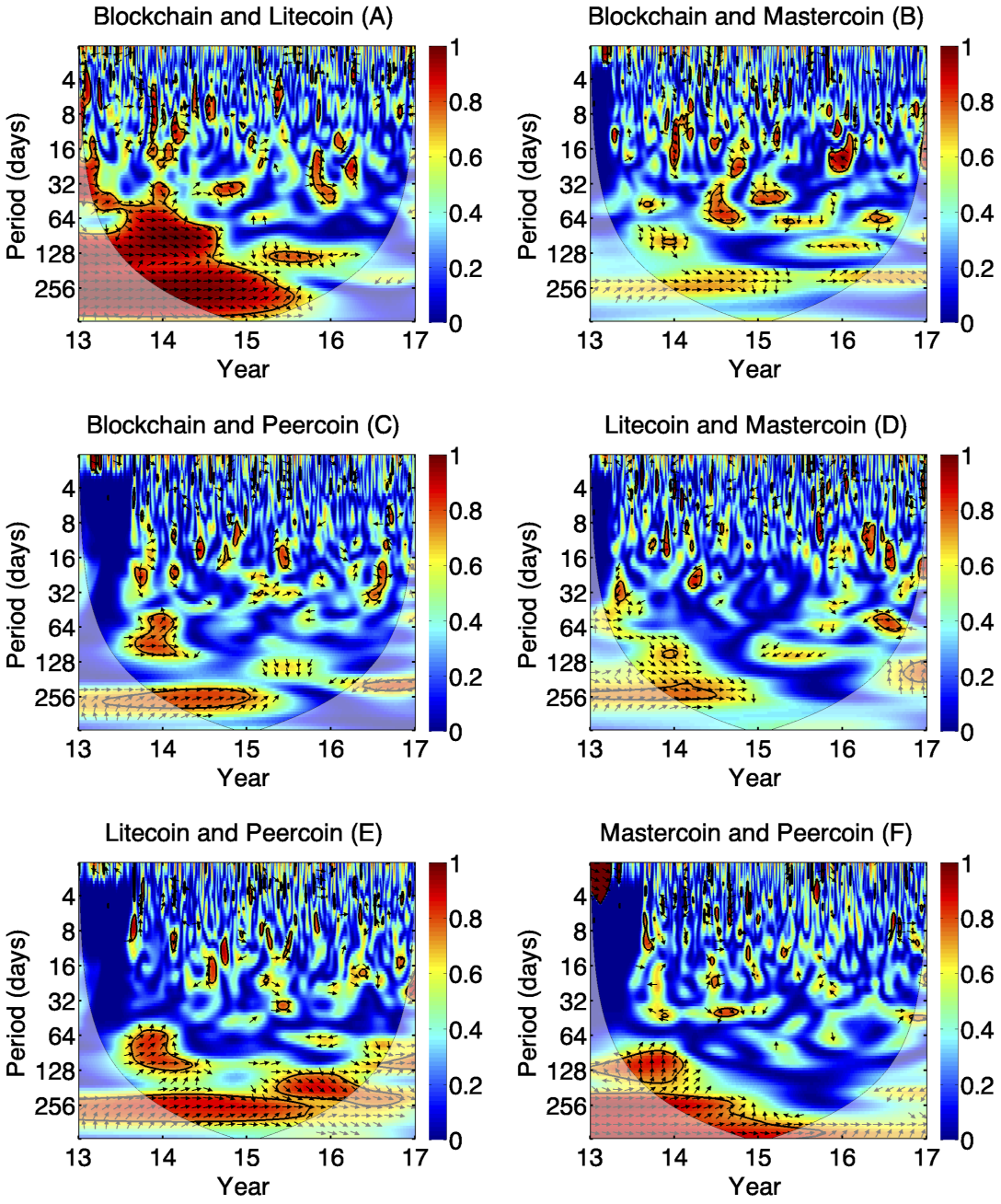

Figure 2.6: Wavelet coherence of the daily GT interest: (A) Blockchain and Litecoin, (B) Blockchain and Mastercoin, (C) Blockchain and Peercoin, (D) Litecoin and Mastercoin, (E) Litecoin and Peercoin, (F) Mastercoin and Peercoin.

increase in Blockchain interest preceds a decrease in Mastercoin interest.

In Fig. 2.6 (C) at lower scales of up to 8 days and at medium scales Blockchain leads Peercoin. There is a region of high coherency between 32 and 128 days frame that occurs from end of 2013 to beginning of 2014, in which the variables are in-phase with Peercoin leading. Blockchain seems to slightly lag between 2014 and 2015 at higher scales of 256 days. There seems to be an apparent phase change mid 2015 at 16 days, again suggesting

that increase of the first variable comes before decrease of the second. We can conclude that post 2015 the relationship is somewhat unstable, without much coherence between the two terms.

Fig. 2.6 (D) shows brief intervals of co-movement across all scales, there is no apparent leader short term, as the relationship between the two terms seems to alternate between phases, however at higher scales from 64 day band onwards, Litecoin seems to lead Mastercoin from mid 2013 to mid 2014. In Fig. 2.6 (E) coherency regions are more significant than in Fig. 2.6 (D), Litecoin is in-phase with Peercoin across higher scales during 2013 to 2017, Litecoin leads Peercoin from 2015 at 128 day band. We can observe that from end of 2013 to 2014 at higher scales of 64-128 days, there is an island of high positive correlation between the two variables, where Peercoin leads Litecoin.

In Fig. 2.6 (F), in the 1-4 day band at the beginning of 2013, Mastercoin is a clear leader for that short period, which could be explained by low Peercoin interest. For the remainder of the examined period, the relationship between the two variables seems to be mostly out of phase across lower scales for the duration of the examined period, with Mastercoin briefly leading in the 32 day band at the end of 2014. However, Mastercoin and Peercoin are highly correlated exhibiting in-phase behaviour at higher scales of 64 days onwards, between 2013 and 2016, with Peercoin evidently leading and Mastercoin lagging.

Fig. 2.7 presents the cross wavelet coherence for the Ethereum interest compared to Bitcoin, Blockchain, Litecoin, Mastercoin, and Peercoin. Figs. 2.7 (A), (B) highlight similar behaviour in terms of co-movement and high power in individual comparisons, Bitcoin and Blockchain evidently drive Ethereum across medium and high scales. At higher scales, past the 128 day band most of the high power island is hidden in the cone of influence, however the sections outside the cone of influence clearly indicate that Ethereum is lagging at higher scales. In Fig. 2.7 (A), in the 16-128 day band between the end of 2014 and beginning of 2016, there are islands of higher in-phase correlation where Bitcoin leads Ethereum; in Fig. 2.7 (B) the same behaviour is observed between 2016 and 2017. In Figs. 2.7 (A), (B) Ethereum briefly leads both Bitcoin and Blockchain at lower scale in the 4-16 day band for a short period of time in September to October 2016, overall there is no evident leader at the lower scale comparisons, the datasets alternate between in-phase and antiphase movements.

Figs. 2.7 (C), (D) there are areas of high correlation in the long term band, however those are under the cone of influence, hence have no significance in this instance. In Fig. 2.7 (E), there is no evidence of long term relationship between Ethereum and Peercoin,

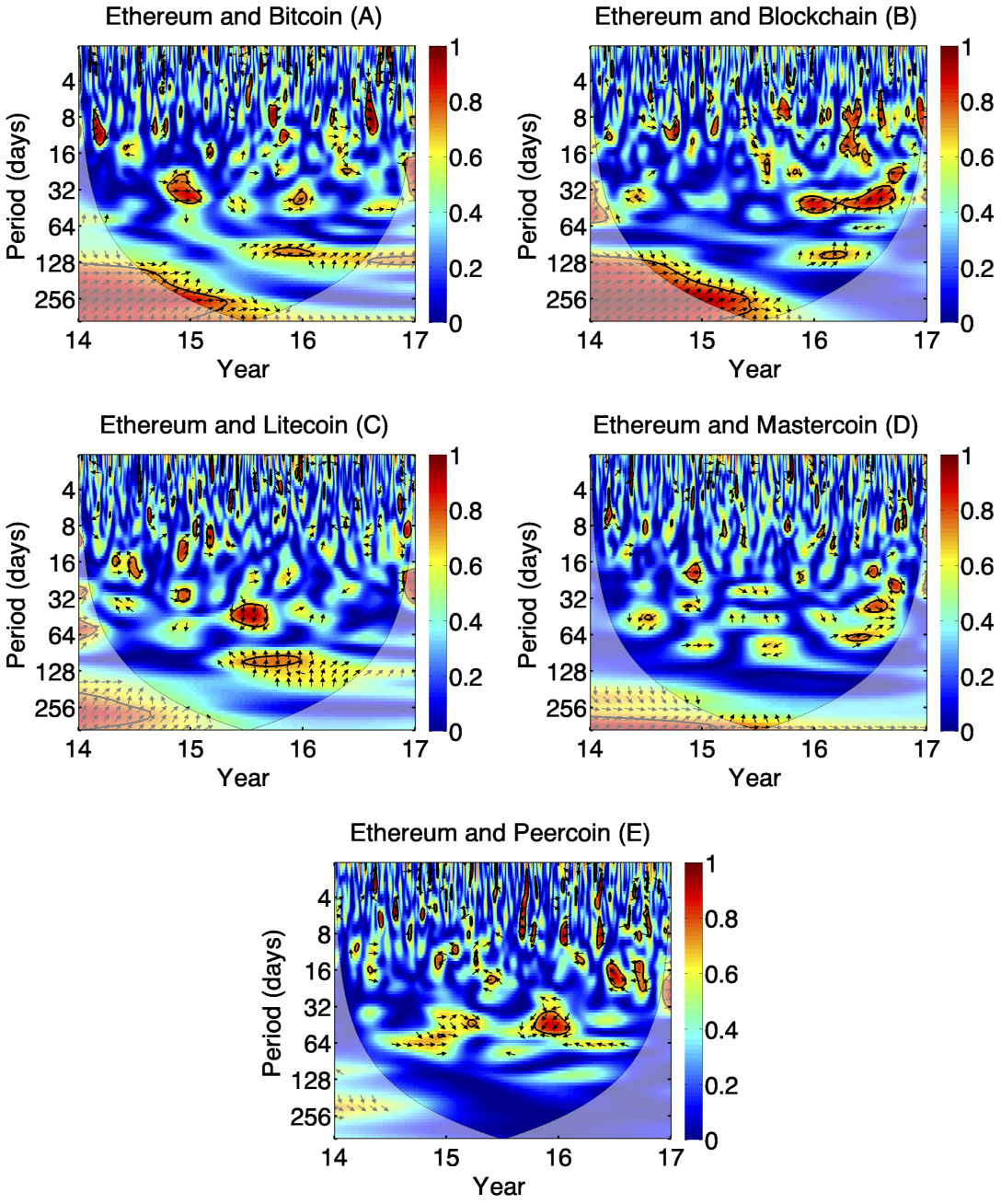

Figure 2.7: Wavelet coherence of the daily GT interest: (A) Ethereum and Bitcoin, (B) Ethereum and Blockchain, (C) Ethereum and Litecoin, (D) Ethereum and Mastercoin, (E) Ethereum and Peercoin.

there are also limited areas of short term co-movement with no clear pattern in their behaviour, with antiphase dominating across all scales.

2.3 Discussion

Bitcoin at the moment is the most extensive and acknowledged application based on the Blockchain technology, it can be looked at as the trendsetter, as it triggered the launch of many other cryptocurrencies, due to its initial success. Blockchain, the technology underpinning Bitcoin, is itself only just starting to come into prominence and diverge into various other fields, the conducted analysis can help make predictions and draw conclusions on its possible short and long term behaviour. Bitcoin has revealed the practical possibility of maintaining irrevocable records of transactions and ownership using its consensus process or the Proof of Work, so it is clear that the underlying Blockchain technology works and can be used for other non-financial applications, as has been successfully demonstrated by Ethereum.

With the help of Blockchain technology more applications besides cryptocurrency can be developed to aid its growth and potential. Tracking and managing digital identities, such as citizenship documentation, national security, healthcare, can be made both secure and efficient with the use of Blockchains, where identity can be uniquely authenticated in an irrefutable, immutable, and secure manner, reducing fraud and avoiding outpaced spreadout identity-based security innovations. Most of the applications mentioned above are still being developed, so now is a good time for companies to start focusing on how this technology could be of benefit to them. The future potential of applications of Blockchain technology is still unwinding. Regardless of which application comes next on a global scale, it is predicted that Blockchain is a permanent addition and will transform how the digital society functions.

The comparison of Google Trends data for a number of cryptocurrencies allowed for validation of the modelling approach, with similar qualitative behaviour suggesting its feasibility. Similarities in cryptocurrency behaviour suggest that there is no evident competition between them, as they tend to grow and decay at roughly the same rate. Blockchain and Ethereum data both showed a growing trend, which can be attributed to their diversification into various non-financial fields and a growing range of applications, so the interest levels are much higher compared to cryptocurrencies.

The wavelet analysis indicated that most of the cryptocurrencies tend to move together very tightly, with the exception of Ethereum, which we attribute to its continuing growth. Bitcoin appears to be the leading cryptocurrency, as it clearly is the driver in all one-to-one comparisons at higher timescales, i.e., long term, however short term the lead-lag relationship alternates between scales. Overall the long term relationship between all

cryptocurrencies starts to break down closer to the end of 2016. We can also conclude that the Mastercoin peak in 2014 observed in Fig. 2.3 (A) was driven by more popular cryptocurrencies such as Bitcoin, Litecoin, Peercoin, and general interest in Blockchain technology. Similarly with Peercoin, there is clear leadership in one-to-one comparisons with Bitcoin, Litecoin, and Blockchain; each coin is leading Peercoin in 2014 when it reached its highest GT score.

The lack of competition between the reviewed cryptocurrencies is again highlighted by the co-movement of Bitcoin, Litecoin, Mastercoin, and Peercoin. When there is a high interest in one cryptocurrency, it attracts interest not only to Bitcoin but also other cryptocurrencies and the underpinning Blockchain technology. Individuals who start becoming interested in well known coins such as Bitcoin and Litecoin, will also explore other Altcoins in their research.

The model considered in this chapter yields results that are comparable with the observed GT patterns of the reviewed cryptocurrencies, this is a good first-hand indication that the model is useful for data validation and analysis, but is also open for improvement which would allow for a greater comprehension of the mathematics underlying the dynamics of cryptocurrencies and Blockchain technology.

Analysis of the dynamics of the presented model suggests that once the interest wanes, and the system settles on some small steady level of miners/users, it will remain there forever, and no other dynamics are possible, unless there are external kicks/perturbations to the system, such as introduction of the new technology, fall in electricity costs, major investment, cultural adoption, etc. Any such changes would have to be incorporated in the mathematical model itself, which can lead to qualitatively different dynamics and stability properties.

Chapter 3

Analysis of Cryptocurrencies: Revisited

3.1 Latest developments

The cryptocurrency research we discussed so far was conducted in preparation for SIAM 2017 conference, since then the popularity and use of cryptocurrencies has increased dramatically. In this section, we revisit the topic and present the latest results, looking from 2013 to 2020. Our initial theory was that cryptocurrency interest moves in the same direction as Bitcoin, and events can trigger peaks in interest. It is now evident that cryptocurrencies and Blockchain are an integral part of our modern life, and the variety of digital currencies available on the market can be overwhelming. As Blockchain applications are still being explored, interest in the cryptocurrencies depending on Blockchain technology will fluctuate.

The NMO model introduced in Chapter 2 provides a good approximation in fitting the model to the interest data. The level of GT interest varies, however the general pattern is recursive so the model can be re-applied to other surges of interest. From December 2017, the price and the interest dropped considerably, but after this drop the number of searches of the 'Bitcoin' term remained at a high level, higher than before the peak. This is likely to continue gradually growing. After the next significant peak, the number of searches will increase as the awareness of the cryptocurrency will grow.

The objective of this chapter is to further analyse the interdependence between interest and prices of Bitcoin and top cryptocurrency alternatives. We are curious as to whether Bitcoin is the driver for the prices of Altcoins. The patterns between Bitcoin and Altcoin's prices are quite similar. Not only is the price for most Altcoins measured with Bitcoins,

but for many businesses and consumers Bitcoin can be the expected medium of exchange. This gives us a strong indication that Bitcoin and Altcoin prices are interdependent.

We focus on cryptocurrencies that are successful in price and market capitalisation, as analysing their performance enables us to see patterns that would otherwise not be very visible with lower end cryptocurrencies; Bitcoin, Ethereum and Litecoin match this description. Peercoin and Mastercoin are no longer considered as they are positioned low in terms of market capitalisation but are stable in the market, and there have not been any interesting developments worth exploring at this stage.

In this chapter we introduce Ripple (XPR) - another Altcoin launched in 2012, based on Ethereum. The key differences with Ripple are that it is not based on Blockchain, and it is not designed to be mined, hence why it was not considered in our original research. Ripple has 100 billion pre-mined coins, with around half of those available on the market, the rest are in Ripple labs and can be periodically released. However now, at the end of 2020, we can see that Ripple followed the same pattern as the other cryptocurrencies in terms of interest growth and decline, thus further supporting our initial hypothesis.

We observe the interest, price, and supply properties of the cryptocurrencies. Analysing GT behaviour with price of a cryptocurrency gives us invaluable insight into the relationship between the two. We also consider supply, as this can potentially affect both interest and price; some cryptocurrencies can be harder to get hold of due to their supply limitations. Rarity and capacity of obtaining a coin can have a large impact on its price, and trigger interest from individuals looking for challenges. Studying patterns in these relationships would allow making reasonable predictions about the future interest and price movements. These forecasts are of great importance to those that are looking to invest their time, and/or money, in cryptocurrencies.

Over the last few years, the market capitalisations of the cryptocurrencies have had many fluctuations. In mid 2013, Bitcoin's market capitalisation value was 1.5 billion USD, with a 95% share in the cryptocurrency market. With the rise of Altcoins, Bitcoin's market share decreased to just over 85% at the beginning of 2017, but its strong growth ensured a market capitalisation of 15 billion USD. It reached its highest ever, at 324 billion USD, in the beginning of 2018, however at the same time, the market share dropped to its lowest at 32%. Bitcoin has gradually been regaining the market share since, having reached around 60% in October 2020. Although the market capitalisation also declined after 2018, Bitcoin maintains a dominant position, with 240 billion USD at the time of writing. Market capitalisation is constantly oscillating; Bitcoin prices are currently on the rise so we expect

the market capitalisation to increase over the next few months. Ethereum is the largest Altcoin with a market share of approximately 10%. The rest of the Altcoins account for less than 5% of the market share each. Analysing these significant developments that happened over the past few years could help better understand future price movements and what drives them.

3.1.1 Search queries

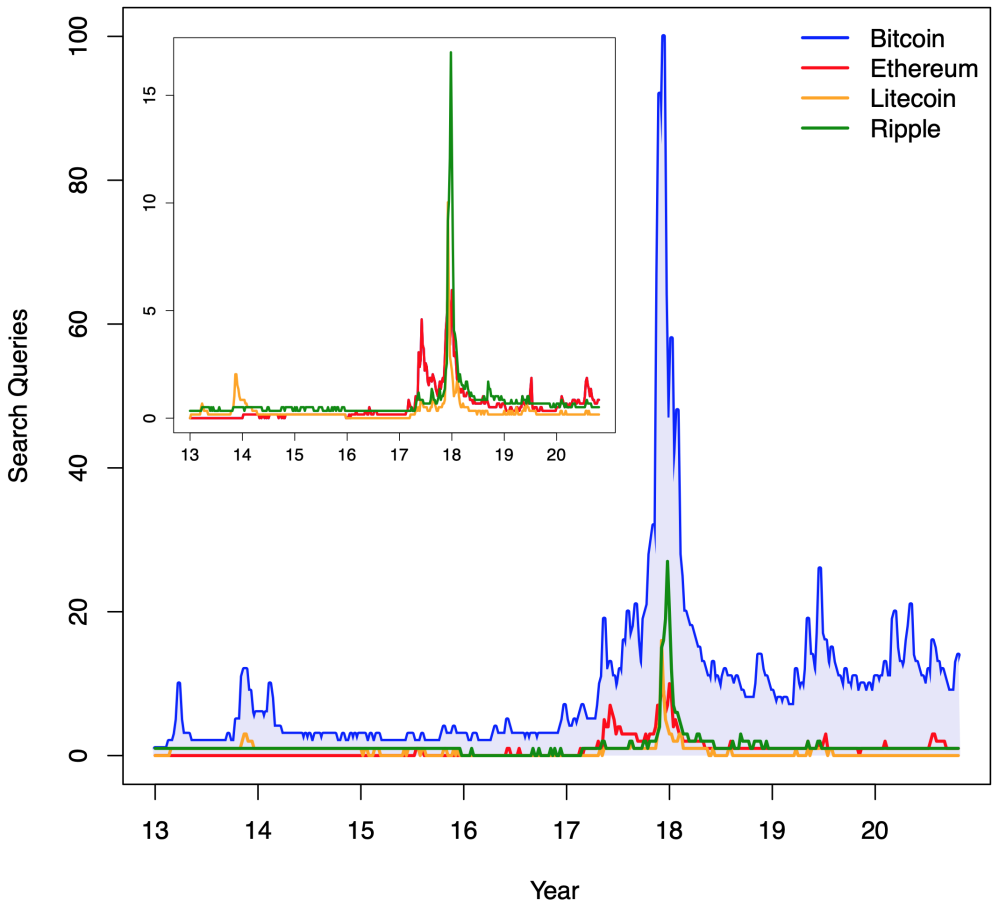

Figure 3.1: Worldwide Google search interest: Bitcoin, Ethereum, Litecoin, Ripple, search terms GT data fitting.

Fig. 3.1 highlights the GT patterns of Bitcoin, Ethereum, Litecoin and Ripple, covering a period from 2013 to 2020 (Fig. B.1 in Appendix B visualises the time series of Fig. 3.1 on the semilogy axis). It is clear from the plot that these cryptocurrencies follow the same pattern, with Bitcoin still remaining the leader. With Bitcoin removed, we can see that the peaks of the other three cryptocurrencies are more pronounced, highlighting the resemblance in their behaviour. As discussed earlier, each peak is followed by a steady low time period as interest stabilises. The peaks occur in cycles, however in recent years, it is

evident that the steady period is shorter with new peaks appearing more often. Between peaks, the interest does not drop by much; interest remains above a certain threshold, this is consistent between all four cryptocurrencies. It remains at a steady level until an event triggers a spike of interest. In the recent years, even when the interest wanes to its lowest, it is still significantly higher than the initial years of the cryptocurrencies.

3.1.2 Market capitalisation

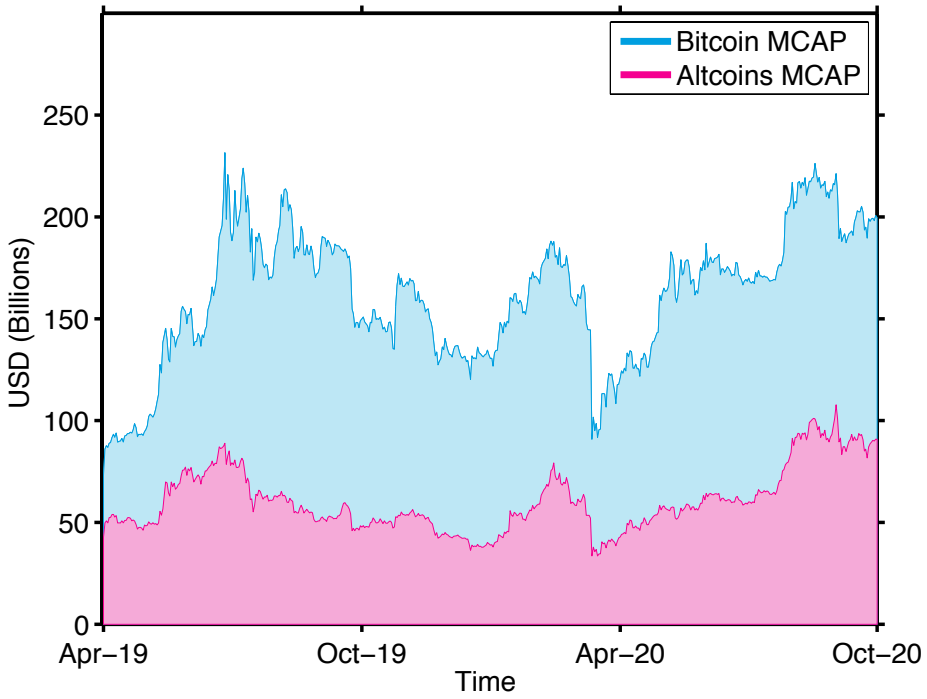

Figure 3.2: Market capitalisation of Bitcoin compared to top ten Altcoins, expressed in USD (billion) for the period April 2019 to October 2020. The data is obtained by multiplying the current market price of the cryptocurrency coin in USD, with the total number of coins in circulation. The market capitalisation of top ten Altcoins is calculated as the sum of their values.

Bitcoin is still maintaining its place as one of the strongest cryptocurrencies in the market. We take ten Altcoins [14] with the highest market capitalisation as of October 2020 and a launch date before 2018, and compare their sum with Bitcoin [16]. The combined market capitalisation of these ten most influential Altcoins is still lower than Bitcoin's, as shown in Fig. 3.2, highlighting Bitcoin's dominance. Appendix B Fig. B.2 displays the average market capitalisation of the top ten Altcoins compared to Bitcoin. However, the true gap between Bitcoin's market capitalisation and the average of Altcoins would be significantly

wider if all Altcoins in the market were taken into account. The ten Altcoins in descending order are Ethereum [21], Tether [24], Ripple [23], Bitcoin Cash [17], Chainlink [20], Binance Coin [15], Litecoin [22], Bitcoin SV [18], Cardano [19], and USD Coin [25], ranging from 46 billion USD to 2.8 billion USD (these figures were obtained in October 2020). As market capitalisation is dependent on the price of the coin and the total number of coins in circulation, it will fluctuate over time.

3.2 Discussion

In the world of cryptocurrencies, it is common for investors and those with an interest to categorise Altcoins into 'oscillators' and 'degenerators' [149]. Dividing them into two segments is a good strategy for estimating their viability and added value as alternative investments. The value of oscillating cryptocurrencies tends to remain over time, their market behaviour resembles Bitcoin trading movements, their price usually increases when Bitcoin rises and decreases when it falls. Degenerative Altcoins tend to go down in value over time; most cryptocurrencies belong to the degenerator category. In many cases, these appear very promising initially, but ultimately fail to overcome periods of bearish markets and lose their price [44, 139].

By comparing Altcoin's performance with Bitcoin, we can get a coherent view of the cryptocurrency market. For Altcoins, Bitcoin is the de facto source of liquidity, which makes it an ideal reference point for this comparison. Ethereum, Ripple, Litecoin are oscillators as they all follow Bitcoin's price performance closely and remain well correlated with Bitcoin. Altcoins fitting the degenerator segment, do not oscillate with Bitcoin.

It is recommended to distinguish between oscillator and degenerator cryptocurrencies before making investments. Observing the market performance for the past four years should be enough to obtain an idea. As per the Lindy effect [68, 100] theory, the future life expectancy of non-perishable items is proportional to its current age. Cryptocurrencies belong to that group, therefore if a cryptocurrency has successfully survived for four years, it suggests that it will continue to do so in the the next four years. The longer it has survived, the higher the likelihood that it will survive the same period of time again. Examining the behaviour of a cryptocurrency during Bear and Bull cycles of Bitcoin markets allows one to know whether that cryptocurrency can retain its value [44, 139].

When an event or news triggers a trend, it attracts both types of groups of individuals, those who are already interested in cryptocurrencies, and those who are unaware of cryptocurrencies or want to find out more.

Observing GT interest popularity behaviour is not uncommon for investors deciding on the right time to buy/sell Bitcoins, or Altcoins. Early stages of rising interests are likely to continue, especially if the price is also rising, until the interest and price reach a stable point. Equally some may choose to observe when the interest declines, which usually results in price declining as well, consequently choosing the right time to invest. Some also use historical data to make predictions and to work out how long each stage (one peak) usually lasts. Careful observation may help recognise early stages of a peak and determine when the peak might reach its highest point, before it starts to decline again.

In 2016, we conducted the analysis for the 2013 to 2015 time period for Bitcoin, Litecoin, Peercoin and Mastercoin cryptocurrencies. As there were no further spikes in interest past 2014, the 2015 was a reasonable cut-off point. However, we can see now that at the beginning of 2017, both the interest and the price of the cryptocurrencies began experiencing large movements. Our analysis for Ethereum terminated at end of 2016. Now, it is visible that Ethereum's behaviour resembles that of Bitcoin and Litecoin. The interest was low in the early years, but then two distinct peaks occurred one shortly after the other.

3.3 Analysis: Google Trends interest and price comparison

3.3.1 GT search queries and price index

We are interested in the dynamics of the connection between GT search queries and the cryptocurrency price. The production and consumption of information on cryptocurrencies has soared over the years, leading to an increase in market capitalisation as well as general interest. We are curious as to whether the price and the volume of interest of a cryptocurrency are symmetric; i.e., an increase in price comes with an increase in interest, or vice versa. One of these properties may potentially be the driving force for the other one; changes in price could lead to changes in interest. Figs. 3.3 - 3.6 highlight evolution of GT searches compared to the price index of Bitcoin [10], Ethereum [11], Litecoin [12], and Ripple [13]. We observe a highest and fastest price increase throughout 2017, followed by a sudden substantial drop early 2018. Since hitting the peak in December 2017, all four coins have fluctuated extensively. Post 2018, all four cryptocurrencies follow the same scenario in which the price index is subject to occurrences of explosive bubbles followed by rectifications, that tend to be higher than the starting value of the pre-bubble phase, however none have come close to retesting the highs of December 2017.

Throughout 2017 the market's attention was firmly focused on Bitcoin's price tag, with

the value of a single Bitcoin increasing over 2000%, from 800 USD in January to a high of nearly 20000 USD in December. Ethereum, Litecoin, and Ripple achieved even greater gains ranging from 5000% to 20000% January to December 2017.

For each cryptocurrency, we obtain daily price and market capitalisation data from [14]. The time period is from the earliest month data available (this varies for each coin), to October 2020. The same time period for GT search interest data is selected. We apply the same rescaling method as from Chapter 2.

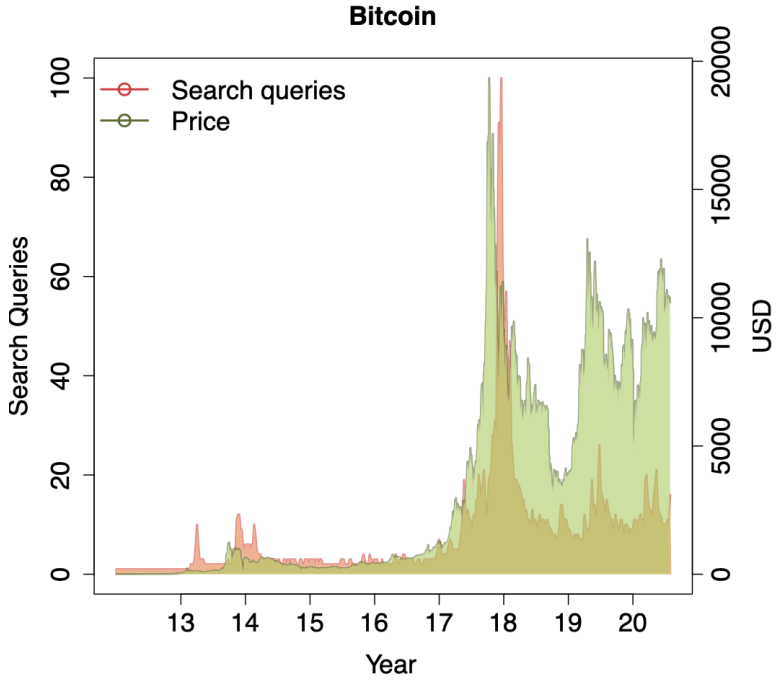

Figure 3.3: Bitcoin GT interest compared to Bitcoin price.

When a cryptocurrency hits a milestone price, it often is mentioned in the news, which makes it more likely for people to search for the cryptocurrency on Google - either to find out more about it, or to get involved to buy/sell the cryptocurrency. This activity in turn can cause fluctuations in price. Growing popularity of cryptocurrencies and Blockchain technology results in higher search volumes, which in turn result in increased social media activity on this subject. More interest encourages the investment into cryptocurrencies by individual users, aiding price increases, which ultimately reflects on the search volumes.

An examination of millions of transactions revealed that Tether, another cryptocurrency, was used to purchase Bitcoin at key moments when it was declining in 2017, and it is believed that this played a major role in the Bitcoin price surge [70]. Several factors may have contributed to the bubble bursting in 2018. A South Korean cryptocurrency

exchange, Coinrail, was hacked and lost in the region of 40 million USD. The US Security and Exchange Commission (SEC) did not approve a Bitcoin exchange trade fund (ETF) due to worries that cryptocurrency is subject to manipulation as shown in Griffin *et al.* [70]. Both these events occurred in 2018 and may have had an impact on the bubble burst. Bitcoin halving took place in May 2020, this may have been a trigger for the Bitcoin price movements in 2019, as cryptocurrency enthusiasts race to secure Bitcoin before the halving event. The halving makes mining more difficult, as supply goes down. This means Bitcoins could become rare, so individuals invest in Bitcoin with the hopes to make profit later on.

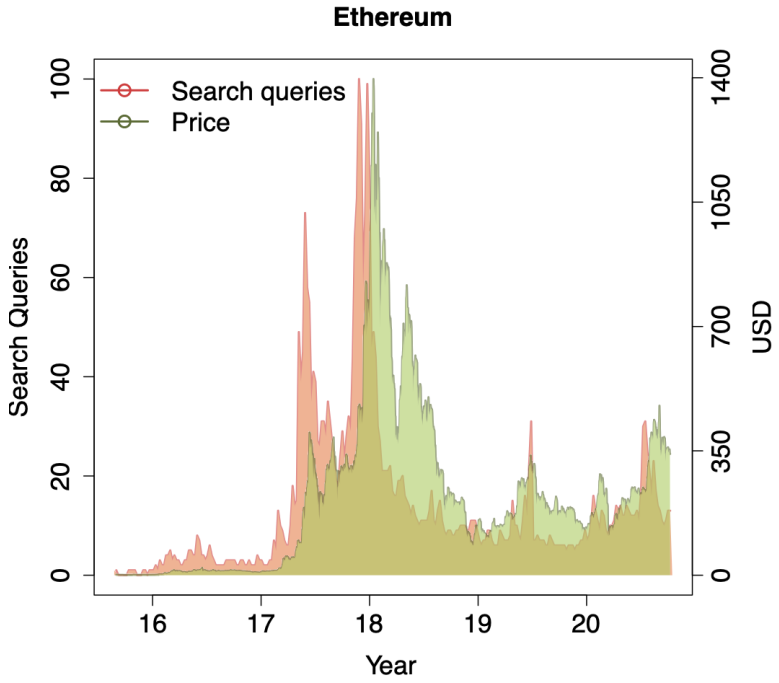

Figure 3.4: Ethereum GT interest compared to Ethereum Price.

Cryptocurrency price movements have tracked GT search queries quite closely, all four figures show how Google Trends scores proceed in the same direction of BTC, ETH, LTC, XRP prices, emphasising prominent similarity between them.

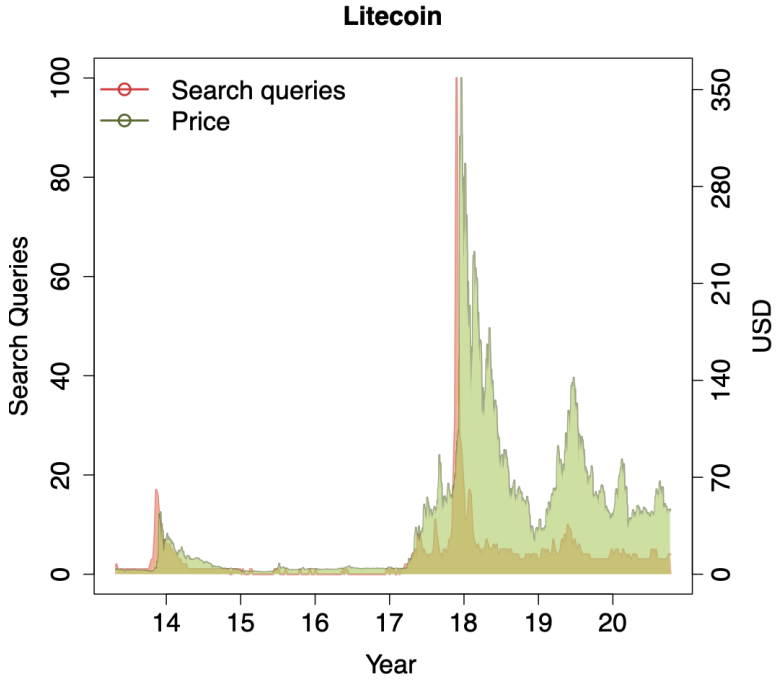

Figure 3.5: Litecoin GT interest compared to Litecoin Price.

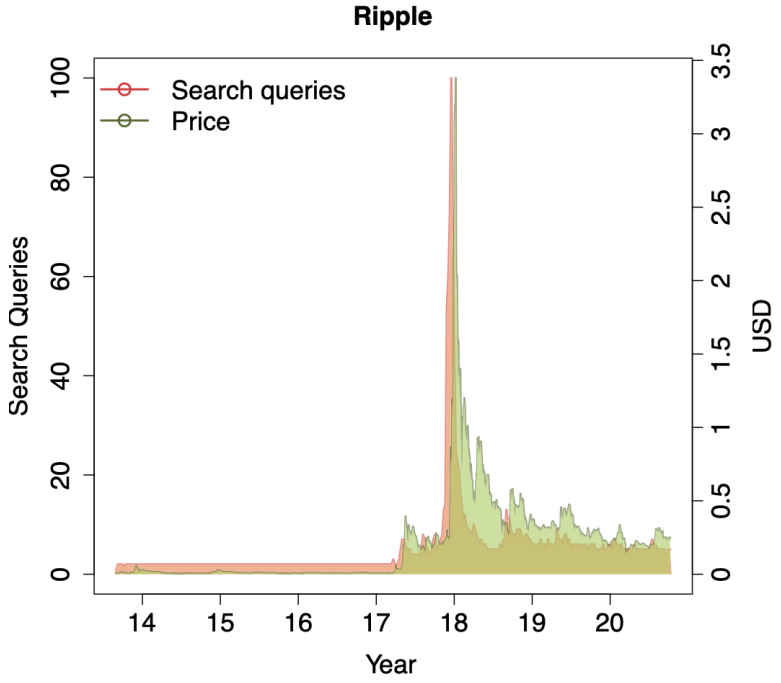

Figure 3.6: Ripple GT interest compared to Ripple Price.

The growing hype around cryptocurrencies has encouraged more people to want to learn about crypto. If this trend continues, there could be another healthy development like the one seen in 2017, with price and in GT interest. Bitcoin, Ethereum, Litecoin, and

Ripple show a strong positive trend in the price development over the past two years. The mounting trend of price changes in all four graphs seem to follow a similar pattern, which implies that the prices of considered cryptocurrencies could be driven by the same external driver, or the prices of Altcoins are following the price of Bitcoin, as the market leader. These developments are the reason why we are interested in the individual relationships of the cryptocurrencies and their effect on each other, and Bitcoin's leadership status over this period of time.

3.3.2 Wavelet coherence: GT search queries and price index

The work in this chapter will revisit and extend the application of wavelet coherence analysis conducted in Chapter 2, incorporating additional factors, such as price and supply, covering new data period, to determine the leading or lagging dynamics of these relationships. We examine relationships in time frequency space between two time series, in particular this section studies the relationship between GT interest and the price index of the associated cryptocurrency. We take the datasets from Figs. 3.3 to 3.6 and calculate log returns, to study the co-movement of GT interest and prices. Plots of the daily data, and corresponding log returns can be found in Appendix B Figs. B.3 - B.10.

As specified in the previous chapter, the statistically significant correlations are indicated by the thick black contour. The region below the thin black line indicates the cone of influence, and is shown as a blurred light blue shade separating less reliable regions. The colour bar corresponds to the significance level of the Monte-Carlo test, 1 (red) indicates high correlation between two time series, 0 (blue) no correlation.

The phase differences between the two data series are indicated by arrows. Arrows pointing to the right show in-phase behaviour (positive correlation). Arrows pointing to the right and up, indicate that the two datasets are positively correlated and the second is leading, if they point to the right and down then the same relationship holds but the second one lags. If the arrows point down, then the first dataset is leading and the second is lagging. Arrows pointing up indicate that the second dataset is leading and the first is lagging. Arrows pointing to the left illustrate that the variables are out-of-phase (negative correlation). If the arrows point to the left and up, the first dataset is leading, and if they point to the left and down, the first dataset is lagging.

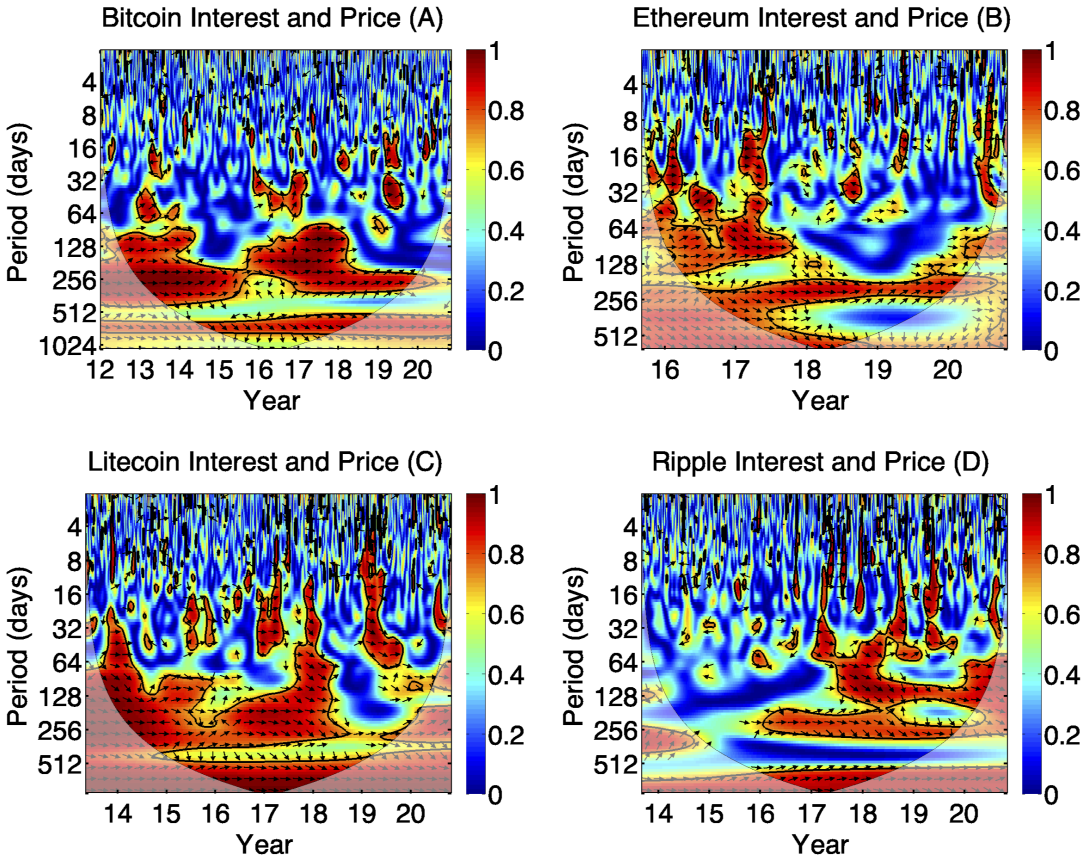

Figure 3.7: Wavelet coherence of GT interest and price index of (A) Bitcoin, (B) Ethereum, (C) Litecoin, (D) Ripple.

Fig. 3.7 shows the squared wavelet coherence between cryptocurrency interest and the price. Fig. 3.7 (A) features the co-movement of Bitcoin's GT interest and price index, covering the period from 2012 to 2020. The two datasets are highly positively correlated across medium and long term scales. At high scales between 512 and 1024 day band, interest leads the price. Across medium scales of 128 to 512 days we observe mostly strong positive correlation, with interest predominantly leading from 2012 to 2015. We then see a change in the relationship where price leads interest for approximately a year, from 2015 to 2016, after which interest takes lead, followed by the two variables moving in-phase, with no evident leader. From 2018 onwards, interest seems to slightly lag at medium time scales. Short term, the relationship is somewhat unstable and alternates between phases. In the 32-64 day band in 2013 (around the first price and interest peak, see Fig. 3.3) price seems to drive interest, similar dynamics seem to be present in 2016-2017 and 2019 when Bitcoin started experiencing price oscillations again.

In Fig. 3.7 (B), looking at higher time bands of 128 to 512 days, we notice that from 2016 to the end of 2018 interest is a clear leader in the Ethereum comparison. In the

128-256 day band from the end of 2018 to the end of 2019 price is the driver. Between 2016 and 2017 at medium scales (32-64 days) the relationship between the variables starts off with interest leading for the first couple of months in 2016, from approximately March onwards price briefly leads interest. In 2017, a change in relationship is apparent with interest leading price for approximately a year. Interestingly, in Ethereum comparison, as opposed to Fig. 3.7 (A), at short term scales (4-32 days) interest predominantly leads the price.

In Fig. 3.7 (C), the Litecoin interest and price comparison highlights a clear leader, the two variables are strongly positively correlated. Interest seems to drive the price across all scales and reliable regions, with an exception of a brief change of leadership around 2016 at higher scales, where interest lagged. However, the latter cannot be attributed to any major price or interest changes (see Fig. 3.5).

From Fig. 3.7 (D), we can also observe that it is predominantly the interest that drives the price of Ripple. At the higher scale of 512 days onwards between mid 2016 and mid 2017 price seems to slightly lead interest. The two datasets are strongly positively correlated, but only from the beginning of 2016, prior to that most of the dynamics at the higher scales fall outside the reliable region.

There is a strong causal relationship between prices and the interest. This is bi-directional, the prices have an impact on search queries, and the volume of interest has an impact on prices. Across all comparisons interest is an evident leader, especially at higher scales, i.e., in the long term.

3.3.3 Wavelet coherence: One-to-one comparisons of GT search queries and price index

In this section, we further explore the relationship between considered cryptocurrencies, by pairing them up with each other and analysing the dynamics. We explore the co-movement of GT interest and price index of individual coins in one-to-one comparison, covering a four-year period, mid 2016 to mid 2020. Analysis of price co-movement between different cryptocurrencies is key to understand short and long term relationship between them, which would be of interest to those wishing to diversify and broaden their digital coin investment portfolio.

Altcoins differ from each other in terms of network and transaction setup. We can expect that these differences affect the price formation and how closely they follow the Bitcoin prices. They will also have an impact on interest, as each cryptocurrency will

have its own benefits and costs, also causing a differentiated price formation. We expect that the Altcoins with price formation mechanisms similar to Bitcoin, will closely follow Bitcoin's price development.

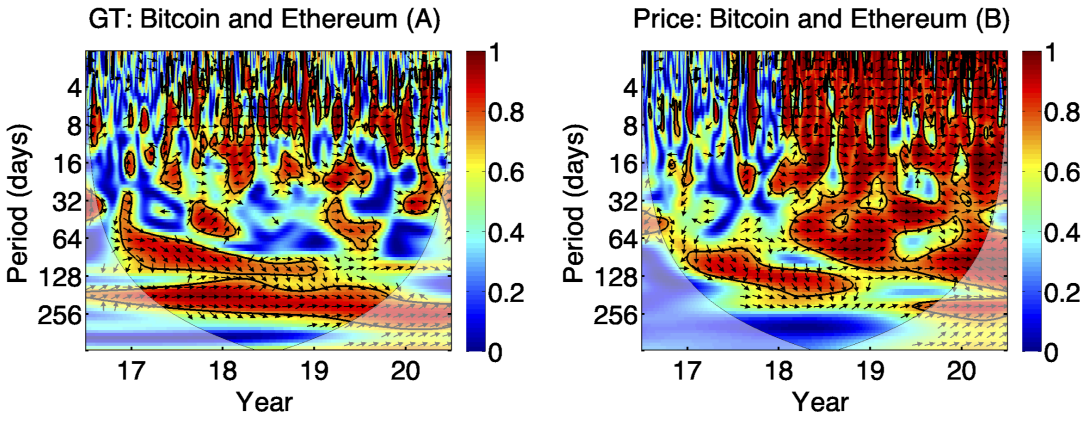

Figure 3.8: Wavelet coherence of Bitcoin and Ethereum: (A) GT interest, (B) Price index.

In Fig. 3.8 (A), we observe a distinct evolution of the Bitcoin and Ethereum search interest compared to the time periods considered in Chapter 2 (refer to Fig. 2.7 (A)). At lower scales we observe a number of high coherency regions, with in-phase relation across the considered time period. There is no apparent leader in the short term band (4-16 days), however Bitcoin seems to drive Ethereum at the end of 2018 and in the first half of 2019. We get a clearer picture in the medium scales between 16 and 64 day bands, Ethereum leads Bitcoin for around a year from mid 2017 to mid 2018, after which the relationship changes and Bitcoin becomes the driver. In the 64-128 day band Bitcoin is an evident leader, however in the 128-256 day band the two variables are mainly in-phase with Bitcoin taking lead from the end of 2018.

From Fig. 3.8 (B), we can see that there is not much high power in the lower and medium scales during the first year, and across the entire examined period past the 256 day band. We observe a section of high positive correlation in the 64-256 day band between 2017 and 2018, where Bitcoin is a clear leader of Ethereum price. From 2018 onwards we notice high coherency between the two variables across all scales, there is no evident leader in the shorter term relationship, however from around April 2020 Ethereum price seems to lead (16-64 days).

Fig. 3.9 (A) looks at the GT interest comparison, Bitcoin and Litecoin are positively correlated across all significant regions. Over short and medium term scales we notice a number of high coherency islands, mainly concentrated in the post 2017 section; there is no strong leader, Litecoin seems to be the driver around 2017 and Bitcoin interest seems

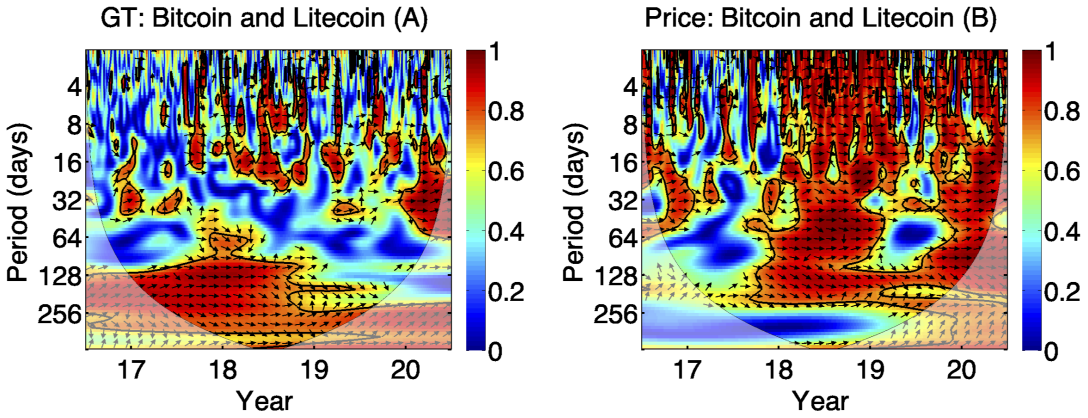

Figure 3.9: Wavelet coherence of Bitcoin and Litecoin: (A) GT interest, (B) Price index.

to slightly drive Litecoin closer to 2018. In the 64-128 day band at the end of 2017 to the beginning of 2018, Bitcoin is a clear leader. Long term the relationship varies over time, until 2019 Bitcoin seems to drive Litecoin, after which the relationship starts to break down and there is no apparent leader.

Fig. 3.9 (B) highlights lack of long term relationship for the first year of examined period. During the same period at lower scales (1-16 days) we observe frequent islands of high positive coherency, where changes in Bitcoin price seem to lead Litecoin short term, prior to the relationship changing, where Bitcoin's price starts to lag at the end of 2017 to beginning of 2018. From there onwards, in the short scale band there is no apparent leader and both variables are positively correlated. At medium scales between 16 and 64 day band Litecoin briefly leads Bitcoin at the end of 2016, followed by an in-phase movement of both variables and then a quiet phase. At the end of 2017 for a short period of time in the same medium scale band Bitcoin drives Litecoin. From 2018, the two datasets are highly positively correlated with no obvious leader, however Bitcoin seems to lead more often than Litecoin. The long term relationship between Bitcoin and Litecoin only appears at the end of 2017, when the price of both coins was on the rise (refer to Figs. 3.3 and 3.5), Bitcoin is a clear leader at higher scales in the 128-256 day band.

In Fig. 3.10 (A), Bitcoin and Ripple exhibit strong positive correlation from 2017 onwards at higher scales between approximately 100 and 500 days, where Bitcoin is a strong leader. The long term relationship between the two variables starts to break down in 2019. In the low and medium scales the significant correlations mainly appear from 2018 onwards, with no evident leader, however Bitcoin seems to slightly lag in 2018 and 2019. Interestingly, in Fig. 3.10 (B), all significant co-movement seems to happen post 2018. The two datasets are highly correlated and move together at almost all scales. At

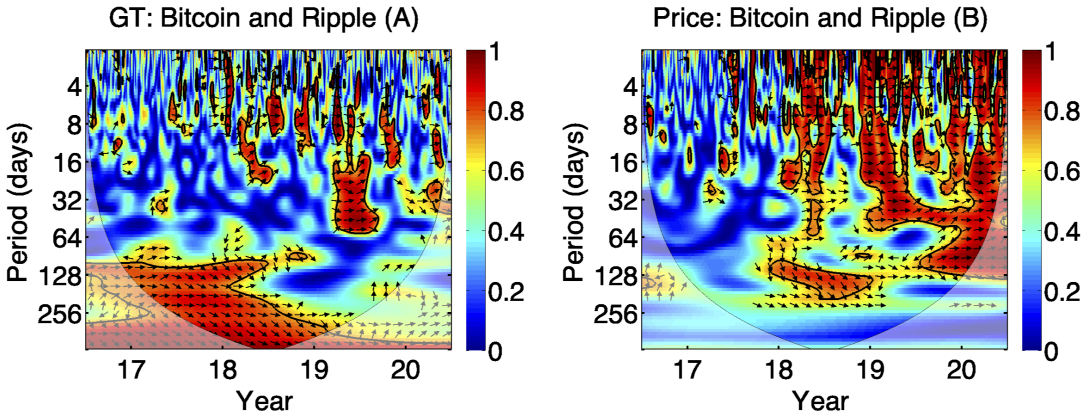

Figure 3.10: Wavelet coherence of Bitcoin and Ripple: (A) GT interest, (B) Price index.

lower and medium scales the lead/lag relationship alternates, both cryptocurrencies are in-phase, with Ripple briefly leading in 2018 and 2019, similar movement as Fig. 3.10 (A), and Bitcoin taking lead at the end of 2019. In the higher scales of approximately 100-256 day band, between 2018 and 2019, Bitcoin is again a strong leader.

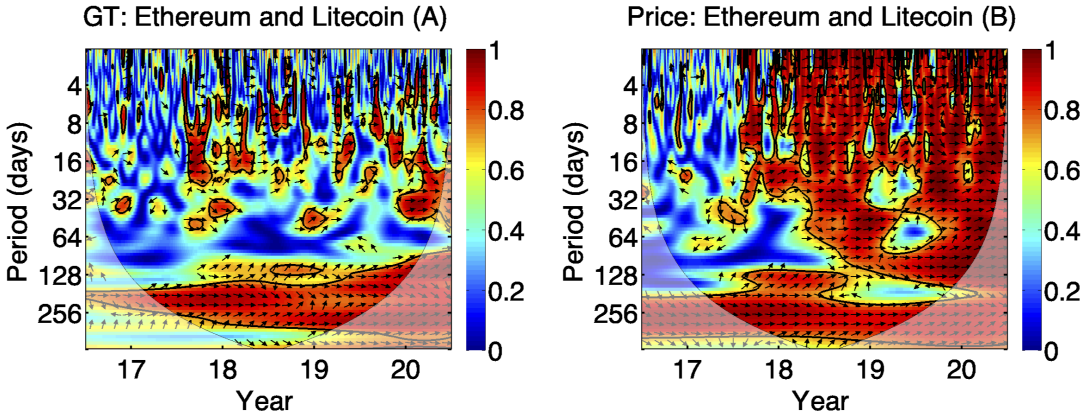

Figure 3.11: Wavelet coherence of Ethereum and Litecoin: (A) GT interest, (B) Price index.

Fig. 3.11 (A) indicates that Ethereum and Litecoin are positively correlated across all scales and during the entire examined period. There is no evident leader in the relationship. At lower and medium scales the lead/lag relationship alternates between the two variables. In Fig. 3.11 (B), we see that Ethereum and Litecoin move together across all scales from the end of 2017 onwards. The two datasets are highly positively correlated. The relationship changes somewhat and the two variables are mainly in-phase, however Litecoin seems to be the leader in the price comparison, especially at higher scales around 2018.

Fig. 3.12 (A) lacks co-movement at medium scales, however in the islands of high coherency that are present in the 16-64 day band, Ripple takes lead. At lower scales, there

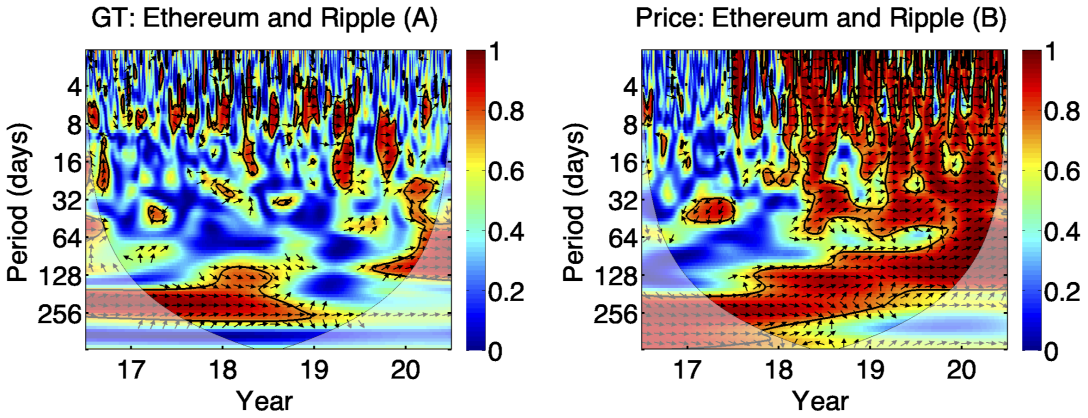

Figure 3.12: Wavelet coherence of Ethereum and Ripple: (A) GT interest, (B) Price index.

is no evident leader, but the two variables are positively correlated. At higher scales, the relationship between Ethereum and Ripple seems to break off in 2019, prior to which we observe in-phase behaviour, with Ethereum leading in 2018. In Fig. 3.12 (B), similarly to the previous two price comparisons, significant coherence regions can be observed closer to 2018, which we can attribute to major price increases in 2017 across all considered cryptocurrencies. We mainly observe in-phase movement, however Ripple seems to slightly lead across all scales.

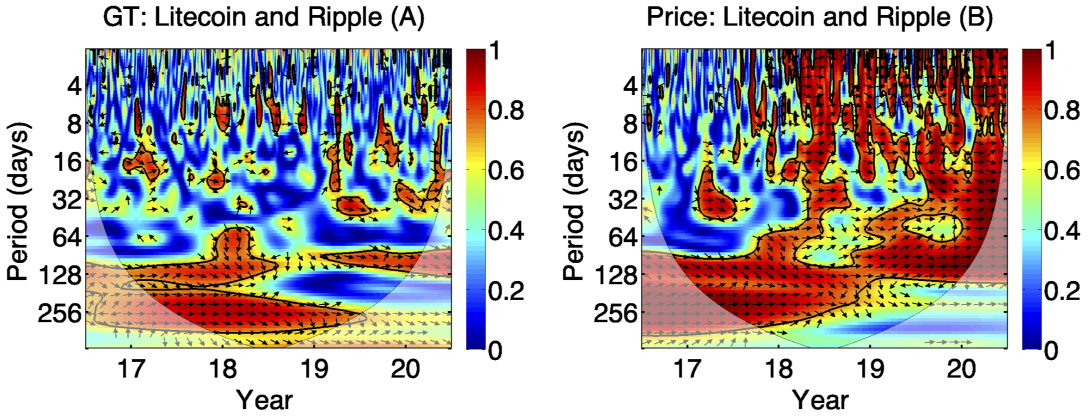

Figure 3.13: Wavelet coherence of Litecoin and Ripple: (A) GT interest, (B) Price index.

In Fig. 3.13 (A), there is no evident leader at lower scales, at medium scales Litecoin leads between 16 and 64 day band from 2019. At higher scales, Litecoin is a strong leader. Fig. 3.13 (B) shows high coherence across all scales. Litecoin is a clear leader in higher scales between approximately 90 and 300 days, the long term relationship starts to vanish at around 2019. Between 2019 and 2020 in the 32-128 day band Ripple price is the driver. The short term lead/lag relationship at lower scales is somewhat unstable, but Litecoin seems to lead more often than Ripple.

We can observe that initially the lower scale correlation between Bitcoin and Altcoin prices is sparse until mid 2017, indicating the lack of co-movement between short term traders. High positive coherence is present in all comparisons covering the considered period, with the exception of Bitcoin and Ripple (Fig. 3.10 (B)), indicating a possible increased presence of long term investors and users. As the market capitalisation and market share increase, co-movement also increases from the second half of 2017, which is indicative of both short and long term investors and users across the Bitcoin and the Altcoin markets.

3.3.4 Wavelet coherence: coin supply

As with fiat currencies, the price of a cryptocurrency is determined by its supply and demand. This is applicable in the short, medium, and long run. The more transactions there are, the higher the demand. Shifts in demand will have a direct impact on the price of the cryptocurrency. We can expect that coin supply limitation will also affect prices.

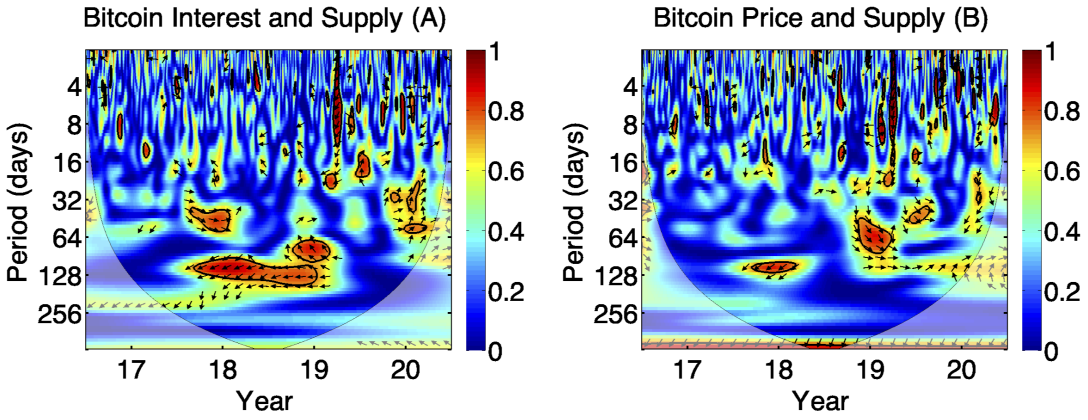

Figure 3.14: Wavelet coherence of Bitcoin GT interest and price index compared to coin supply: (A) Interest, (B) Price.

In Fig. 3.14 (A), Bitcoin's interest and supply are negatively correlated at higher scales between 64 and 256 day band from end of 2017 to beginning of 2019, at around 128 days in 2018, interest lags, and in the 64-128 day band in 2019, interest leads. However the two variables are in-phase around 2020 with supply driving the interest, in the lead to reward halving which took place in May 2020. There is no evident leader in the lower scales and the phase relationship alternates.

Interestingly, we observe two islands of high positive coherence in Fig. 3.14 (B) from the end of 2018 to 2020 between the 32-128 day band with Bitcoin price leading, followed by a phase change in 2020 around April time with supply being the driver, just before

the reward halving event. From the end of 2017 to beginning of 2018 at higher scales of around 128 days there is a single island of high correlation, the two variables are antiphase with supply leading, it also coincides with major Bitcoin price movements at the time (refer to Fig. 3.3). At higher scales at around 128 day band from mid 2019, the price and supply of Bitcoin are positively correlated with supply driving the price. Most of the dynamics is concentrated in the 2019 to 2020 region; interpreting the lead/lag relationship at lower scales is challenging as there is not much co-movement between the datasets and no apparent leader.

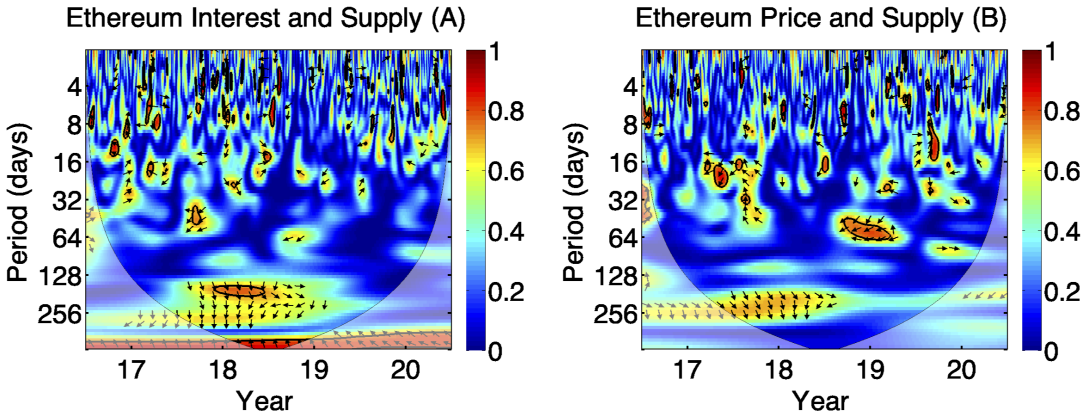

Figure 3.15: Wavelet coherence of Ethereum GT interest and price index compared to coin supply: (A) Interest, (B) Price.

In Fig. 3.15 (A), we observe a lot of phase changes short term in the low and medium scales, and there is no evident leader in the lead/lag relationship. Ethereum interest is positively correlated with its supply in the long term between 128 and 256 days from end of 2017 to 2019, in the statistically significant at 5% region interest is the driver. At higher scales of approximately 300 to 500 day band the variables are highly correlated and antiphase, most of the dynamics are in the cone of influence, the reliable section indicates that interest leads supply. As expected the price and supply of Ethereum in Fig. 3.15 (B) are mainly negatively correlated across lower and medium scales. At higher scales of approximately 128-300 day band around 2018 there is a segment of strong, but not statistically significant at the 5% level, positive correlation between the variables where price leads supply.

In Fig. 3.16 (A), we can observe a few phase changes at lower scales, and as expected there is no evident leader in the 1-8 day band. Overall in the medium and higher scales the variables are mainly positively correlated. In the 8-32 day band, there are a couple of islands of high coherency where supply seems to drive interest. In the 32-128 day band

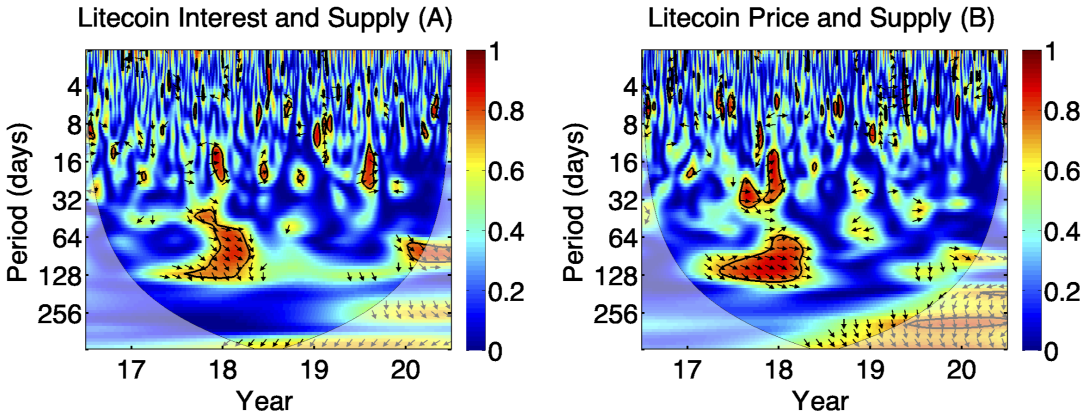

Figure 3.16: Wavelet coherence of Litecoin GT interest and price index compared to coin supply: (A) Interest, (B) Price.

around 2018 and again around 2020, interest is a strong leader. At higher scales past the 256 day band, there is a segment of strong, but not statistically significant at the 5% level, negative correlation between the variables where supply leads interest.

Fig. 3.16 (B) shows some in-phase and antiphase co-movement at lower scales (1-8 days), from 2017 to 2020 the relationship is lead by supply. Price and supply are highly positively correlated around 2018 at medium scales; between 16 and 32 days, supply drives the price, between 64 and 128 days, price starts to lead. There are islands of strong, but not statistically significant at the 5% level, negative correlation past 2018 where supply is the driver in the 16-128 day band.

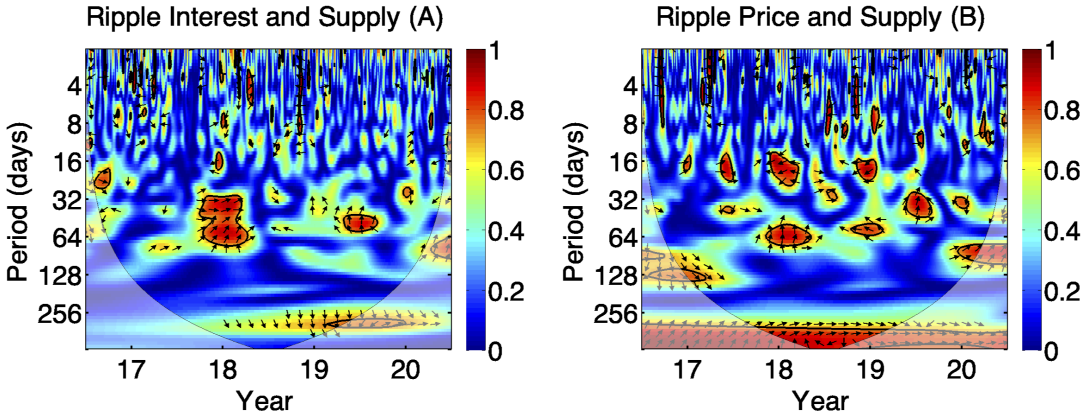

Figure 3.17: Wavelet coherence of Ripple GT interest and price index compared to coin supply: (A) Interest, (B) Price.

In the interest and supply comparison of Ripple (Fig. 3.17 (A)), the long term dynamics is behind the cone of influence, hence cannot be interpreted as reliable. At medium scales between approximately 32 and 80 day band around 2018, there are two regions of high

coherency where supply leads interest. At lower scales there is not much co-movement and no apparent leader. In Fig. 3.17 (B), most of the long term dynamics (approximately 256-500 day band) is again hidden in the cone of influence, hence cannot be treated as reliable, however the middle section outside the cone of influence suggests that supply of Ripple drives its price in the long run. There are a number of islands of high coherency across lower and medium scales, the relationship alternates between phases, however supply clearly leads the price of the coin.

Cryptocurrencies with a limited maximum coin supply, such as Bitcoin, Litecoin, and Ripple seem to have more correlation present in the plots. Coin supply has an effect on both, interest and the price, and supply drives the price. Ripple has the highest supply cap of 100 billion and it is reflected in the long term relationship in the cross-wavelet comparison. However, in the case of Ethereum the coin supply is not limited, hence it is the interest and the price that drive the supply, i.e., it is the search queries and price increases that get miners and investors interested in the coin.

3.4 Conclusion

Blockchain technology has been serious contender from the beginning. It aimed to tackle the centralisation and monopolistic nature of banks. The idea was not immediately welcomed however we can see that there is growing interest and many industries, including banks, are now integrating Blockchain. Comparing our Chapter 2 analysis with the one in Chapter 3, it is clear that cryptocurrencies are on the rise. Blockchain and Bitcoin are both past their respective acceptance stages, and people have started to realise the potential opportunities they offer. Social media platform Facebook are developing Libra, a Blockchain based cryptocurrency; banks, such as HSBC, are investing in distributed ledger technologies; Russia are looking into CryptoRuble as a new digital currency also based on Blockchain; lender companies like Nexo allow loans (including mortgages) with Bitcoins; no doubt more companies will follow suit. Blockchain is recognised as a secure and trustworthy solution with applications in several fields. Bitcoin has now been around for over 10 years. Having survived Bull and Bear cycles, Bitcoin has proved its worth and is highly likely to stay for many more years to come.

In the individual coin comparisons, we notice a significant increase in activity from 2018 onwards, which is undoubtedly due to the Bitcoin market share dropping, and the market share and capitalisation of Altcoins increasing. We can also conclude that cryptocurrency's interest (GT interest) is an evident driver of the price index. Hence, increasing interest in

the cryptocurrency, assists in increasing demand and therefore increasing prices. Bitcoin and Altcoin prices are indeed interdependent, the lead/lag relationship tends to alternate between low and medium scales, i.e., short term; however long term Bitcoin seems to lead more often. Cryptocurrency supply influences both, prices and interest/demand, the impact is stronger at lower and medium scales, i.e., in the short run.

Using cryptocurrency exchanges has become easier over the years; the coins that cannot be mined or are hard to mine have been made accessible by these exchanges and fintech companies like Revolut. As a result, there are well over 3000 cryptocurrencies out there, with different types of consensus mechanisms. There are also many cryptocurrencies that are released as an improvement to their predecessors. For example, Ethereum 2.0 will be the next version of Ethereum, and it will support Proof of Stake as the consensus mechanism, which requires significantly less computing power as not all participants are required to attempt to solve the hash.

Since there exists such a vast range of cryptocurrencies, investors should evaluate these to assess the risk of investment, and miners should pay attention to the consensus mechanism. Some cryptocurrencies are easier to mine than others, some provide extremely fast block creation times, e.g. Ripple can confirm transactions within 5 seconds, a considerable difference to Bitcoin's 10 minute average. Not all cryptocurrencies are based on Blockchain, but the trend is similar.

Chapter 4

System of two coupled phase oscillators with distributed time delays

In this chapter, we introduce a system of coupled Kuramoto oscillators [89], which describes the oscillatory dynamics of nodes in the network. The coupling function incorporates a delay term, consisting of weighted influences from past times [81], with a probability given by a delay distribution kernel. The case of discrete delay was considered in [51]. The elements of the network are assumed to be identical, and the natural frequency is eliminated. The system admits synchronous and antisynchronous frequency locked solutions, i.e., in-phase and antiphase.

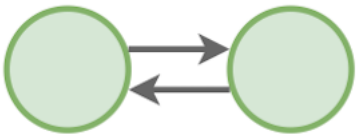

Figure 4.1: Two mutually coupled oscillators.

We investigate the effect of distributed time delay on the synchronisation of nonlinear oscillators. The two coupled delay-differential equations describing the phase dynamics are

$$\begin{aligned} \dot{\theta_1}(t) &= 1 + \kappa \sin\left[\int_0^\infty g(s)\theta_2(t-s)ds - \theta_1(t)\right], \\ \dot{\theta_2}(t) &= 1 + \kappa \sin\left[\int_0^\infty g(s)\theta_1(t-s)ds - \theta_2(t)\right], \end{aligned} \tag{4.1}$$

where θ_1, θ_2 are the phases of the oscillator, κ is the coupling strength, and $g(\cdot)$ is the

kernel of the delay distribution, which is assumed to be positive definite and normalised to unity

$$g(s) \geq 0 \quad \text{and} \quad \int_0^\infty g(s)ds = 1.$$

If the delay distribution is governed by the Dirac delta function $g(s) = \delta(s)$, the two oscillators in System (4.1) are interacting instantaneously reducing it to the Adler equation [29], and if $g(s) = \delta(s - \tau)$, then System (4.1) reduces to the case of discrete time-delayed coupling between oscillators, considered in [51].

Phase-locked solutions in steady state are characterised by a collective frequency ω, with which all oscillators evolve in time, and a common phase shared by all oscillators in the system, i.e., in-phase, antiphase. The focus is on solutions with fixed frequency of oscillation; rotating wave solutions. The coupling is attractive when the coupling strength κ is positive, so the oscillators progress towards a symmetric state, i.e., in-phase. The coupling is repulsive when the coupling strength κ is negative, so the oscillators tend towards an antiphase oscillation. As a result of the symmetry of a coupling function, stable in-phase and antiphase solutions interchange when the coupling strength κ changes from positive to negative, and vice versa. Delayed coupling induces multiple solutions with different locking frequencies in the frequency locked symmetric and antisymmetric states.

The ansatz for the in-phase solutions is $\theta_1(t) = \theta_2(t) = \omega t$, and signifies linear growth of the phases with the global frequency ω. The frequencies can be found by solving

$$\begin{aligned}
\omega =& 1 + \kappa \sin\left[\int_0^\infty g(s)\omega(t-s)ds - \omega t\right] \\
=& 1 + \kappa \sin\left[\omega\left(t\int_0^\infty g(s)ds - \int_0^\infty sg(s)ds\right) - \omega t\right] \\
=& 1 - \kappa \sin\left[\omega \int_0^\infty sg(s)ds\right].
\end{aligned} \tag{4.2}$$

Similarly for the anti-phase solutions $\theta_1(t) = \theta_2(t) + \pi = \omega t$, the system of equations reduces to solving

$$\omega = 1 + \kappa \sin\left[\omega \int_0^\infty sg(s)ds\right]. \tag{4.3}$$

We have that (4.2) and (4.3) are the implicit in-phase and antiphase expressions for collective frequency ω. Both equations are only dependent on the mean of the delay distribution $g(s)$. The shape of distribution $g(s)$ does not affect the equation, nor does the quantity of oscillators in the system.

4.1 In-phase solution analysis - linearisation

Linear stability analysis deduces the linear stability of a solution to a dynamical system. The synchronised system in steady state is affected by small perturbations in the case of linearised dynamics, valid only close to the steady state. Perturbations will grow for unstable steady states as the system is not attracted back to the steady state. However for stable steady states, the perturbation will approach zero. When the linear stability analysis cannot determine the stability of a steady state, higher order terms must be taken into consideration [130].

To linearise System (4.1), a small perturbation is added to the in-phase solution

$$\theta_1(t) = \omega t + \epsilon\phi_1(t),$$
$$\theta_2(t) = \omega t + \epsilon\phi_2(t),$$

where $0 < \epsilon \ll 1$, substituting this into the system of equations (4.1) yields

$$\omega + \epsilon\dot{\phi_1}(t) = 1 + \kappa \sin\left[\int_0^\infty g(s)\big(\omega(t-s) + \epsilon\phi_2(t-s)\big)ds - \omega t - \epsilon\phi_1(t)\right]$$

$$1 - \kappa \sin\left[\omega\int_0^\infty sg(s)ds\right] + \epsilon\dot{\phi_1}(t) = 1 + \kappa \sin\left[\omega\int_0^\infty g(s)(t-s)ds - \omega t + \epsilon\int_0^\infty g(s)\phi_2(t-s)ds - \epsilon\phi_1(t)\right]$$

$$\begin{aligned}\epsilon\dot{\phi_1}(t) &= \kappa \sin\left[\omega\left(t\int_0^\infty g(s)ds - \int_0^\infty sg(s)ds\right)\right] + \kappa \sin\left[\omega\int_0^\infty sg(s)ds\right] \\ &\quad + \kappa \sin\left[\epsilon\int_0^\infty g(s)\phi_2(t-s)ds - \omega t - \epsilon\phi_1(t)\right] \\ &= -\kappa \sin\left[\omega\int_0^\infty sg(s)ds - \epsilon\int_0^\infty g(s)\phi_2(t-s)ds + \epsilon\phi_1(t)\right] \\ &\quad + \kappa \sin\left[\omega\int_0^\infty sg(s)ds\right].\end{aligned}$$

Taylor expansion for $\epsilon \ll 1$ leads to

$$\begin{aligned}\epsilon\dot{\phi_1}(t) &= \kappa \sin\left[\omega\int_0^\infty sg(s)ds\right] - \kappa\left[\sin\left(\omega\int_0^\infty sg(s)ds\right)\right. \\ &\quad \left. + \left(-\epsilon\int_0^\infty g(s)\phi_2(t-s)ds + \epsilon\phi_1(t)\right)\cos\left(\omega\int_0^\infty sg(s)ds\right)\right] \\ &= -\kappa\left[\epsilon\left(-\int_0^\infty g(s)\phi_2(t-s)ds + \phi_1(t)\right)\right]\cos\left[\omega\int_0^\infty sg(s)ds\right].\end{aligned}$$

Hence the two linear equations are

$$\begin{aligned}\dot{\phi_1}(t) =&\kappa \cos\left[\omega \int_0^\infty sg(s)ds\right]\left[\int_0^\infty g(s)\phi_2(t-s)ds - \phi_1(t)\right],\\ \dot{\phi_2}(t) =&\kappa \cos\left[\omega \int_0^\infty sg(s)ds\right]\left[\int_0^\infty g(s)\phi_1(t-s)ds - \phi_2(t)\right].\end{aligned} \tag{4.4}$$

4.1.1 In-phase solution analysis - characteristic equation

The solutions of (4.4) are linear combinations of exponentials for general linear dynamical systems [74]. To determine whether the perturbation grows or decays as the system changes, we consider $\phi_i(t) = c_i e^{\lambda t}$, where $i = 1, 2$ and $\lambda \in \mathbb{C}$. The characteristic equation derived from (4.4) describes the linear dynamics of the perturbation.

The stability of a solution is decided by the sign of the real part of λ [75]. A solution is stable when the real part is negative, the perturbation decays exponentially. A solution is unstable when the real part is positive, here, the perturbation grows exponentially. When the real part is 0, the solution is neutral; in this case the linearised dynamics are insufficient to decide the stability (higher order terms need to be examined) [54, 130]. The value of the real part of λ determines the rate at which the perturbation grows/decays. The imaginary part of λ represents the frequency of oscillation of the perturbation growth/decay dynamics.

$$\begin{pmatrix}\dot{\phi_1}\\ \dot{\phi_2}\end{pmatrix} = \begin{pmatrix}-a & 0\\ 0 & -a\end{pmatrix}\begin{pmatrix}\phi_1\\ \phi_2\end{pmatrix} + \begin{pmatrix}0 & a\\ a & 0\end{pmatrix}\begin{pmatrix}\int_0^\infty g(s)\phi_1(t-s)ds\\ \int_0^\infty g(s)\phi_2(t-s)ds\end{pmatrix},$$

where $a = \kappa \cos\left[\omega \int_0^\infty sg(s)ds)\right]$,

$$\begin{pmatrix}c_1\lambda e^{\lambda t}\\ c_2\lambda e^{\lambda t}\end{pmatrix} = \begin{pmatrix}-a & 0\\ 0 & -a\end{pmatrix}\begin{pmatrix}c_1 e^{\lambda t}\\ c_2 e^{\lambda t}\end{pmatrix} + \begin{pmatrix}0 & a\\ a & 0\end{pmatrix}\begin{pmatrix}\int_0^\infty g(s)c_1\lambda e^{\lambda(t-s)}ds\\ \int_0^\infty g(s)c_2\lambda e^{\lambda(t-s)}ds\end{pmatrix}$$

$$\begin{pmatrix}\lambda & 0\\ 0 & \lambda\end{pmatrix}\begin{pmatrix}c_1 e^{\lambda t}\\ c_2 e^{\lambda t}\end{pmatrix} = \begin{pmatrix}-a & 0\\ 0 & -a\end{pmatrix}\begin{pmatrix}c_1 e^{\lambda t}\\ c_2 e^{\lambda t}\end{pmatrix} + \begin{pmatrix}0 & a\\ a & 0\end{pmatrix}\begin{pmatrix}c_1 e^{\lambda t}\{\mathcal{L}g\}(\lambda)\\ c_2 e^{\lambda t}\{\mathcal{L}g\}(\lambda)\end{pmatrix},$$

where $\{\mathcal{L}g\}(\lambda) = \int_0^\infty g(s)e^{-\lambda s}ds$ is the Laplace transform of the function $g(s)$ of the delay distribution.

$$\begin{pmatrix}\lambda & 0\\ 0 & \lambda\end{pmatrix}\begin{pmatrix}\phi_1\\ \phi_2\end{pmatrix} = \begin{pmatrix}-a & 0\\ 0 & -a\end{pmatrix}\begin{pmatrix}\phi_1\\ \phi_2\end{pmatrix} + \begin{pmatrix}0 & a\\ a & 0\end{pmatrix}\begin{pmatrix}\phi_1\\ \phi_2\end{pmatrix}\{\mathcal{L}g\}(\lambda),$$

which has the form

$$\lambda I\boldsymbol{\phi} = L_0\boldsymbol{\phi} + M\{\mathcal{L}g\}(\lambda)\boldsymbol{\phi}$$
$$\boldsymbol{\phi}\big(\lambda I - L_0 - M\{\mathcal{L}g\}(\lambda)\big) = 0.$$

Taking

$$\det\big(\lambda I - L_0 - M\{\mathcal{L}g\}(\lambda)\big) = 0,$$
$$\det\begin{pmatrix} \lambda + \kappa\cos\left[\omega\int_0^\infty sg(s)ds\right] & -\kappa\cos\left[\omega\int_0^\infty sg(s)ds\right]\{\mathcal{L}g\}(\lambda) \\ -\kappa\cos\left[\omega\int_0^\infty sg(s)ds\right]\{\mathcal{L}g\}(\lambda) & \lambda + \kappa\cos\left[\omega\int_0^\infty sg(s)ds\right] \end{pmatrix} = 0,$$

results in the following characteristic equation

$$\left[\lambda + \kappa\cos\left(\omega\int_0^\infty sg(s)ds\right)\right]^2 - \kappa^2\cos^2\left[\omega\int_0^\infty sg(s)ds\right]\big[\{\mathcal{L}g\}(\lambda)\big]^2 = 0. \tag{4.5}$$

The solutions are rotating waves (periodic orbits), hence the characteristic equation (4.5) always has $\lambda = 0$ as an eigenvalue, corresponding to the phase shift symmetry of the oscillators.

4.2 Antiphase solution analysis - linearisation

A small perturbation is added to the antiphase solution

$$\theta_1(t) = \omega t + \epsilon\phi_1(t),$$
$$\theta_2(t) = \omega t - \pi + \epsilon\phi_2(t),$$

where $0 < \epsilon \ll 1$, substituting this into the system of equations (4.1) yields

$$\omega + \epsilon\dot{\phi_1}(t) = 1 + \kappa\sin\left[\int_0^\infty g(s)\big(\omega(t-s) - \pi + \epsilon\phi_2(t-s)\big)ds - \omega t - \epsilon\phi_1(t)\right]$$

$$\begin{aligned} 1 + \kappa\sin\left[\omega\int_0^\infty sg(s)ds\right] + \epsilon\dot{\phi_1}(t) =& 1 + \kappa\sin\left[\omega\int_0^\infty g(s)(t-s)ds - \omega t - \epsilon\phi_1(t)\right. \\ & \left. - \pi\int_0^\infty g(s)ds + \epsilon\int_0^\infty g(s)\phi_2(t-s)ds\right] \end{aligned}$$

$$\begin{aligned}\epsilon\dot{\phi_1}(t) =&\kappa\sin\left[\omega\left(t\int_0^\infty g(s)ds-\int_0^\infty sg(s)ds\right)-\pi+\epsilon\int_0^\infty g(s)\phi_2(t-s)ds-\omega t\right.\\&\left.-\epsilon\phi_1(t)\right]-\kappa\sin\left[\omega\int_0^\infty sg(s)ds\right]\\=&-\kappa\sin\left[\omega\int_0^\infty sg(s)ds-\epsilon\int_0^\infty g(s)\phi_2(t-s)ds+\epsilon\phi_1(t)+\pi\right]\\&-\kappa\sin\left[\omega\int_0^\infty sg(s)ds\right].\end{aligned}$$

Taylor expansion for $\epsilon \ll 1$ leads to

$$\begin{aligned}\epsilon\dot{\phi_1}(t) =&-\kappa\sin\left[\omega\int_0^\infty sg(s)ds\right]+\kappa\left[\sin\left(\omega\int_0^\infty sg(s)ds\right)\right.\\&\left.+\left(-\epsilon\int_0^\infty g(s)\phi_2(t-s)ds+\epsilon\phi_1(t)\right)\cos\left(\omega\int_0^\infty sg(s)ds\right)\right]\\=&\kappa\left[\epsilon\left(-\int_0^\infty g(s)\phi_2(t-s)ds+\phi_1(t)\right)\right]\cos\left[\omega\int_0^\infty sg(s)ds\right].\end{aligned}$$

Hence the two linear equations are

$$\begin{aligned}\dot{\phi_1}(t) =&\kappa\cos\left[\omega\int_0^\infty sg(s)ds\right]\left[-\int_0^\infty g(s)\phi_2(t-s)ds+\phi_1(t)\right],\\\dot{\phi_2}(t) =&\kappa\cos\left[\omega\int_0^\infty sg(s)ds\right]\left[-\int_0^\infty g(s)\phi_1(t-s)ds+\phi_2(t)\right].\end{aligned}\tag{4.6}$$

4.2.1 Antiphase solution analysis - characteristic equation

Similarly to the in-phase analysis we consider $\phi_i(t) = c_i e^{\lambda t}$, where $i = 1, 2$ and $\lambda \in \mathbb{C}$. The characteristic equation for (4.6) is as follows

$$\begin{pmatrix}\dot{\phi_1}\\\dot{\phi_2}\end{pmatrix}=\begin{pmatrix}a&0\\0&a\end{pmatrix}\begin{pmatrix}\phi_1\\\phi_2\end{pmatrix}+\begin{pmatrix}0&-a\\-a&0\end{pmatrix}\begin{pmatrix}\int_0^\infty g(s)\phi_1(t-s)ds\\\int_0^\infty g(s)\phi_2(t-s)ds\end{pmatrix},$$

which has the form

$$\boldsymbol{\phi}\big(\lambda I - L_0 - M\{\mathcal{L}g\}(\lambda)\big) = 0,$$

where $\{\mathcal{L}g\}(\lambda) = \int_0^\infty g(s)e^{-\lambda s}ds$ is the Laplace transform of the function $g(s)$. Now taking

$$\det\big(\lambda I - L_0 - M\{\mathcal{L}g\}(\lambda)\big) = 0,$$

$$\det\begin{pmatrix}\lambda-\kappa\cos\left[\omega\int_0^\infty sg(s)ds\right]&\kappa\cos\left[\omega\int_0^\infty sg(s)ds\right]\{\mathcal{L}g\}(\lambda)\\\kappa\cos\left[\omega\int_0^\infty sg(s)ds\right]\{\mathcal{L}g\}(\lambda)&\lambda-\kappa\cos\left[\omega\int_0^\infty sg(s)ds\right]\end{pmatrix}=0,$$

which results in the following characteristic equation

$$\left[\lambda - \kappa\cos\left(\omega\int_0^\infty sg(s)ds\right)\right]^2 - \kappa^2\cos^2\left[\omega\int_0^\infty sg(s)ds\right]\left[\{\mathcal{L}g\}(\lambda)\right]^2 = 0. \tag{4.7}$$

Characteristic equation (4.7) always has $\lambda = 0$ as an eigenvalue.

4.3 Uniformly distributed delay

In this section, we consider Systems (4.4) and (4.6) with the uniform distribution used as the delay kernel.

4.3.1 In-phase solution

Equations (1.14) and (1.16) transform the in-phase characteristic equation (4.5) to

$$\left[\lambda+\kappa\cos(\omega\tau)+\kappa\cos(\omega\tau)\left(e^{-\lambda\tau}\frac{\sinh(\lambda\rho)}{\lambda\rho}\right)\right]\left[\lambda+\kappa\cos(\omega\tau)-\kappa\cos(\omega\tau)\left(e^{-\lambda\tau}\frac{\sinh(\lambda\rho)}{\lambda\rho}\right)\right] = 0. \tag{4.8}$$

We now consider the solutions in the form $\lambda = i\bar{\omega}$, hence

$$i\bar{\omega} + \kappa\cos(\omega\tau) = \kappa\cos(\omega\tau)\left[\frac{1}{2i\bar{\omega}\rho}e^{-i\bar{\omega}\tau}\left(e^{i\bar{\omega}\rho} - e^{-i\bar{\omega}\rho}\right)\right],$$

resulting in

$$i\bar{\omega} + \kappa\cos(\omega\tau) = \kappa\cos(\omega\tau)(\cos\bar{\omega}\tau - i\sin\bar{\omega}\tau)\delta(\bar{\omega},\rho), \tag{4.9}$$

where

$$\delta(\bar{\omega},\rho) = \frac{\sin\bar{\omega}\rho}{\bar{\omega}\rho}.$$

Separating equation (4.9) into real and imaginary parts gives

$$\begin{aligned}\kappa\cos(\omega\tau) =& \kappa\cos(\omega\tau)\big(\cos(\bar{\omega}\tau)\big)\delta(\bar{\omega},\rho),\\ \bar{\omega} =& \kappa\cos(\omega\tau)\big(-\sin(\bar{\omega}\tau)\big)\delta(\bar{\omega},\rho).\end{aligned} \tag{4.10}$$

Squaring and adding the two equations (4.10) results in

$$\begin{aligned}&\kappa^2\cos^2(\omega\tau) + \bar{\omega}^2 = \kappa^2\cos^2(\omega\tau)\delta^2(\bar{\omega},\rho)(\cos^2(\bar{\omega}\tau) + \sin^2(\bar{\omega}\tau)),\\ \Rightarrow\quad &\kappa^2\cos^2(\omega\tau)(1-\delta^2(\bar{\omega},\rho)) + \bar{\omega}^2 = 0.\end{aligned} \tag{4.11}$$

Since $|\delta(\bar{\omega},\rho)| \leq 1$, this equation has no solutions for $\bar{\omega} > 0$, i.e., there is no possibility for phase locked solutions to lose/gain their stability via a Hopf bifurcation. Hence, any stability change can only occur through a steady-state bifurcation.

Similarly, dividing the two equations (4.10) gives

$$\begin{aligned} \frac{\bar{\omega}}{\kappa\cos(\omega\tau)} &= \frac{\kappa\cos(\omega\tau)(-\sin(\bar{\omega}\tau))\delta(\bar{\omega},\rho)}{\kappa\cos(\omega\tau)(\cos(\bar{\omega}\tau))\delta(\bar{\omega},\rho)}, \\ \Rightarrow \quad \tan(\bar{\omega},\rho) &= -\frac{\bar{\omega}}{\kappa\cos(\omega\tau)}. \end{aligned} \tag{4.12}$$

Now, rewriting the linearised system with the uniformly distributed kernel with $\boldsymbol{\phi} = (\phi_1, \phi_2)$ results in

$$\dot{\boldsymbol{\phi}}(t) = L_0\boldsymbol{\phi}(t) + \frac{1}{2\rho}\int_{-(\tau+\rho)}^{-(\tau-\rho)} M\boldsymbol{\phi}(t+s)ds, \tag{4.13}$$

where

$$L_0 = \begin{pmatrix} -\kappa\cos(\omega\tau) & 0 \\ 0 & -\kappa\cos(\omega\tau) \end{pmatrix}, \quad M = \begin{pmatrix} 0 & \kappa\cos(\omega\tau) \\ \kappa\cos(\omega\tau) & 0 \end{pmatrix},$$

for the in-phase locked frequency.

4.3.2 Antiphase solution

Equations (1.14) and (1.16) transform the antiphase characteristic equation (4.7) to

$$\left[\lambda - \kappa\cos(\omega\tau) + \kappa\cos(\omega\tau)\left(e^{-\lambda\tau}\frac{\sinh(\lambda\rho)}{\lambda\rho}\right)\right]\left[\lambda - \kappa\cos(\omega\tau) - \kappa\cos(\omega\tau)\left(e^{-\lambda\tau}\frac{\sinh(\lambda\rho)}{\lambda\rho}\right)\right] = 0. \tag{4.14}$$

Similarly to the in-phase case, we look for characteristic roots in the form $\lambda = i\bar{\omega}$. Substituting this into (4.14) and separating real and imaginary parts we obtain

$$\kappa^2\cos^2(\omega\tau)(1-\delta^2(\bar{\omega},\rho)) + \bar{\omega}^2 = 0, \tag{4.15}$$

$$\tan(\bar{\omega},\rho) = \frac{\bar{\omega}}{\kappa\cos(\omega\tau)}. \tag{4.16}$$

Rewriting the linearised system with the uniformly distributed kernel with $\boldsymbol{\phi} = (\phi_1, \phi_2)$ results in

$$\dot{\boldsymbol{\phi}}(t) = L_0\boldsymbol{\phi}(t) + \frac{1}{2\rho}\int_{-(\tau+\rho)}^{-(\tau-\rho)} M\boldsymbol{\phi}(t+s)ds, \tag{4.17}$$

where for the antiphase locked frequency we have

$$L_0 = \begin{pmatrix} \kappa\cos(\omega\tau) & 0 \\ 0 & \kappa\cos(\omega\tau) \end{pmatrix}, \quad M = \begin{pmatrix} 0 & -\kappa\cos(\omega\tau) \\ -\kappa\cos(\omega\tau) & 0 \end{pmatrix}.$$

System (4.17) is now in the form suitable for computing the maximum real part of the eigenvalues using the algorithm described in Breda *et al.* [45] and implemented in traceDDE suite in Matlab.

4.3.3 Locking frequencies

This section looks at in-phase and antiphase locking frequencies, i.e., number of total, stable, and unstable solutions. The colour code corresponds to the possible number of solutions, ω, in the specified τ and κ range. As can be seen from Figs. 4.2 and 4.3, the number of locking frequencies increases with increasing delay τ, and coupling strength κ.

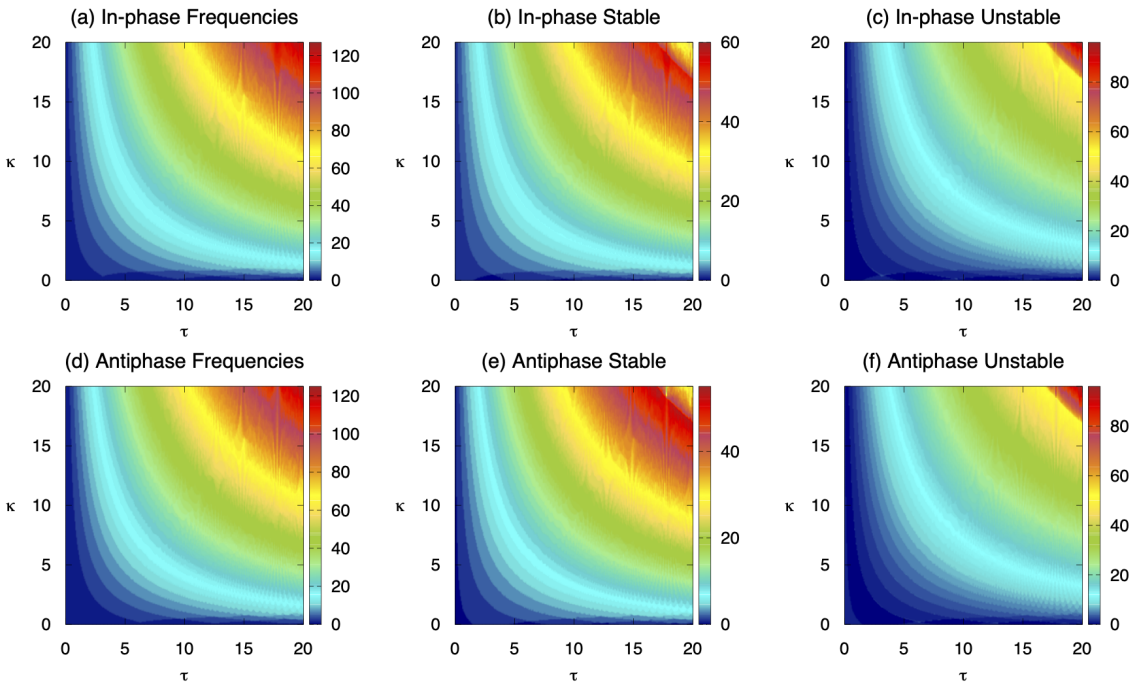

Figure 4.2: In-phase and antiphase locking frequencies (colour bar corresponds to the number of possible frequencies at every point), $\rho = 0.0001$: (a) and (d) total locked frequencies, (b) and (e) stable locking frequencies, (c) and (f) unstable locking frequencies.

We perform numerical simulations to identify the regions of stable in-phase and antiphase solutions for various parameter values. For distribution width ρ, we specify an array of τ, κ, and ω values, for the ranges displayed in the plots (i.e., for Figs. 4.2, 4.3 it is 0 to 20 for both κ and τ, we also note that τ cannot be less than ρ, hence the blank shift in Figs. 4.2 - 4.8 as the width of the distribution, ρ, increases). The transcendental ω equation is then evaluated for all τ, κ, ω. The bigger the range of τ, κ, and ω, the more ω frequencies there are. For each of the ω roots, we use the traceDDE Matlab tool to obtain λ values. We consider the maximum real part of the eigenvalues; stability is declared if the maximum real part is negative, and instability otherwise.

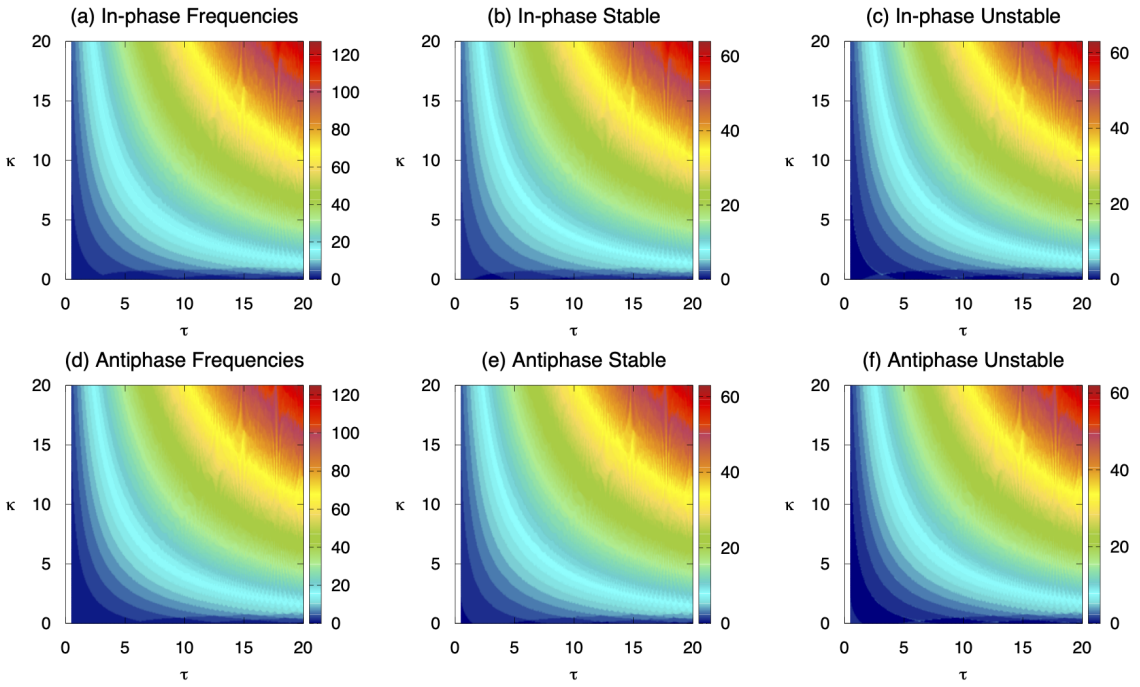

Figure 4.3: In-phase and antiphase locking-frequencies (colour bar corresponds to the number of possible frequencies at every point), $\rho = 0.5$: (a) and (d) total locked frequencies, (b) and (e) stable locking frequencies, (c) and (f) unstable locking frequencies.

For Figs. 4.2, 4.3, 4.5, and 4.6 the total number of stable and unstable solutions we find is recorded for both in-phase and antiphase, and used to plot the results. For the stability regions in Fig. 4.4, and branches in Figs. 4.7 - 4.10, if there exists at least one stable solution in the range of ω roots for a given τ and κ, we say the point is stable, otherwise it is unstable. The two sets of results (in-phase and antiphase) are used to plot stability regions (green for in-phase stable solutions only, grey for antiphase stable solutions only, yellow for both in-phase and antiphase stable solutions), and branches (blue solid line represents stable in-phase, green solid for stable antiphase, magenta dashed is unstable in-phase, and red dashed represents unstable antiphase).

4.3.4 Stability regions and corresponding locking frequencies

Fig. 4.4 highlights a rich framework of coexisting in-phase and antiphase stable solutions with different frequencies. Multistability is more prominent at higher values of τ and κ. For small values of the coupling strength κ, the system alternates between stable in-phase and anti-phase states and increasing the coupling strength allows for both solutions to co-exist. Increasing the mean time delay leads to the shrinking of the stability islands, while increase in the distribution width ρ does not play a role on the overall stability

structure, as those remain identical, unlike the cases considered in [93, 150, 117], though it bounds from below the smallest mean time delay, for which the phase-locked solutions can be observed.

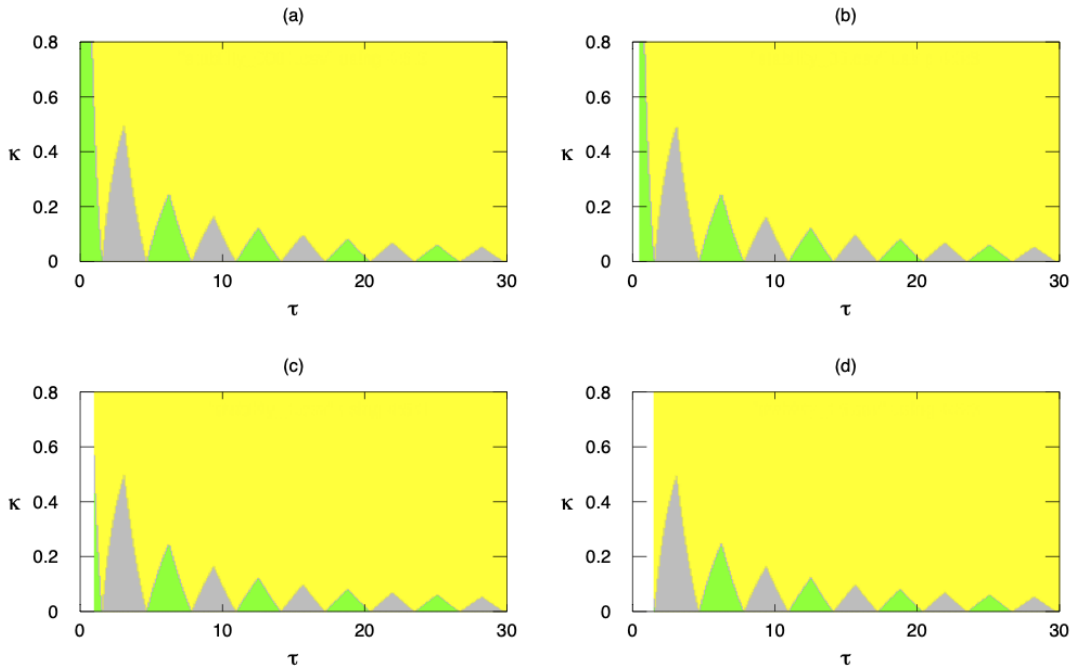

Figure 4.4: Stability regions of in-phase and antiphase solutions. Green: only in-phase solutions are stable, grey: only antiphase solutions are stable, yellow: in-phase and antiphase solutions coexist. (a) $\rho = 0.0001$, (b) $\rho = 0.5$, (c) $\rho = 1$, (d) $\rho = 1.5$.

In Figs. 4.5 and 4.6, we indicate by a colour code the total number of stable solutions for the same range as demonstrated in Fig. 4.4, with varying width of the distribution ρ. The stability map shows high level of symmetry.

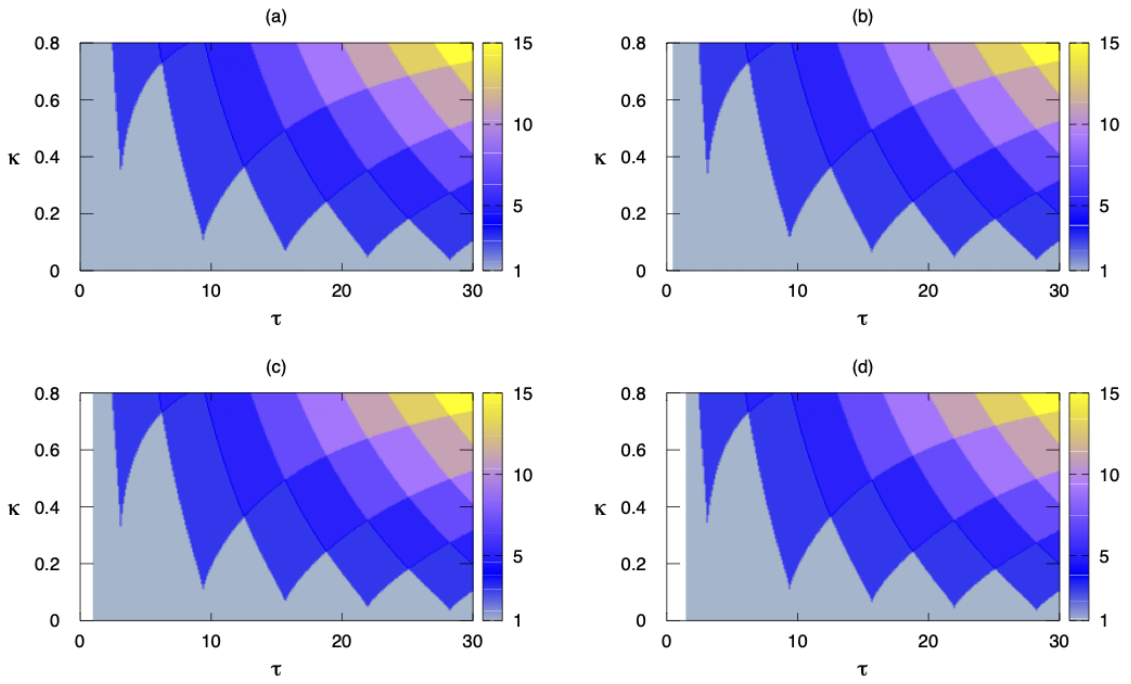

Figure 4.5: Total lock frequencies of stable in-phase solutions (colour bar corresponds to the number of possible frequencies at every point). (a) $\rho = 0.0001$, (b) $\rho = 0.5$, (c) $\rho = 1$, (d) $\rho = 1.5$.

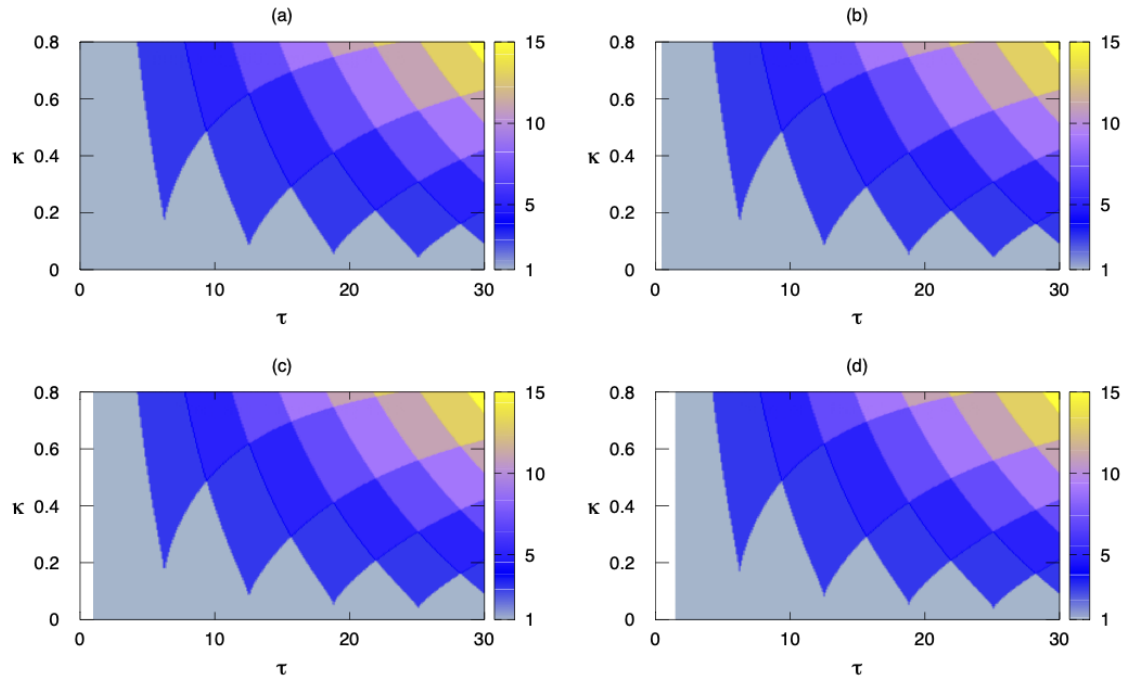

Figure 4.6: Total lock frequencies of stable antiphase solutions (colour bar corresponds to the number of possible frequencies at every point). (a) $\rho = 0.0001$, (b) $\rho = 0.5$, (c) $\rho = 1$, (d) $\rho = 1.5$.

4.3.5 Graphical determination of the locking frequencies

This section presents branches of stability and instability regions with varying mean time delay, τ, coupling strength, κ, and uniform distribution width, ρ. Stable and unstable solutions are represented by full and dashed lines, respectively. Blue solid line corresponds to stable in-phase solutions, green solid line to stable antiphase solutions, dashed magenta and red to unstable in-phase and antiphase solutions, respectively.

Fixed τ

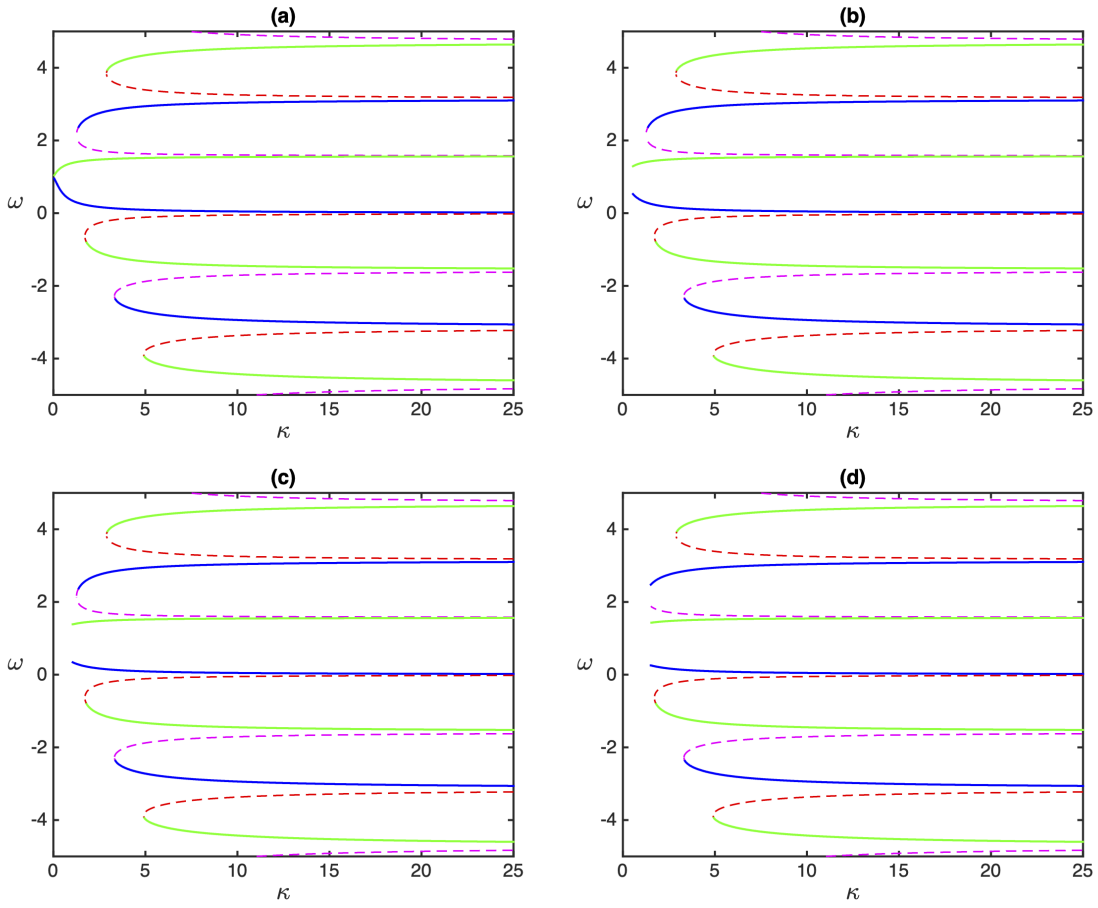

Figure 4.7: Blue solid: stable in-phase, green solid: stable antiphase, magenta dashed: unstable in-phase, red dashed: unstable antiphase. (a) $\tau = 2$, $\rho = 0.0001$, (b) $\tau = 2$, $\rho = 0.5$, (c) $\tau = 2$, $\rho = 1$, (d) $\tau = 2$, $\rho = 1.5$.

In Figs. 4.7 and 4.8, branches of stable and unstable in-phase and antiphase solutions as functions of locking frequencies ω and the coupling strength κ for fixed values of the mean time delay τ and the width of the distribution ρ are illustrated. In-phase and antiphase states alternate, and for positive frequencies upper branches are stable. Increasing the

mean time delay leads to a faster switching between different branches (i.e. a higher number of branches within the same range of possible phase-locked frequencies), whereas higher values of the coupling strength κ and the mean time delay τ enhance multistability. Similarly to the case of stability regions illustrated in Fig. 4.4, one can note that for the same value of the mean time delay, increasing the width of the delay distribution results in the increase of the minimum value of the coupling strength, for which phase-locked solutions can exist.

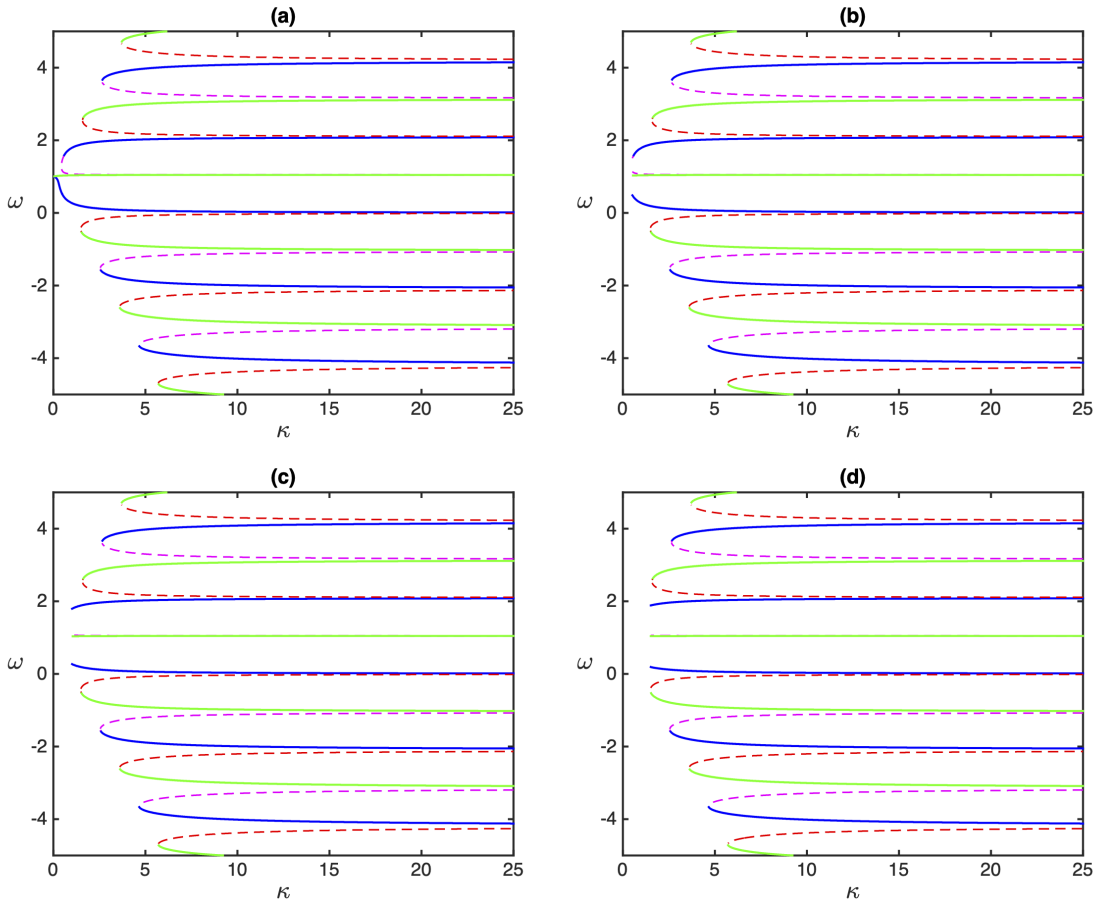

Figure 4.8: Blue solid: stable in-phase, green solid: stable antiphase, magenta dashed: unstable in-phase, red dashed: unstable antiphase. (a) $\tau = 3$, $\rho = 0.0001$, (b) $\tau = 3$, $\rho = 0.5$, (c) $\tau = 3$, $\rho = 1$, (d) $\tau = 3$, $\rho = 1.5$.

Fixed κ

An effect introduced by the delay is the multistability of steady states, as can be seen in Figs. 4.9 and 4.10, there are multiple solutions for the collective frequency ω for sufficiently large values of the mean delay τ and repulsive coupling κ. In Fig. 4.9, it is easy to see that there are lower ranges of τ where only a single frequency is stable, as well as higher ranges of τ where more than one frequency is stable. It is also clear from Fig. 4.10 that the overlapping multistable region increases with increasing value of coupling strength κ.

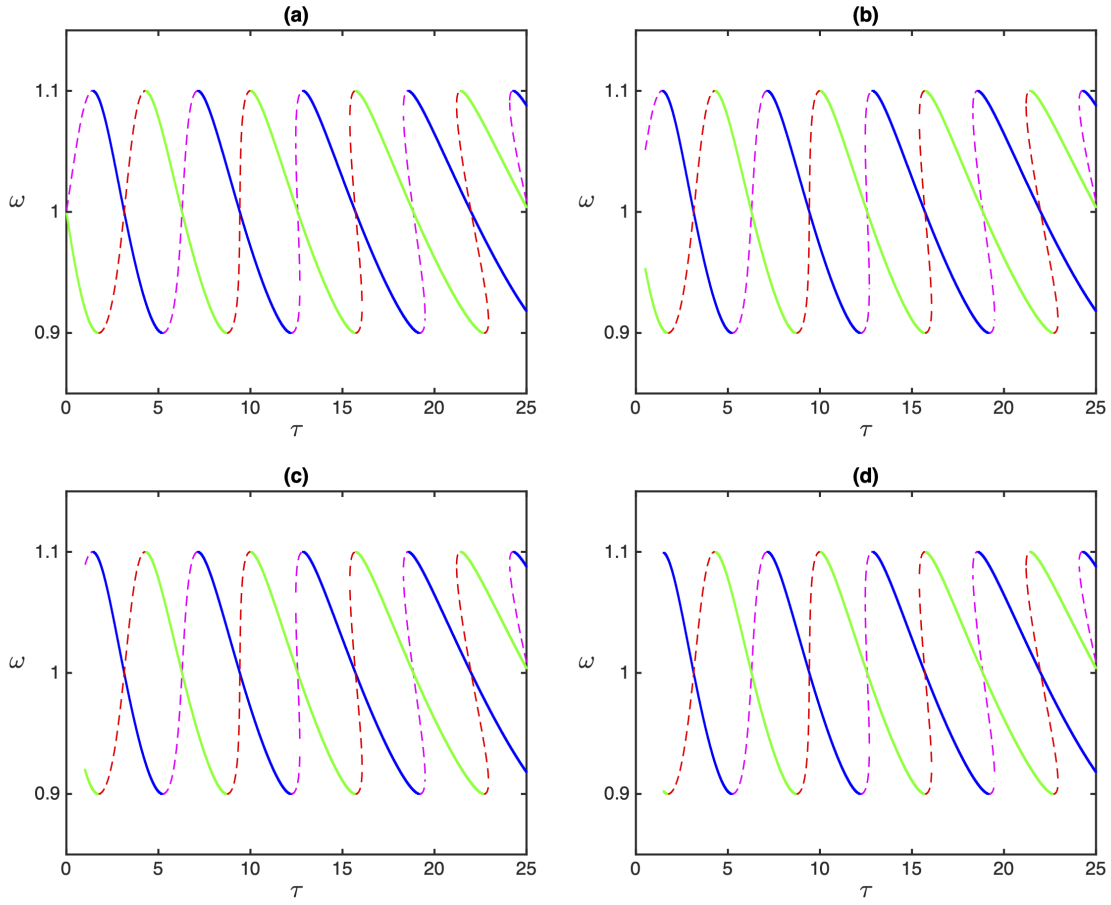

Figure 4.9: Blue solid: stable in-phase, green solid: stable antiphase, magenta dashed: unstable in-phase, red dashed: unstable antiphase. (a) $\kappa = -0.1$, $\rho = 0.0001$, (b) $\kappa = -0.1$, $\rho = 0.5$, (c) $\kappa = -0.1$, $\rho = 1$, (d) $\kappa = -0.1$, $\rho = 1.5$.

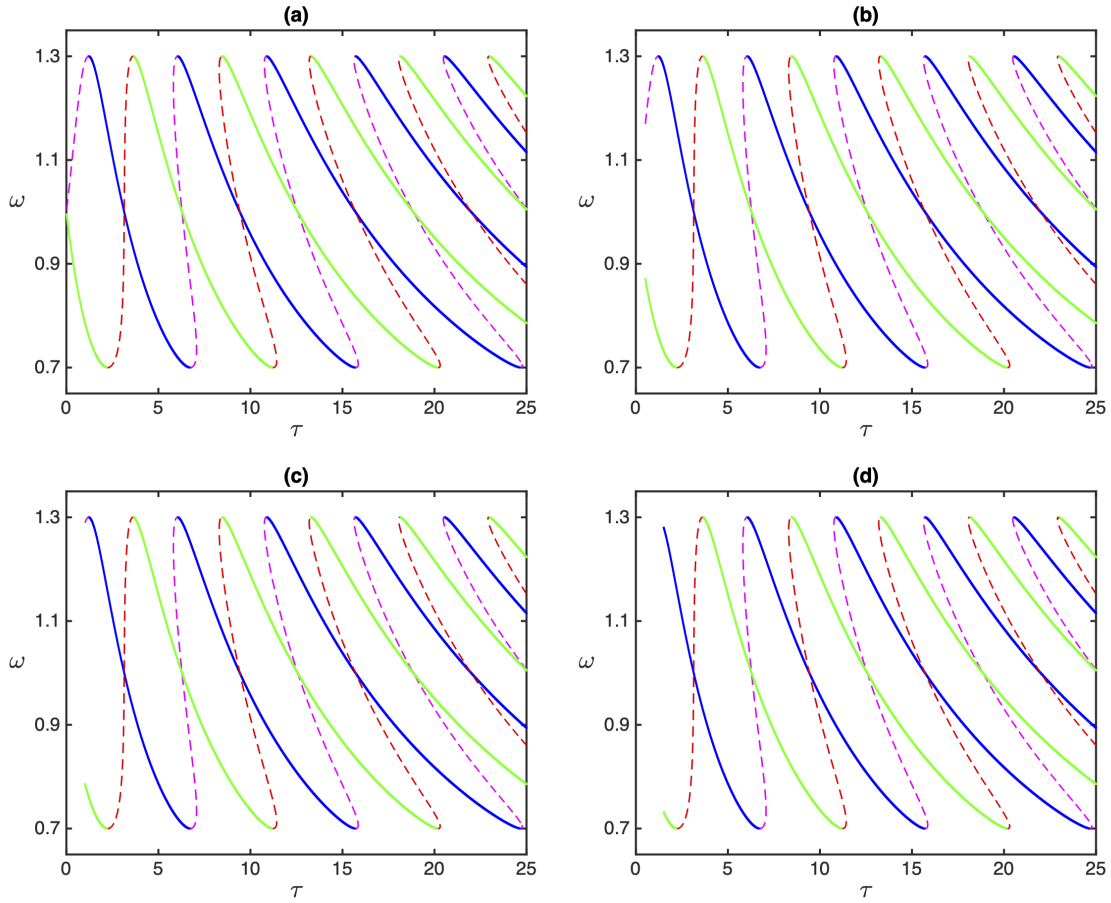

Figure 4.10: Blue solid: stable in-phase, green solid: stable antiphase, magenta dashed: unstable in-phase, red dashed: unstable antiphase. (a) $\kappa = -0.3$, $\rho = 0.0001$, (b) $\kappa = -0.3$, $\rho = 0.5$, (c) $\kappa = -0.3$, $\rho = 1$, (d) $\kappa = -0.3$, $\rho = 1.5$.

4.3.6 Numerical simulations for the uniform distribution kernel

In this section, numerical results are obtained using dde23 suite in MATLAB. We directly approximate the solution of the distributed delay system (4.4) through the trapezoidal rule [49], with the trapezoidal quadrature formula for the integrals as

$$\int_a^b f(x)dx \approx \frac{b-a}{2}\big(f(a) - f(b)\big). \tag{4.18}$$

It follows from above that the in-phase equations are

$$\begin{aligned}
\dot{\phi_1}(t) =& \kappa \cos(\omega\tau)\left[\frac{1}{2}\big(\phi_2(t-\tau_1) + \phi_2(t-\tau_2)\big) - \phi_1(t)\right], \\
\dot{\phi_2}(t) =& \kappa \cos(\omega\tau)\left[\frac{1}{2}\big(\phi_1(t-\tau_1) + \phi_1(t-\tau_2)\big) - \phi_2(t)\right],
\end{aligned} \tag{4.19}$$

where $\tau_1 = \tau - \rho$ and $\tau_2 = \tau + \rho$.

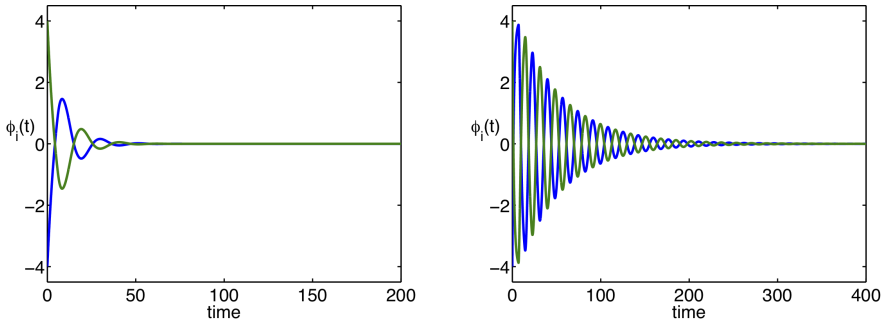

(a) $\kappa = 0.2, \tau = 7, \omega = 0.9406$ (b) $\kappa = 0.6, \tau = 7, \omega = 0.9173$

Figure 4.11: Solutions of System (4.19) for stable in-phase locking frequencies.

We have for the antiphase

$$\begin{aligned}\dot{\phi_1}(t) =& \kappa \cos(\omega\tau)\Big[-\frac{1}{2}\big(\phi_2(t-\tau_1) + \phi_2(t-\tau_2)\big) + \phi_1(t)\Big],\\ \dot{\phi_2}(t) =& \kappa \cos(\omega\tau)\Big[-\frac{1}{2}\big(\phi_1(t-\tau_1) + \phi_1(t-\tau_2)\big) + \phi_2(t)\Big],\end{aligned} \tag{4.20}$$

where $\tau_1 = \tau - \rho$ and $\tau_2 = \tau + \rho$.

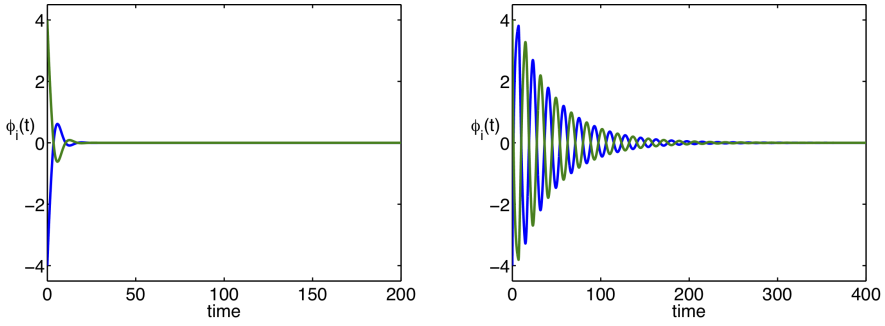

(a) $\kappa = 0.2, \tau = 3, \omega = 1.0177$ (b) $\kappa = 0.6, \tau = 7, \omega = 1.2777$

Figure 4.12: Solutions of System (4.20) for stable antiphase locking frequencies.

Simulations in Figs. 4.11, 4.12 illustrate the stability of in-phase and antiphase locking frequencies of Systems (4.4) and (4.6) in different parameter regimes. Selected parameters are consistent with stability regions in Fig. 4.4.

4.4 Gamma distributed delay

In this section, we consider a gamma distribution kernel. Equations (1.18) and (1.20) transform the in-phase and antiphase characteristic equations (4.5) and (4.7) to

$$\left[\lambda + \kappa \cos\left(\frac{\omega p}{\gamma}\right)\right]^2 - \kappa^2 \cos^2\left(\frac{\omega p}{\gamma}\right)\left[\frac{\gamma^p}{(\lambda+\gamma)^p}\right]^2 = 0, \tag{4.21}$$

$$\left[\lambda - \kappa \cos\left(\frac{\omega p}{\gamma}\right)\right]^2 - \kappa^2 \cos^2\left(\frac{\omega p}{\gamma}\right)\left[\frac{\gamma^p}{(\lambda+\gamma)^p}\right]^2 = 0, \tag{4.22}$$

respectively.

For the general value of p, the characteristic equation is a polynomial of order $p+2$ and has at most $p+2$ roots, in contrast to the characteristic equation of the discrete delay model, which is transcendental and has infinitely many roots.

Stability criterion

Rewriting the equation (4.21), for a general γ and p, and $a = \pm\kappa\cos(\omega\tau_m)$ for in-phase and antiphase, respectively, we have

$$\begin{aligned}(\lambda+a)(\lambda+\gamma)^p &= \pm a\gamma^p \\ |\lambda+a||\lambda+\gamma|^p &= |a\gamma^p|.\end{aligned} \tag{4.23}$$

Rewriting the root λ in a real and imaginary part, $\lambda = x + iy$, we find

$$\sqrt{(x+a)^2+y^2}\left((x+\gamma)^2+y^2\right)^{\frac{p}{2}} = |a|\gamma^p. \tag{4.24}$$

We know that $\gamma > 0$ for a physical delay distribution. Assuming $a > 0$ and $x > 0$, we deduce

$$\sqrt{(x+a)^2+y^2}\left((x+\gamma)^2+y^2\right)^{\frac{p}{2}} \geq (x+a)(x+\gamma)^p > a\gamma^p. \tag{4.25}$$

We have that, if $a > 0$, solutions with $x > 0$ do not exist. Hence we have a stability criterion for any γ and p, for in-phase solutions,

$$a = \kappa\cos(\omega\tau_m) > 0, \tag{4.26}$$

and for antiphase solutions,

$$a = -\kappa\cos(\omega\tau_m) < 0. \tag{4.27}$$

4.4.1 Weak delay kernel, in-phase

The delay kernel with gamma distribution of order $p = 1$ is known as the 'weak' kernel and has exponential form, hence $g(s) = \gamma e^{-\gamma s}$. We use the linear chain trick described in [98] to convert the system with gamma distributed delay into a system of ODEs.

Introducing new variables

$$\begin{aligned}\phi_3(t) &= \int_0^\infty \gamma e^{-\gamma s}\phi_2(t-s)ds, \\ \phi_4(t) &= \int_0^\infty \gamma e^{-\gamma s}\phi_1(t-s)ds,\end{aligned} \tag{4.28}$$

now, let $a = \kappa \cos\left(\frac{\omega}{\gamma}\right)$, we have that System (4.4) can be rewritten as follows

$$\begin{aligned}
\dot{\phi_1}(t) &= a\big(\phi_3(t) - \phi_1(t)\big) \\
\dot{\phi_2}(t) &= a\big(\phi_4(t) - \phi_2(t)\big) \\
\dot{\phi_3}(t) &= \int_0^\infty \gamma e^{-\gamma s}\dot{\phi}_2(t-s)ds \\
&= \int_0^\infty a\gamma e^{-\gamma s}\big(\phi_4(t-s) - \phi_2(t-s)\big)ds \\
&= \int_0^\infty a\gamma e^{-\gamma s}\phi_4(t-s)ds - \int_0^\infty a\gamma^2 e^{-\gamma s}\phi_2(t-s)ds \\
&\quad + \int_0^\infty a(\gamma^2-\gamma)e^{-\gamma s}\phi_2(t-s)ds \\
&= \gamma\int_0^\infty \big(a\gamma e^{-\gamma s}\phi_2(t-s) - ae^{-\gamma s}\phi_4(t-s) - ae^{-\gamma s}\phi_2(t-s)\big)ds - a\gamma\phi_3(t) \\
&= \gamma\int_0^\infty \big((a-1)\gamma e^{-\gamma s}\phi_2(t-s) - \gamma e^{-\gamma s}\phi_2(t-s) + e^{-\gamma s}\dot{\phi}_2(t-s)\big)ds - a\gamma\phi_3(t) \\
&= -a\gamma\phi_3(t) + \gamma(a-1)\phi_3(t) + \gamma\phi_2(t).
\end{aligned}$$

Hence, a new system of equations is

$$\begin{aligned}
\dot{\phi_1}(t) &= \kappa\cos\left(\frac{\omega}{\gamma}\right)\phi_3(t) - \kappa\cos\left(\frac{\omega}{\gamma}\right)\phi_1(t), \\
\dot{\phi_2}(t) &= \kappa\cos\left(\frac{\omega}{\gamma}\right)\phi_4(t) - \kappa\cos\left(\frac{\omega}{\gamma}\right)\phi_2(t), \\
\dot{\phi_3}(t) &= -\gamma\phi_3(t) + \gamma\phi_2(t), \\
\dot{\phi_4}(t) &= -\gamma\phi_4(t) + \gamma\phi_1(t).
\end{aligned} \tag{4.29}$$

From (4.21) we have that the in-phase characteristic equation is of the form

$$\left[\lambda + \kappa\cos\left(\frac{\omega}{\gamma}\right)\right]^2 - \kappa^2\cos^2\left(\frac{\omega}{\gamma}\right)\left[\frac{\gamma}{\lambda+\gamma}\right]^2 = 0, \tag{4.30}$$

which can be reduced to $\lambda_1 = 0,\ \lambda_2 = -\gamma - \kappa\cos\left(\frac{\omega}{\gamma}\right)$, and

$$\lambda^2 + \lambda\left[\gamma + \kappa\cos\left(\frac{\omega}{\gamma}\right)\right] + 2\gamma\kappa\cos\left(\frac{\omega}{\gamma}\right) = 0, \tag{4.31}$$

where the stability condition is $\cos\left(\frac{\omega}{\gamma}\right) > 0$.

4.4.2 Weak delay kernel, antiphase

Following the same method as for the in-phase solutions, we introduce new variables

$$\begin{aligned}\phi_3(t) &= \int_0^\infty \gamma e^{-\gamma s}\phi_2(t-s)ds,\\ \phi_4(t) &= \int_0^\infty \gamma e^{-\gamma s}\phi_1(t-s)ds,\end{aligned} \tag{4.32}$$

and rewrite System (4.6) as

$$\begin{aligned}\dot{\phi_1}(t) &= -\kappa\cos\left(\frac{\omega}{\gamma}\right)\phi_3(t) + \kappa\cos\left(\frac{\omega}{\gamma}\right)\phi_1(t),\\ \dot{\phi_2}(t) &= -\kappa\cos\left(\frac{\omega}{\gamma}\right)\phi_4(t) + \kappa\cos\left(\frac{\omega}{\gamma}\right)\phi_2(t),\\ \dot{\phi_3}(t) &= -\gamma\phi_3(t) + \gamma\phi_2(t),\\ \dot{\phi_4}(t) &= -\gamma\phi_4(t) + \gamma\phi_1(t).\end{aligned} \tag{4.33}$$

The antiphase characteristic equation (4.22) for the weak gamma kernel is

$$\left[\lambda - \kappa\cos\left(\frac{\omega}{\gamma}\right)\right]^2 - \kappa^2\cos^2\left(\frac{\omega}{\gamma}\right)\left[\frac{\gamma}{\lambda+\gamma}\right]^2 = 0, \tag{4.34}$$

similarly to the in-phase, we have that $\lambda_1 = 0,\ \lambda_2 = -\gamma + \kappa\cos\left(\frac{\omega}{\gamma}\right)$, and

$$\lambda^2 + \lambda\left[\gamma - \kappa\cos\left(\frac{\omega}{\gamma}\right)\right] - 2\gamma\kappa\cos\left(\frac{\omega}{\gamma}\right) = 0, \tag{4.35}$$

where the stability condition is $\cos\left(\frac{\omega}{\gamma}\right) < 0$.

4.4.3 Locking frequencies and stability regions, weak delay kernel

This section looks at in-phase and antiphase locking frequencies, i.e., number of total, stable, and unstable solutions, as well as the stability dynamics. The colour code corresponds to the possible number of solutions, ω, in the specified γ and κ range. As can be seen from Fig. 4.13 the number of in-phase and antiphase locking frequencies mainly increases with the increase of coupling strength κ.

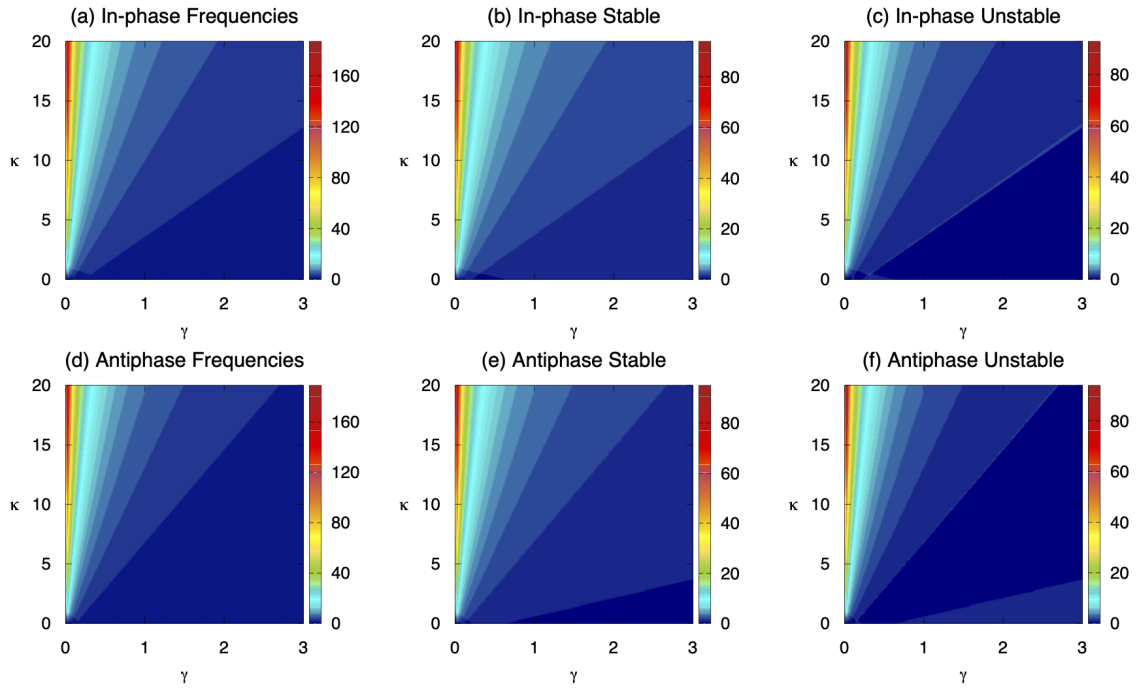

Figure 4.13: Locking-frequencies of in-phase and antiphase solutions (colour bar corresponds to the number of possible frequencies at every point): (a) and (d) total locked frequencies, (b) and (e) stable locking frequencies, (c) and (f) unstable locking frequencies.

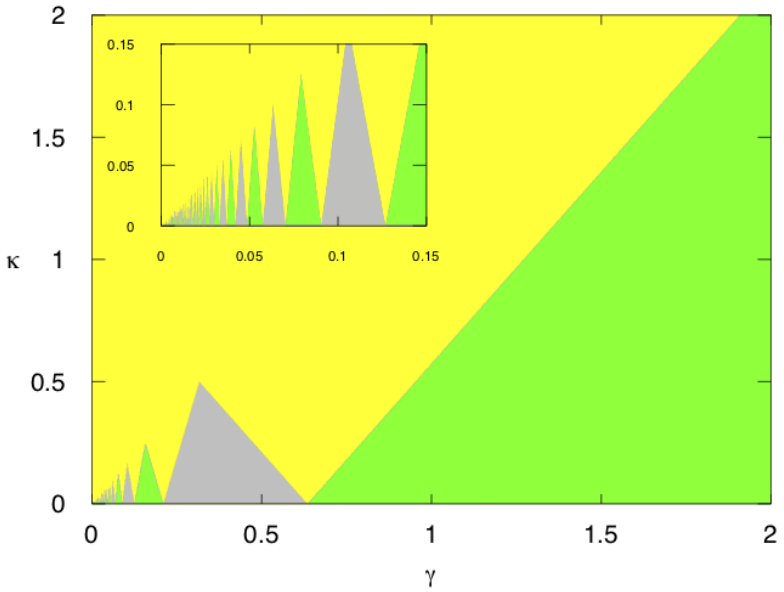

Figure 4.14: Stability regions of in-phase and antiphase solutions. Green: only in-phase solutions are stable, grey: only antiphase solutions are stable, yellow: in-phase and antiphase solutions coexist.

Figs. 4.14 and 4.15 show a dynamical phase diagram as a function of the parameters γ and

κ. Here again a rich structure of coexisting in-phase and antiphase solutions with different frequencies is present, and multistability is more pronounced at higher values of κ.

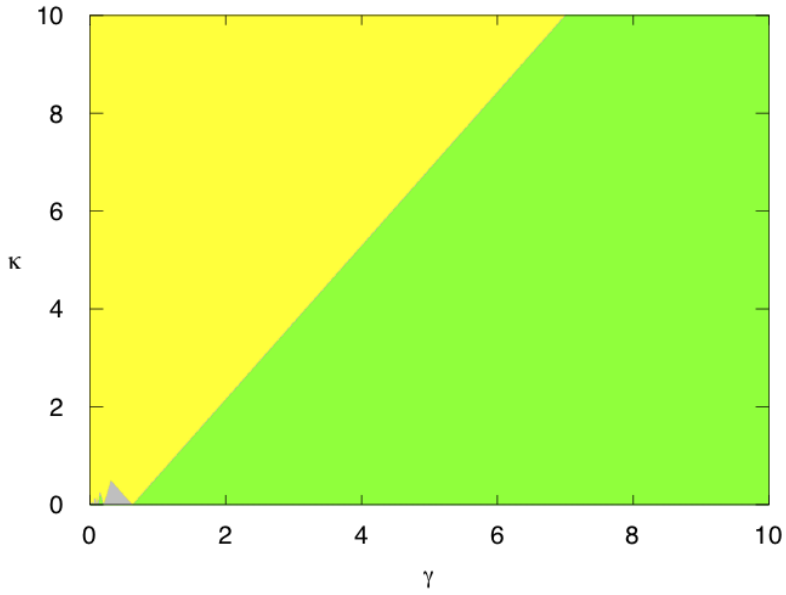

Figure 4.15: Stability regions of in-phase and antiphase solutions. Green: only in-phase solutions are stable, grey: only antiphase solutions are stable, yellow: in-phase and antiphase solutions coexist.

Smaller values of γ (large value of τ_m) with sufficiently small coupling strength κ induce multiple switches between stable in-phase and antiphase solutions, and the size of parameter regions. Increasing the coupling strength leads to simultaneous stabilisation of multiple branches, and the resulting multistability, as can be seen in Figs. 4.14 and 4.15.

4.4.4 Branches of solutions, weak delay kernel

This section presents branches of stability and instability regions with varying γ and coupling strength, κ. Stable and unstable solutions are represented by full and dashed lines, respectively. Blue solid line corresponds to stable in-phase solutions, green solid line to stable antiphase solutions, dashed magenta and red to unstable in-phase and antiphase solutions, respectively. In Fig. 4.16 increasing γ, which corresponds to reducing the mean time delay, in-phase and antiphase states alternate, and for positive frequencies upper branches are stable. The number of possible multistable solutions decreases, and phase-locked solutions only appear starting with larger values of the coupling strength.

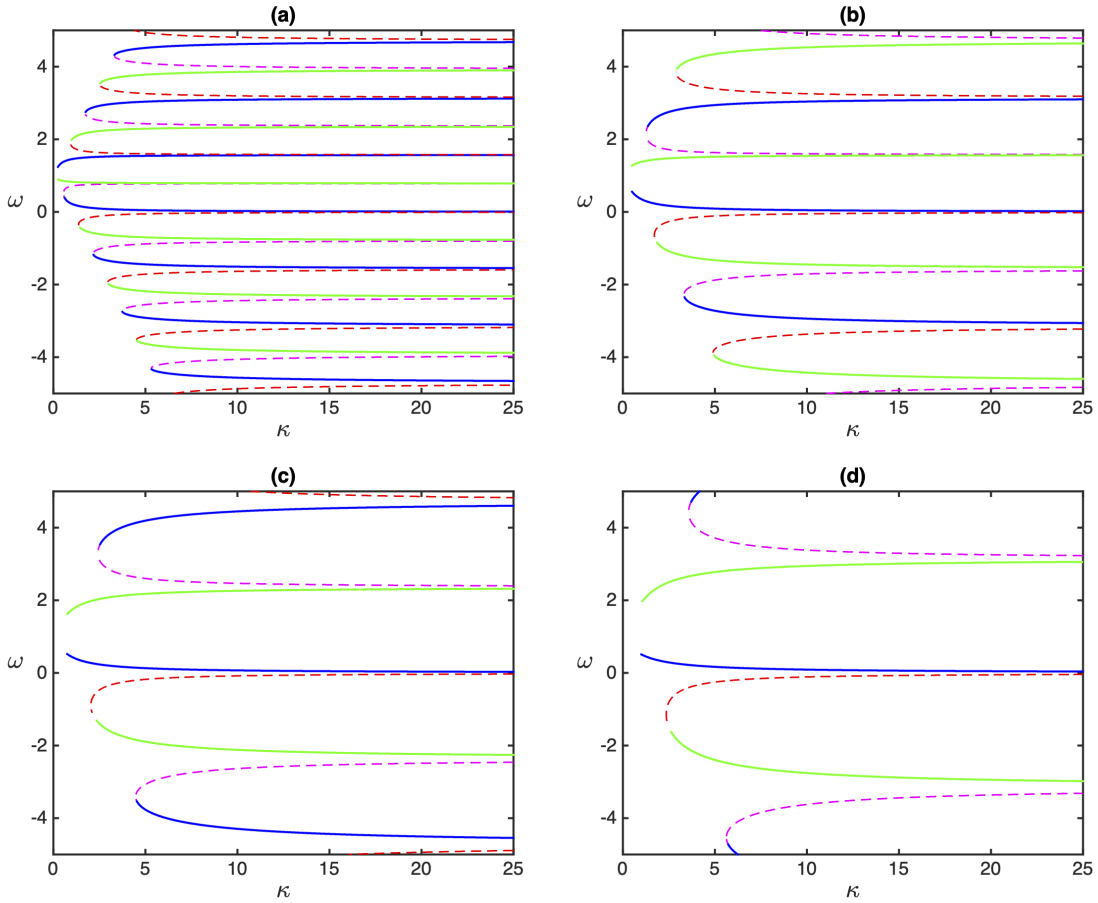

Figure 4.16: Blue solid: stable in-phase, green solid: stable antiphase, magenta dashed: unstable in-phase, red dashed: unstable antiphase. (a) $\gamma = 0.25$, (b) $\gamma = 0.5$, (c) $\gamma = 0.75$, (d) $\gamma = 1$.

4.4.5 Strong delay kernel, in-phase

We now consider gamma distribution of order $p = 2$, referred to as the strong delay kernel, where we have $g(s) = \gamma^2 s e^{-\gamma s}$, similarly to the weak delay kernel, we introduce the following new variables

$$\begin{aligned}
\phi_3(t) &= \int_0^\infty \gamma e^{-\gamma s}\phi_2(t-s)ds, \\
\phi_4(t) &= \int_0^\infty \gamma^2 s e^{-\gamma s}\phi_2(t-s)ds, \\
\phi_5(t) &= \int_0^\infty \gamma e^{-\gamma s}\phi_1(t-s)ds, \\
\phi_6(t) &= \int_0^\infty \gamma^2 s e^{-\gamma s}\phi_1(t-s)ds,
\end{aligned} \tag{4.36}$$

now, let $a = \kappa \cos\left(\frac{2\omega}{\gamma}\right)$, substituting (4.36) into (4.4), we have that System (4.4) can be

rewritten as follows

$$\dot{\phi}_1(t) = a\big(\phi_4(t) - \phi_1(t)\big),$$
$$\dot{\phi}_2(t) = a\big(\phi_6(t) - \phi_2(t)\big),$$

we follow the same method as for the weak delay kernel to obtain the equations for $\dot{\phi}_3(\theta)$ and $\dot{\phi}_5(\theta)$. We now consider

$$\begin{aligned}
\dot{\phi}_4(t) &= \int_0^\infty a\gamma^2 s e^{-\gamma s}\dot{\phi}_2(t-s)\big)ds \\
&= \int_0^\infty a\gamma^2 s e^{-\gamma s}\big(\phi_6(t-s) - \phi_2(t-s)\big)ds \\
&= \int_0^\infty a\gamma^2 s e^{-\gamma s}\phi_6(t-s)ds - \int_0^\infty a(\gamma^3 - (\gamma^3 - \gamma^2))s e^{-\gamma s}\phi_2(t-s)ds \\
&= \int_0^\infty a\gamma^2 s e^{-\gamma s}\phi_6(t-s)ds - \int_0^\infty a\gamma^3 s e^{-\gamma s}\phi_2(t-s)ds \\
&\quad + \int_0^\infty a\gamma^2(\gamma-1) s e^{-\gamma s}\phi_2(t-s)ds \\
&= \gamma^2 \int_0^\infty \big(a\gamma s e^{-\gamma s}\phi_2(t-s) + a s e^{-\gamma s}\phi_6(t-s) - a s e^{-\gamma s}\phi_2(t-s)\big)ds - a\gamma\phi_4(t) \\
&= \gamma^2 \int_0^\infty \big(a s e^{-\gamma s}(\phi_6(t-s) - \phi_2(t-s)) + ((a-1)+1)\gamma s e^{-\gamma s}\phi_2(t-s)\big)ds \\
&\quad - a\gamma\phi_4(t) \\
&= \gamma^2 \int_0^\infty \big((a-1)\gamma s e^{-\gamma s}\phi_2(t-s) + \gamma s e^{-\gamma s}\phi_2(t-s) + s e^{-\gamma s}\dot{\phi}_2(t-s)\big)ds \\
&\quad - a\gamma\phi_4(t) \\
&= \gamma^2 \int_0^\infty (a-1)\gamma s e^{-\gamma s}\phi_2(t-s)ds - \gamma\phi_3(t) - a\gamma\phi_3(t) \\
&= \gamma(a-1)\phi_4(t) + \gamma\phi_3(t) - a\gamma\phi_4(t).
\end{aligned}$$

Hence, a new system of equations is

$$\begin{aligned}
\dot{\phi}_1(t) &= \kappa\cos\left(\frac{2\omega}{\gamma}\right)\phi_4(t) - \kappa\cos\left(\frac{2\omega}{\gamma}\right)\phi_1(t), \\
\dot{\phi}_2(t) &= \kappa\cos\left(\frac{2\omega}{\gamma}\right)\phi_6(t) - \kappa\cos\left(\frac{2\omega}{\gamma}\right)\phi_2(t), \\
\dot{\phi}_3(t) &= -\gamma\phi_3(t) + \gamma\phi_2(t), \\
\dot{\phi}_4(t) &= -\gamma\phi_4(t) + \gamma\phi_3(t), \\
\dot{\phi}_5(t) &= -\gamma\phi_5(t) + \gamma\phi_1(t), \\
\dot{\phi}_6(t) &= -\gamma\phi_6(t) + \gamma\phi_5(t).
\end{aligned} \tag{4.37}$$

The in-phase characteristic equation (4.21) combined with (1.18) and (1.20), is transformed to

$$\begin{aligned}
&\left[\lambda(\lambda+\gamma)^2 + \kappa(\lambda+\gamma)^2\cos\left(\frac{2\omega}{\gamma}\right) + \kappa\gamma^2\cos\left(\frac{2\omega}{\gamma}\right)\right] \\
&\quad\times\left[\lambda(\lambda+\gamma)^2 + \kappa(\lambda+\gamma)^2\cos\left(\frac{2\omega}{\gamma}\right) - \kappa\gamma^2\cos\left(\frac{2\omega}{\gamma}\right)\right] = 0.
\end{aligned} \tag{4.38}$$

4.4.6 Strong delay kernel, antiphase

A new system of equations is

$$\begin{aligned}
\dot{\phi_1}(t) = & -\kappa\cos\left(\frac{2\omega}{\gamma}\right)\phi_4(t) + \kappa\cos\left(\frac{2\omega}{\gamma}\right)\phi_1(t),\\
\dot{\phi_2}(t) = & -\kappa\cos\left(\frac{2\omega}{\gamma}\right)\phi_6(t) + \kappa\cos\left(\frac{2\omega}{\gamma}\right)\phi_2(t),\\
\dot{\phi_3}(t) = & -\gamma\phi_3(t) + \gamma\phi_2(t),\\
\dot{\phi_4}(t) = & -\gamma\phi_4(t) + \gamma\phi_3(t),\\
\dot{\phi_5}(t) = & -\gamma\phi_5(t) + \gamma\phi_1(t),\\
\dot{\phi_6}(t) = & -\gamma\phi_6(t) + \gamma\phi_5(t).
\end{aligned} \tag{4.39}$$

Antiphase characteristic equation (4.22) is transformed to

$$\begin{aligned}
&\left[\lambda(\lambda+\gamma)^2 - \kappa(\lambda+\gamma)^2\cos\left(\frac{2\omega}{\gamma}\right) + \kappa\gamma^2\cos\left(\frac{2\omega}{\gamma}\right)\right]\\
&\quad\times\left[\lambda(\lambda+\gamma)^2 - \kappa(\lambda+\gamma)^2\cos\left(\frac{2\omega}{\gamma}\right) - \kappa\gamma^2\cos\left(\frac{2\omega}{\gamma}\right)\right] = 0.
\end{aligned} \tag{4.40}$$

The eigenvalues for the characteristic equations for the in-phase (4.37) and antiphase (4.39) systems are $\lambda_1 = 0$, $\lambda_2 = -\gamma \mp \kappa\cos\left(\frac{2\omega}{\gamma}\right)$, both of multiplicity two. We have for in-phase and antiphase, respectively,

$$\lambda^2 + \lambda\left[\gamma \pm \kappa\cos\left(\frac{2\omega}{\gamma}\right)\right] \pm 2\gamma\kappa\cos\left(\frac{2\omega}{\gamma}\right) = 0, \tag{4.41}$$

which gives similar conditions $\kappa\cos(\omega\tau_m) > 0$ and $\kappa\cos(\omega\tau_m) < 0$ for stability of the in-phase and the antiphase solutions, respectively, with the mean time delay $\tau_m = \frac{2}{\gamma}$.

4.4.7 Locking frequencies and stability regions, strong delay kernel

This section looks at in-phase and antiphase locking frequencies, i.e., number of total, stable, and unstable solutions, as well as the stability dynamics. The colour code corresponds to the possible number of solutions, ω, in the specified γ and κ range. As can be seen from Fig. 4.17, the number of in-phase and antiphase locking frequencies mainly increases with the increase of coupling strength κ.

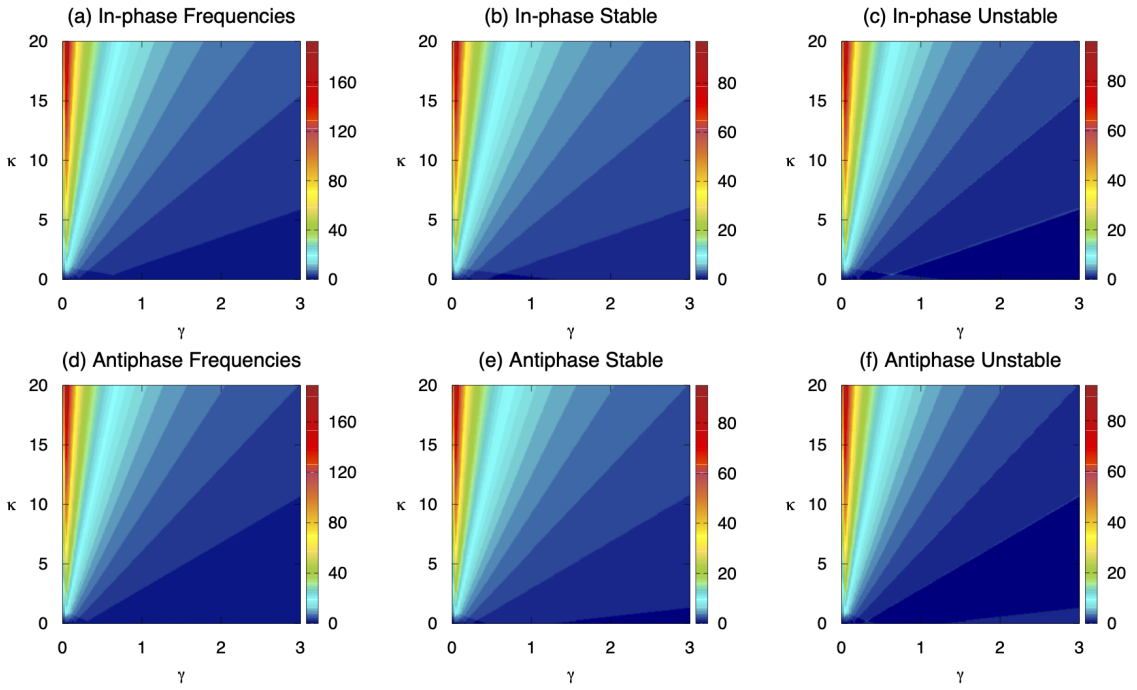

Figure 4.17: Locking-frequencies of in-phase and antiphase solutions (colour bar corresponds to the number of possible frequencies at every point): (a) and (d) total locked frequencies, (b) and (e) stable locking frequencies, (c) and (f) unstable locking frequencies.

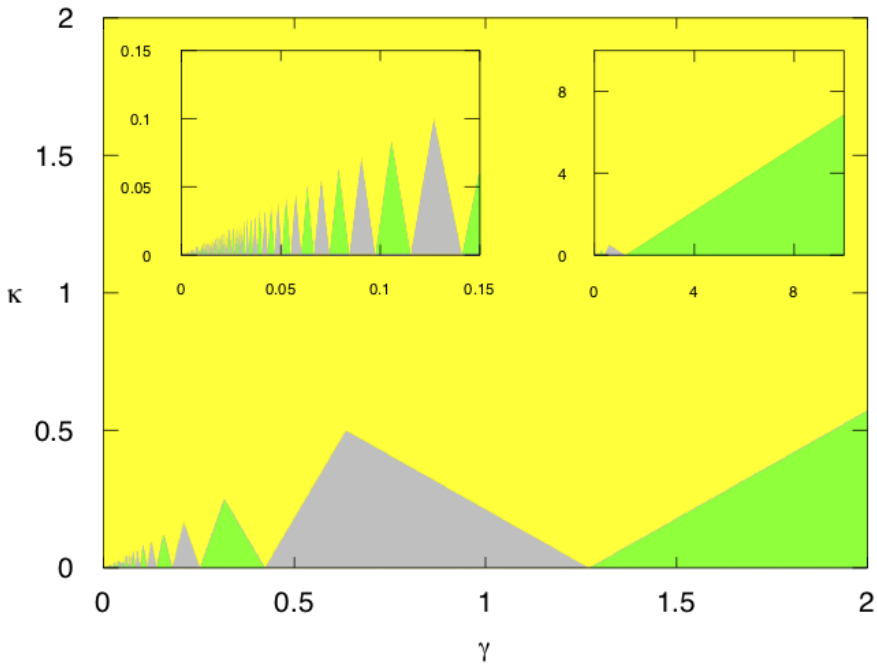

Figure 4.18: Stability regions of in-phase and antiphase solutions. Green: only in-phase solutions are stable, grey: only antiphase solutions are stable, yellow: in-phase and antiphase solutions coexist.

Fig. 4.18 shows a dynamical phase diagram as a function of the parameters γ and κ, we observe regions of stability of different solutions. Here, again, a rich structure of coexisting in-phase and antiphase solutions with different frequencies is present, and multistability is more pronounced at higher values of κ and γ. Similarly to the case of weak gamma distribution, there are alternating regions where only in-phase or antiphase solutions are stable for smaller values of κ, whereas for sufficiently high κ, we observe multistability. We note that for the same values of γ, multistability occurs for smaller values of the coupling strength, and for the same values of κ, stability regions are wider in terms of γ values.

4.4.8 Branches, strong delay kernel

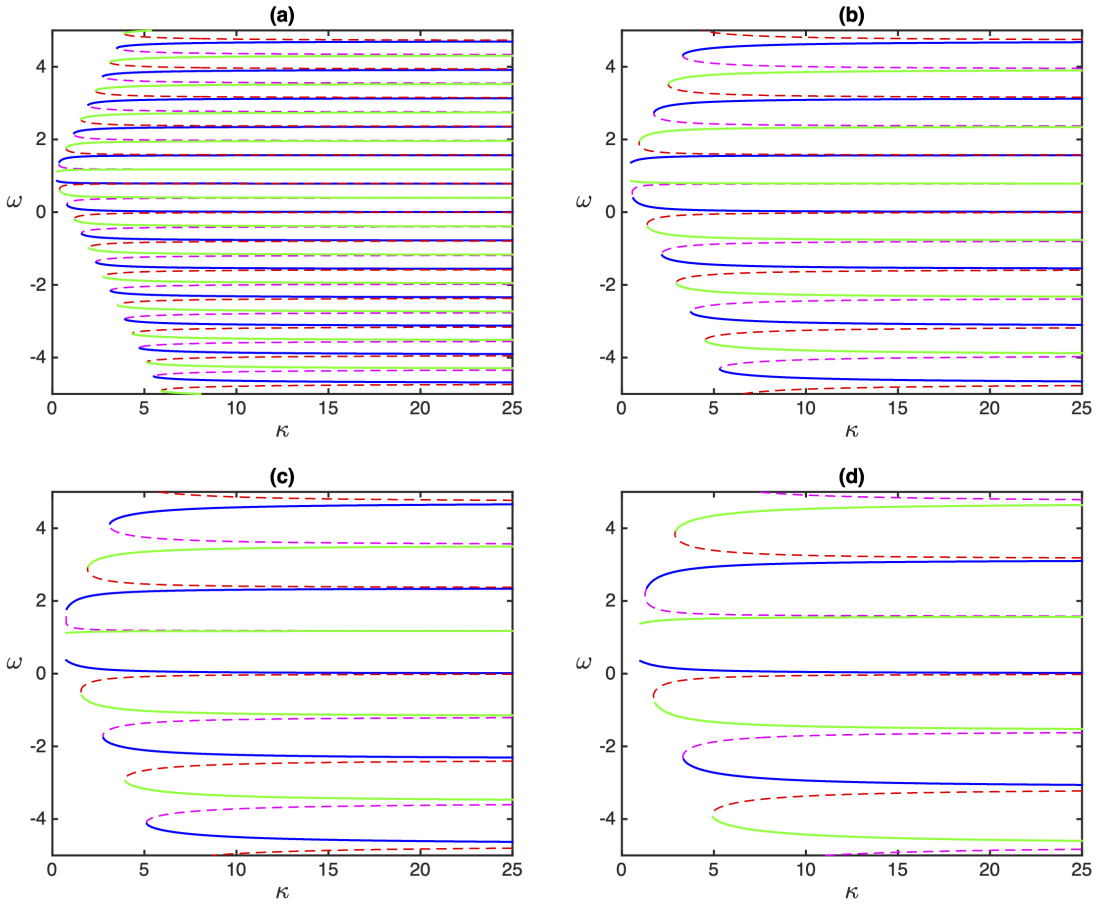

Figure 4.19: Blue solid: stable in-phase, green solid: stable antiphase, magenta dashed: unstable in-phase, red dashed: unstable antiphase. (a) $\gamma = 0.25$, (b) $\gamma = 0.5$, (c) $\gamma = 0.75$, (d) $\gamma = 1$.

This section presents branches of stability and instability regions with varying γ and coupling strength, κ. Stable and unstable solutions are represented by full and dashed lines, respectively. Blue solid line corresponds to stable in-phase solutions, green solid line

to stable antiphase solutions, dashed magenta and red to unstable in-phase and antiphase solutions, respectively. In Fig. 4.19 for varying γ, in-phase and antiphase states alternate, and for positive frequencies upper branches are stable.

4.4.9 Numerical simulations for gamma distributed delay

In this section, we numerically solve the ODE systems (4.29), (4.33), (4.37), (4.39), obtained after employing the linear chain trick on Systems (4.4) and (4.6). Simulations in Fig. 4.20, illustrate the stability of in-phase and antiphase locking frequencies of Systems (4.4) and (4.6) for weak delay kernel in different parameter regimes, corresponding to Fig. 4.14. Simulations in Figs. 4.21, 4.22 illustrate the frequency stability of Systems (4.4) and (4.6) for strong delay kernel in different parameter regimes, in-phase and antiphase, respectively. Selected parameters are consistent with stability regions in Fig. 4.18.

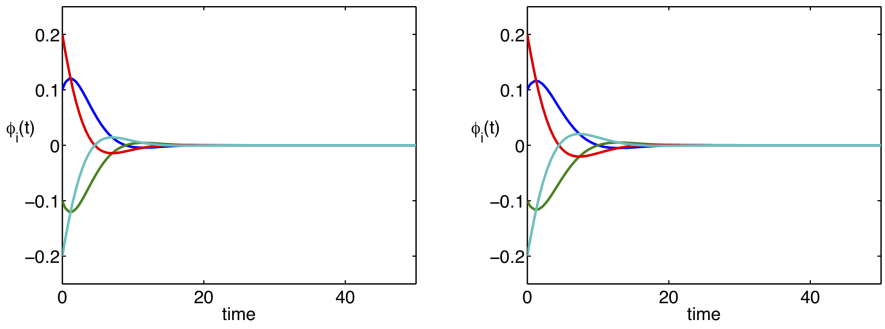

(a) $\kappa = 0.5472, \gamma = 0.25, \omega = 1.3807$ (b) $\kappa = 0.31604, \gamma = 0.25, \omega = 0.88044$

Figure 4.20: Solutions of Systems (4.29) and (4.33) for stable (a) in-phase, and (b) antiphase locking frequencies, weak delay kernel.

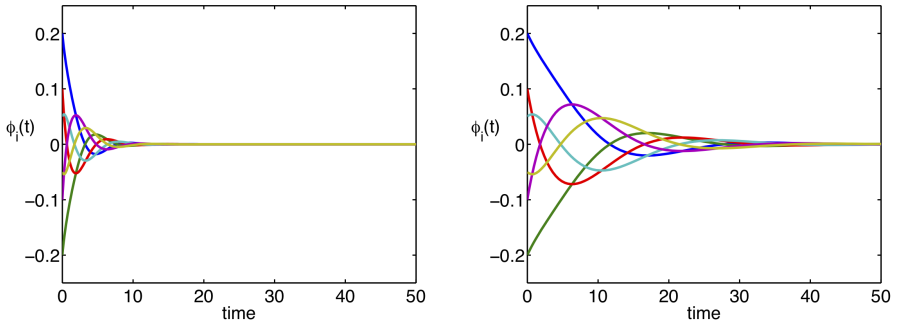

(a) $\kappa = 1.25, \gamma = 0.75, \omega = 0.29015$ (b) $\kappa = 0.46464, \gamma = 0.25, \omega = 1.4257$

Figure 4.21: Solutions of System (4.37) for stable in-phase locking frequencies, strong delay kernel.

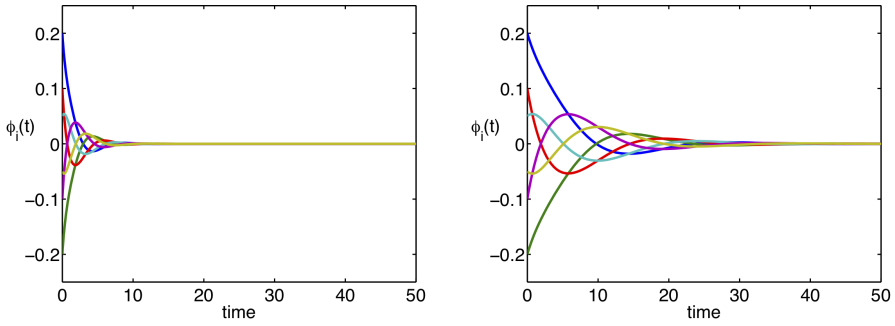

(a) $\kappa = 1.3, \gamma = 0.75, \omega = 1.1406$ (b) $\kappa = 0.31604, \gamma = 0.25, \omega = 0.1.1256$

Figure 4.22: Solutions of System (4.39) for stable antiphase locking frequencies, strong delay kernel.

4.5 Summary

In this chapter, we introduced the model (4.1) for a system of identical phase mutually coupled oscillators, with a delay term in the coupling function. We assume that the delay is distributed and model the delay using uniform and gamma distribution kernels. In the next chapter, we add a delayed self feedback term to System (4.1).

Chapter 5

System of two coupled phase oscillators with feedback and uniformly distributed time delay

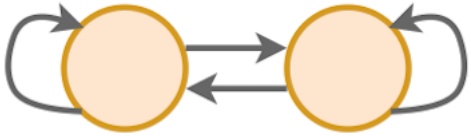

Figure 5.1: Two mutually coupled oscillators with self feedback.

We investigate the influence of self feedback and the effect of distributed time delay on the synchronisation of nonlinear oscillators. The two coupled delay-differential equations describing the phase dynamics are

$$\begin{aligned}\dot{\theta_1}(t) &= 1 + \frac{\kappa}{2}\left[\sin\left(\int_0^\infty g(s)\theta_2(t-s)ds - \theta_1(t)\right) + \sin\left(\int_0^\infty g(s)\theta_1(t-s)ds - \theta_1(t)\right)\right],\\ \dot{\theta_2}(t) &= 1 + \frac{\kappa}{2}\left[\sin\left(\int_0^\infty g(s)\theta_1(t-s)ds - \theta_2(t)\right) + \sin\left(\int_0^\infty g(s)\theta_2(t-s)ds - \theta_2(t)\right)\right],\end{aligned} \tag{5.1}$$

where θ_1, θ_2 are the phases of the oscillator, κ is the coupling strength, and $g(\cdot)$ is the kernel of the delay distribution, which is assumed to be positive definite and normalised to unity:

$$g(s) \geq 0 \quad \text{and} \quad \int_0^\infty g(s)ds = 1.$$

Due to the delay coupling, multiple solutions with different locking frequencies are possible.

For the in-phase solutions $\theta_1(t) = \theta_2(t) = \omega t$, the frequencies can be found by solving

$$\begin{aligned}\omega &= 1 + \frac{\kappa}{2}\left[\sin\left(\int_0^\infty g(s)\omega(t-s)ds - \omega t\right) + \sin\left(\int_0^\infty g(s)\omega(t-s)ds - \omega t\right)\right] \\ &= 1 + \frac{\kappa}{2}\left[\sin\left(\omega t\int_0^\infty g(s)ds - \omega\int_0^\infty sg(s)ds - \omega t\right)\right. \\ &\quad \left. + \sin\left(\omega t\int_0^\infty g(s)ds - \omega\int_0^\infty sg(s)ds - \omega t\right)\right] \\ &= 1 - \kappa\sin\left[\omega\int_0^\infty sg(s)ds\right].\end{aligned} \tag{5.2}$$

For the in-phase solution the locking frequency is the same as (4.2), hence it does not change with introduction of feedback. However, for the anti-phase solutions $\theta_1(t) = \theta_2(t) + \pi = \omega t$, the system of equations reduces to solving

$$\omega = 1 - \frac{\kappa}{2}\left[\sin\left(\int_0^\infty sg(s)ds + \pi\right) + \sin\left(\int_0^\infty sg(s)ds\right)\right] = 1, \tag{5.3}$$

when the oscillators are antiphase there is only one locking frequency, $\omega = 1$.

5.1 In-phase solution analysis - linearisation

To linearise System (5.1), a small perturbation is added to the in-phase solution

$$\begin{aligned}\theta_1(t) &= \omega t + \epsilon\phi_1(t), \\ \theta_2(t) &= \omega t + \epsilon\phi_2(t),\end{aligned}$$

where $0 < \epsilon \ll 1$, substituting this into the system of equations (5.1) yields

$$\begin{aligned}\omega + \epsilon\dot{\phi_1}(t) = 1 + \frac{\kappa}{2}\Bigg[&\sin\left(\int_0^\infty g(s)\big(\omega(t-s) + \epsilon\phi_2(t-s)\big)ds - \omega t - \epsilon\phi_1(t)\right) \\ &+ \sin\left(\int_0^\infty g(s)\big(\omega(t-s) + \epsilon\phi_1(t-s)\big)ds - \omega t - \epsilon\phi_1(t)\right)\Bigg],\end{aligned}$$

$$\begin{aligned}1 - \kappa\sin\left[\omega\int_0^\infty sg(s)ds\right] + \epsilon\dot{\phi_1}(t) = 1 + \frac{\kappa}{2}\Bigg[&\sin\left(\omega t\int_0^\infty g(s)ds - \omega\int_0^\infty g(s)ds\right. \\ &\left. + \epsilon\int_0^\infty g(s)\phi_2(t-s)ds - \omega t - \epsilon\phi_1(t)\right) \\ &+ \sin\left(\omega t\int_0^\infty g(s)ds - \omega\int_0^\infty sg(s)ds\right. \\ &\left. + \epsilon\int_0^\infty g(s)ds\phi_1(t-s)ds - \omega t - \epsilon\phi_1(t)\right)\Bigg],\end{aligned}$$

$$\epsilon\dot{\phi_1}(t) = \frac{\kappa}{2}\Big[-\sin\Big(\omega\int_0^\infty sg(s)ds - \epsilon\int_0^\infty g(s)\phi_2(t-s)ds + \epsilon\phi_1(t)\Big) - \sin\Big(\omega\int_0^\infty sg(s)ds - \epsilon\int_0^\infty g(s)\phi_1(t-s)ds\epsilon\phi_1(t)\Big)\Big] + \kappa\sin\Big(\omega\int_0^\infty sg(s)ds\Big).$$

Taylor expansion for $\epsilon \ll 1$ leads to

$$\epsilon\dot{\phi_1}(t) = -\frac{\kappa}{2}\cos\Big(\omega\int_0^\infty sg(s)\Big)\Big[-\epsilon\int_0^\infty g(s)\phi_2(t-s)ds + \epsilon\phi_1(t) - \epsilon\int_0^\infty g(s)\phi_1(t-s)ds + \epsilon\phi_1(t)\Big].$$

Hence the two linear equations are

$$\begin{aligned}\dot{\phi_1}(t) =& \frac{\kappa}{2}\cos\Big(\omega\int_0^\infty sg(s)ds\Big)\Big[\int_0^\infty g(s)\phi_2(t-s)ds + \int_0^\infty g(s)\phi_1(t-s)ds - 2\phi_1(t)\Big],\\ \dot{\phi_2}(t) =& \frac{\kappa}{2}\cos\Big(\omega\int_0^\infty sg(s)ds\Big)\Big[\int_0^\infty g(s)\phi_1(t-s)ds + \int_0^\infty g(s)\phi_2(t-s)ds - 2\phi_2(t)\Big].\end{aligned} \tag{5.4}$$

5.1.1 In-phase solution analysis - characteristic equation

To determine whether the perturbation grows or decays as the system evolves we consider $\phi_i(t) = c_i e^{\lambda t}$, where $i = 1, 2$ and $\lambda \in \mathbb{C}$. The characteristic equation derived from (5.4) describes the linear dynamics of the perturbation

$$\begin{pmatrix}\dot{\phi_1}\\ \dot{\phi_2}\end{pmatrix} = \begin{pmatrix}-2a & 0\\ 0 & -2a\end{pmatrix}\begin{pmatrix}\phi_1\\ \phi_2\end{pmatrix} + \begin{pmatrix}a & a\\ a & a\end{pmatrix}\begin{pmatrix}\int_0^\infty g(s)\phi_1(t-s)ds\\ \int_0^\infty g(s)\phi_2(t-s)ds\end{pmatrix},$$

where $a = \frac{\kappa}{2}\cos\Big[\omega\int_0^\infty sg(s)ds)\Big]$. Now, we have that $\{\mathcal{L}g\}(\lambda) = \int_0^\infty g(s)e^{-\lambda s}ds$ is the Laplace transform of the function $g(s)$, hence

$$\begin{pmatrix}\lambda & 0\\ 0 & \lambda\end{pmatrix}\begin{pmatrix}\phi_1\\ \phi_2\end{pmatrix} = \begin{pmatrix}-2a & 0\\ 0 & -2a\end{pmatrix}\begin{pmatrix}\phi_1\\ \phi_2\end{pmatrix} + \begin{pmatrix}a & a\\ a & a\end{pmatrix}\begin{pmatrix}\phi_1\\ \phi_2\end{pmatrix}\{\mathcal{L}g\}(\lambda),$$

which has the form

$$\begin{aligned}\lambda I\boldsymbol{\phi} &= L_0\boldsymbol{\phi} + M\{\mathcal{L}g\}(\lambda)\boldsymbol{\phi}\\ \boldsymbol{\phi}\big(\lambda I - L_0 - M\{\mathcal{L}g\}(\lambda)\big) &= 0.\end{aligned}$$

Now taking

$$\det\big(\lambda I - L_0 - M\{\mathcal{L}g\}(\lambda)\big) = 0,$$

$$\det\begin{pmatrix} \lambda + 2a - a\{\mathcal{L}g\}(\lambda) & -a\{\mathcal{L}g\}(\lambda) \\ -a\{\mathcal{L}g\}(\lambda) & \lambda + 2a - a\{\mathcal{L}g\}(\lambda) \end{pmatrix} = 0,$$

substituting $a = \frac{\kappa}{2}\cos\left[\omega\int_0^\infty sg(s)ds)\right]$ back in, we get the following characteristic equation

$$\left[\lambda + \kappa\cos\left(\omega\int_0^\infty sg(s)ds\right) - \frac{\kappa}{2}\cos\left(\omega\int_0^\infty sg(s)ds\right)\{\mathcal{L}g\}(\lambda)\right]^2 - \frac{\kappa^2}{4}\cos^2\left(\omega\int_0^\infty sg(s)ds\right)\left[\{\mathcal{L}g\}(\lambda)\right]^2 = 0,$$

hence the in-phase characteristic equation can be written as

$$\left[\lambda + \kappa\cos\left(\omega\int_0^\infty sg(s)ds\right)\right]\left[\lambda - \kappa\cos\left(\omega\int_0^\infty sg(s)ds\right)\{\mathcal{L}g\}(\lambda) + \kappa\cos\left(\omega\int_0^\infty sg(s)ds\right)\right] = 0. \tag{5.5}$$

Characteristic equation (5.5) always has $\lambda = 0$ as an eigenvalue.

5.2 Antiphase solution analysis - linearisation

A small perturbation is added to the antiphase solution

$$\theta_1(t) = \omega t + \epsilon\phi_1(t),$$
$$\theta_2(t) = \omega t - \pi + \epsilon\phi_2(t),$$

where $0 < \epsilon \ll 1$, substituting this into the system of equations (5.1) yields

$$\omega + \epsilon\dot{\phi_1}(t) = 1 + \frac{\kappa}{2}\left[\sin\left(\int_0^\infty g(s)\big(\omega(t-s) - \pi + \epsilon\phi_2(t-s)\big)ds - \omega t - \epsilon\phi_1(t)\right) + \sin\left(\int_0^\infty g(s)\big(\omega(t-s) + \epsilon\phi_1(t-s)\big)ds - \omega t - \epsilon\phi_1(t)\right)\right],$$

$$1 + \epsilon\dot{\phi_1}(t) = 1 + \frac{\kappa}{2}\left[\sin\left(\omega t\int_0^\infty g(s)ds - \omega\int_0^\infty sg(s)ds - \pi\int_0^\infty g(s)ds + \epsilon\int_0^\infty \phi_2(t-s)g(s)ds - \omega t - \epsilon\phi_1(t)\right) + \sin\left(\omega t\int_0^\infty g(s)ds - \omega\int_0^\infty sg(s)ds + \epsilon\int_0^\infty \phi_1(t-s)g(s)ds - \omega t - \epsilon\phi_1(t)\right)\right],$$

$$\epsilon\dot{\phi}_1(t) = -\frac{\kappa}{2}\Bigg[\sin\left(\omega\int_0^\infty sg(s)ds + \pi + \epsilon\int_0^\infty \phi_2(t-s)g(s)ds + \epsilon\phi_1(t)\right) + \sin\left(\omega\int_0^\infty sg(s)ds - \epsilon\int_0^\infty \phi_1(t-s)g(s)ds + \epsilon\phi_1(t)\right)\Bigg].$$

Taylor expansion for $\epsilon \ll 1$ leads to

$$\epsilon\dot{\phi}_1(t) = \frac{\kappa}{2}\cos\left(\omega\int_0^\infty sg(s)ds\right)\Bigg(-\epsilon\int_0^\infty g(s)\phi_2(t-s)ds + \epsilon\phi_1(t) + \epsilon\int_0^\infty \phi_1(t-s)g(s)ds + \epsilon\phi_1(t)\Bigg).$$

Hence the two linear equations are

$$\begin{aligned}\dot{\phi}_1(t) &= \frac{\kappa}{2}\cos\left(\omega\int_0^\infty sg(s)ds\right)\Bigg[-\int_0^\infty \phi_2(t-s)g(s)ds + \int_0^\infty \phi_1(t-s)g(s)ds\Bigg],\\ \dot{\phi}_2(t) &= \frac{\kappa}{2}\cos\left(\omega\int_0^\infty sg(s)ds\right)\Bigg[-\int_0^\infty \phi_1(t-s)g(s)ds + \int_0^\infty \phi_2(t-s)g(s)ds\Bigg].\end{aligned} \tag{5.6}$$

5.2.1 Antiphase solution analysis - characteristic equation

Similarly to the in-phase analysis we consider $\phi_i(t) = c_i e^{\lambda t}$, where $i = 1, 2$ and $\lambda \in \mathbb{C}$. The characteristic equation for (5.6) is as follows, with $a = \frac{\kappa}{2}\cos\left[\omega\int_0^\infty sg(s)ds)\right]$

$$\begin{pmatrix}\dot{\phi}_1\\ \dot{\phi}_2\end{pmatrix} = \begin{pmatrix} a & -a\\ -a & a\end{pmatrix}\begin{pmatrix}\int_0^\infty g(s)\phi_1(t-s)ds\\ \int_0^\infty g(s)\phi_2(t-s)ds\end{pmatrix},$$

which has the form

$$\boldsymbol{\phi}\big(\lambda I - M\{\mathcal{L}g\}(\lambda)\big) = 0,$$

where $\{\mathcal{L}g\}(\lambda) = \int_0^\infty g(s)e^{-\lambda s}ds$ is the Laplace transform of the function $g(s)$. Now taking

$$\det\big(\lambda I - M\{\mathcal{L}g\}(\lambda)\big) = 0,$$

$$\det\begin{pmatrix}\lambda - a\{\mathcal{L}g\}(\lambda) & a\{\mathcal{L}g\}(\lambda)\\ a\{\mathcal{L}g\}(\lambda) & \lambda - a\{\mathcal{L}g\}(\lambda)\end{pmatrix} = 0,$$

which results in the following characteristic equation

$$\left[\lambda - \frac{\kappa}{2}\cos\left(\omega\int_0^\infty sg(s)ds\right)\{\mathcal{L}g\}(\lambda)\right]^2 - \frac{\kappa^2}{4}\cos^2\left(\omega\int_0^\infty sg(s)ds\right)\left[\{\mathcal{L}g\}(\lambda)\right]^2 = 0,$$

which simplifies to

$$\lambda^2 - \lambda\kappa\cos\left(\omega\int_0^\infty sg(s)ds\right)\{\mathcal{L}g\}(\lambda) = 0. \tag{5.7}$$

Characteristic equation (5.7) always has $\lambda = 0$ as an eigenvalue.

5.3 Uniformly distributed delay

5.3.1 In-phase solution

Equations (1.14) and (1.16) transform the in-phase characteristic equation (5.5) to

$$\left[\lambda + \kappa\cos(\omega\tau)\right]\left[\lambda + \kappa\cos(\omega\tau) - \kappa\cos(\omega\tau)\left(e^{-\lambda\tau}\frac{\sinh(\lambda\rho)}{\lambda\rho}\right)\right] = 0. \tag{5.8}$$

Rewriting the linearised system with the uniformly distributed kernel with $\boldsymbol{\phi} = (\phi_1, \phi_2)$ results in

$$\dot{\boldsymbol{\phi}}(t) = L_0\boldsymbol{\phi}(t) + \frac{1}{2\rho}\int_{-(\tau+\rho)}^{-(\tau-\rho)} M\boldsymbol{\phi}(t+s)ds, \tag{5.9}$$

where

$$L_0 = \begin{pmatrix} -\kappa\cos(\omega\tau) & 0 \\ 0 & -\kappa\cos(\omega\tau) \end{pmatrix}, \quad M = \begin{pmatrix} \frac{\kappa}{2}\cos(\omega\tau) & \frac{\kappa}{2}\cos(\omega\tau) \\ \frac{\kappa}{2}\cos(\omega\tau) & \frac{\kappa}{2}\cos(\omega\tau) \end{pmatrix},$$

for the in-phase locked frequency.

5.3.2 Antiphase solution

Equations (1.14) and (1.16) transform the antiphase characteristic equation (5.7) to

$$\lambda^2 - \lambda\kappa\cos(\omega\tau)\left(e^{-\lambda\tau}\frac{\sinh(\lambda\rho)}{\lambda\rho}\right) = 0. \tag{5.10}$$

Now, rewriting the linearised system with the uniformly distributed kernel with $\boldsymbol{\phi} = (\phi_1, \phi_2)$ results in

$$\dot{\boldsymbol{\phi}}(t) = \frac{1}{2\rho}\int_{-(\tau+\rho)}^{-(\tau-\rho)} M\boldsymbol{\phi}(t+s)ds, \tag{5.11}$$

where for the antiphase locked frequency we have

$$M = \begin{pmatrix} \frac{\kappa}{2}\cos(\omega\tau) & -\frac{\kappa}{2}\cos(\omega\tau) \\ -\frac{\kappa}{2}\cos(\omega\tau) & \frac{\kappa}{2}\cos(\omega\tau) \end{pmatrix}.$$

Systems (5.9) and (5.11) are now in the form suitable for computing the maximum real part of the eigenvalues using the algorithm described in Breda *et al.* [45] and implemented in traceDDE suite in Matlab.

5.4 Locking frequencies and stability regions

This section looks at in-phase locking frequencies, i.e., number of total, stable, and unstable solutions. The colour code corresponds to the possible number of solutions, ω, in the specified τ and κ range. As can be seen from Figs. 5.2 and 5.3, the number of locking frequencies increases with increasing delay τ, and coupling strength κ. The width of the distribution, ρ, does not alter the dynamics.

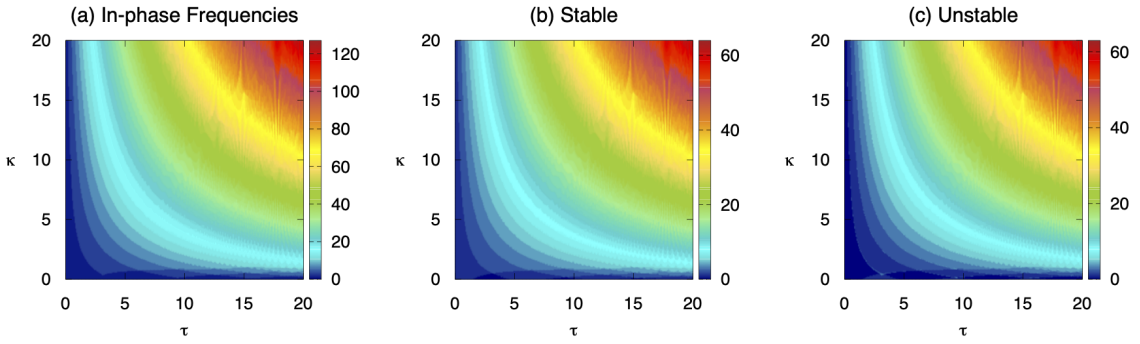

Figure 5.2: In-phase locking frequencies (colour bar corresponds to the number of possible frequencies at every point), $\rho = 0.0001$: (a) total locked frequencies, (b) stable locking frequencies, (c) unstable locking frequencies.

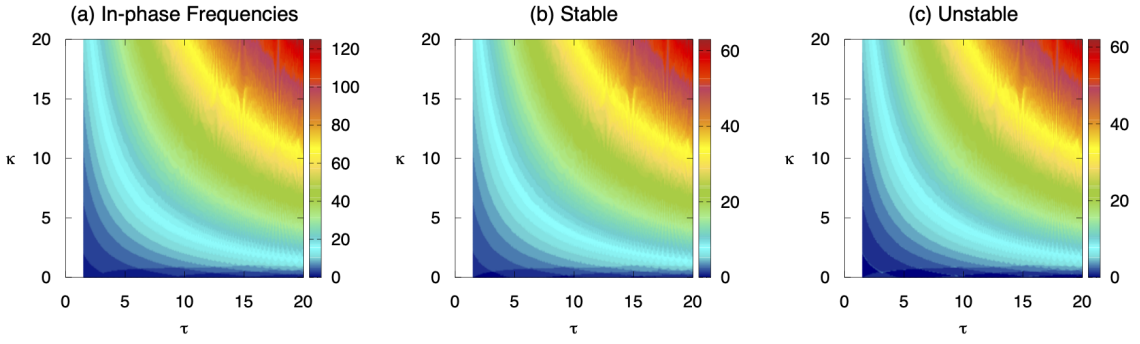

Figure 5.3: In-phase locking frequencies (colour bar corresponds to the number of possible frequencies at every point), $\rho = 1.5$: (a) total locked frequencies, (b) stable locking frequencies, (c) unstable locking frequencies.

Fig. 5.4 shows stable in-phase and antiphase solutions. The alternation between in-phase and antiphase stable frequencies is present at lower values of coupling strength, κ. Multistability is now less prominent at higher values of τ and κ. The in-phase states are stable for a larger range of delay, τ, compared to the antiphase. The stability regions are identical for varying width of the distribution, ρ.

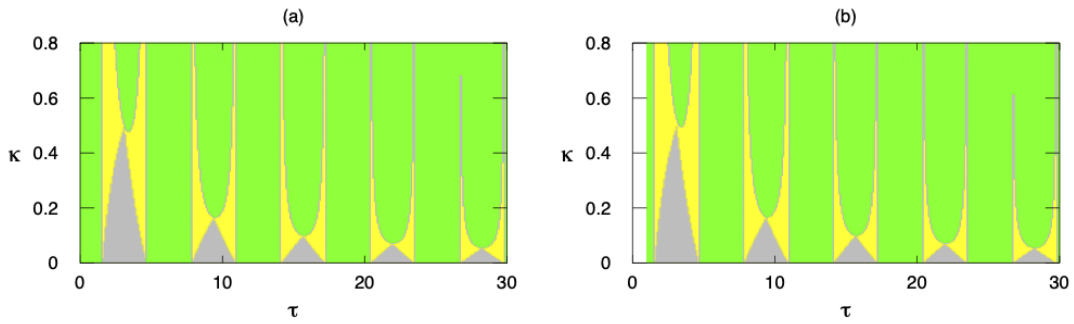

Figure 5.4: Stability regions of in-phase and antiphase solutions. Green: only in-phase solutions are stable, grey: only antiphase solutions are stable, yellow: in-phase and antiphase solutions coexist. (a) $\rho = 0.0001$, (b) $\rho = 1$.

The system with delayed feedback (5.1) has a stronger symmetry compared to the system without feedback (4.1) - regardless of whether the oscillators are in-phase or antiphase, they will always get the same input, whereas components in a system without feedback only get the same input given that they are in-phase or antiphase. Both systems, with and without feedback, only admit synchronous or antisynchronous frequency-locked solutions. For the in-phase solutions, the locking frequencies are not affected by the presence of feedback, as can be seen in the next section.

5.4.1 Graphical determination of the locking frequencies

This section presents branches of stability and instability regions with varying mean time delay, τ, coupling strength, κ, and uniform distribution width, ρ. Stable and unstable solutions are represented by full and dashed lines, respectively. Blue solid line corresponds to stable in-phase solutions, dashed magenta corresponds to unstable in-phase solutions. From Figs. 5.5 and 5.6, we can see that stability alternates between upper and lower branches of solutions, similarly to the model without feedback delay term (4.1). The width of the distribution, ρ, does not alter the stability properties.

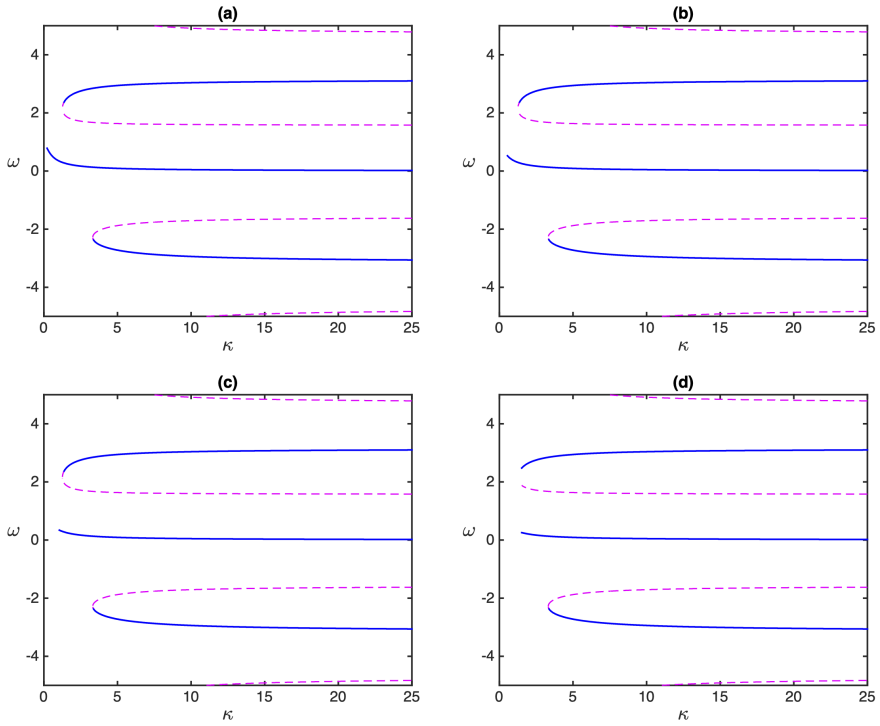

Figure 5.5: Blue solid: stable in-phase, magenta dashed: unstable in-phase. (a) $\tau = 2$, $\rho = 0.0001$, (b) $\tau = 2$, $\rho = 0.5$, (c) $\tau = 2$, $\rho = 1$, (d) $\tau = 2$, $\rho = 1.5$.

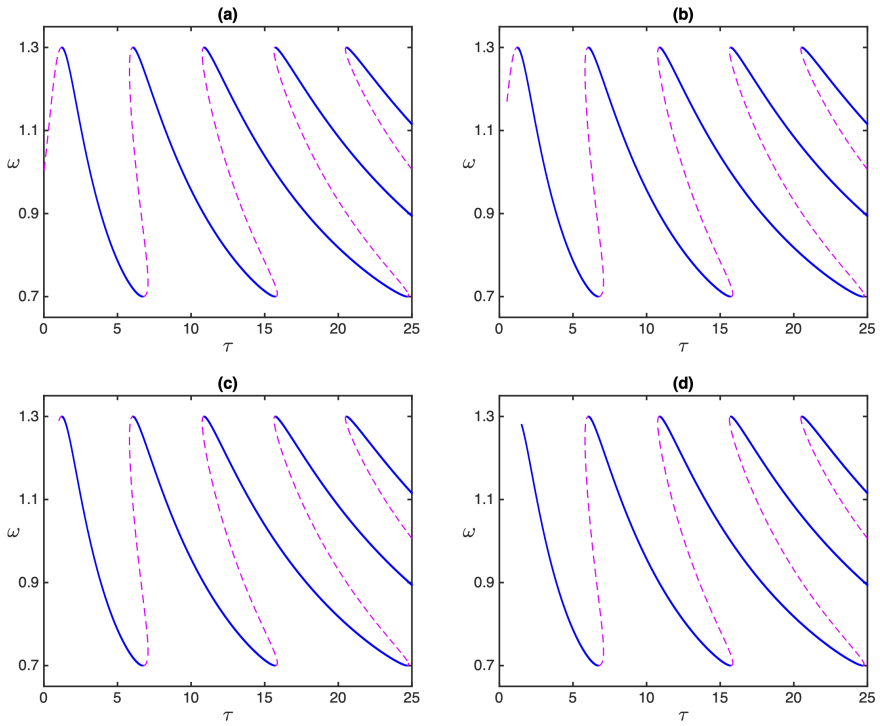

Figure 5.6: Blue solid: stable in-phase, magenta dashed: unstable in-phase. (a) $\kappa = -0.3$, $\rho = 0.0001$, (b) $\kappa = -0.3$, $\rho = 0.5$, (c) $\kappa = -0.3$, $\rho = 1.5$, (d) $\kappa = -0.3$, $\rho = 2$.

5.5 Numerical simulations

We follow the same method as in Chapter 4, by directly approximating the solution of the distributed delay system through the trapezoidal rule [49]. Making use of the trapezoidal quadrature formula (4.18) for the integrals, we obtain the in-phase equations as

$$\begin{aligned}\dot{\phi}_1(t) =&\frac{\kappa}{2}\cos(\omega\tau)\left[\frac{1}{2}\big(\phi_2(t-\tau_1)+\phi_2(t-\tau_2)+\phi_1(t-\tau_1)+\phi_1(t-\tau_2)\big)-2\phi_1(t)\right],\\ \dot{\phi}_2(t) =&\frac{\kappa}{2}\cos(\omega\tau)\left[\frac{1}{2}\big(\phi_1(t-\tau_1)+\phi_1(t-\tau_2)+\phi_2(t-\tau_1)+\phi_2(t-\tau_2)\big)-2\phi_2(t)\right],\end{aligned} \tag{5.12}$$

where $\tau_1 = \tau - \rho$ and $\tau_2 = \tau + \rho$.

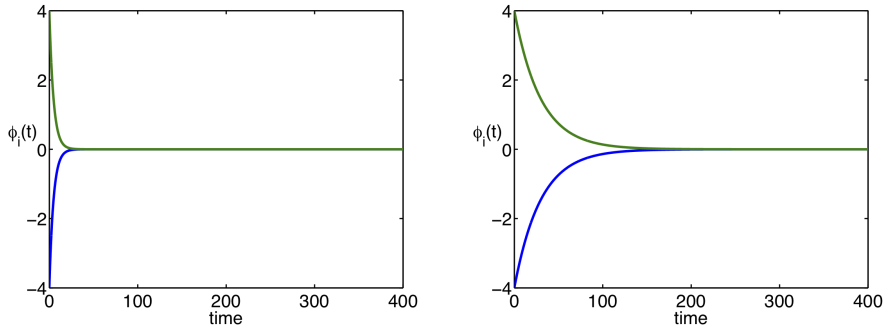

(a) $\kappa = -0.3, \tau = 5, \omega = 0.7866$ (b) $\kappa = 0.3, \tau = 3, \omega = 0.5011$

Figure 5.7: Solutions of System (5.12) for stable in-phase locking frequencies.

We have for the antiphase

$$\begin{aligned}\dot{\phi}_1(t) =& -\frac{\kappa}{4}\cos(\omega\tau)\Big[\phi_2(t-\tau_1)+\phi_2(t-\tau_2)+\phi_1(t-\tau_1)+\phi_1(t-\tau_2)\Big],\\ \dot{\phi}_2(t) =& -\frac{\kappa}{4}\cos(\omega\tau)\Big[\phi_1(t-\tau_1)+\phi_1(t-\tau_2)+\phi_2(t-\tau_1)+\phi_2(t-\tau_2)\Big],\end{aligned} \tag{5.13}$$

where $\tau_1 = \tau - \rho$ and $\tau_2 = \tau + \rho$.

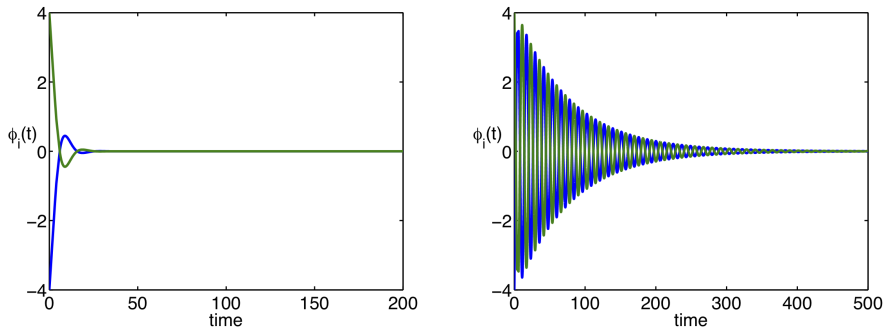

(a) $\kappa = 0.2, \tau = 3, \omega = 1$ (b) $\kappa = 0.5, \tau = 3, \omega = 1$

Figure 5.8: Solutions of System (5.13) for stable antiphase locking frequencies.

Simulations in Figs. 5.7 and 5.8 illustrate the stability of in-phase and antiphase locking frequencies of Systems (5.4) and (5.6) in different parameter regimes.

5.6 Summary

In Chapters 4 and 5, we considered two identical coupled phase oscillators with distributed delay, and investigated the solutions with constant frequency, Chapter 5 briefly looked at the influence of self feedback on the system. A typical implementation of the delay distribution is considered in these chapters. We discovered that the solutions themselves are the same as for a constant delay (equal to the mean delay). In Chapter 6, we consider an alternative way to implement delay-distributed coupling.

Chapter 6

System of two coupled phase oscillators with an untypical distributed time delay

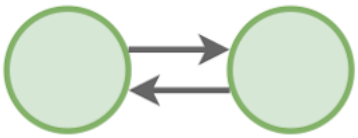

Figure 6.1: Two mutually coupled oscillators.

We consider an alternative way to implement a distributed delay, where the distribution is outside the sine function

$$\begin{aligned} \dot{\theta_1}(t) &= 1 + \kappa \int_0^\infty g(s) \sin\big(\theta_2(t-s) - \theta_1(t)\big) ds, \\ \dot{\theta_2}(t) &= 1 + \kappa \int_0^\infty g(s) \sin\big(\theta_1(t-s) - \theta_2(t)\big) ds, \end{aligned} \tag{6.1}$$

where θ_1, θ_2 are the phases of the oscillator, κ is the coupling strength, and $g(\cdot)$ is the kernel of the delay distribution, which is assumed to be positive definite and normalised to unity:

$$g(s) \geq 0 \quad \text{and} \quad \int_0^\infty g(s) ds = 1.$$

The ansatz for the in-phase solutions $\theta_1(t) = \theta_2(t) = \omega t$, the frequencies can be found by

solving

$$\begin{aligned}\omega =&1+\kappa\int_0^\infty g(s)\sin(-\omega s)ds\\ =&1-\kappa\int_0^\infty g(s)\sin(\omega s)ds.\end{aligned}\tag{6.2}$$

This denotes linear growth of the phases with the global frequency ω. Similarly for the anti-phase solutions $\theta_1(t)=\theta_2(t)+\pi=\omega t$, the system of equations reduces to solving

$$\begin{aligned}\omega =&1+\kappa\int_0^\infty g(s)\sin(\omega(t-s)-\pi-\omega t)ds,\\ =&1+\kappa\int_0^\infty g(s)\sin(\omega s)ds.\end{aligned}\tag{6.3}$$

6.1 In-phase solution

To linearise System (6.1), a small perturbation is added to the in-phase solution

$$\begin{aligned}\theta_1(t)&=\omega t+\epsilon\phi_1(t),\\ \theta_2(t)&=\omega t+\epsilon\phi_2(t),\end{aligned}$$

where $0<\epsilon\ll 1$, substituting this into the system of equations (6.1) yields

$$\begin{aligned}\omega+\epsilon\dot{\phi_1}(t)&=1+\kappa\int_0^\infty g(s)\sin\big(\omega(t-s)+\epsilon\phi_2(t-s)-\omega t-\epsilon\phi_1(t)\big)ds\\ &=1+\int_0^\infty g(s)\sin\big(-\omega s+\epsilon\phi_2(t-s)-\epsilon\phi_1(t)\big)ds\\ &=1+\kappa\int_0^\infty g(s)\Big(\sin(-\omega s)+\big(\epsilon\phi_2(t-s)-\epsilon\phi_1(t)\big)\cos(\omega s)\Big)ds\\ &=1-\kappa\int_0^\infty g(s)\sin(\omega s)ds+\kappa\epsilon\int_0^\infty g(s)\big(\phi_2(t-s)-\phi_1(t)\big)\cos(\omega s)ds.\end{aligned}$$

Hence the two linear equations are

$$\begin{aligned}\dot{\phi_1}(t)=&\kappa\int_0^\infty g(s)\cos(\omega s)\phi_2(t-s)ds-\kappa\phi_1(t)\int_0^\infty g(s)\cos(\omega s)ds,\\ \dot{\phi_2}(t)=&\kappa\int_0^\infty g(s)\cos(\omega s)\phi_1(t-s)ds-\kappa\phi_2(t)\int_0^\infty g(s)\cos(\omega s)ds,\end{aligned}\tag{6.4}$$

where $a=\kappa\int_0^\infty g(s)\cos(\omega s)ds$, hence

$$\begin{aligned}\dot{\phi_1}(t)=&\kappa\int_0^\infty g(s)\cos(\omega s)\phi_2(t-s)ds-a\phi_1(t)\\ =&a\Big(\int_0^\infty\frac{\kappa g(s)\cos(\omega s)}{a}\phi_2(t-s)ds-\phi_1(t)\Big)\\ =&a\Big(G(s)\phi_2(t-s)ds-\phi_1(t)\Big),\end{aligned}$$

where we have

$$\int_0^\infty G(s)ds = \int_0^\infty \frac{\kappa g(s)\cos(\omega s)}{a}ds = \frac{1}{a}\int_0^\infty \kappa g(s)\cos(\omega s)ds = 1.$$

Combining the above, we have

$$\begin{aligned}\dot{\phi_1}(t) =& a\Big(\int_0^\infty G(s)\phi_2(t-s)ds - \phi_1(t)\Big),\\ \dot{\phi_2}(t) =& a\Big(\int_0^\infty G(s)\phi_1(t-s)ds - \phi_2(t)\Big).\end{aligned} \tag{6.5}$$

Similarly to our previous analysis, we have the characteristic equation as

$$\det\big(\lambda I - L_0 - M\{\mathcal{L}G\}(\lambda)\big) = 0, \text{ where}$$

$$L_0 = \begin{pmatrix} -a & 0 \\ 0 & -a \end{pmatrix}, \quad M = \begin{pmatrix} 0 & a \\ a & 0 \end{pmatrix},$$

resulting in the following expression

$$\begin{aligned}&\Big[\lambda + \kappa\int_0^\infty g(s)\cos(\omega s)ds + \kappa\int_0^\infty g(s)\cos(\omega s)ds\{\mathcal{L}G\}(\lambda)\Big]\\ &\quad\times\Big[\lambda + \kappa\int_0^\infty g(s)\cos(\omega s)ds - \kappa\int_0^\infty g(s)\cos(\omega s)ds\{\mathcal{L}G\}(\lambda)\Big] = 0.\end{aligned} \tag{6.6}$$

where λ is an eigenvalue of the Jacobian, and $\{\mathcal{L}G\}(\lambda)$ is the Laplace transform of the function $G(s)$. Characteristic equation (6.6) always has $\lambda = 0$ as an eigenvalue.

6.2 Antiphase solution

A small perturbation is added to the antiphase solution

$$\begin{aligned}\theta_1(t) &= \omega t + \epsilon\phi_1(t),\\ \theta_2(t) &= \omega t - \pi + \epsilon\phi_2(t),\end{aligned}$$

where $0 < \epsilon \ll 1$, substituting this into the system of equations (6.1) yields

$$\begin{aligned}\omega + \epsilon\dot{\phi_1}(t) &= 1 + \kappa\int_0^\infty g(s)\sin\big(\omega(t-s) - \pi + \epsilon\phi_2(t-s) - \omega t - \epsilon\phi_1(t)\big)ds\\ &= 1 + \kappa\int_0^\infty g(s)\sin\big(-\omega s - \pi + \epsilon\phi_2(t-s) - \epsilon\phi_1(t)\big)ds\\ &= 1 + \kappa\int_0^\infty g(s)\sin\big(\omega s - \epsilon\phi_2(t-s) + \epsilon\phi_1(t)\big)ds\\ &= 1 + \kappa\int_0^\infty g(s)\big(\sin(\omega s) + (-\epsilon\phi_2(t-s) + \epsilon\phi_1(t))\cos(\omega s)\big)ds\\ &= 1 + \kappa\int_0^\infty g(s)\sin(\omega s)ds + \kappa\epsilon\int_0^\infty g(s)\big(-\phi_2(t-s) + \phi_1(t)\big)\cos(\omega s)ds.\end{aligned}$$

Hence the linear equation is

$$\dot{\phi_1}(t) = -\kappa \int_0^\infty g(s)\cos(\omega s)\phi_2(t-s)ds + \kappa\phi_1(t)\int_0^\infty g(s)\cos(\omega s)ds, \tag{6.7}$$

with $a = \kappa \displaystyle\int_0^\infty g(s)\cos(\omega s)ds$, resulting in a system of linear equations

$$\begin{aligned}\dot{\phi_1}(t) =& a\Big(-\int_0^\infty G(s)\phi_2(t-s)ds + \phi_1(t)\Big),\\ \dot{\phi_2}(t) =& a\Big(-\int_0^\infty G(s)\phi_1(t-s)ds + \phi_2(t)\Big),\end{aligned} \tag{6.8}$$

where $G(s) = \dfrac{1}{a}\kappa g(s)\cos(\omega s)$.

Similarly to the in-phase case, the characteristic equation is

$$\det\big(\lambda I - L_0 - M\{\mathcal{L}G\}(\lambda)\big) = 0, \text{ where}$$

$$L_0 = \begin{pmatrix} a & 0 \\ 0 & a \end{pmatrix}, \quad M = \begin{pmatrix} 0 & -a \\ -a & 0 \end{pmatrix},$$

the antiphase characteristic equation can be written as

$$\begin{aligned}&\Big[\lambda - \kappa\int_0^\infty g(s)\cos(\omega s)ds + \kappa\int_0^\infty g(s)\cos(\omega s)ds\{\mathcal{L}G\}(\lambda)\Big]\\ &\quad\times\Big[\lambda - \kappa\int_0^\infty g(s)\cos(\omega s)ds - \kappa\int_0^\infty g(s)\cos(\omega s)ds\{\mathcal{L}G\}(\lambda)\Big] = 0.\end{aligned} \tag{6.9}$$

Characteristic equation (6.9) always has $\lambda = 0$ as an eigenvalue.

6.3 Uniformly distributed delay

In this section, we consider a uniformly distributed kernel. Taking into account the Laplace transform (1.16) of the distribution $g(s)$, since

$$\begin{aligned}a = \kappa\int_0^\infty g(s)\cos(\omega s)ds &= \kappa\int_{\tau-\rho}^{\tau+\rho}\frac{\cos(\omega s)}{2\rho}ds\\ &= \frac{\kappa}{2\rho\omega}\big(\sin(\omega(\tau+\rho)) - \sin(\omega(\tau-\rho))\big).\end{aligned} \tag{6.10}$$

Now, from (1.14) and (1.16) we have

$$G(s) = \frac{\kappa g(s)\cos(\omega s)}{a} = \frac{\kappa g(s)\cos(\omega s)}{\dfrac{\kappa}{2\rho\omega}\Big[\sin\big(\omega(\tau+\rho)\big) - \sin\big(\omega(\tau-\rho)\big)\Big]}$$

$$= \begin{cases} \dfrac{\omega\cos(\omega s)}{\sin\big(\omega(\tau+\rho)\big) - \sin\big(\omega(\tau-\rho)\big)} & \text{when} \quad \tau-\rho \le s \le \tau+\rho,\\ 0 & \text{otherwise,}\end{cases}$$

hence,

$$
\begin{aligned}
\{\mathcal{L}G\}(\lambda) =& \frac{\omega}{\sin\big(\omega(\tau+\rho)\big) - \sin\big(\omega(\tau-\rho)\big)} \int_{\tau-\rho}^{\tau+\rho} e^{-\lambda s}\cos(\omega s) ds \\
=& \frac{\kappa}{2\rho a} \int_{\tau-\rho}^{\tau+\rho} e^{-\lambda s}\cos(\omega s) ds \\
=& \frac{\kappa}{2\rho a}\left[\frac{-\lambda}{\lambda^2+\omega^2}\Big(e^{-\lambda(\tau+\rho)}\cos\big(\omega(\tau+\rho)\big) - e^{-\lambda(\tau-\rho)}\cos\big(\omega(\tau-\rho)\big)\Big)\right. \\
&\left. + \frac{\omega}{\lambda^2+\omega^2}\Big(e^{-\lambda(\tau+\rho)}\sin\big(\omega(\tau+\rho)\big) - e^{-\lambda(\tau-\rho)}\sin\big(\omega(\tau-\rho)\big)\Big)\right] \\
=& \frac{\kappa e^{-\lambda\tau}}{2\rho a(\lambda^2+\omega^2)}\left[-\lambda\Big(e^{-\lambda\rho}\cos\big(\omega(\tau+\rho)\big) - e^{\lambda\rho}\cos\big(\omega(\tau-\rho)\big)\Big)\right. \\
&\left. + \omega\Big(e^{-\lambda\rho}\sin\big(\omega(\tau+\rho)\big) - e^{\lambda\rho}\sin\big(\omega(\tau-\rho)\big)\Big)\right].
\end{aligned}
\tag{6.11}
$$

Rewriting the linearised system with the uniformly distributed kernel with $\boldsymbol{\phi} = (\phi_1, \phi_2)$ results in

$$
\dot{\boldsymbol{\phi}}(t) = L_0\boldsymbol{\phi}(t) + \frac{1}{2\rho}\int_{-(\tau+\rho)}^{-(\tau-\rho)} M\boldsymbol{\phi}(t+s) ds, \tag{6.12}
$$

where

$$
L_0 = \begin{pmatrix} -a & 0 \\ 0 & -a \end{pmatrix}, \quad M = \begin{pmatrix} 0 & a \\ a & 0 \end{pmatrix},
$$

for the in-phase locked frequency, and the following for the antiphase locked frequency

$$
L_0 = \begin{pmatrix} a & 0 \\ 0 & a \end{pmatrix}, \quad M = \begin{pmatrix} 0 & -a \\ -a & 0 \end{pmatrix},
$$

where $a = \dfrac{\kappa}{2\rho\omega}\Big(\sin\big(\omega(\tau+\rho)\big) - \sin\big(\omega(\tau-\rho)\big)\Big) = \dfrac{\kappa}{\rho\omega}\cos(\omega\tau)\sin(\omega\rho)$. System (6.12) is now in the form suitable for computing the maximum real part of the eigenvalues using the algorithm described in Breda *et al.* [45] and implemented in traceDDE suite in Matlab.

6.3.1 Locking frequencies

This section looks at in-phase and antiphase locking frequencies, i.e., number of total, stable, and unstable solutions. The colour code corresponds to the possible number of solutions, ω, in the specified τ and κ range. As can be seen from Figs. 6.2 - 6.5, the number of locking frequencies increases with increasing delay τ, and coupling strength κ. Unlike in previous two chapters, here we also notice the number of frequencies reducing with the increase of the distribution width, ρ.

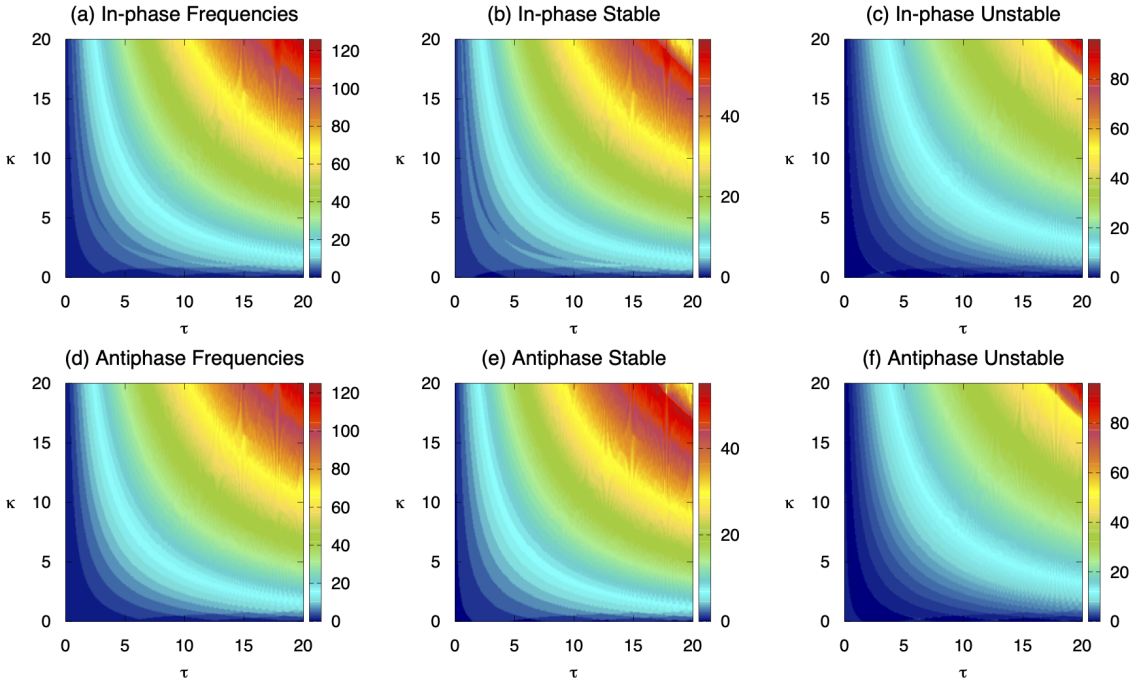

Figure 6.2: In-phase and antiphase locking-frequencies (colour bar corresponds to the number of possible frequencies at every point), $\rho = 0.0001$: (a) and (d) total locked frequencies, (b) and (e) stable locking frequencies, (c) and (f) unstable locking frequencies.

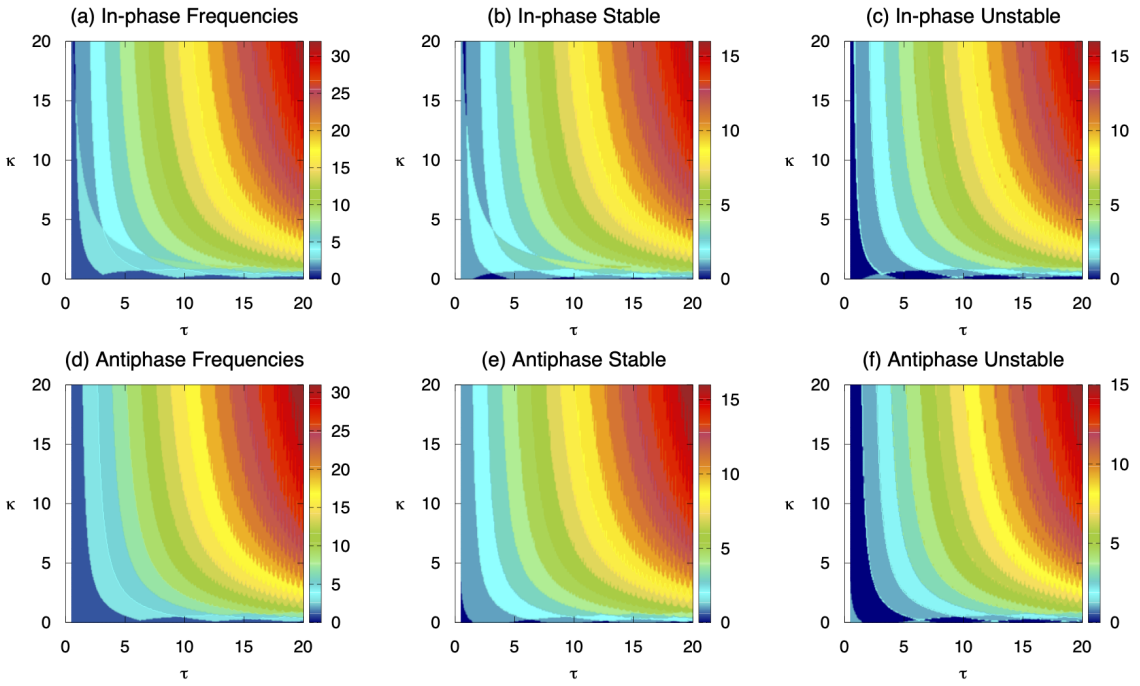

Figure 6.3: In-phase and antiphase locking-frequencies (colour bar corresponds to the number of possible frequencies at every point), $\rho = 0.5$: (a) and (d) total locked frequencies, (b) and (e) stable locking frequencies, (c) and (f) unstable locking frequencies.

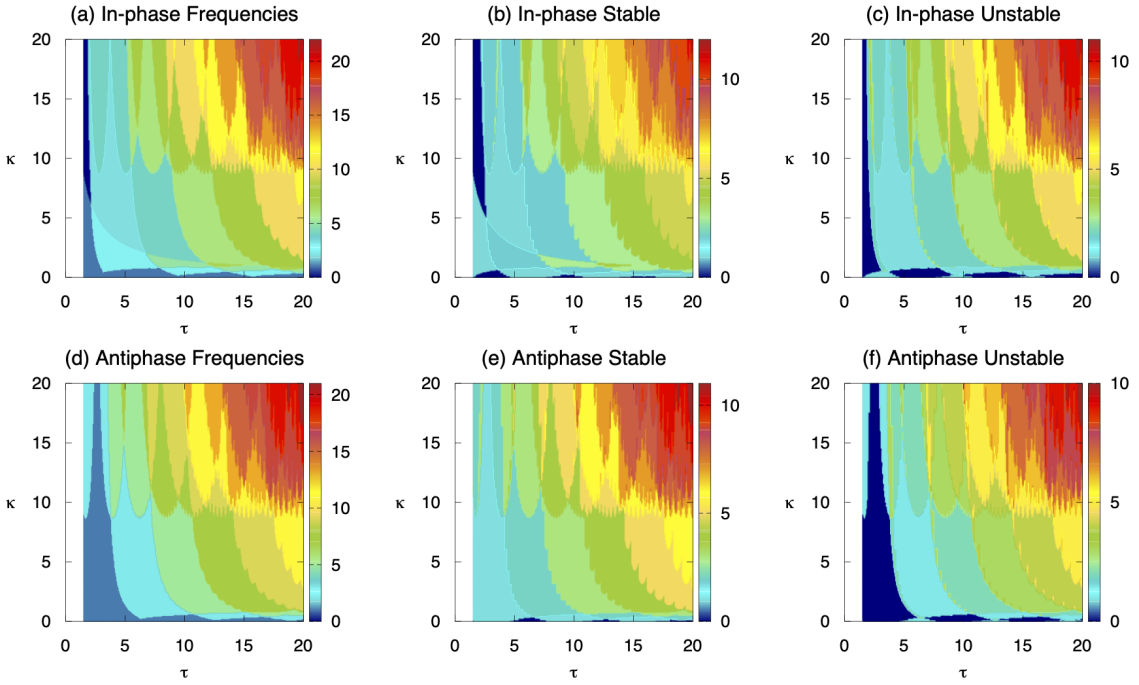

Figure 6.4: In-phase and antiphase locking-frequencies (colour bar corresponds to the number of possible frequencies at every point), $\rho = 1.5$: (a) and (d) total locked frequencies, (b) and (e) stable locking frequencies, (c) and (f) unstable locking frequencies.

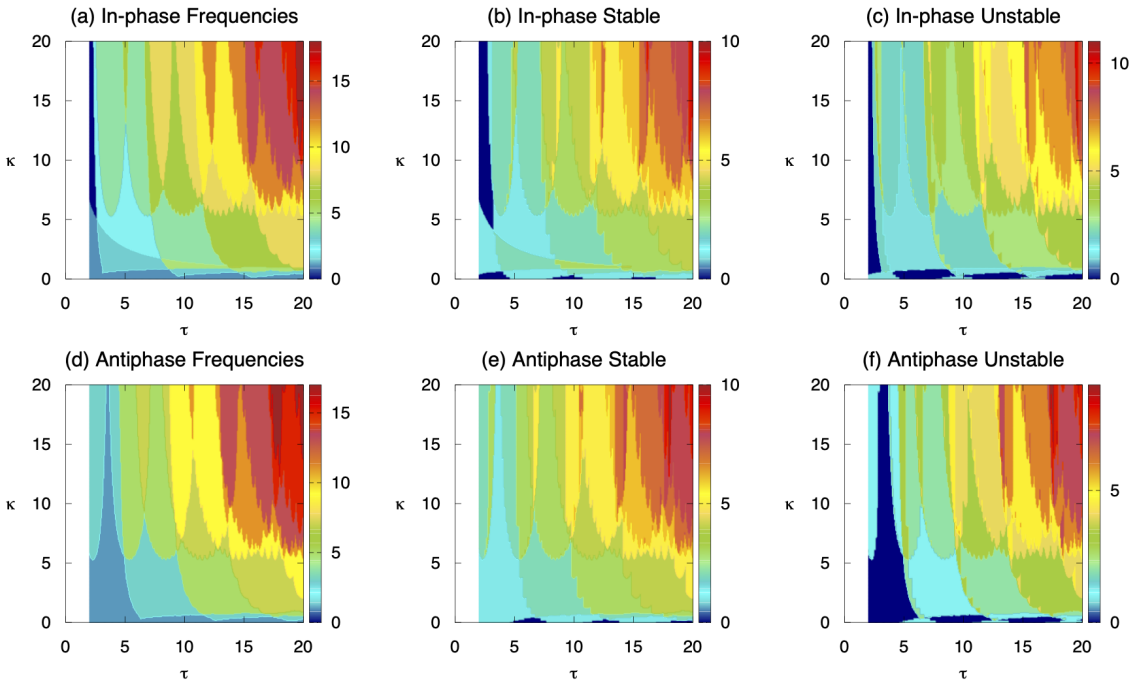

Figure 6.5: In-phase and antiphase locking-frequencies (colour bar corresponds to the number of possible frequencies at every point), $\rho = 2$: (a) and (d) total locked frequencies, (b) and (e) stable locking frequencies, (c) and (f) unstable locking frequencies.

6.3.2 Stability regions and corresponding locking frequencies

In Fig. 6.6, we again notice a rich framework of coexisting in-phase and antiphase stable solutions with different frequencies. Stable in-phase and antiphase solutions are alternating for small coupling strength κ; an increase in the coupling strength results in multistability, hence multistability is more prominent at higher values of τ and κ.

The increasing width of the distribution, ρ, has an effect on the dynamical behaviour of the stability regions, by increasing the regions where stable in-phase or antiphase solutions occur, in particular, increasing the range of values of the coupling strength κ where only one type of stable phase-locked solutions is observed. With increasing ρ the two states still alternate with respect to each other, however the stable in-phase and antiphase regions increase with increasing coupling strength.

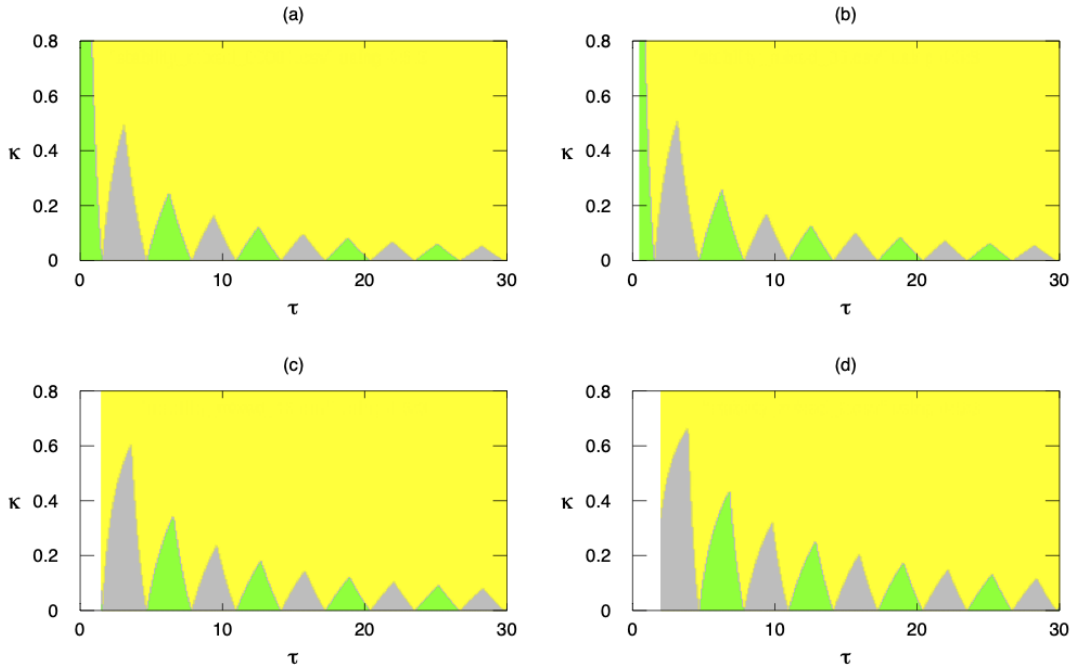

Figure 6.6: Stability regions of in-phase and antiphase solutions. Green: only in-phase solutions are stable, grey: only antiphase solutions are stable, yellow: in-phase and antiphase solutions coexist. (a) $\rho = 0.0001$, (b) $\rho = 0.5$, (c) $\rho = 1.5$, (d) $\rho = 2$.

In Figs. 6.7 and 6.8, we indicate by a colour code the total number of stable solutions for the same parameter range as demonstrated in Fig. 6.6, with varying width of the distribution ρ. A decreasing number of stable, in-phase and antiphase frequencies is observed, as ρ increases. Increasing the width of distribution ρ drives a decrease in the number of stable in-phase solutions and a slight increase in the number of stable antiphase solutions.

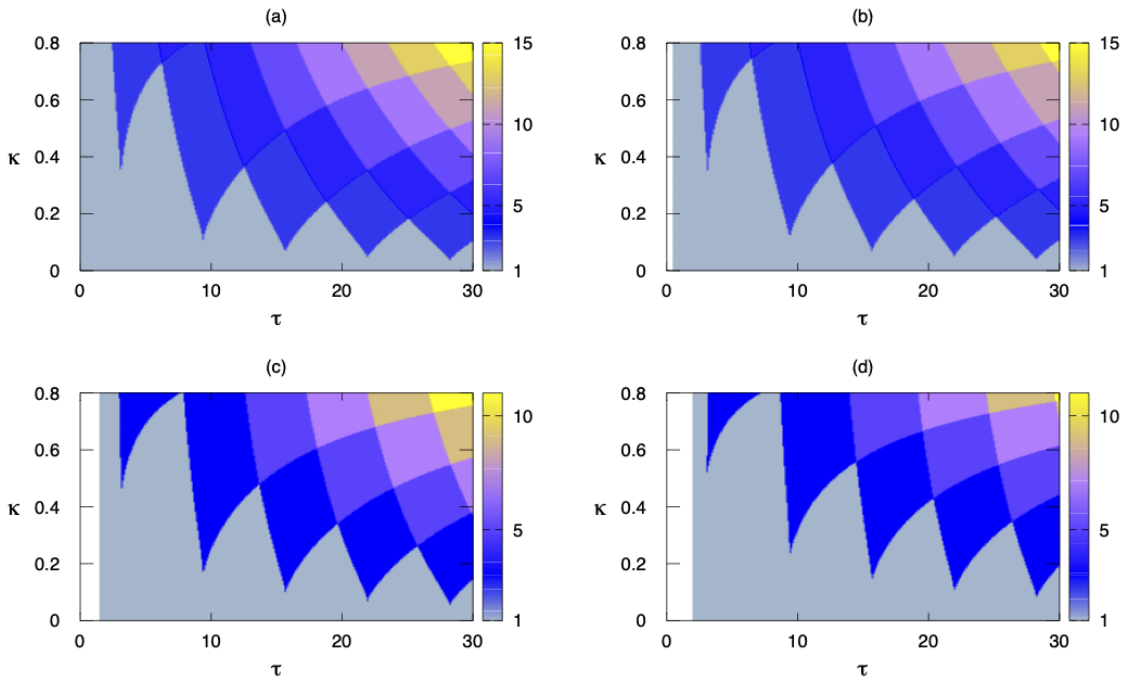

Figure 6.7: Total lock frequencies of stable in-phase solutions (colour bar corresponds to the number of possible frequencies at every point). (a) $\rho = 0.0001$, (b) $\rho = 0.5$, (c) $\rho = 1.5$, (d) $\rho = 2$.

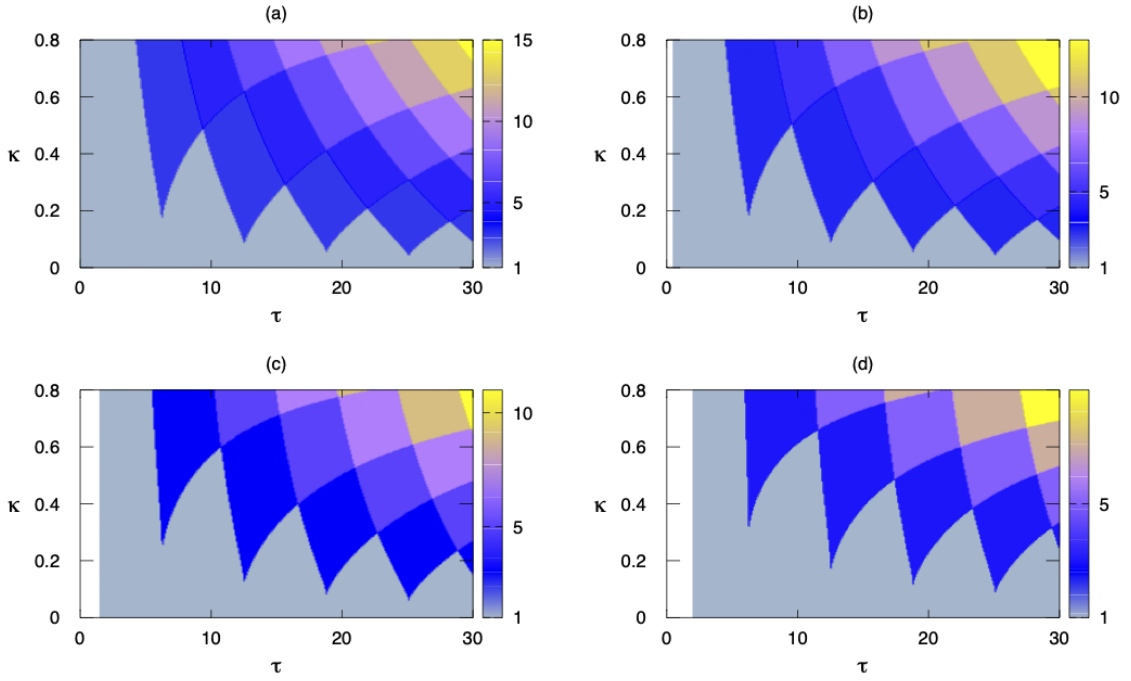

Figure 6.8: Total lock frequencies of stable antiphase solutions (colour bar corresponds to the number of possible frequencies at every point). (a) $\rho = 0.0001$, (b) $\rho = 0.5$, (c) $\rho = 1.5$, (d) $\rho = 2$.

6.3.3 Graphical determination of the locking frequencies

This section presents branches of stability and instability regions with varying mean time delay, τ, coupling strength, κ, and uniform distribution width, ρ. Stable and unstable solutions are represented by full and dashed lines, respectively. Blue solid line corresponds to stable in-phase solutions, green solid line to stable antiphase solutions, dashed magenta and red to unstable in-phase and antiphase solutions, respectively.

Fixed τ

In Figs. 6.9 and 6.10 for varying time delay τ, in-phase and antiphase states alternate for small distribution widths, $\rho = 0.0001$, $\rho = 0.5$, and for positive frequencies upper branches are stable. As we increase ρ, the branches of solutions for higher coupling strength, κ, start to disappear, and we notice a change in stability of in-phase and antiphase branches.

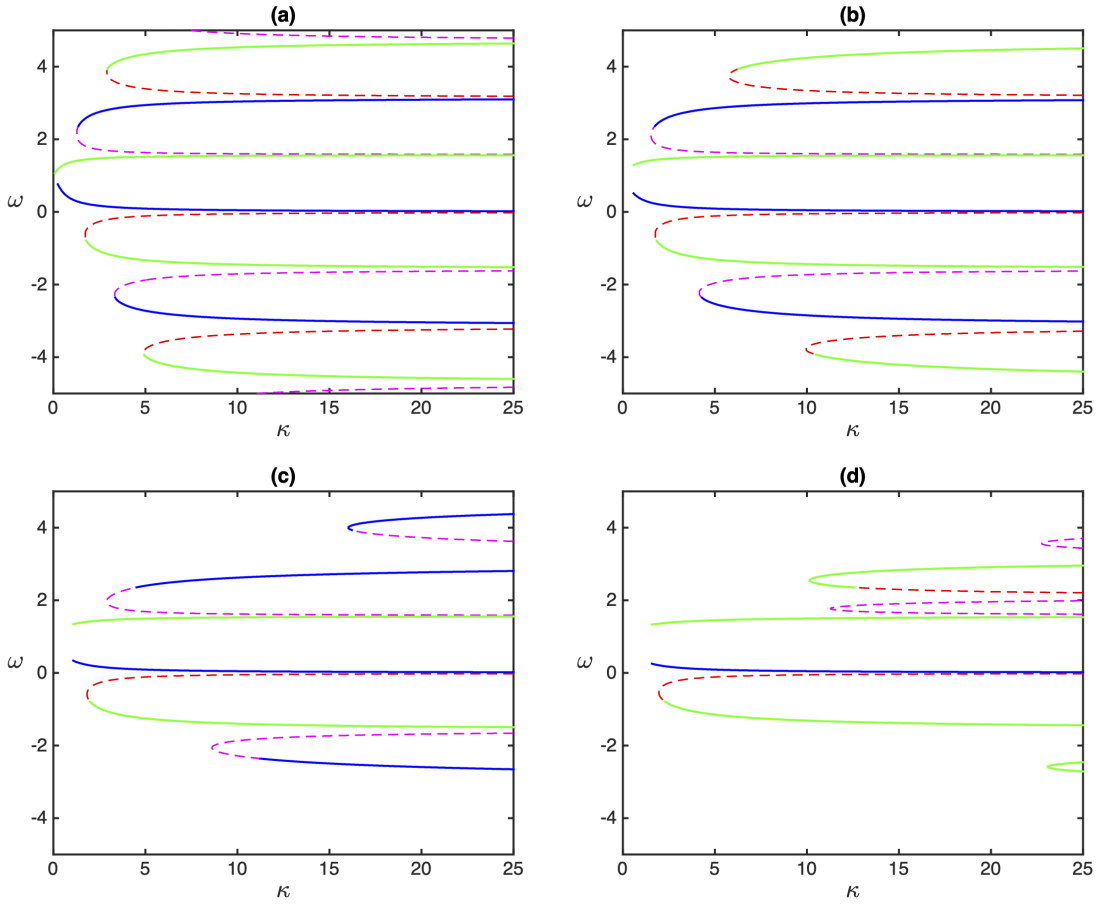

Figure 6.9: Blue solid: stable in-phase, green solid: stable antiphase, magenta dashed: unstable in-phase, red dashed: unstable antiphase. (a) $\tau = 2$, $\rho = 0.0001$, (b) $\tau = 2$, $\rho = 0.5$, (c) $\tau = 2$, $\rho = 1$, (d) $\tau = 2$, $\rho = 1.5$.

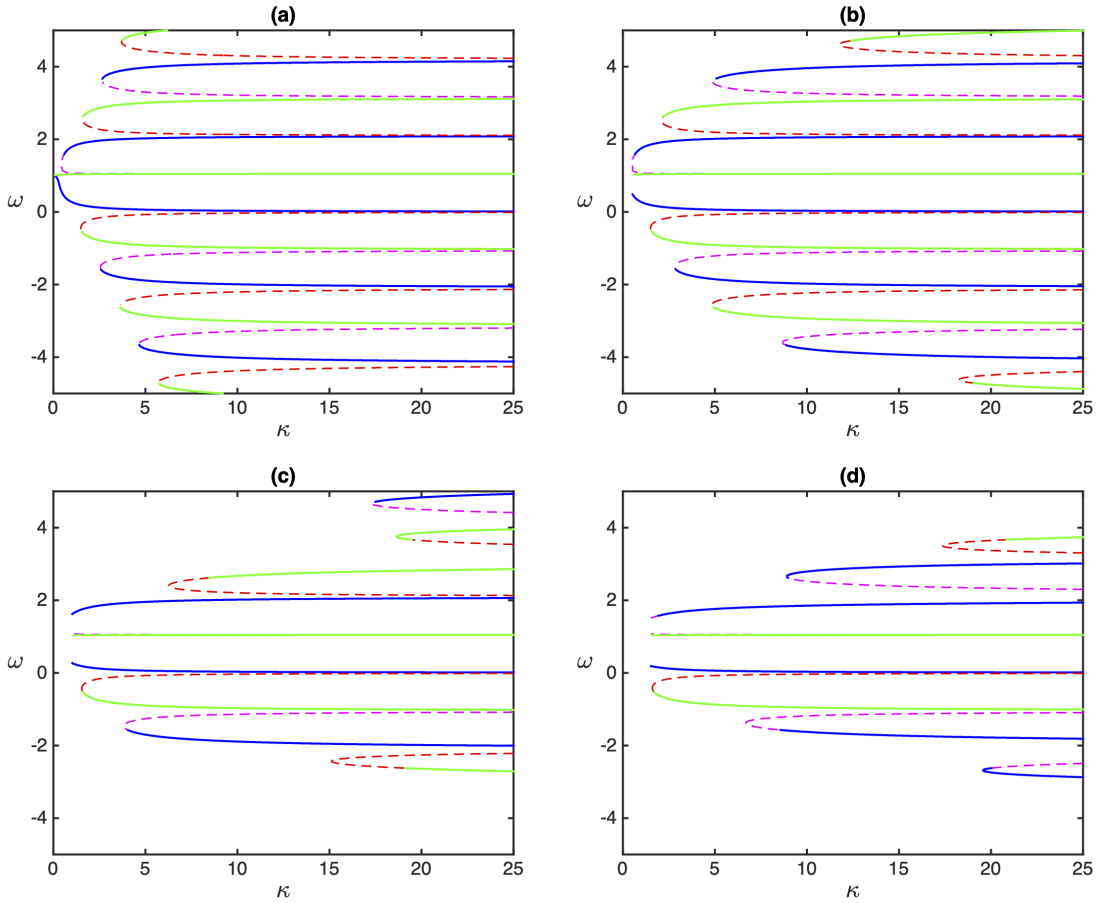

Figure 6.10: Blue solid: stable in-phase, green solid: stable antiphase, magenta dashed: unstable in-phase, red dashed: unstable antiphase. (a) $\tau = 3$, $\rho = 0.0001$, (b) $\tau = 3$, $\rho = 0.5$, (c) $\tau = 3$, $\rho = 1$, (d) $\tau = 3$, $\rho = 1.5$.

Further increasing ρ, with $\tau = 2$, leads to the loss of almost all stable in-phase solutions as shown in Fig. 6.9 (d). In contrast, for larger τ, stable in-phase branches persist even for rather large widths ρ, as is observed in Fig. 6.10 (d). In both of these figures, weaker coupling strength κ, and larger distribution width ρ, are associated with a reduction in the number of possible stable and unstable branches, together with a change in stability of in-phase and anti-phase branches.

Fixed κ

As can be seen in Figs. 6.11 and 6.12, there are multiple solutions for the collective frequency ω for sufficiently large values of the mean delay τ with repulsive coupling. Again, from Fig. 6.11 it is easy to see that there are lower ranges of τ where only a single frequency is stable, as well as higher ranges of τ where more than one frequency is stable.

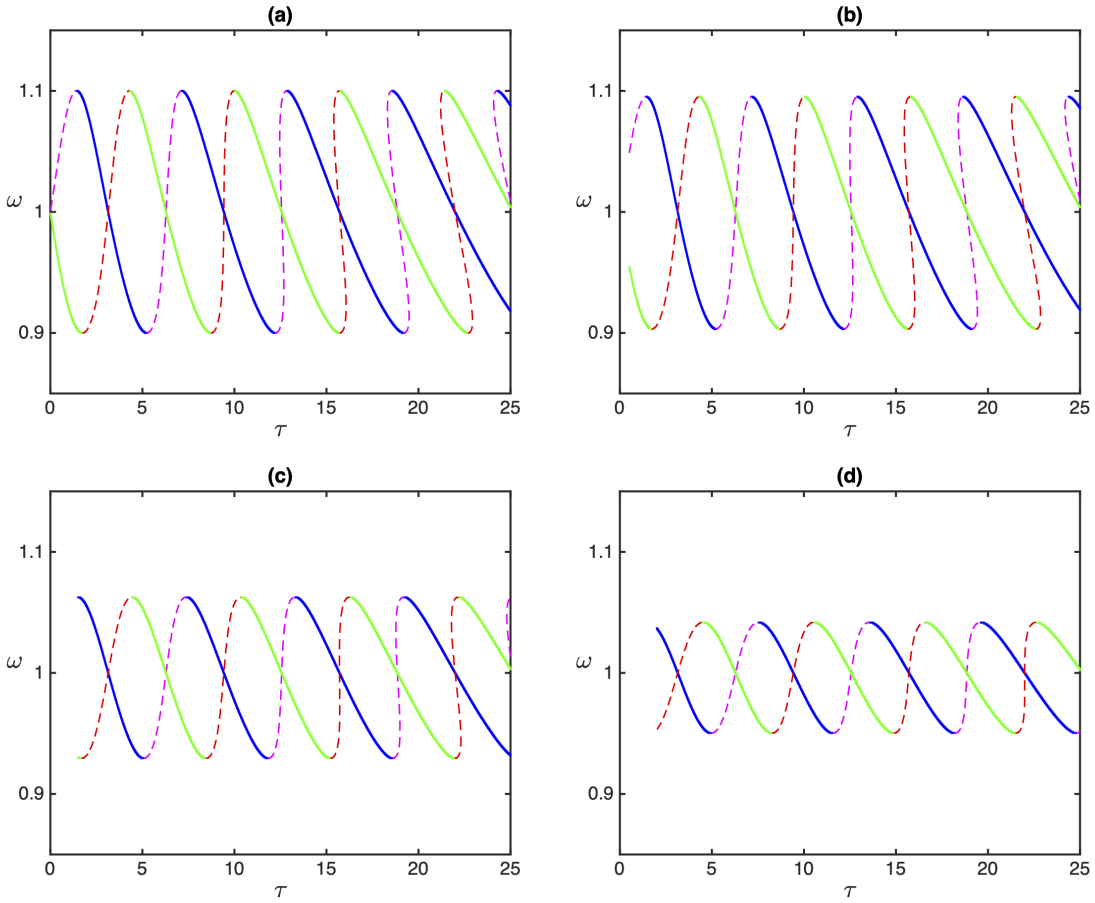

Figure 6.11: Blue solid: stable in-phase, green solid: stable antiphase, magenta dashed: unstable in-phase, red dashed: unstable antiphase. (a) $\kappa = -0.1$, $\rho = 0.0001$, (b) $\kappa = -0.1$, $\rho = 0.5$, (c) $\kappa = -0.1$, $\rho = 1.5$, (d) $\kappa = -0.1$, $\rho = 2$.

While only a single frequency is stable for smaller τ, as the value of τ increases, this leads to the emergence of several simultaneously stable frequencies. Fig. 6.12 highlights well that the overlapping multistable region increases with increasing value of coupling strength κ.

Comparison of Figs. 6.11 and 6.12 illustrates that the overlapping multistable region increases with increasing value of the coupling strength κ. At the same time, as we increase the width of the distribution, ρ, i.e., make the distribution broader, this narrows the spectrum of locking frequencies.

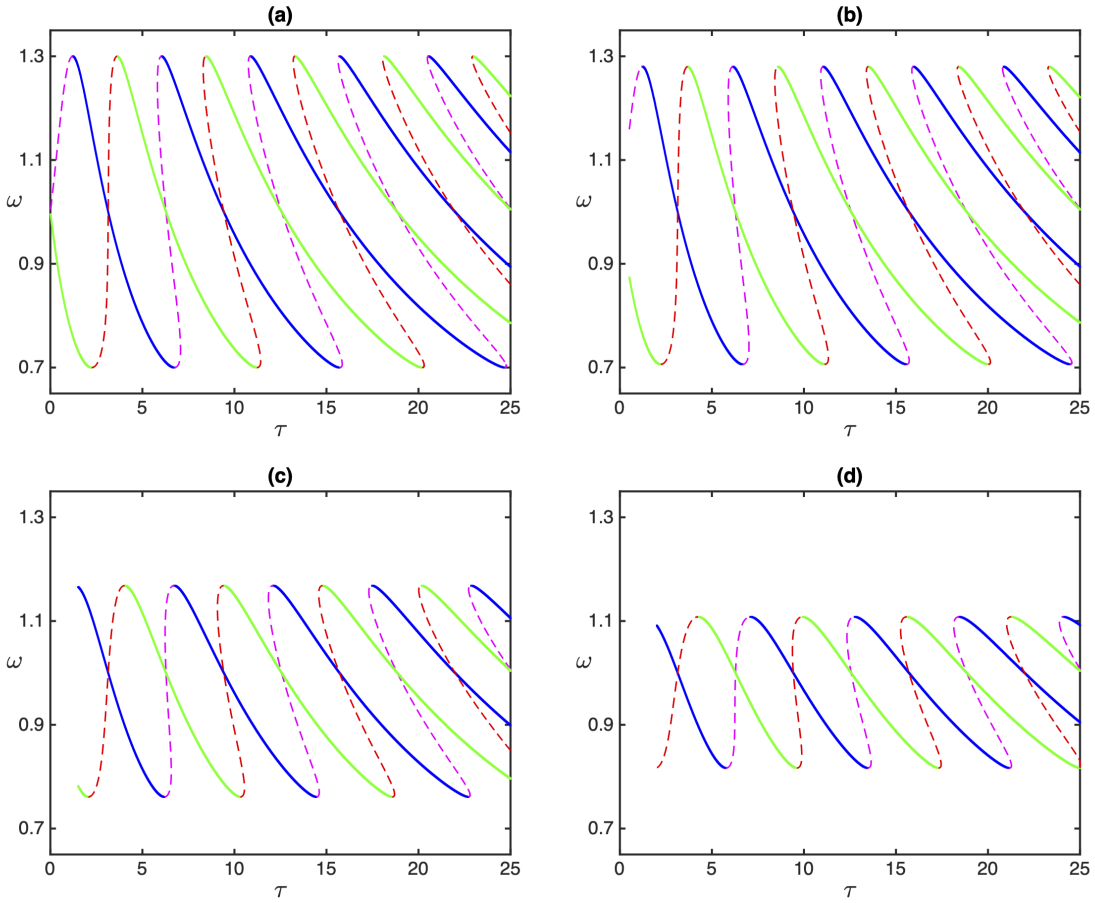

Figure 6.12: Blue solid: stable in-phase, green solid: stable antiphase, magenta dashed: unstable in-phase, red dashed: unstable antiphase. (a) $\kappa = -0.3$, $\rho = 0.0001$, (b) $\kappa = -0.3$, $\rho = 0.5$, (c) $\kappa = -0.3$, $\rho = 1.5$, (d) $\kappa = -0.3$, $\rho = 2$.

6.3.4 Numerical simulations for the uniform distribution kernel

We follow the same method as in the previous two chapters, by directly approximating the solution of the distributed delay system through the trapezoidal rule [49]. Making use of the trapezoidal quadrature formula (4.18) for the integrals, we obtain the in-phase equations as

$$\begin{aligned}
\dot{\phi}_1(t) =& \frac{\kappa}{2}\Big[\cos(\omega\tau_1)\phi_2(t-\tau_1) + \cos(\omega\tau_2)\phi_2(t-\tau_2)\Big] - \frac{\kappa}{2}\phi_1(t)\Big[\cos(\omega\tau_1) + \cos(\omega\tau_2)\Big], \\
\dot{\phi}_2(t) =& \frac{\kappa}{2}\Big[\cos(\omega\tau_1)\phi_1(t-\tau_1) + \cos(\omega\tau_2)\phi_1(t-\tau_2)\Big] - \frac{\kappa}{2}\phi_2(t)\Big[\cos(\omega\tau_1) + \cos(\omega\tau_2)\Big],
\end{aligned} \tag{6.13}$$

where $\tau_1 = \tau - \rho$ and $\tau_2 = \tau + \rho$. Similarly, for the antiphase we have

$$\begin{aligned}
\dot{\phi}_1(t) &= -\frac{\kappa}{2}\Big[\cos(\omega\tau_1)\phi_2(t-\tau_1) + \cos(\omega\tau_2)\phi_2(t-\tau_2)\Big] + \frac{\kappa}{2}\phi_1(t)\Big[\cos(\omega\tau_1) + \cos(\omega\tau_2)\Big], \\
\dot{\phi}_2(t) &= -\frac{\kappa}{2}\Big[\cos(\omega\tau_1)\phi_1(t-\tau_1) + \cos(\omega\tau_2)\phi_1(t-\tau_2)\Big] + \frac{\kappa}{2}\phi_2(t)\Big[\cos(\omega\tau_1) + \cos(\omega\tau_2)\Big],
\end{aligned} \tag{6.14}$$

where $\tau_1 = \tau - \rho$ and $\tau_2 = \tau + \rho$.

Simulations in Figs. 6.13 and 6.14 illustrate the stability of in-phase and antiphase locking frequencies of Systems (6.5) and (6.8) in different parameter regimes. We take the width of the distribution into account, to highlight the impact. Selected parameters are consistent with stability regions in Fig. 6.6.

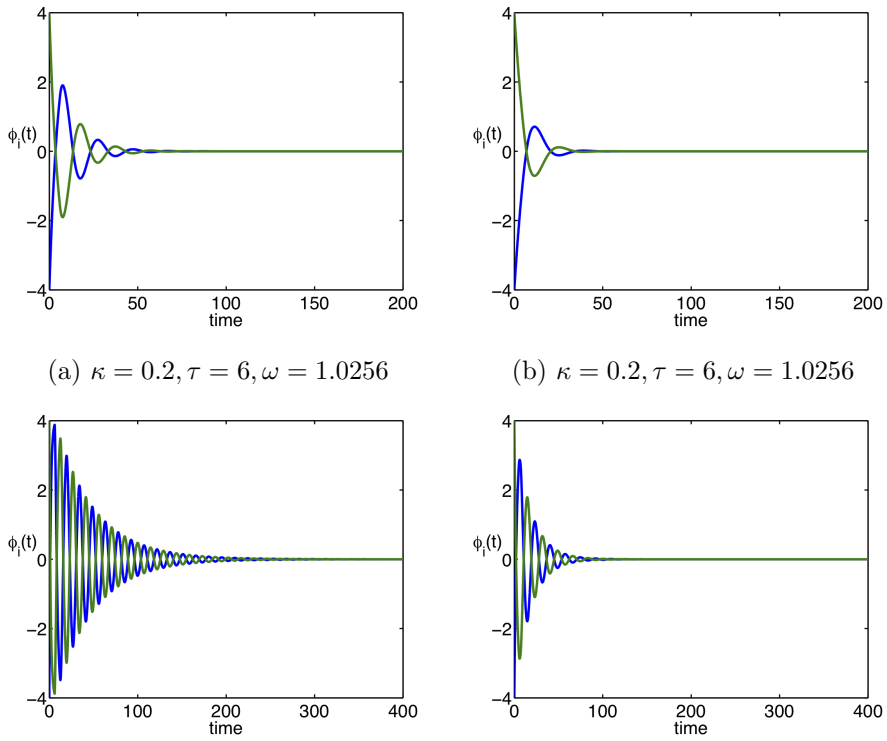

(a) $\kappa = 0.2, \tau = 6, \omega = 1.0256$ (b) $\kappa = 0.2, \tau = 6, \omega = 1.0256$

(c) $\kappa = 0.7, \tau = 6, \omega = 1.0381$ (d) $\kappa = 0.7, \tau = 6, \omega = 1.0381$

Figure 6.13: Solutions of System (6.13) for stable in-phase locking frequencies, (a) and (c) $\rho = 0.0001$, (b) and (d) $\rho = 1$.

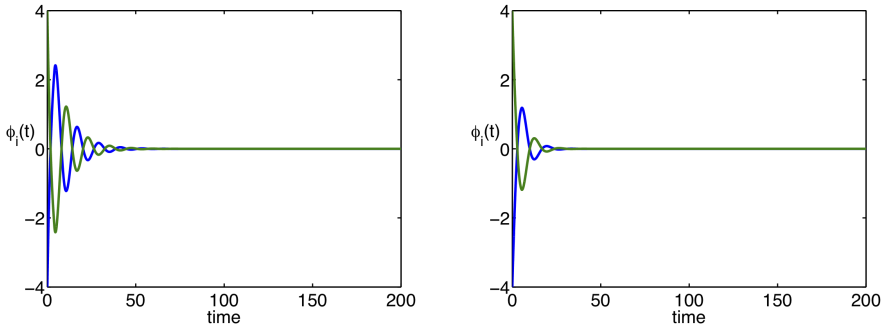

(a) $\kappa = 0.4, \tau = 4, \omega = 0.8689$

(b) $\kappa = 0.4, \tau = 4, \omega = 0.8689$

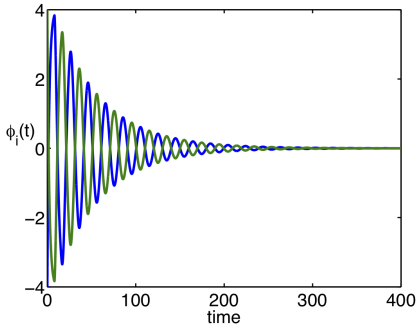

(c) $\kappa = 0.7, \tau = 8, \omega = 0.4938$

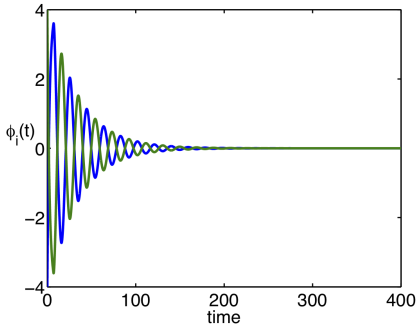

(d) $\kappa = 0.7, \tau = 8, \omega = 0.4938$

Figure 6.14: Solutions of System (6.14) for stable antiphase locking frequencies, (a) and (c) $\rho = 0.0001$, (b) and (d) $\rho = 1$.

6.4 Gamma distributed delay

6.4.1 Weak delay kernel

In this section, we consider the delay kernel with gamma distribution of order $p = 1$, hence $g(s) = \gamma e^{-\gamma s}$. We follow the same method as in Chapter 4, of employing the linear chain trick described in [98]. From (6.5) we have that,

$$a = \kappa \int_0^\infty \gamma e^{-\gamma s} \cos(\omega s) ds, \quad \text{hence} \quad G(s) = \frac{\gamma e^{-\gamma s} \cos(\omega s)}{\int_0^\infty \gamma e^{-\gamma s} \cos(\omega s) ds}. \tag{6.15}$$

Introducing new variables

$$\begin{aligned}
\phi_3(t) =& \frac{1}{b} \int_0^\infty \gamma e^{-\gamma s} \cos(\omega s) \phi_2(t-s) ds, \\
\phi_4(t) =& \frac{1}{b} \int_0^\infty \omega e^{-\gamma s} \sin(\omega s) \phi_2(t-s) ds, \\
\phi_5(t) =& \frac{1}{b} \int_0^\infty \gamma e^{-\gamma s} \cos(\omega s) \phi_1(t-s) ds, \\
\phi_6(t) =& \frac{1}{b} \int_0^\infty \omega e^{-\gamma s} \sin(\omega s) \phi_1(t-s) ds,
\end{aligned} \tag{6.16}$$

with $b = \int_0^\infty \gamma e^{-\gamma s}\cos(\omega s)ds$. Now, we have that System (6.5) can be rewritten as follows

$$\begin{aligned}
\dot{\phi_1}(t) &= a\big(\phi_3(t) - \phi_1(t)\big),\\
\dot{\phi_2}(t) &= a\big(\phi_5(t) - \phi_2(t)\big),\\
\dot{\phi_3}(t) &= \frac{1}{b}\int_0^\infty \gamma e^{-\gamma s}\cos(\omega s)\dot{\phi}_2(t-s)ds,
\end{aligned}$$

for $\dot{\phi}_3(t)$ we have, $\int_0^\infty \frac{d}{ds}\big(e^{-\gamma s}\cos(\omega s)\phi_2(t-s)\big)ds = -\phi_2(t)$, also

$$\begin{aligned}
\int_0^\infty \frac{d}{ds}\big(e^{-\gamma s}\cos(\omega s)\phi_2(t-s)\big)ds &= \int_0^\infty -\gamma e^{-\gamma s}\cos(\omega s)\phi_2(t-s)ds\\
&+ \int_0^\infty -\omega e^{-\gamma s}\sin(\omega s)\phi_2(t-s)ds + \int_0^\infty e^{-\gamma s}\cos(\omega s)\frac{d\phi_2(t-s)}{ds}ds\\
&= -\int_0^\infty \gamma e^{-\gamma s}\cos(\omega s)\phi_2(t-s)ds - \int_0^\infty \omega e^{-\gamma s}\sin(\omega s)\phi_2(t-s)ds\\
&- \int_0^\infty e^{-\gamma s}\cos(\omega s)\dot{\phi}_2(t-s)ds = -b\phi_3(t) - b\phi_4(t) - \frac{b}{\gamma}\dot{\phi}_3(t),
\end{aligned}$$

combining the two, we get $\dot{\phi}_3(t) = \frac{\gamma}{b}\phi_2(t) - \gamma\phi_3(t) - \gamma\phi_4(t)$. Similarly for $\dot{\phi}_4(t)$, we have

$$\begin{aligned}
&\dot{\phi}_4(t) = \frac{1}{b}\int_0^\infty \omega e^{-\gamma s}\sin(\omega s)\dot{\phi}_2(t-s)ds, \text{ where } \int_0^\infty \frac{d}{ds}\big(e^{-\gamma s}\sin(\omega s)\phi_2(t-s)\big)ds = 0,\\
&\text{also, } \int_0^\infty \frac{d}{ds}\big(e^{-\gamma s}\sin(\omega s)\phi_2(t-s)\big)ds = \int_0^\infty -\gamma e^{-\gamma s}\sin(\omega s)\phi_2(t-s)ds\\
&\quad + \int_0^\infty \omega e^{-\gamma s}\cos(\omega s)\phi_2(t-s)ds - \int_0^\infty e^{-\gamma s}\sin(\omega s)\dot{\phi}_2(t-s)ds,
\end{aligned}$$

combining the two, we get $\dot{\phi}_4(t) = -\gamma\phi_4(t) + \frac{\omega^2}{\gamma^2}\phi_3(t)$. We follow the same approach for $\dot{\phi}_5(t)$ and $\dot{\phi}_6(t)$, hence, the new system of equations for in-phase solutions is

$$\begin{aligned}
\dot{\phi_1}(t) &= a\big(\phi_3(t) - \phi_1(t)\big),\\
\dot{\phi_2}(t) &= a\big(\phi_5(t) - \phi_2(t)\big),\\
\dot{\phi_3}(t) &= \frac{\gamma}{b}\phi_2(t) - \gamma\phi_3(t) - \gamma\phi_4(t),\\
\dot{\phi_4}(t) &= -\gamma\phi_4(t) + \frac{\omega^2}{\gamma^2}\phi_3(t),\\
\dot{\phi_5}(t) &= \frac{\gamma}{b}\phi_1(t) - \gamma\phi_5(t) - \gamma\phi_6(t),\\
\dot{\phi_6}(t) &= -\gamma\phi_6(t) + \frac{\omega^2}{\gamma^2}\phi_5(t).
\end{aligned} \tag{6.17}$$

Similarly, for antiphase we have

$$\begin{aligned}
\dot{\phi}_1(t) &= a\big(-\phi_3(t)+\phi_1(t)\big),\\
\dot{\phi}_2(t) &= a\big(-\phi_5(t)+\phi_2(t)\big),\\
\dot{\phi}_3(t) &= \frac{\gamma}{b}\phi_2(t)-\gamma\phi_3(t)-\gamma\phi_4(t),\\
\dot{\phi}_4(t) &= -\gamma\phi_4(t)+\frac{\omega^2}{\gamma^2}\phi_3(t),\\
\dot{\phi}_5(t) &= \frac{\gamma}{b}\phi_1(t)-\gamma\phi_5(t)-\gamma\phi_6(t),\\
\dot{\phi}_6(t) &= -\gamma\phi_6(t)+\frac{\omega^2}{\gamma^2}\phi_5(t),
\end{aligned} \tag{6.18}$$

with $b=\displaystyle\int_0^\infty \gamma e^{-\gamma s}\cos(\omega s)ds=\frac{\gamma^2}{\gamma^2+\omega^2}$, and $a=\kappa\displaystyle\int_0^\infty \gamma e^{-\gamma s}\cos(\omega s)ds=\frac{\kappa\gamma^2}{\gamma^2+\omega^2}$.

In-phase and antiphase characteristic equations

Equations (1.18) and (1.20), with $g(s)=\gamma e^{-\gamma s}$ and $a=\dfrac{\kappa\gamma^2}{\gamma^2+\omega^2}$, hence $G(s)=\dfrac{\gamma^2+\omega^2}{\gamma}e^{-\gamma s}\cos(\omega s)$ with $\{\mathcal{L}G\}(\lambda)=\dfrac{\lambda+\gamma}{\omega^2+(\lambda+\gamma)^2}$ transform the in-phase characteristic equation (6.6), to the following

$$\begin{aligned}
&\Big[\lambda\big(\gamma^2+\omega^2\big)\big(\omega^2+(\lambda+\gamma)^2\big)+\kappa\gamma^2\big(\omega^2+(\lambda+\gamma)^2\big)+\kappa\gamma^2\Big]\\
&\qquad\times\Big[\lambda\big(\gamma^2+\omega^2\big)\big(\omega^2+(\lambda+\gamma)^2\big)+\kappa\gamma^2\big(\omega^2+(\lambda+\gamma)^2\big)-\kappa\gamma^2\Big]=0,
\end{aligned} \tag{6.19}$$

similarly from (6.9) we have that the antiphase characteristic equation is of the form

$$\begin{aligned}
&\Big[\lambda\big(\gamma^2+\omega^2\big)\big(\omega^2+(\lambda+\gamma)^2\big)-\kappa\gamma^2\big(\omega^2+(\lambda+\gamma)^2\big)+\kappa\gamma^2\Big]\\
&\qquad\times\Big[\lambda\big(\gamma^2+\omega^2\big)\big(\omega^2+(\lambda+\gamma)^2\big)-\kappa\gamma^2\big(\omega^2+(\lambda+\gamma)^2\big)-\kappa\gamma^2\Big]=0.
\end{aligned} \tag{6.20}$$

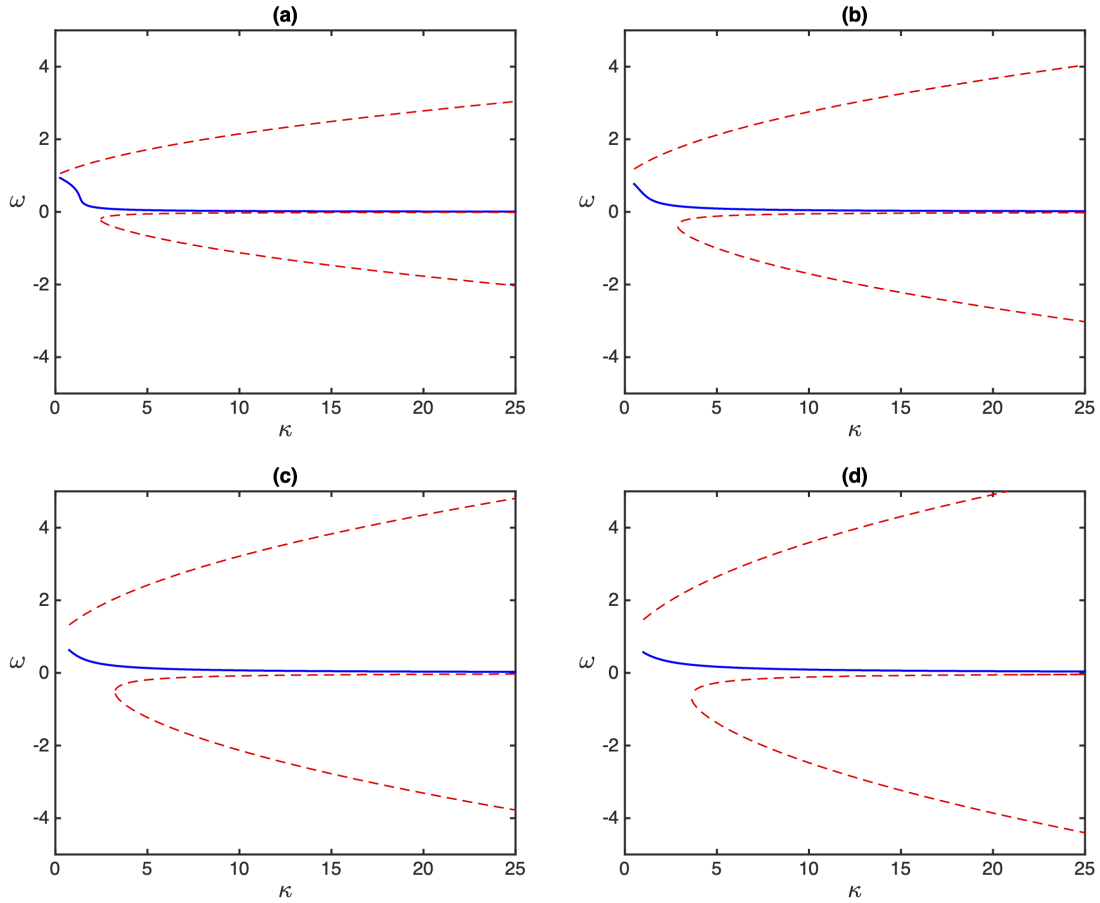

Figure 6.15: Blue solid: stable in-phase, red dashed: unstable antiphase. (a) $\gamma = 0.25$, (b) $\gamma = 0.5$, (c) $\gamma = 0.75$, (d) $\gamma = 1$.

Fig. 6.15 shows that in the case of weak gamma distributed kernel, only in-phase solutions are stable, and all antiphase solutions are unstable, independently of the coupling strength κ and the values of γ, which is completely different to the case of the same distribution kernel considered in Chapter 4. Increasing the parameter γ, i.e., reducing the mean time delay, leads to an increase in the range of locking frequencies ω, where neither in-phase nor antiphase solutions are found for sufficiently small coupling strengths.

6.4.2 Strong delay kernel

In this section, we consider System (6.4) the delay kernel with gamma distribution of order $p = 2$, hence $g(s) = \gamma^2 s e^{-\gamma s}$. Similarly to the weak delay kernel case from (6.5) we have for the in-phase system that,

$$a = \kappa\gamma^2 \int_0^\infty s e^{-\gamma s}\cos(\omega s)ds = \frac{\kappa\gamma^2(\gamma^2-\omega^2)}{(\gamma^2+\omega^2)^2}, \text{ hence } G(s) = \frac{1}{b}\gamma^2 s e^{-\gamma s}\cos(\omega s),$$

where $b = \int_0^\infty g(s)\cos(\omega s)ds$. Introducing new variables

$$\begin{aligned}
\phi_3(t) =& \frac{1}{b}\int_0^\infty \gamma e^{-\gamma s}\cos(\omega s)\phi_2(t-s)ds,\\
\phi_4(t) =& \frac{1}{b}\int_0^\infty \omega e^{-\gamma s}\sin(\omega s)\phi_2(t-s)ds,\\
\phi_5(t) =& \frac{1}{b}\int_0^\infty \gamma^2 s e^{-\gamma s}\cos(\omega s)\phi_2(t-s)ds,\\
\phi_6(t) =& \frac{1}{b}\int_0^\infty \omega s e^{-\gamma s}\sin(\omega s)\phi_2(t-s)ds,\\
\phi_7(t) =& \frac{1}{b}\int_0^\infty \gamma e^{-\gamma s}\cos(\omega s)\phi_1(t-s)ds,\\
\phi_8(t) =& \frac{1}{b}\int_0^\infty \omega e^{-\gamma s}\sin(\omega s)\phi_1(t-s)ds,\\
\phi_9(t) =& \frac{1}{b}\int_0^\infty \gamma^2 s e^{-\gamma s}\cos(\omega s)\phi_1(t-s)ds,\\
\phi_{10}(t) =& \frac{1}{b}\int_0^\infty \omega s e^{-\gamma s}\sin(\omega s)\phi_2(t-s)ds,
\end{aligned} \tag{6.21}$$

with $b = \int_0^\infty \gamma^2 s e^{-\gamma s}\cos(\omega s)ds$. For $\dot{\phi}_5(t) = \frac{1}{b}\int_0^\infty \gamma^2 s e^{-\gamma s}\cos(\omega s)\dot{\phi}_2(t-s)ds$, we have that

$$\begin{aligned}
&\int_0^\infty \frac{d}{ds}(s e^{-\gamma s}\cos(\omega s)\phi_2(t-s))ds = 0, \quad \text{also}\\
&\int_0^\infty \frac{d}{ds}(s e^{-\gamma s}\cos(\omega s)\phi_2(t-s))ds = \int_0^\infty e^{-\gamma s}\cos(\omega s)\phi_2(t-s)ds\\
&\quad + \int_0^\infty -\gamma s e^{-\gamma s}\cos(\omega s)\phi_2(t-s)ds + \int_0^\infty -\omega s e^{-\gamma s}\sin(\omega s)\phi_2(t-s)ds\\
&\quad - \int_0^\infty s e^{-\gamma s}\cos(\omega s)\dot{\phi}_2(t-s)ds,
\end{aligned}$$

combining the two we get $\dot{\phi}_5(t) = \gamma\phi_3(t) - \gamma\phi_5(t) - \gamma^2\phi_6(t)$. Now, for $\dot{\phi}_6(t)$, we have

$$\begin{aligned}
&\dot{\phi}_6(t) = \frac{1}{b}\int_0^\infty \omega s e^{-\gamma s}\sin(\omega s)\dot{\phi}_2(t-s)ds, \text{ where}\\
&\int_0^\infty \frac{d}{ds}(s e^{-\gamma s}\sin(\omega s)\phi_2(t-s))ds = 0, \quad \text{also}\\
&\int_0^\infty \frac{d}{ds}(s e^{-\gamma s}\sin(\omega s)\phi_2(t-s))ds = \int_0^\infty e^{-\gamma s}\sin(\omega s)\phi_2(t-s)ds\\
&\quad + \int_0^\infty -\gamma s e^{-\gamma s}\sin(\omega s)\phi_2(t-s)ds + \int_0^\infty -\omega s e^{-\gamma s}\cos(\omega s)\phi_2(t-s)ds\\
&\quad - \int_0^\infty s e^{-\gamma s}\sin(\omega s)\dot{\phi}_2(t-s)ds,
\end{aligned}$$

again, combining the above we get $\dot{\phi}_6(t) = \gamma\phi_4(t) - \gamma\phi_6(t) + \frac{\omega^2}{\gamma^2}\phi_5(t)$. Now, we have that System (6.4) can be rewritten as follows

$$
\begin{aligned}
\dot{\phi}_1(t) &= a\big(\phi_5(t) - \phi_1(t)\big),\\
\dot{\phi}_2(t) &= a\big(\phi_9(t) - \phi_2(t)\big),\\
\dot{\phi}_3(t) &= \frac{\gamma}{b}\phi_2(t) - \gamma\phi_3(t) - \gamma\phi_4(t),\\
\dot{\phi}_4(t) &= -\gamma\phi_4(t) + \frac{\omega^2}{\gamma^2}\phi_3(t),\\
\dot{\phi}_5(t) &= \gamma\phi_3(t) - \gamma\phi_5(t) - \gamma^2\phi_6(t),\\
\dot{\phi}_6(t) &= \gamma\phi_4(t) - \gamma\phi_6(t) + \frac{\omega^2}{\gamma^2}\phi_5(t),\\
\dot{\phi}_7(t) &= \frac{\gamma}{b}\phi_1(t) - \gamma\phi_7(t) - \gamma\phi_8(t),\\
\dot{\phi}_8(t) &= -\gamma\phi_8(t) + \frac{\omega^2}{\gamma^2}\phi_7(t),\\
\dot{\phi}_9(t) &= \gamma\phi_7(t) - \gamma\phi_9(t) - \gamma^2\phi_{10}(t),\\
\dot{\phi}_{10}(t) &= \gamma\phi_8(t) - \gamma\phi_{10}(t) + \frac{\omega^2}{\gamma^2}\phi_9(t).
\end{aligned}
\tag{6.22}
$$

Similarly, for strong gamma antiphase, we have that the system can be written as

$$
\begin{aligned}
\dot{\phi}_1(t) &= a\big(-\phi_5(t) + \phi_1(t)\big),\\
\dot{\phi}_2(t) &= a\big(-\phi_9(t) + \phi_2(t)\big),\\
\dot{\phi}_3(t) &= \frac{\gamma}{b}\phi_2(t) - \gamma\phi_3(t) - \gamma\phi_4(t),\\
\dot{\phi}_4(t) &= -\gamma\phi_4(t) + \frac{\omega^2}{\gamma^2}\phi_3(t),\\
\dot{\phi}_5(t) &= \gamma\phi_3(t) - \gamma\phi_5(t) - \gamma^2\phi_6(t),\\
\dot{\phi}_6(t) &= \gamma\phi_4(t) - \gamma\phi_6(t) + \frac{\omega^2}{\gamma^2}\phi_5(t),\\
\dot{\phi}_7(t) &= \frac{\gamma}{b}\phi_1(t) - \gamma\phi_7(t) - \gamma\phi_8(t),\\
\dot{\phi}_8(t) &= -\gamma\phi_8(t) + \frac{\omega^2}{\gamma^2}\phi_7(t),\\
\dot{\phi}_9(t) &= \gamma\phi_7(t) - \gamma\phi_9(t) - \gamma^2\phi_{10}(t),\\
\dot{\phi}_{10}(t) &= \gamma\phi_8(t) - \gamma\phi_{10}(t) + \frac{\omega^2}{\gamma^2}\phi_9(t).
\end{aligned}
\tag{6.23}
$$

In-phase and antiphase characteristic equations

Equations (1.18) and (1.20), with $g(s) = \gamma^2 s e^{-\gamma s}$ and $a = \dfrac{\kappa\gamma^2(\gamma^2-\omega^2)}{(\gamma^2+\omega^2)^2}$, hence $G(s) = \dfrac{(\gamma^2+\omega^2)^2}{(\gamma^2-\omega^2)} s e^{-\gamma s}\cos(\omega s)$, with

$$
\{\mathcal{L}G\}(\lambda) = \frac{d}{d\lambda}\left(\frac{(\lambda^2+\omega^2)^2}{\gamma^2-\omega^2}\frac{\lambda+\gamma}{\omega^2+(\lambda+\gamma)^2}\right) = -\frac{(\gamma^2+\omega^2)^2}{\gamma^2-\omega^2}\frac{\omega^2-(\lambda+\gamma)^2}{(\omega^2+(\lambda+\gamma)^2)^2},
$$

transform the in-phase characteristic equation (6.6), to the following

$$\begin{aligned}&\Big[\lambda(\gamma^2+\omega^2)^2+\kappa\gamma^2(\gamma^2-\omega^2)+\kappa\gamma^2(\gamma^2-\omega^2)\{\mathcal{L}G\}(\lambda)\Big]\\&\quad\times\Big[\lambda(\gamma^2+\omega^2)^2+\kappa\gamma^2(\gamma^2-\omega^2)-\kappa\gamma^2(\gamma^2-\omega^2)\{\mathcal{L}G\}(\lambda)\Big]=0,\end{aligned}\tag{6.24}$$

similarly from (6.9) we have that the antiphase characteristic equation is of the form

$$\begin{aligned}&\Big[\lambda(\gamma^2+\omega^2)^2-\kappa\gamma^2(\gamma^2-\omega^2)+\kappa\gamma^2(\gamma^2-\omega^2)\{\mathcal{L}G\}(\lambda)\Big]\\&\quad\times\Big[\lambda(\gamma^2+\omega^2)^2-\kappa\gamma^2(\gamma^2-\omega^2)-\kappa\gamma^2(\gamma^2-\omega^2)\{\mathcal{L}G\}(\lambda)\Big]=0.\end{aligned}\tag{6.25}$$

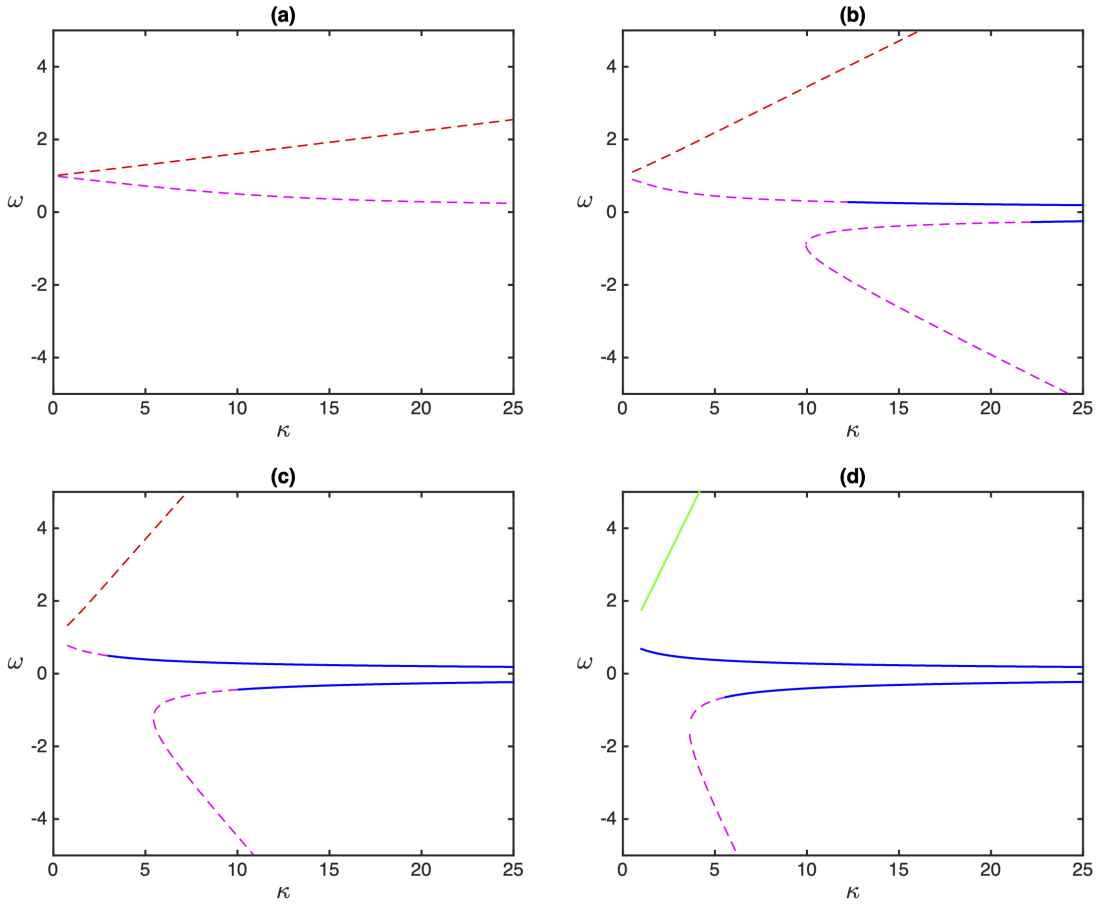

Figure 6.16: Blue solid: stable in-phase, green solid: stable antiphase, magenta dashed: unstable in-phase, red dashed: unstable antiphase. (a) $\gamma = 0.25$, (b) $\gamma = 0.5$, (c) $\gamma = 0.75$, (d) $\gamma = 1$.

Fig. 6.16 illustrates the branches of stable and unstable in-phase and anti-phase solutions in the case of strong gamma distribution for increasing values of γ. For small values of γ, all branches of phase-locked solutions are unstable for any values of κ, but as γ is

increased, for large enough values of the coupling strength κ, in Fig. 6.16 (b), there appear branches of stable in-phase solutions. A further increase in γ allows for the stable in-phase solutions to exist for weaker coupling κ, and for very large γ, an antiphase solution also gets stabilised for a sufficiently weak coupling strength and large enough locking frequency ω.

6.4.3 Numerical simulations for gamma distributed delay

In this section, we numerically solve the ODE systems (6.17), (6.18), (6.22), (6.23), obtained after employing the linear chain trick on Systems (6.5) and (6.8). Simulations in Fig. 6.17, illustrate the stability of in-phase locking frequencies of System (6.5) for weak delay kernel in different parameter regimes. Simulations in Fig. 6.18 illustrate the frequency stability of Systems (6.5) and (6.8) for strong delay kernel in different parameter regimes, in-phase and antiphase, respectively.

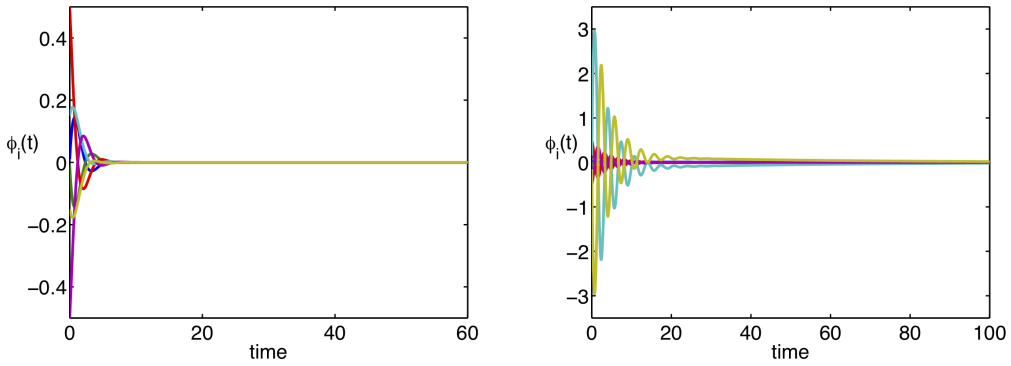

(a) $\kappa = 1.25, \gamma = 0.75, \omega = 0.52026$ (b) $\kappa = 0.25, \gamma = 0.25, \omega = 0.93547$

Figure 6.17: Solutions of Systems (6.17) for stable in-phase locking frequencies, weak delay kernel.

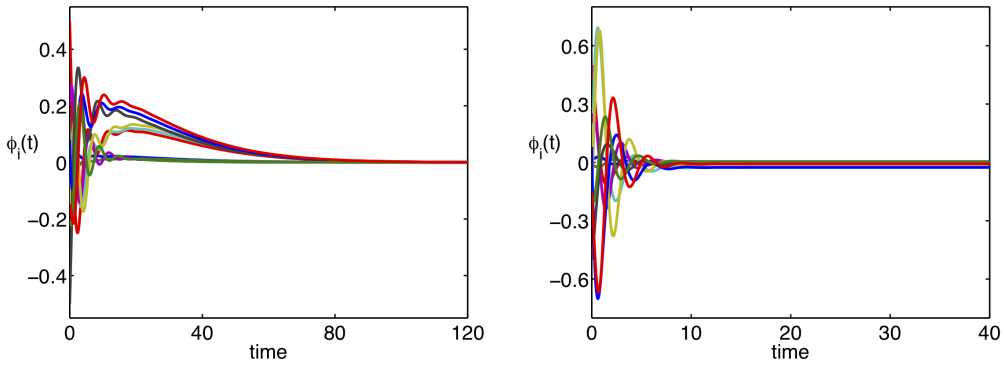

(a) $\kappa = 1.3, \gamma = 0.75, \omega = 0.67534$ (b) $\kappa = 1.5, \gamma = 1, \omega = 2.2911$

Figure 6.18: Solutions of Systems (6.22) and (6.23) for stable (a) in-phase, and (b) anti-phase locking frequencies, strong delay kernel.

6.5 Summary

In this chapter, we considered the case of two mutually coupled Kuramoto oscillators, where the distribution is taken outside of the coupling function. In this case, the distribution does have an effect on the constant frequency solutions. For a uniform distribution, the width of the distribution modulates the effective coupling strength, and for a suitable choice of parameters the delay distribution can make the coupling vanish or reverse the coupling phase. The results indicate that having the distribution outside the coupling function does play a role in terms of both existence, as well as stability of phase-locked solutions. Moreover, not only the mean time delay, but also the type of distribution kernel is an important factor in determining when/whether such solutions exist and are stable.

Chapter 7

Overview

Blockchain technology is in many ways similar to networks. The structure of Blockchain itself is a type of network as the topology is a chain, with each node (block) linked to the next in a linear sequence, with the first and last nodes (blocks) having just one link and the rest having two links. Additionally, the miners/users of Blockchain are connected to one another in a decentralised, P2P network; each miner/user can be represented as a node in the network. Depicting Blockchain/cryptocurrencies as networks and analysing their characteristics is an area that would benefit from further exploration.

In Chapters 4-6, we look at coupled oscillators. We first consider two phase oscillators with distributed delay, and investigate the solutions with constant frequency. In Chapters 4 and 5, we consider a typical implementation of the delay distribution. Implementing in-phase and antiphase synchronous states, we find transcendental equations for the locking frequencies ω. For uniform and gamma distribution kernels we look at stability regions. In this case, the solutions themselves are the same as for a constant delay (equal to the mean delay).

In Chapter 6, we introduce the new formulation of the system of delay coupled phase oscillators with distributed delays and investigated phase-locked solutions of uniform and gamma delay distribution kernels. We find that the distributed delay has an effect on the constant frequency solutions, by narrowing the spectrum of locking frequencies.

We paid attention to identical individual elements, as our interest was in symmetry networks, as well as the effect of distributed delays on the stability regions. Potential progression of this work could include extensions to other network topologies, such as unidirectional and bidirectional rings, as well as inclusion of parameter mismatch.

Appendix A

Appendix (Chapter 2)

A.1 Parameter sweep method

Table A.1: Bitcoin, parameter sweep values

	1	2	3
β	1.167	0.8	1.8
v	0.709	0.333	0.167
α	0.003	0.003	0.003
μ	0.003	0.006	0.004

Table A.2: Litecoin, parameter sweep values

	1	2	3
β	0.45	1.5	2.1
v	0.974	0.8	0.125
α	0.202	0.004	0.001
μ	0.003	0.00004	0.001

Table A.3: Mastercoin, parameter sweep values

	1	2	3
β	0.5	0.825	0.625
v	0.739	0.75	0.425
α	0.401	0.0015	0.001
μ	0.202	0.005	0.001

Table A.4: Peercoin, parameter sweep values

	1	2	3
β	0.5	1.3	0.65
v	0.358	1.1	0.4
α	0.003	0.02	0.001
μ	0.202	0.0095	0.02

Table A.5: Ethereum, parameter sweep values

	1	2	3
β	1.1	0.4	0.5
v	0.875	0.07	0.3
α	0.002	0.001	0.005
μ	0.2	0.3	0.05

Table A.6: Blockchain, parameter sweep values

	1	2	3
β	0.85	0.546	0.15
v	0.75	0.25	0.025
α	0.006	0.001	0.001
μ	0.0074	0.04	0.045

A.2 GT interest and corresponding log returns

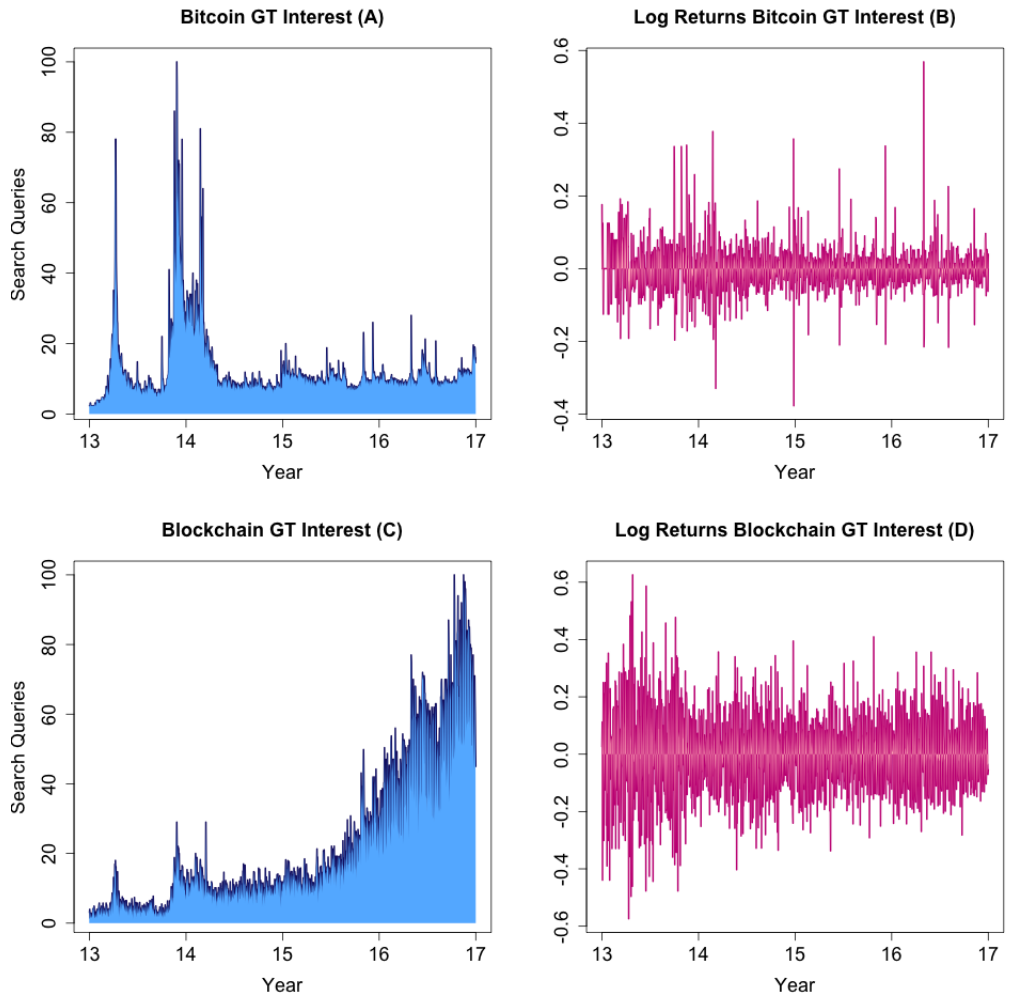

Figure A.1: GT interest and corresponding log returns for Bitcoin (A) and (B), Blockchain (C) and (D).

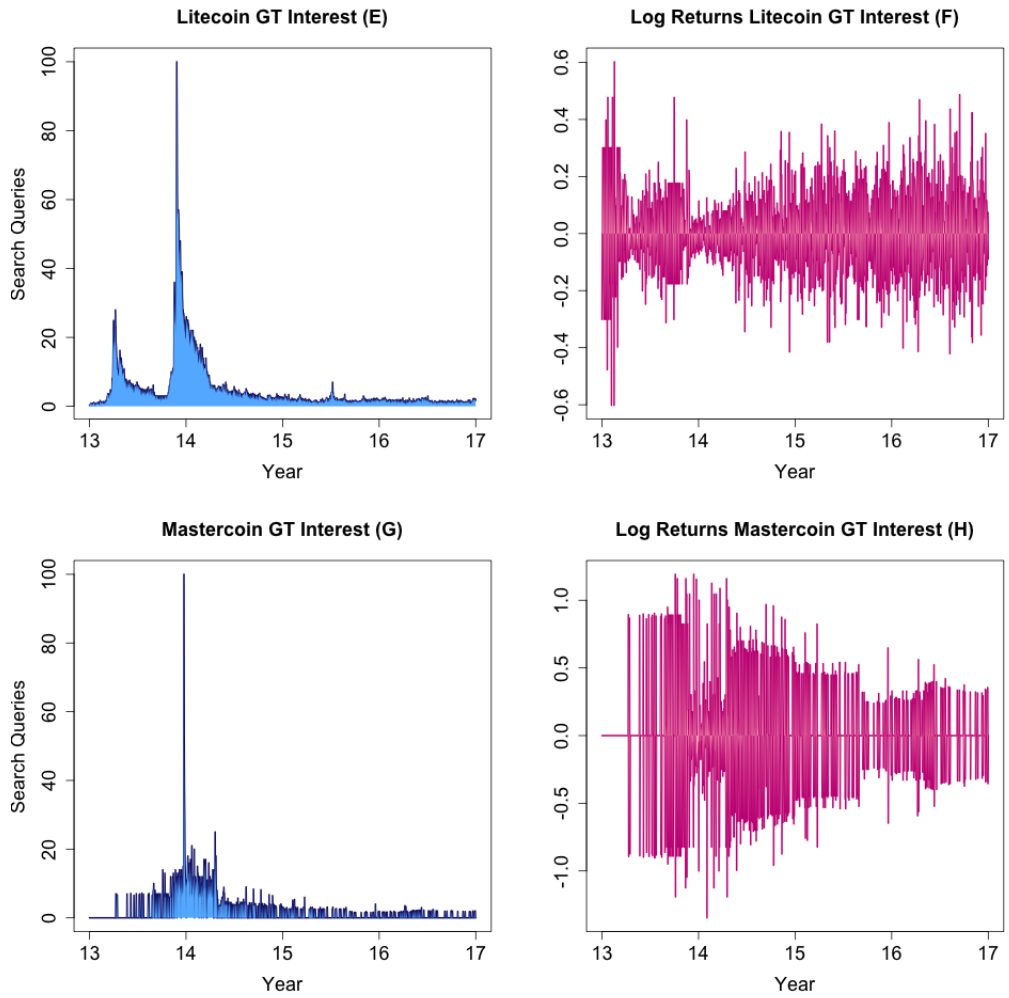

Figure A.2: GT interest and corresponding log returns for Litecoin (E) and (F), Mastercoin (G) and (H).

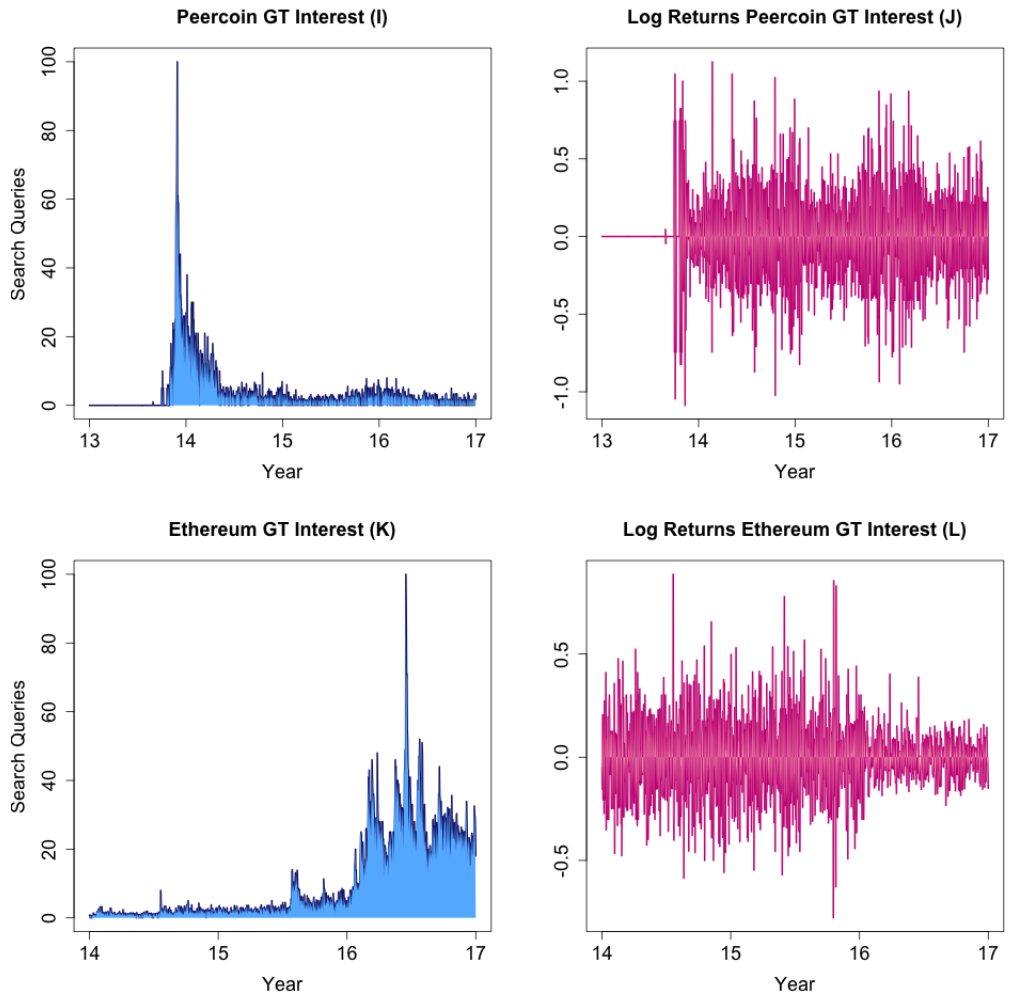

Figure A.3: GT interest and corresponding log returns for Peercoin (I) and (J), Ethereum (K) and (L).

Appendix B

Appendix (Chapter 3)

B.1 Search queries

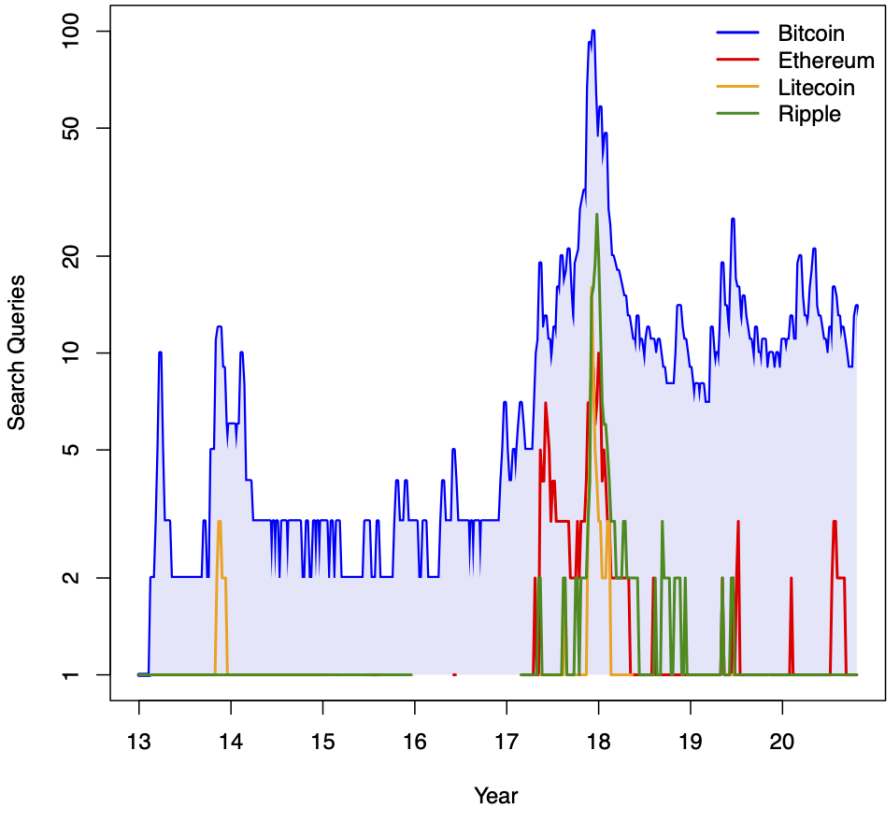

Figure B.1: Semilog plot. Worldwide Google search interest: Bitcoin, Ethereum, Litecoin, Ripple, search terms GT data fitting.

B.2 Market capitalisation

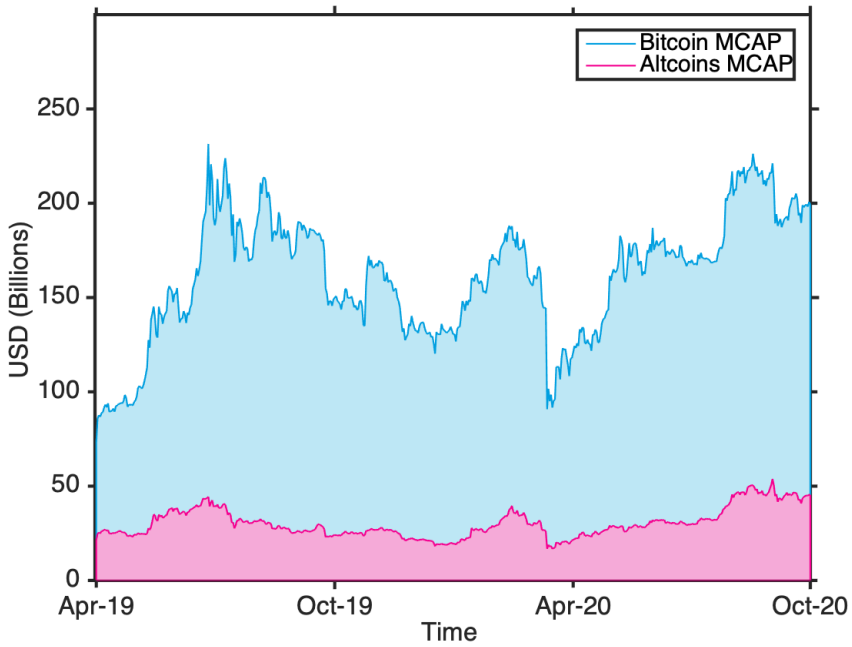

Figure B.2: Market capitalisation. Bitcoin compared to the average of top ten Altcoins.

B.3 GT interest, price and corresponding log returns

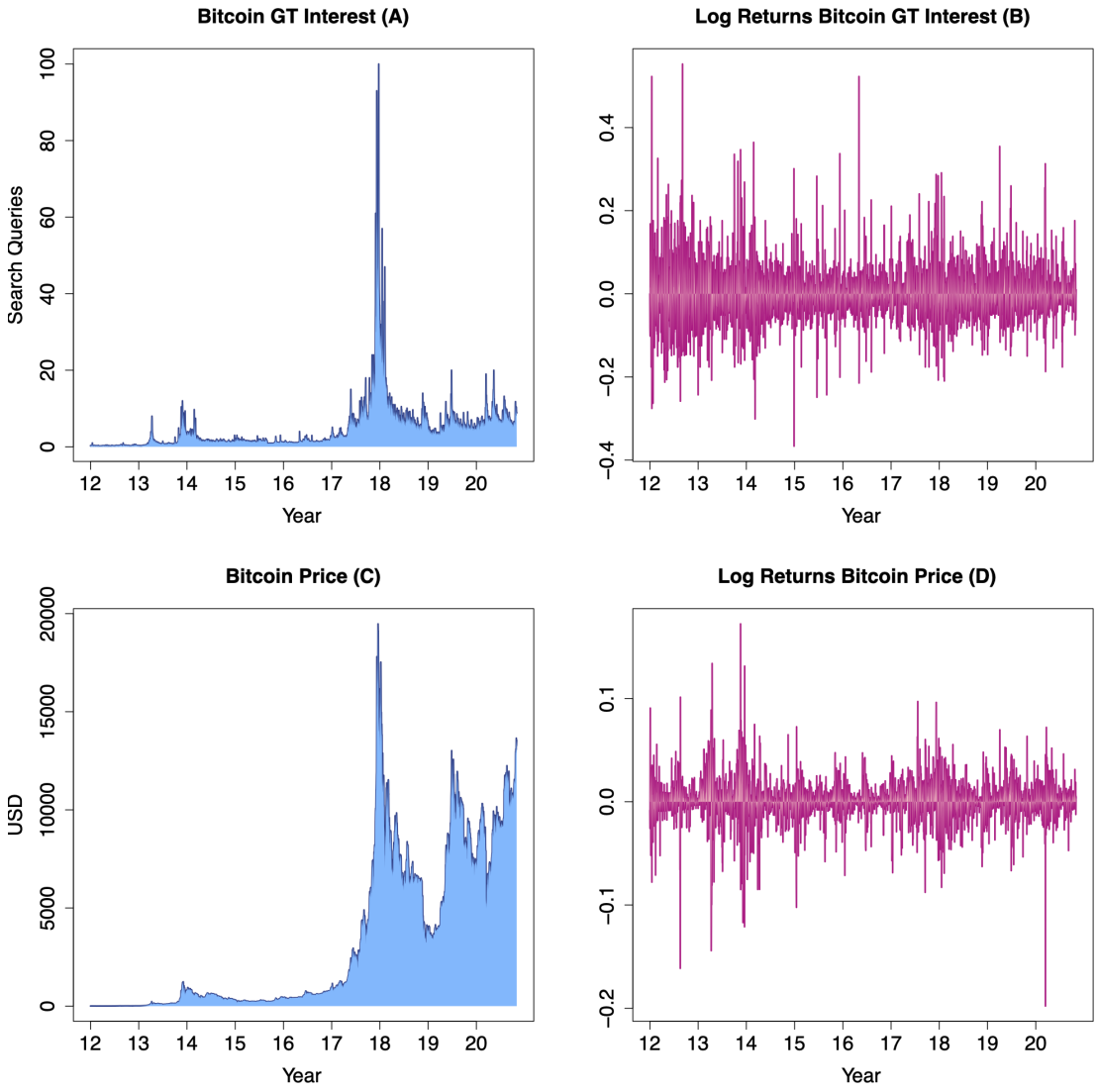

Figure B.3: Bitcoin GT interest (A), price (C), and corresponding log returns (B) and (D).

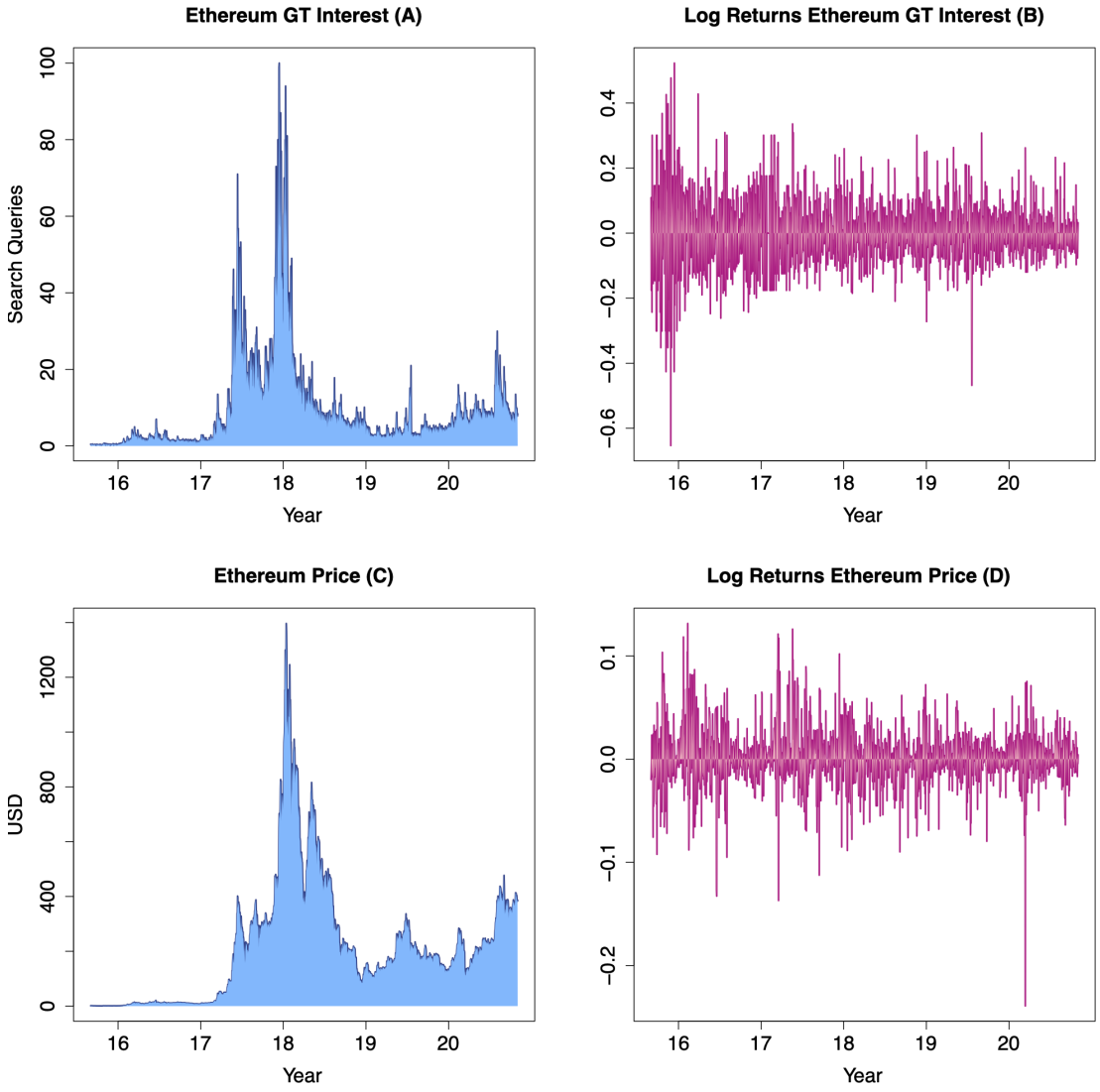

Figure B.4: Ethereum GT interest (A), price (C), and corresponding log returns (B) and (D).

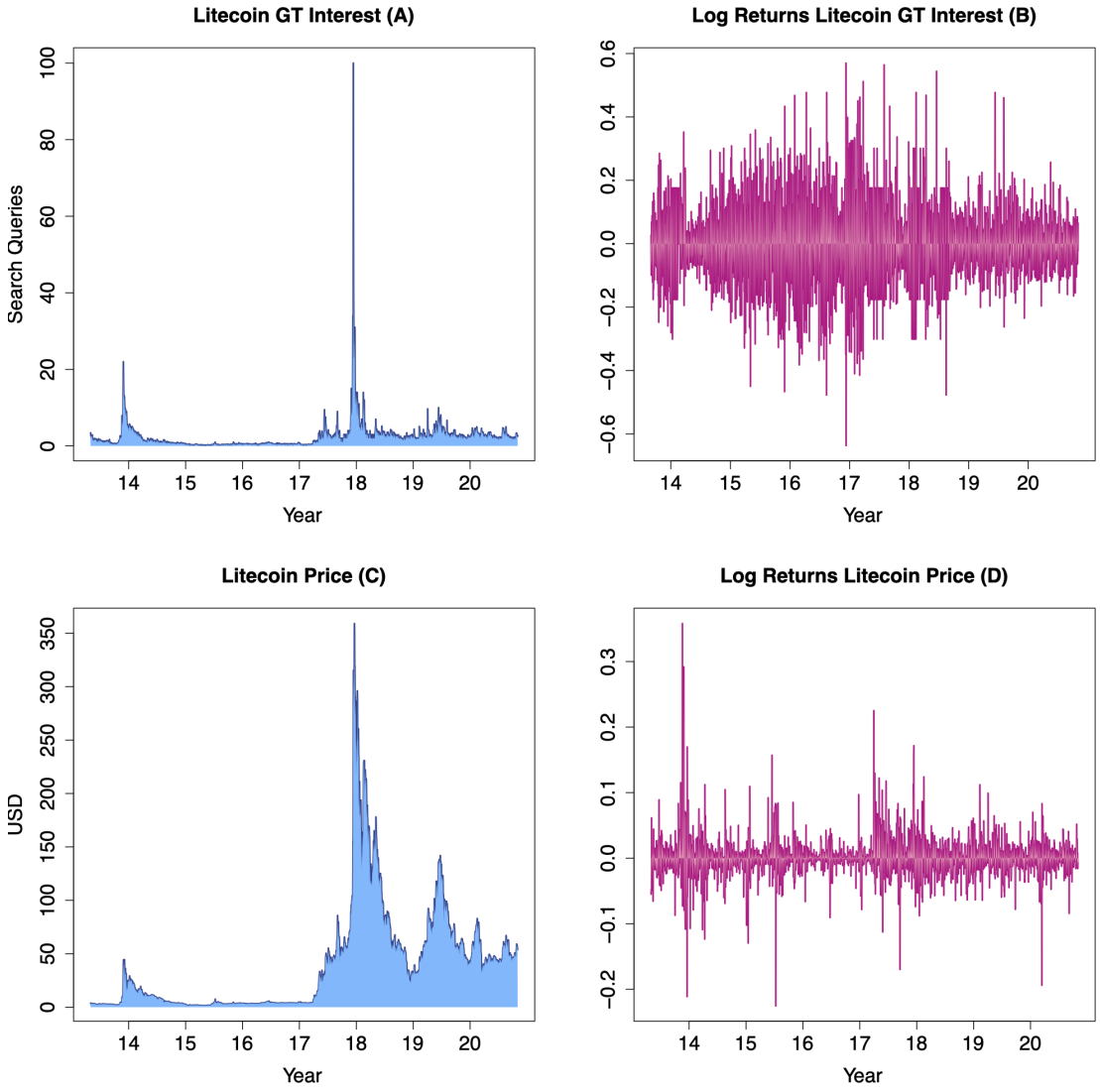

Figure B.5: Litecoin GT interest (A), price (C), and corresponding log returns (B) and (D).

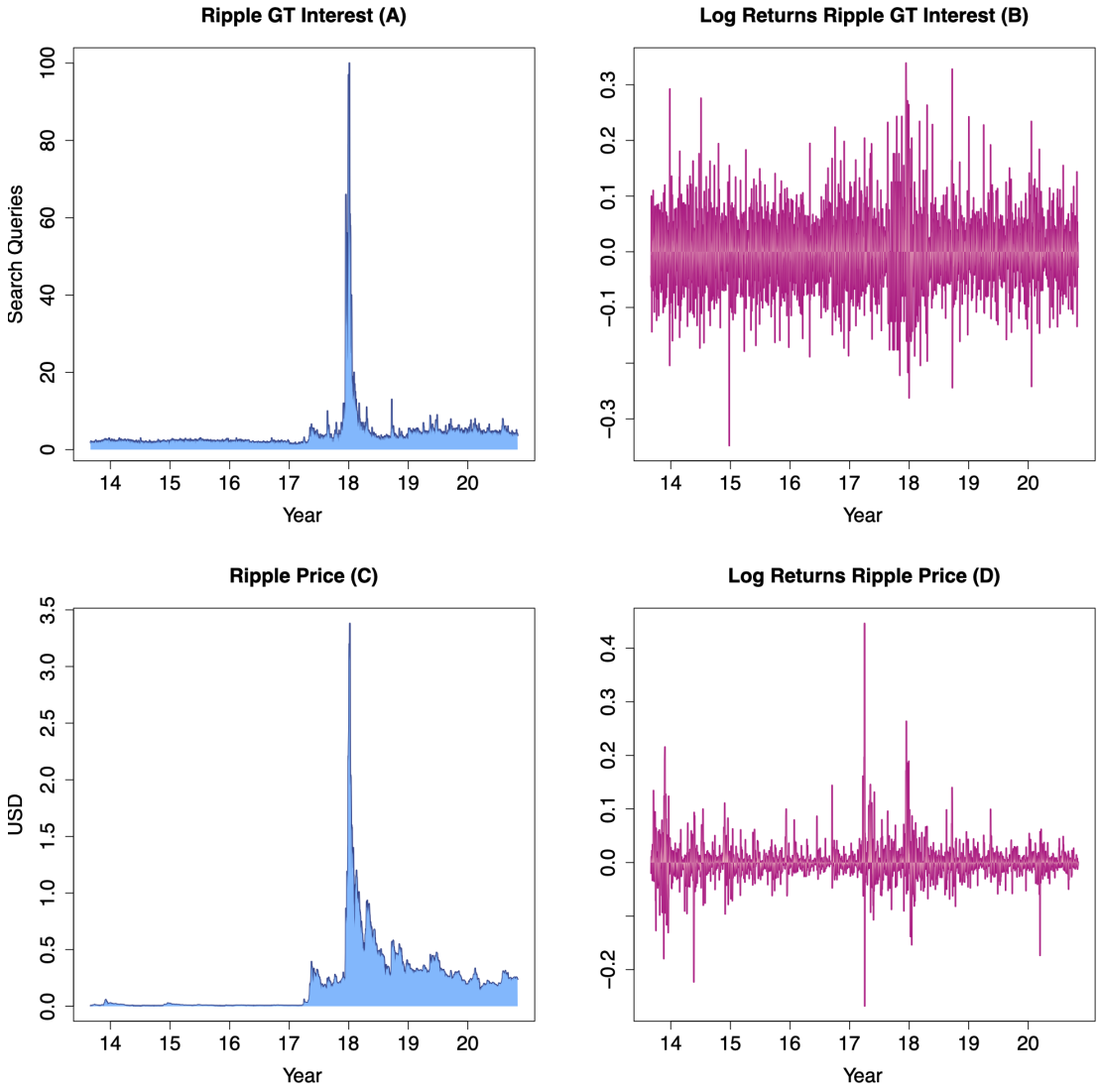

Figure B.6: Ripple GT interest (A), price (C), and corresponding log returns (B) and (D).

B.4 GT interest, price, supply and corresponding log returns

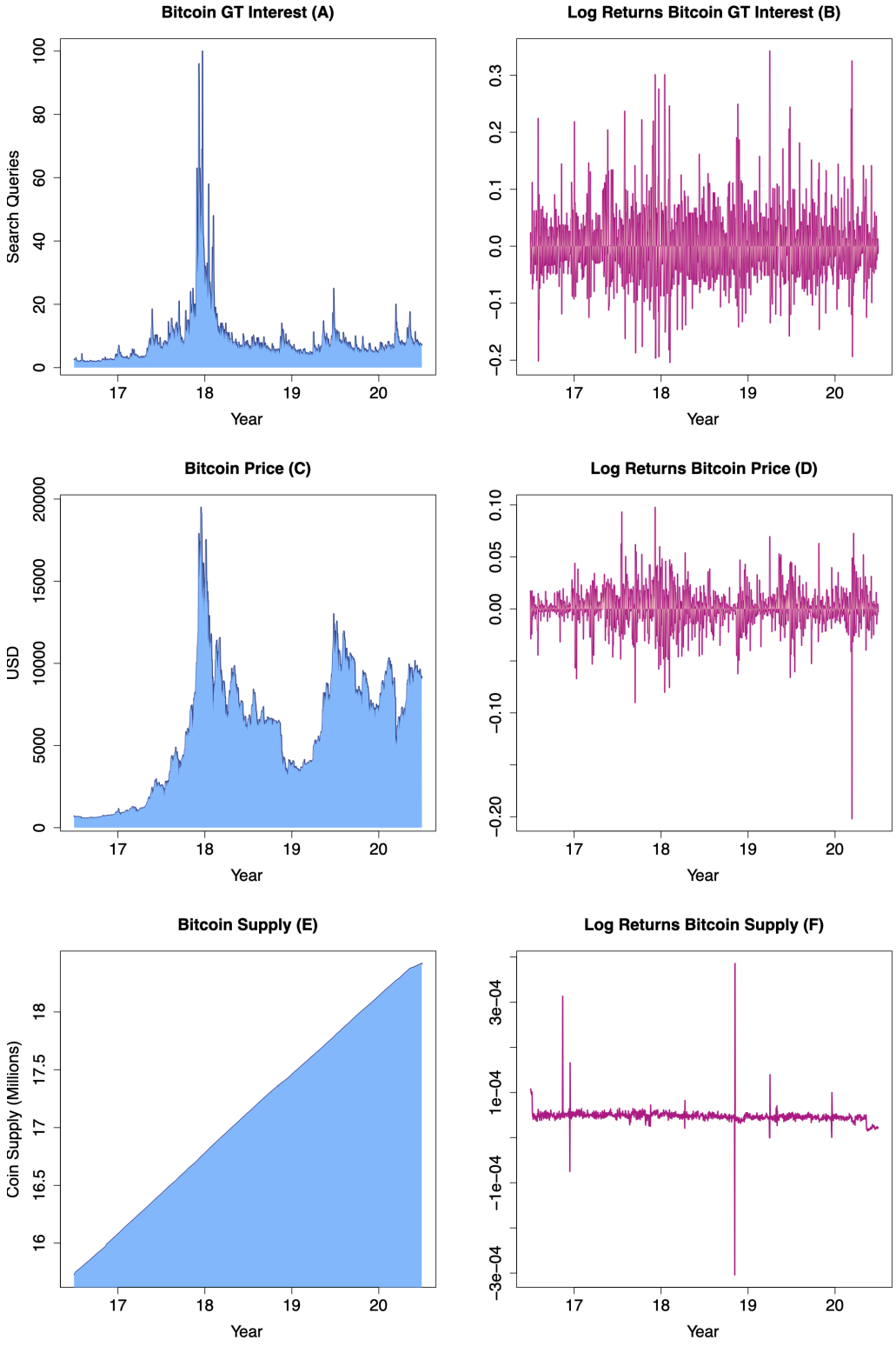

Figure B.7: Bitcoin GT interest (A), price (C), supply (E), and corresponding log returns (B), (D), (F).

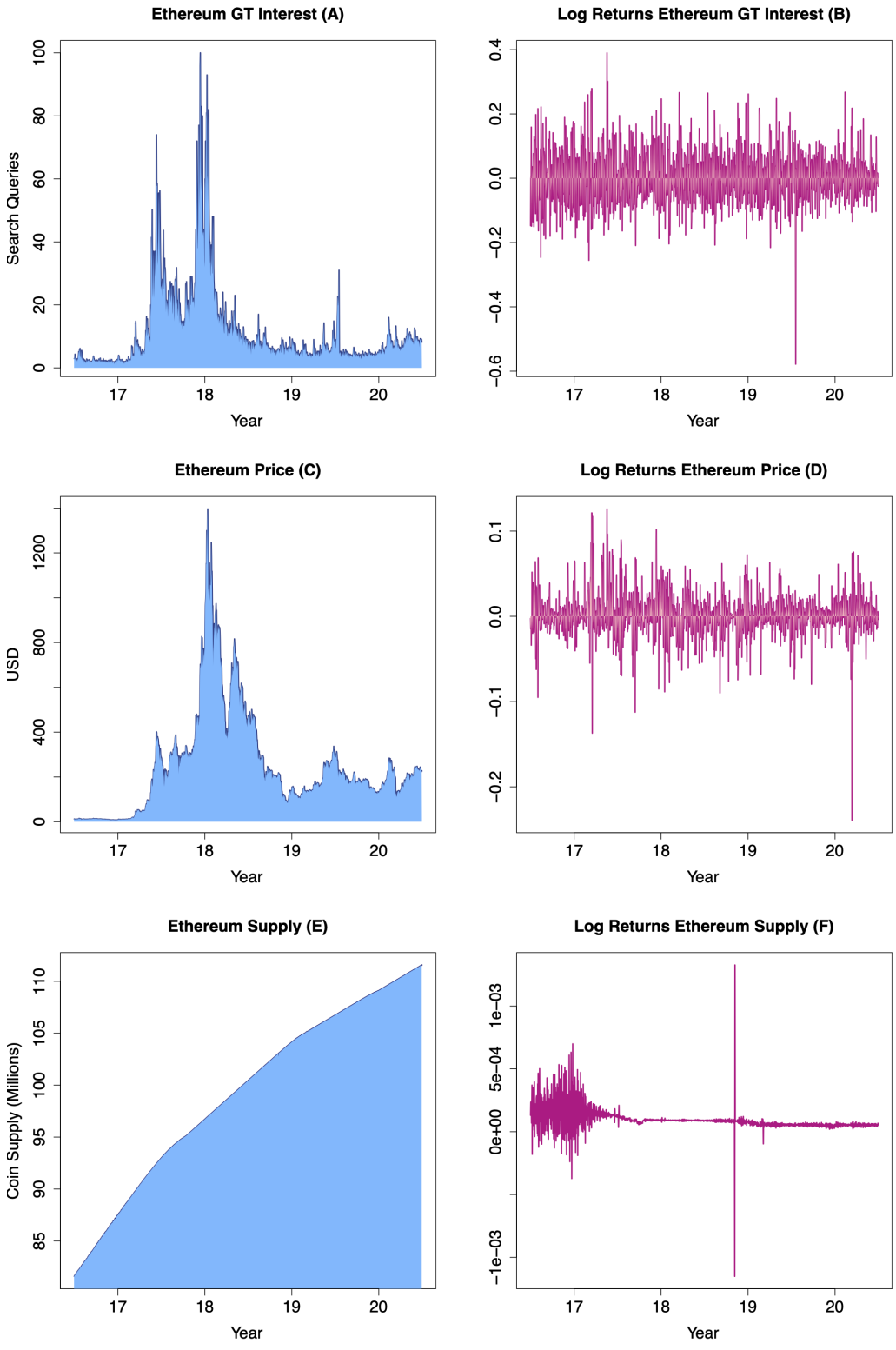

Figure B.8: Ethereum GT interest (A), price (C), supply (E), and corresponding log returns (B), (D), (F).

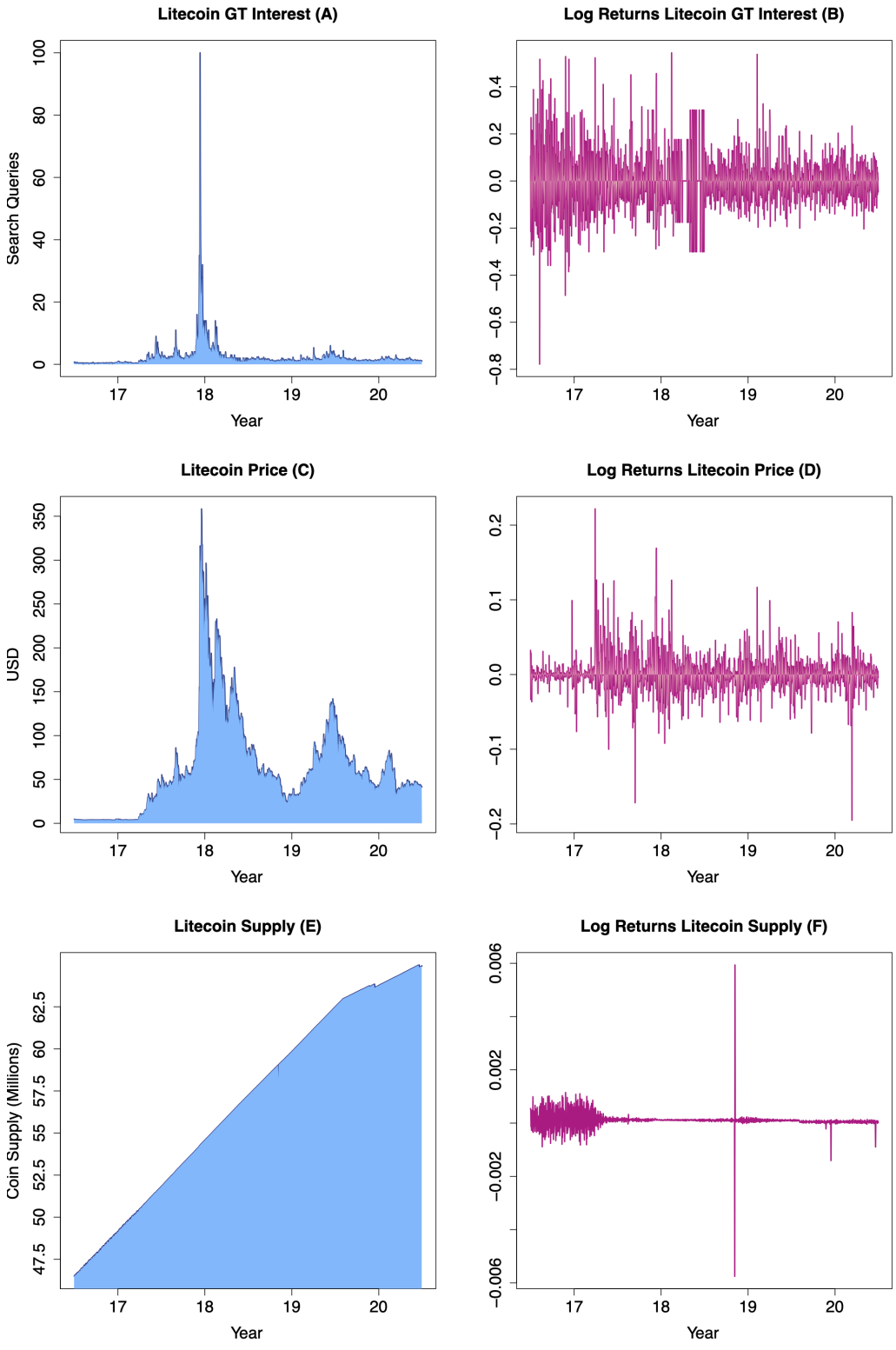

Figure B.9: Litecoin GT interest (A), price (C), supply (E), and corresponding log returns (B), (D), (F).

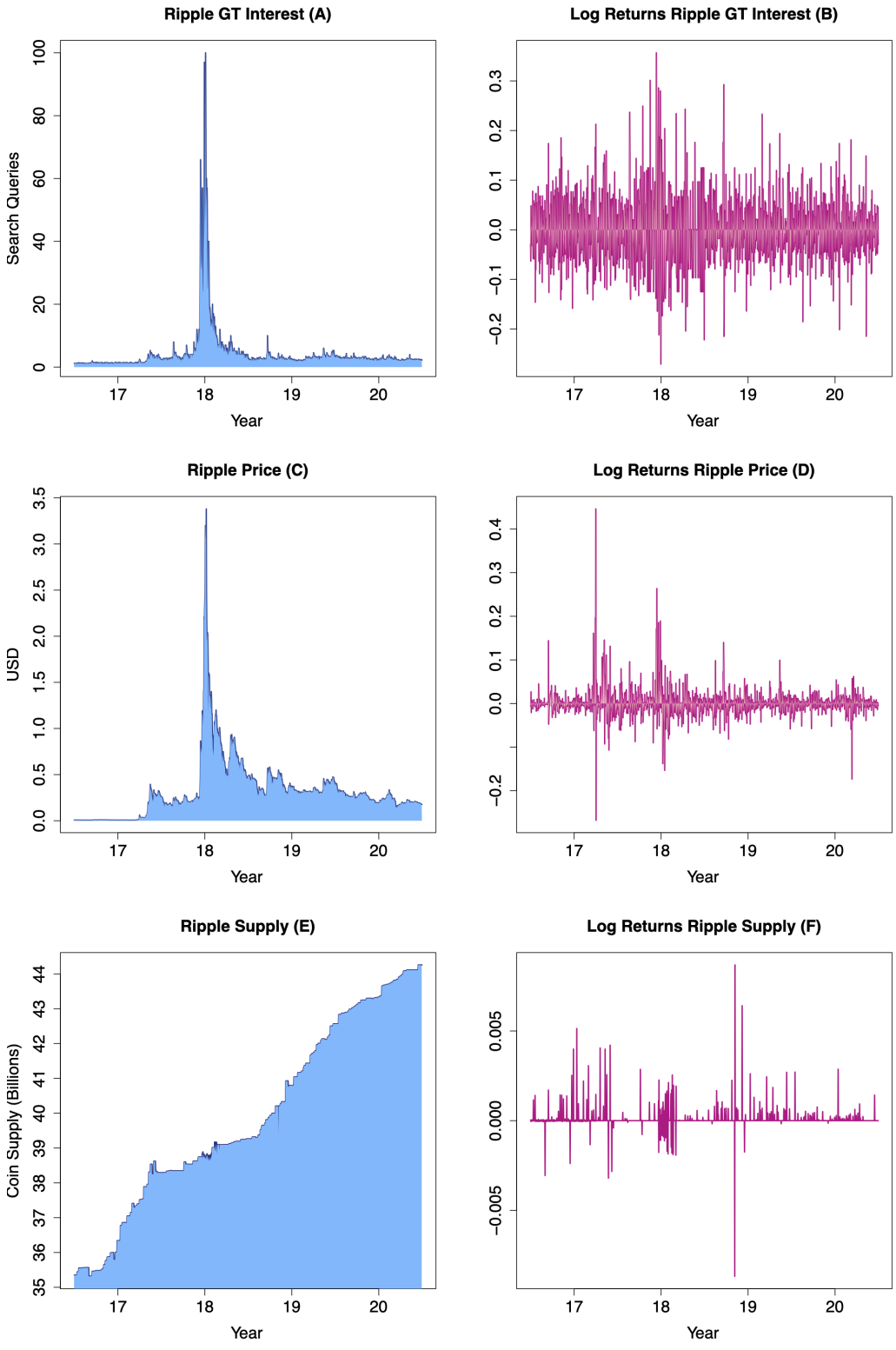

Figure B.10: Ripple GT interest (A), price (C), supply (E), and corresponding log returns (B), (D), (F).

Bibliography

[1] Bitcoin charts, 2017. URL https://bitcoinhelp.net/know/more/price-chart-history. 29

[2] idatavox analysis, 2017. URL http://www.idatavox.com/cases/bitcoin-dynamics/. 25

[3] Litecoin charts, 2017. URL http://www.ltc-charts.com. 29

[4] Ether Explained - Chapter 6: Ethereum vs. Bitcoin (part 1), 2019. URL https://investerest.vontobel.com/en-se/articles/13356/ether-explained--chapter-6-ethereum-vs-bitcoin-part-1/. 6

[5] Blockchain, 2020. URL http://www.blockchain.com. 2

[6] Blockchain security made simple, 2020. URL https://www.accenture.com/gb-en/service-blockchain-security. 2

[7] Blockchain in advertising - Is it the answer to digital advertising's trust and transparency gap?, 2020. URL https://www.pwc.com/us/en/industries/tmt/library/blockchain-in-advertising.html. 4

[8] Making sense of bitcoin, cryptocurrency and blockchain, 2020. URL https://www.pwc.com/us/en/industries/financial-services/fintech/bitcoin-blockchain-cryptocurrency.html. 2

[9] Google Trends, 2020. URL https://www.google.com/trends. 10, 24, 27

[10] Bitcoin Historical Data, 2020. URL https://www.investing.com/crypto/bitcoin/historical-data. 44

[11] Ethereum Historical Data, 2020. URL https://www.investing.com/crypto/ethereum/historical-data. 44

[12] Litecoin Historical Data, 2020. URL https://www.investing.com/crypto/litecoin/historical-data. 44

[13] Ripple Historical Data, 2020. URL https://www.investing.com/crypto/xrp/historical-data. 44

[14] Price movement of cryptocurrencies, 2020. URL https://coinmarketcap.com. 10, 31, 42, 45

[15] Binance Coin (BNB) Historical Data, 2020. URL https://coinmarketcap.com/currencies/binance-coin/historical-data/. 43

[16] Bitcoin (BTC) Historical Data, 2020. URL https://coinmarketcap.com/currencies/bitcoin/historical-data/. 42

[17] Bitcoin Cash (BCH) Historical Data, 2020. URL https://coinmarketcap.com/currencies/bitcoin-cash/historical-data/. 43

[18] Bitcoin SV (BSV) Historical Data, 2020. URL https://coinmarketcap.com/currencies/bitcoin-sv/historical-data/. 43

[19] Cardano (ADA) Historical Data, 2020. URL https://coinmarketcap.com/currencies/cardano/historical-data/. 43

[20] Chainlink (LINK) Historical Data, 2020. URL https://coinmarketcap.com/currencies/chainlink/historical-data/. 43

[21] Ethereum (ETH) Historical Data, 2020. URL https://coinmarketcap.com/currencies/ethereum/historical-data/. 43

[22] Litecoin (LTC) Historical Data, 2020. URL https://coinmarketcap.com/currencies/litecoin/historical-data/. 43

[23] Ripple (XRP) Historical Data, 2020. URL https://coinmarketcap.com/currencies/xrp/historical-data/. 43

[24] Tether (USDT) Historical Data, 2020. URL https://coinmarketcap.com/currencies/tether/historical-data/. 43

[25] USD Coin (USDC) Historical Data, 2020. URL https://coinmarketcap.com/currencies/usd-coin/historical-data/. 43

[26] Banking Is Only The Beginning: 58 Big Industries Blockchain Could Transform, 2021. URL https://www.cbinsights.com/research/industries-disrupted-blockchain/. 2

[27] D. Abrams and S. H. Strogatz. Modelling the dynamics of language death. *Nature*, 424(6951), 2003. 1

[28] M. Adimy, F. Crauste, and S. Ruan. A mathematical study of the hematopoiesis process with applications to chronic myelogenous leukemia. *SIAM Journal on Applied Mathematics*, 65(4):1328–1352, 2005. 22

[29] R. Adler. A Study of Locking Phenomena in Oscillators. *Proceedings of the IRE*, 34:351 – 357, 1946. 61

[30] L. Aguiar-Conraria, N. Azevedo, and M. J. Soares. Using wavelets to decompose the time-frequency effects of monetary policy. *Physica*, 387:2863–2878, 2008. 8, 9

[31] C. Aloui and B. Hkiri. Co-movements of GCC emerging stock markets: New evidence from wavelet coherence analysis. *Economic Modelling*, 36:421–431, 2014. 8

[32] A. M. Antonopoulos. *Mastering Bitcoin: Unlocking Digital Cryptocurrencies*. O'Reilly Media, 2014. 3, 4

[33] A. Arenas, A. Díaz-Guilera, J. Kurths, Y. Moreno, and C. Zhou. Synchronization in complex networks. *Physics Reports*, 469(3):93–153, 2008. 14

[34] F. M. Atay. *Complex time-delay systems: theory and applications*. Springer, 2010. 14, 17

[35] M. Bank, M. Larch, and G. Peter. Google search volume and its influence on liquidity and returns of German stocks. *Financial Markets and Portfolio Management*, 25: 239–264, 2011. 25

[36] M. Barrio, K. Burrage, A. Leier, and T. Tian. Oscillatory Regulation of Hes1: Discrete Stochastic Delay Modelling and Simulation. *PLoS Comput Biol*, 2(9):e117, 2006. 22

[37] J. Barunik, L. Vacha, and L. Krištoufek. Comovement of Central European stock markets using wavelet coherence: Evidence from high-frequency data. *Econstor*, 22/2011, 2011. 10

[38] L. Bettencourt, A. Cintrón-Arias, D. Kaiser, and C. Castillo-Chávez. The power of a good idea: Quantitative modeling of the spread of ideas from epidemiological models. *Physica A*, 364:513–536, 2006. 1, 12

[39] D. Bianchini. 10 stats to justify SEO, 2012. URL https://danielbianchini.co.uk/10-stats-to-justify-seo/. 25

[40] C. Bick, M. Goodfellow, C. R. Laing, and E. A. Martens. Understanding the dynamics of biological and neutral oscillator networks through exact mean-field reductions: a review. *arXiv*, 1902:05307, 2020. 14

[41] L. Bijl, G. Kringhaug, P. Molnár, and E. Sandvik. Google searches and stock returns. *International Review of Financial Analysis*, 45:150–156, 2016. 25

[42] S. P. Blythe, R. M. Nisbet, W. S. C. Gurney, and N. MacDonald. Stability switches in distributed delay models. *Journal of Mathematical Analysis and Applications*, 109(2):388–396, 1985. 22

[43] I. Bordino, S. Battiston, G. Caldarelli, M. Cristelli, A. Ukkonen, and I. Weber. Web search queries can predict stock market volumes. *PLOS ONE*, 7:p. e40014, 2012. 25

[44] E. Bouri, M. Das, R. Gupta, and D. Roubaud. Spillovers between Bitcoin and other assets during bear and bull markets. *Applied Economics*, 50:5935–5949, 2018. 43

[45] D. Breda, S. Maset, and R. Vermiglio. Pseudospectral approximation of eigenvalues of derivative operators with non-local boundary conditions. *Applied Numerical Mathematics*, 56(3):318–331, 2006. 67, 94, 104

[46] A. Burnie. Exploring the Interconnectedness of Cryptocurrencies using Correlation Networks. *arXiv*, 1806:06632, 2018. 16

[47] J. Cannarella and J. Spechler. Epidemiological modelling of online social network dynamics. *arXiv*, 1401.4208, 2014. 1, 11, 12, 26

[48] K. L. Cooke and Z. Grossman. Discrete delay, distributed delay and stability switches. *Journal of Mathematical Analysis and Applications*, 86(2):592–627, 1982. 22

[49] G. Dahlquist and A. Björck. *Numerical methods in scientific computing, volume i*. SIAM, Philadelphia, 2007. 75, 98, 112

[50] A. K. Dey, C. G. Akcora, Y. R. Gel, and M. Kantarcioglu. On the role of local blockchain network features in cryptocurrency price formation. *Canadian Journal of Statistics*, 48(3), 2020. 16

[51] O. D'Huys, R. Vicente, T. Erneux, J. Danckaert, and I. Fischer. Synchronization properties of network motifs: Influence of coupling delay and symmetry. *Chaos: An Interdisciplinary Journal of Non-linear Science*, 18, 2008. 17, 22, 60, 61

[52] S. Dong, F.-H. Fan, and Y.-C. Huang. Studies on the population dynamics of a rumor-spreading model in online social networks. *Physica A: Statistical Mechanics and its Applications*, 492:10–20, 2018. 11

[53] F. Dörfler and F. Bullo. Synchronization in complex networks of phase oscillators: A survey. *Automatica*, 50:1539–1564, 2014. 14

[54] M. G. Earl and S. H. Strogatz. Synchronisation in oscillator networks with delayed coupling: A stability criterion. *Physical Review*, 67:036204, 2003. 23, 63

[55] T. Erneux. *Applied Delay Differential Equations*. Springer, 2009. 17

[56] T. Erneux, J. Javaloyes, M. Wolfrum, and S. Yanchuk. Introduction to Focus Issue: Time-delay dynamics. *Chaos: An Interdisciplinary Journal of Nonlinear Science*, 27(11):114201, 2017. 14, 17

[57] J. Fell and N. Axmacher. The role of phase synchronisation in memory processes. *Nature Reviews Neuroscience*, 12(2):105–118, 2011. 14

[58] S. Ferretti and G. D'Angelo. On the Ethereum Blockchain Structure: a Complex Networks Theory Perspective. *Concurrency Computat Pract Exper.*, 32, 2020. 16

[59] G. Fibich. Bass-SIR model for diffusion of new products. *arXiv*, 1605.0361, 2018. 12

[60] V. Flunkert, I. Fischer, and E. Schöll. Dynamics, control and information in delay-coupled systems: an overview. *Philosophical Transactions of the Royal Society*, 2013. 14, 19

[61] C. J. Francés, P. Grau-Carles, and D. J. Arellano. The cryptocurrency market: A network analysis. *Esic Market Economics and Business Journal*, 49(3):569–583, 2018. 16

[62] H. Fukuda, N. Nakamichi, M. Hisatsune, H. Murase, and T. Mizuno. Synchronization of plant circadian oscillators with a phase delay effect of the vein network. *Physical Review Letters*, 99:098102, 2007. 14

[63] S. Funk and V. A. A. Jansen. *Modeling the Interplay Between Human Behavior and the Spread of Infectious Diseases*. Springer, 2013. 13

[64] M. Gallegati and W. Semmler. *Wavelet Applications in Economics and Finance*. Springer, 2014. 9

[65] D. Garcia, C. Tessone, P. Mavrodiev, and N. Perony. The digital traces of bubbles: feedback cycles between socio-economic signals in the Bitcoin economy. *Journal of the Royal Society Interface*, 11:20140623, 2014. 25

[66] A. Gjurchinovski and V. Urumov. Stabilization of unstable steady states by variable-delay feedback control. *EPL (Europhysics Letters)*, 84(4):40013, 2008. 22

[67] L. Glass. Synchronization and rhythmic processes in physiology. *Nature*, 410:277–284, 2001. 14

[68] A. Goldman. Lindy's Law. *The New Republic*, 1964. 43

[69] J. W. Goodell and S. Goutte. Co-movement of COVID-19 and Bitcoin: Evidence from wavelet coherence analysis. *Finance Research Letters*, 101625, 2020. 10

[70] J. M. Griffin and A. Shams. Is Bitcoin Really Untethered? *The Journal of Finance*, 75:1913–1964, 2020. 45, 46

[71] A. Grinsted, J. Moore, and S. Jevrejeva. Application of the cross wavelet transform and wavelet coherence to geophysical time series. *Nonlinear Proc. Geophys.*, 11: 561–566, 2004. 8, 9, 10, 27, 32

[72] A. Groth and M. Ghil. Synchronization of world economic activity. *Chaos: An Interdisciplinary Journal of Nonlinear Science*, 27(12):127002, 2017. 14, 15

[73] J. M. Gushing. *Mathematics of Biology*. Springer, 2011. 22

[74] J. K. Hale and S. M. Verduyn Lunel. *Introduction to Functional Differential Equations*. Springer-Verlag, 1993. 63

[75] R. Hilborn. *Chaos and nonlinear dynamics: and introduction for scientists and engineers*. Oxford University Press, 2000. 63

[76] A. L. Hill, D. G. Rand, M. A. Nowak, and N. A. Christakis. Emotions as infectious diseases in a large social network: the SISa model. *Physica A: Statistical Mechanics and its Applications*, 277:3827–3835, 2010. 12

[77] G. Iredale. Public Vs Private Blockchain: How Do They Differ?, 2021. URL https://101blockchains.com/public-vs-private-blockchain/. 3

[78] J. Iribarren and E. Moro. Impact of human activity patterns on the dynamics of information diffusion. *Physical Review Letters*, 103:038702, 2009. 1

[79] F. Jian and S. Dandan. Complex Network Theory and Its Application Research on P2P Networks. *Applied Mathematics and Nonlinear Sciences*, 1:45–52, 2016. 16

[80] S.-P. Jun, H. S. Yoo, and S. Choi. Ten years of research change using Google Trends: From the perspective of big data utilizations and applications. *Technological Forecasting and Social Change*, 130:69–87, 2018. 25

[81] W. Just, A. Pelster, M. Schanz, and E. Schöll. Delayed complex systems: an overview. *Philosophical Transactions of the Royal Society*, 368(1911):303–304, 2010. 14, 19, 60

[82] M. Kapilkov. Nearly 30000 blockchain votes were recorded in Russian elections - The most ever, 2020. URL https://cointelegraph.com/news/nearly-30-000-blockchain-votes-were-recorded-in-russian-elections-the-most-ever. 5

[83] W. Kermack and A. McKendrick. A contribution to the mathematical theory of epidemics. *Proceedings of the Royal Society of London*, 115:700–721, 1927. 11, 25

[84] L. Krištoufek. Can Google Trends search queries contribute to risk diversification? *Scientific Reports*, 3:Article number: 2713, 2013. 25

[85] L. Krištoufek. Bitcoin meets Google Trends and Wikipedia: Quantifying the relationship between phenomena of the Internet era. *Science Report*, 3:3415, 2013. 25

[86] L. Krištoufek. Power-law correlations in finance-related Google searches, and their cross-correlations with volatility and traded volume: Evidence from the Dow Jones Industrial components. *Physica A: Statistical Mechanics and its Applications*, 428: 194–205, 2015. 25

[87] L. Krištoufek. What Are the Main Drivers of the Bitcoin Price? Evidence from Wavelet Coherence Analysis. *PLOS ONE*, 10(4), 2015. 9, 10, 27, 31

[88] Y. Kuramoto. Self-entrainment of a population of coupled non-linear oscillators. In International Symposium on Mathematical Problems in Theoretical Physics. *Lecture Notes in Physics, Springer, Berlin*, 39:420–422, 1975. 14, 15

[89] Y. Kuramoto. *Chemical oscillations, waves, and turbulence*. Springer-Verlag, New York, 1984. 14, 60

[90] Y. N. Kyrychko and S. J. Hogan. On the use of delay equations in engineering applications. *Journal of Vibration and Control*, 16:943–960, 2010. 17

[91] Y. N. Kyrychko and I. B. Schwartz. Enhancing noise-induced switching times in systems with distributed delays. *Chaos: An Interdisciplinary Journal of Nonlinear Science*, 28(6):063106, 2018. 22

[92] Y. N. Kyrychko, K. B. Blyuss, and E. Schöll. Amplitude death in systems of coupled oscillators with distributed-delay coupling. *European Physical Journal B: Condensed Matter and Complex Systems*, 84(2):307–315, 2011. 22

[93] Y. N. Kyrychko, K. B. Blyuss, and E. Schöll. Amplitude and phase dynamics in oscillators with distributed-delay coupling. *Philosophical Transactions A: Mathematical, Physical and Engineering Sciences*, 371:20120466, 2013. 22, 70

[94] Y. N. Kyrychko, K. B. Blyuss, and E. Schöll. Synchronization of networks of oscillators with distributed delay coupling. *Chaos*, 24:043117, 2014. 22

[95] K. Lehnerz, C. Geier, T. Rings, and K. Stahn. Capturing time-varying brain dynamics. *EPJ Nonlinear Biomedical Physiscs*, 5, 2017. 14

[96] K. Leibnitz, T. Hoßfeld, N. Wakamiya, and M. Murata. *Modeling of Epidemic Diffusion in Peer-to-Peer File-Sharing Networks*. Springer-Verlag, 2006. 13

[97] A. Lella. comScore report, 2015. URL http://www.comscore.com/Insights/Rankings/comScore-Releases-January-2015-US-Desktop-Search-Engine-Rankings. 25

[98] N. MacDonald. *Time lags in biological systems*. New York, NY:Springer, 1978. 77, 114

[99] E. Mallada and A. Tang. Synchronization of Weakly Coupled Oscillators: Coupling, Delay and Topology. *arXiv*, 1303.7248, 2013. 17

[100] B. B. Mandelbrot. *The Fractal Geometry of Nature*. Freeman and Co., 1982. 43

[101] R. P. Mann, J. Faria, D. J. T. Sumpter, and J. Krause. The dynamics of audience applause. *Journal of the Royal Society, Interface*, 10(85):20130466, 2013. 13

[102] N. Massad and J. V. Andersen. Three Different Ways Synchronization Can Cause Contagion in Financial Markets. *Risks*, 6(4):104, 2018. 15

[103] D. Massessi. Public Vs Private Blockchain In A Nutshell, 2018. URL https://medium.com/coinmonks/public-vs-private-blockchain-in-a-nutshell-c9fe284fa39f. 3

[104] M. McCartney and D. Glass. A three-state dynamical model for religious affiliation. *Physica A*, 419:145–152, 2015. 1

[105] W. Mensi, M. Ur-Rehman, K. H. Al-Yahyaee, I. M. W. Al-Jarrah, and S. H. Kang. Time frequency analysis of the commonalities between Bitcoin and major Cryptocurrencies: Portfolio risk management implications. *The North American Journal of Economics and Finance*, 48:283–294, 2019. 10

[106] J. E. Mittler, B. Sulzer, A. U. Neumann, and A. S. Perelson. Influence of delayed viral production on viral dynamics in HIV-1 infected patients. *Mathematical biosciences*, 152(2):143–163, 1998. 22

[107] E. Mutlu, A. Rajabi, and I. Garibay. CD-SEIZ: Cognition-Driven SEIZ Compartmental Model for the Prediction of Information Cascades on Twitter. 2020. 12

[108] S. Nakamoto. Bitcoin: A Peer-to-Peer Electronic Cash System. 2008. URL https://bitcoin.org/bitcoin.pdf. 2

[109] M. A. Nasir, T. L. D. Huynh, S. P. Nguyen, and D. Duong. Forecasting cryptocurrency returns and volume using search engines. *Financial Innovation*, 5:Article number:2, 2019. 25

[110] M. Nekovee, Y. Moreno, G. Bianconi, and M. Marsili. Theory of rumour spreading in complex social networks. *Physica A: Statistical Mechanics and its Applications*, 374:457–470, 2007. 11, 12

[111] R. Pathak. How blockchain will dominate the digital advertising industry in 2020, 2020. URL https://www.searchenginewatch.com/2020/02/26/how-blockchain-will-dominate-the-digital-advertising-industry-in-2020/. 4

[112] D. B. Percival and A. T. Walden. *Wavelet Methods for Time series Analysis*. Cambridge University Press, 2000. 7

[113] T. Peron and F. A. Rodrigues. Collective behavior in financial markets. *EPL (Europhysics Letters)*, 96(4):48004, 2011. 15

[114] R. C. Phillips and D. Gorse. Cryptocurrency price drivers: Wavelet coherence analysis revisited. *PLOS ONE*, 13(4), 2018. 10

[115] A. Pikovsky, M. Rosenblum, and J. Kurths. *Synchronization. A Universal Concept in Nonlinear Sciences*. Cambridge University Press, 2001. 14, 17

[116] T. Preis, H. S. Moat, and H. E. Stanley. Quantifying trading behavior in financial markets using google trends. *Scientific Reports*, 3:Article number: 1684, 2013. 25

[117] B. Rahman, K. B. Blyuss, and Y. N. Kyrychko. Dynamics of neural systems with discrete and distributed time delays. *SIAM Journal on Applications of Dynamical Systems*, 14:2069–2095, 2015. 22, 70

[118] B. Rahman, K. B. Blyuss, and Y. N. Kyrychko. Aging transition in systems of oscillators with global distributed-delay coupling. *Physical Review E*, 96(3):032203, 2017. 22

[119] H. S. Rodrigues. Application of SIR epidemiological model: new trends. *International Journal of Applied Mathematics and Informatics*, 10:92–97, 2016. 11

[120] H. S. Rodrigues and M. J. Fonseca. Can information be spread as a virus? Viral Marketing as epidemiological model. *arXiv*, 1611.04529, 2016. 13

[121] O. Roesch, H. Roth, and S.-I. Niculescu. Effects of distributed delays in helicopter elevation control over networks. 22

[122] M. Rohden, A. Sorge, M. Timme, and D. Witthaut. Self-organized synchronization in decentralized power grids. *Physical Review Letters*, 109:064101, 2012. 14

[123] A. Ross. Thesis Raw Data, 2021. URL https://github.com/aleksandraross/thesis-raw-data. 10

[124] A. Rua and L. C. Nunes. International comovement of stock market returns: A wavelet analysis. *Journal of Empirical Finance*, 16:632–639, 2009. 8

[125] H. G. Schuster and P. Wagner. Mutual Entrainment of Two Limit Cycle Oscillators with Time Delayed Coupling. *Progress of Theoretical Physics*, 81:939–945, 1989. 22

[126] R. Sipahi, S.-I. Niculescu, and F. M. Atay. Effects of short-term memory of drivers on stability interpretations of traffic flow dynamics. pages 3112–3117. 22

[127] R. Sipahi, F. M. Atay, and S.-I. Niculescu. Stability of Traffic Flow Behavior with Distributed Delays Modeling the Memory Effects of the Drivers. *SIAM Journal on Applied Mathematics*, 68:738–759, 2007. 22

[128] J. Skazaa and B. Blais. Modelling the Infectiousness of Twitter Hashtags. *Physica A*, 465:289–296, 2017. 1, 26

[129] D. Stošić, D. Stosic, T. B. Ludermir, and T. Stosic. Collective behavior of cryptocurrency price changes. *Physica A: Statistical Mechanics and its Applications*, 507: 499–509, 2018. 16

[130] S. H. Strogatz. *Nonlinear dynamics and chaos: with applications to physics, biology, chemistry, and engineering*. Westview Press, 1994. 62, 63

[131] S. H. Strogatz. From Kuramoto to Crawford: exploring the onset of synchronization in populations of coupled oscillators. *Physica D: Nonlinear Phenomena*, 143(1):1–20, 2000. 14

[132] S. H. Strogatz. Exploring complex networks. *Nature*, 410(6825):268–276, 2001. 14

[133] S. H. Strogatz. *Sync: The Emerging Science of Spontaneous Order*. Hyperion, New York, 2004. 14

[134] S. H. Strogatz and I. Stewart. Coupled Oscillators and Biological Synchronization. *Scientific American*, 269:102–109, 1993. 14

[135] C. Torrence and G. P. Compo. A practical guide to wavelet analysis. *Bulletin of the American Meteorological Society*, 79:61–78, 1998. 8, 32

[136] C. Torrence and P. J. Webster. The annual cycle of persistence in the el niñosouthern oscillation. *Quarterly Journal of the Royal Meteorological Society*, 124:1985–2004, 1998. 9

[137] S. Towers, 2017. URL https://www.sherrytowers.com. 27

[138] L. Vacha and J. Barunik. Co-movement of energy commodities revisited: Evidence from waveletcoherence analysis. *Energy Economics*, 34:241–247, 2012. 8

[139] T. Walther, T. Klein, and E. Bouri. Exogenous drivers of Bitcoin and Cryptocurrency volatility - A mixed data sampling approach to forecasting. *Journal of International Financial Markets, Institutions and Money*, 63:101133, 2019. 43

[140] L. Wang and B. Wood. An epidemiological approach to model the viral propagation of memes. *Applied Mathematical Modelling*, 35:5442–5447, 2011. 1

[141] D. Watts. A simple model of global cascades on random networks. *National Academy of Sciences*, 99(9):5766–5771, 2002. 1

[142] D. V. Widder. *The Laplace Transform*. Princeton Mathematical Series, 1946. 20, 21

[143] K. Wiesenfeld, P. Colet, and S. Strogatz. Synchronization transitions in a disordered josephson series array. *Physical Review Letters*, 76:404–407, 1996. 14

[144] A. T. Winfree. Biological rhythms and the behavior of populations of coupled oscillators. *Journal of Theoretical Biology*, 16(1):15–42, 1967. 14

[145] A. T. Winfree. *The geometry of biological time*. Springer, New York, 1980. 14

[146] W. Woo. Data visualisation: altcoins that achieved $5m market cap vs bitcoin, 2016. URL https://woobull.com/data-visualisation-alt-coins-that-achieved-5m-market-cap-vs-bitcoin/. 5

[147] W. Woo. Data visualisation: 118 coins plotted over time this is why HODL altcoin indexes don't work, 2016. URL https://woobull.com/data-visualisation-118-coins-plotted-over-time-this-is-why-hodl-alt-coin-indexes-dont-work/. 5

[148] W. Woo. Using Google Trends to detect Bitcoin price bubbles, and best times to buy, 2017. URL https://woobull.com/using-google-trends-to-detect-bitcoin-price-bubbles-and-best-times-to-buy/. 5

[149] W. Woo. The two types of Altcoins, an investor's view, 2019. URL https://woobull.com/the-two-types-of-altcoins-an-investors-view/. 43

[150] S. Yanchuk and P. Perlikowski. Delay and periodicity. *Physical Review E*, 79:046221, 2009. 70

[151] L. Yang, X. J. Cai, H. Zhang, and S. Hamori. Interdependence of foreign exchange markets: A wavelet coherence analysis. *Economic Modelling*, 55:6–14, 2016. 9

[152] I. Yuichi, A. Hideaki, and Y. Hiroshi. Synchronization and the Coupled Oscillator Model in International Business Cycles. *Research Institute of Economy, Trade and Industry*, 13089, 2013. 14, 15

[153] L. Zhao, J. Wang, Y. Chen, Q. Wang, J. Cheng, and H. Cui. SIHR rumor spreading model in social networks. *Physica A: Statistical Mechanics and its Applications*, 391: 2444–2453, 2012. 11